Development of Heterogeneous Photocatalytic Water Purification Technology for Storm and Wastewater Reuse

A thesis submitted in fulfilment of the requirements for the degree of

Doctor of Philosophy

By

SABER AHMED

August 2011

School of Engineering and Built-Environment
Faculty of Sciences, Engineering and Health
CQUniversity
Rockhampton, Queensland 4702
Australia

ABSTRACT

Developing strategies for storm and wastewater purification to enable its reuse is an important issue within the wider water recycling paradigm. In response to the inadequacy of conventional water purification processes, heterogeneous photocatalytic oxidation process employing titanium dioxide (TiO_2) and UV light has emerged as a promising method to degrade and mineralise a wide spectrum of recalcitrant organic substances such as phenol, pesticides, herbicides and dyes into relatively innocuous end products e.g. carbon dioxide and water. Due to the lack of a suitable computational model, the application of this technique on an industrial scale poses a number of challenges which emphasize the need to understand further the hydrodynamic behaviour of the photocatalytic system and to investigate the ways of improving their performance. Inadequate mixing and turbulence in an immobilised photocatalytic reactor limits the performance of the reactor in terms of pollutant mass transport to the catalyst surface and pollutant degradation. The application of baffles and roughness elements can enhance the agitation in the system which is beneficial in maintaining a completely mixed reactor system and can add dissolved oxygen to the reactive medium. Under such conditions, the reactor becomes more effective to continuously transfer reactants (pollutants) to the catalyst surface and products to the reaction medium.

In this study, the performance of a flat plate photocatalytic reactor for degrading and mineralising storm and wastewater pollutants is investigated. This research aims to lay the groundwork for the performance of the flat plate photocatalytic reactor using computational fluid dynamics (CFD) simulation as a first step. Then an extensive study is performed to evaluate the role of mixing and turbulence promoters in the photocatalytic reactor to improve its design to meet the needs of a prototype photocatalytic reactor. The CFD simulation results are validated with experimentally measured data under various flow conditions. The experimentally measured velocity and benzoic acid concentration was found to be in good agreement with the results of the simulation. The results showed that the model can accurately predict the velocity and the outlet concentration of benzoic acid for various hydrodynamic conditions. Using various turbulence sub-models, the flow profile in the flat plate reactor was simulated for various flow conditions. No discernible variation on the flow profiles was observed regardless of the turbulence models tested. Furthermore, the performance of the reactor for the degradation of phenol as a model pollutant was predicted which was observed to decrease with increased flow rates.

To elucidate the role of mixing and turbulence promoters, additional investigation was conducted using various baffle arrangements in the reactive section of the flat plate reactor. Three different approaches were examined which involves the use of top and bottom baffles and top baffle with roughness elements respectively in the reactive module of the flat plate reactor. As to the top baffle, the distribution of local hydrodynamic parameters such as stream line contours, velocity field, static pressure, turbulence characteristics, and shear stress on the TiO_2 coated surface were observed to depend on baffle height under various flow regimes. Also, the influence of baffle spacing appears to govern the distribution of wall shear stress on the catalyst coated surface. The pressure drop was minimal for the low flow condition. The height of bottom baffle was found to improve the extent of recirculation zones and turbulence intensity in the reactive section. However, the loss of contact with the bottom baffle may impair the effectiveness of the reactive module since part of the catalyst coated surface can be unexposed to the polluted water stream.

In order to improve our understanding for effective use of turbulence and mixing promoters, a new approach that includes top baffles on the upper wall and a set of roughness elements on the bottom wall of the reactive section has been examined. Simulations have been performed for low and high flow conditions to investigate the distribution of significant hydrodynamic parameters in the photocatalytic reactor. In the combined reactive module, the pressure drop was dependent on the roughness element types at high flow rates and was independent of roughness elements at low flow conditions. The reported results suggest that the combined top baffle and roughness element can be a promising approach in terms of turbulence intensity and pressure drop at low flow regime which merits further attention to determine its suitability for large scale application of the flat plate reactor. The detailed local information of the simulated system can help understand the reactor behaviour for an accurate insight to the role of mixing and turbulence promoters. Although very encouraging results were found from this study, additional investigation into the hydrodynamic effects and the light model validation should be pursued to determine the next steps for model revision to improve its applicability. Further study is also necessary to fully define the potential of the flat plate reactor design in industrial settings including treatment of storm and wastewater with varying characteristics, reactor design scaling and the long-term stability of this design for solar-driven operation.

TABLE OF CONTENTS

LIST OF FIGURES

LIST OF TABLES

NOMENCLATURE

Symbols	Units	Descriptions
$C_{1}\varepsilon$	[-]	constant in *k*-ε model
$C_{2\varepsilon}$	[-]	constant in *k*-ε model
C_{μ}	[-]	constant in *k*-ε model
P	[Pa]	pressure
Re	[-]	Reynolds number
t	[s]	time
U	[m s^{-1}]	velocity
$\check{n}$	[-]	unit vector normal to the surface
J	[-]	diffusive flux
D_T	[m^2s^{-1}]	eddy (or turbulent) diffusivity for species concentration
Γ	[m^2s^{-1}]	diffusivity coefficient
k_{ap}	[min^{-1}]	first-order reaction rate constant,
k_{ph} & k_I	[mM m^{-1} $s^{-1}W^{-1}$]	first-order rate constants for phenol & intermediates
k_c,k_{mBA}	[ms^{-1}]	mass transfer coefficient
K	[-]	adsorption equilibrium constant
I	[W/m^2]	radiation intensity
C_i	[-]	concentration of species, *i*
Sc_t	[-]	turbulent Schmidt number
R_i	[-]	net production of species, *i*
Y_i	[-]	mass fraction of species, *i*
Greek symbols		
ρ	[kg/m^3]	density
τ	[-]	viscous stress tensor
κ	[m^2/s^2]	turbulent kinetic energy
ε	[m^2/S^3]	turbulent dissipation rate

$\sigma_k,\sigma_\varepsilon$	[-]	turbulent Prandtl numbers for κ and ε
μ, μ_t,	[kg/m s]	dynamic viscosity, turbulent viscosity
η_o, β	[-]	constant in RNG k-ε model
P_k	[-]	generation of turbulent kinetic energy
S	[s^{-1}]	modulus of mean rate-of-strain tensor
ν , ν_T	[-]	kinematic molecular and eddy viscosity
ω	[-]	specific dissipation rate
Ωij	[-]	mean rotation tensor
l	[m]	turbulence length scale
y^+	[-]	dimensionless wall distance
y_p	[-]	distance from the first computational node P to wall
δ	[m]	boundary layer thickness
θ	[-]	surface coverage
τ_w	[-]	wall shear stress
η	[-]	dimensionless efficiency
λ	[-]	wave length

Abbreviations

B	Bulk liquid phase
BA	Benzoic acid
FA	Formic acid
FVM	Finite volume method
TKE	Turbulent kinetic energy
SST	Shear stress transport
RSM	Reynolds stress model
RNG	Renormalization group
EWT	Enhanced wall treatment
EWF	Enhanced wall function
CV	Control volume

ACKNOWLEDGEMENTS

I would like to extend my sincere gratitude to CQUniversity for offering me a research scholarship throughout the tenure of my study. I wish to express my sincere thanks to every member of the Centre for Plant and Water Science (CPWS), Faculty of Sciences, Engineering and Health for their support, friendship and hosting me over the entire study period. This study is supported under an Australian Research Council (ARC) linkage grant (LP# 0776793) in collaboration with CM Concrete Private limited and Department of Public Works, QLD Government. The author gratefully acknowledges the financial support provided by ARC.

Firstly I would like to express my deep appreciation to my supervisors Associate Professor Mohammad Rasul (CQUniversity) and Associate Professor Richard Brown (Queensland University of Technology) for their support, guidance and encouragement. I am also thankful for their continuous counseling and insightful comments on my early ideas which transformed into a successful research work. I would also like to thank Dr Wayde A Martens and Massimiliano Vezzoli who assisted me in numerous occasions at QUT and offered necessary help whenever it was needed.

I would like to thank Dr Nur Hassan for his time and patience in discussing CFD related topics at different times. I owe a significant debt to Dr Esteban Duran to enhance and clear my conception on photocatalytic reactor modelling using CFD. Without his effective suggestions, enthusiasm and cooperation, the reaction modelling would not have been as meaningful, as well researched or completed on time. I am also thankful to Dr Suvash Saha and Dr M. A. Kabir for helpful suggestions. I wish to express my sincere appreciation to all of my colleagues here in the Office of Research and in the Faculty of Sciences, Engineering and Health. I am grateful to Mr Tim McSweeney, Ashfaq Ahmed Chowdhury, Dr Delwar Akbar and the Rockybangla community as a whole, for their assistance towards me. Their support and friendship has made this time more enjoyable.

And of course, I am thankful to my parents and all family members who provided constant support and encouragement, and unwavering positive attitude. It was a source of inspiration throughout this tenure.

DECLARATION

The work contained in this thesis has not been previously submitted either in whole or in part for a degree at CQUniversity or any other tertiary institution. To the best of my knowledge and belief, the material presented in this thesis is original except where due reference is made in the text.

(Saber Ahmed)

August , 2011

COPYRIGHT STATEMENT

(Saber Ahmed)

August , 2011

LIST OF PUBLICATIONS

Refereed Conference Papers

- **Saber Ahmed**, Rasul, M. G. Marten, W. and Brown, R. 2009. Sustainable reuse of storm/waste-water resources: A Review on solar photocatalytic purification processes. *Proceedings of the Central Region Conference-CREC 2009*, CD ROM, CQ University, Rockhampton, 14-15 August 2009, Australia (This paper won the conference "Best Paper Award")
- **Saber Ahmed**, Rasul, M.G. Marten, W. and Brown, R. 2009. A Review on the role of operating parameters in heterogenous photocatalytic water purification process for storm/waste water reuse. *Proceedings of the 5th WSEAS International Conference on ENERGY & ENVIRONMENT (EE'10)*, University of Cambridge, Cambridge, UK, February 23-25, 2010, ISBN: 978-960-474-159-5
- **Saber Ahmed**, Rasul, M.G. Marten, W. and Brown, R. 2009. Recent developments in photocatalytic degradation of pesticides and phenols in storm and wastewater effluent. *Proceedings of the Environmental Research Event, ERE-2010* conference held in June, 2010, Rockhampton, Australia
- **Saber Ahmed**, M.G. Rasul, R. Brown, N.M. S, Hasan. Computational fluid dynamics analysis of a flat plate photocatalytic reactor for storm and wastewater reuse. *Proceedings of the 13th Asian Congress of Fluid Mechanics*, 17-21 December 2010, Dhaka. ERA Ranking- A
- **Saber Ahmed**, M. G. Rasul, R. J. Brown and N. M. S. Hassan. Computational fluid dynamics modelling of flow in a photocatalytic reactor for wastewater treatment (Paper ref. Ahmed_206). *Proceedings of the NAFEMS World Congress 2011 (NWC11*), 24-26th May 2011, Boston, USA
- **Saber Ahmed**, M. G. Rasul, R.J. Brown and N. M. S. Hassan. CFD simulation of turbulence promoters in a water treatment reactor (Paper ref. Ahmed_243). *Proceedings of the NAFEMS world congress 2011 (NWC11)*, 24-26th May 2011, Boston, USA

- **Saber Ahmed**, M.G. Rasul, R. Brown, J.E. Duran. 2011. Flow field investigation in a water treatment reactor using computational fluid dynamics (Paper ref. AJK 2011-3061). *Proceedings of ASME-JSME-KSME Joint Fluids Engineering Conference 2011 AJK2011-FED*, July 24-29, 2011, Hamamatsu, Shizuoka, JAPAN
- **Saber Ahmed**, M.G. Rasul, R. Brown, J.E. Duran. 2011. Numerical simulation of flow in a photocatalytic reactor containing baffles (Paper ref. AJK 2011-3062). *Proceedings of ASME-JSME-KSME Joint Fluids Engineering Conference 2011 AJK2011-FED*, July 24-29, 2011, Hamamatsu, Shizuoka, JAPAN

Refereed Journals Articles

- **Saber Ahmed**, M.G. Rasul, W.N. Martens, R. Brown, M. A. Hashib. Heterogeneous photocatalytic degradation of phenols in wastewater: A review on current status and developments. *Desalination* 2011, 261(1-2), 3-18, Elsevier Publishing Ltd.
- **Saber Ahmed**, M.G. Rasul, W.N. Marten, R. Brown., M.A. Hashib. Advances in Heterogeneous Photocatalytic Degradation of Phenols and Dyes in Wastewater: A Review. *Water Air Soil Pollution* (2011) 215: 3-29 DOI 10.1007/s11270-010-0456-3(Springer)
- **Saber Ahmed**, M.G. Rasul, R. Brown., and M.A. Hashib. Influence of Parameters on the Hetererogeneous Photocatalytic Degradation of Pesticides and Phenolic Contaminants in Wastewater: A short review. *Journal of Environmental Management* 92(3), 2011, 311-330, Elsevier Publishing Ltd.
- **Saber Ahmed**, M.G. Rasul, R. Brown. CFD simulation of flow in a photocatalytic reactor containing baffles. (*In preparation)*

CHAPTER ONE

INTRODUCTION

1.1 Background and Significance

Secure and sustainable access to water is a precondition for human development. Water is valued for its industrial uses, recreational benefits and place in the landscape and environment. In the last century, the world population has multiplied by four times (from 1.6 billion people in 1900 to over 6 billion at present). In contrast, water consumption has multiplied by nine times (HDR, 2006). The demand for non-potable water for residential, irrigation, and industrial uses and potable water exceeds the limits of sustainable supply and impacts on the availability of water resources for users both in Australia and worldwide (Mitchell *et al.*, 2002). In a recent study on integrated water resource management, it is estimated that currently one third of the world's population lives in countries that experience medium to high water stress. This ratio is expected to grow to two thirds by 2025 (HDR, 2006). Current critical shortages of fresh water in Australia have emphasized the need for greater reuse and recycling of waste and storm water resources (Radcliffe, 2004, 2006). Reuse and recycling of storm and wastewater effluent is a key approach in a sustainable water management portfolio by water utilities both in Australia and in other parts of the world to minimize the growing water demand in a water scarce environment (DEH, 2002; Radcliffe, 2006). Reuse of storm and wastewater offers both a potential source of alternative water supply for non-drinking purposes and an option to further reduce the storm water pollution load in receiving waterways or bodies.

Storm water pollution is inherently related with human activities. Uses of detergent, oily substances from car washing, garden waste, and dropped litter contribute mostly to stormwater pollution. Lack of appropriate measures for reducing storm water pollution further influences water reuse, threatens human health and the functioning of aquatic ecosystems thereby reducing effective availability and increasing competition for water of adequate quality. Over recent years, storm water harvesting and reuse have emerged as a new field of sustainable water resource management. However, re-using water, including storm water, treated sewage effluent, treated industrial discharge and grey water, (household) waste water has been neglected to some extent. In Australia, currently 97% of urban runoff (Dillon,

2002) and 91% of effluent water is unproductive; thus, developing methods to recycle and reuse storm water and effluent water/waste water has become an important and urgent issue to ensure minimal environmental risk. Reuse of domestic and industrial effluent streams are also key strategies identified in the 2nd World Water Development Review (*http://www.unesco.org/water/wwap/wwdr2/table-contents.shtml*) along with the strategy of matching water quality to usable standards. The problem is not confined to increasing the reuse of waste water, but also the quality of water available in Europe it is estimated that in excess of 194,000 kg of benzene, toluene, ethylbenzene and xylenes were released directly into water in 2003, and there is an urgent need to remove these sorts of organic pollutants from the environment.

The frequent occurrence of pesticides and phenolic compounds in wastewater and associated environmental hazards has heightened concerns over public health due to their high toxicity and bio-recalcitrant structure (Eriksson *et al.,* 2007). These contaminants are being continuously released into the aquatic environment through various anthropogenic inputs. The detection of toxic organic compounds in storm and waste water effluent is reported to be a major obstacle as regards wide ranging acceptance of water recycling (DEC, 2006, Mahmoodi *et al*., 2007). Further, their variety, toxicity and persistence can directly impact the health of ecosystem and present a threat to humans through contamination of drinking water supplies e.g surface and ground water (DEH, 2002; Eriksson *et al*., 2007). The response has been the drive to achieve efficient removal of persistent organic pollutants from waste water effluent to lessen the risk of pollution problems from such toxic chemicals to enable its reuse. Consequently, considerable efforts have been devoted to developing a suitable purification method that can easily destroy these bio-recalcitrant organic contaminants. Due to their incomplete removal during wastewater treatment, they are ubiquitous in secondary wastewater effluents, rivers and lakes at low concentrations. Despite their low concentrations, these contaminants are a major health concern due to their extremely high endocrine disrupting potency and geno toxicity (Arques *et al*., 2007). These findings enunciate the necessity for further research on the removal of trace contaminants to minimize their accumulation, particularly prior to indirect or direct reuse of reclaimed water. While the advanced treatment technologies such as membrane filtration, Ozone oxidation and activated carbon adsorption have been shown to be instrumental in propelling water recycling forward, several obstacles coupled with the occurrence of toxic organic compounds in treated water

remain unresolved (Nghiem and Schäfer, 2006). An extensive amount of research has been focused on the application of advanced treatment processes to remove such contaminants in water recycling. While they have been generally demonstrated to be promising, numerous uncertainties and knowledge gaps persist (Nghiem and Schäfer, 2006). Removal of many of these pollutants is incomplete or results in other problems and risks. This study aims to address these issues by developing a technology for the treatment of storm and wastewater into re-useable or potable freshwater.

1.2 Motivation for this Study

Conventional water purification technologies such as activated carbon adsorption, membrane filtration, precipitation and air stripping can only transfer the contaminants from one phase to another phase rather than destruction. Moreover, it requires additional steps to handle and dispose the generated wastes. The presence of persistent and recalcitrant organic compounds in storm/waste water has prompted the use of the Advanced Oxidation Process. Heterogeneous photocatalytic oxidation (HPO) employing catalyst TiO_2 and UV light has emerged as an efficient method to remove a wide range of toxic contaminants from polluted waters as it can destroy a wide spectrum of organic compounds including the non-biodegradable ones into relatively innocuous end products such as CO_2 and H_2O. In this process, destruction of organic pollutants is caused by the presence of a semiconductor photocatalyst, an energetic light source and an oxidising agent. In addition, the process can be driven by solar UV and visible light which constitutes up to 5% of total solar light (Goswami, 1997). As a result development of a large scale photocatalytic reactor for water purification has received considerable interest. The efficiency of a photocatalytic reactor for water purification strongly depends on the hydrodynamics of the reactor and light intensity distribution, which is determined by a number of factors; namely (i) reactor geometry (Taghipour and Sozzi, 2005; Bandala and Estrada, 2007; Elyasi and Taghipour, 2007; Greens *et al*., 2006) (ii) presence of baffles (Periyathamby and Ray, 1999, Duran *et al*., 2010a, 2010b) (iii) UV lamp type with optimal size, shape and power (iv) optical properties of the medium, and (v) the nature of the reactor walls (Pareek *et al.,* 2003, 2005, 2008). Different reactors even those using the same lamp type can have significantly different efficiency for a particular water and contaminant due to reactor characteristics, such as lamp spacing, lamp configuration (horizontal, vertical, parallel, perpendicular and angled), place of inlet and

outlet piping relevant to lamps, baffles and other interior mixing devices (Taghipour and Mohseni, 2005; Sozzi and Taghipour, 2006). Enhancement of fluid mixing by means of internals such as baffles or by any means help to remove adsorbed contaminants and its intermediates from the catalyst surface and increasing available active sites for reaction, and thereby increasing the region of constancy of the overall rate for the pollutants (Sengupta *et al*., 2001; Periyathamby and Ray, 1999; Dutta and Ray, 2004). Fluid mixing is an important criterion in efficient photocatalytic reactor design as the transport of reactants from the bulk of the liquid to the catalyst surface determines the extent of fluid-catalyst contacting and overall degradation (Ray, 1998).

The design optimization of the photoreactor is also crucial to ensure its sustainable operation. Techno-economic analysis and feasibility evaluation require the development of a reliable model and the simulation of the photocatalytic reactor performance with various operating conditions and configurations (Taghipour and Sozzi, 2005; Alexiadis and Mazzarino, 2005). Over recent years, low-cost supported catalyst consisting of photoactive material deposited on the transparent and inert bodies improved significantly the feasibility of immobilized reactors. In terms of solar visible light utilization, flat plate photocatalytic reactors are considered an efficient solar photo-reactor for commercial applications because this reactor provides a high surface area to volume ratio and can treat polluted water effectively. Reactor modelling has received significant interest towards the implementation of this technology. In this perspective, new contaminants with higher degradation requirements increase the importance of reactor hydraulics. In spite of some work in the modelling of photo reactors for water disinfection, the modelling of photocatalytic reactors for water purification has received limited attention. There are several studies in computational fluid dynamics (CFD) modelling for light intensity distribution in photocatalytic reactors (Pareek *et al.*, 2003, 2004, Trujillo *et al*., 2007, 2008; Denny *et al*., 2009), but CFD has not been applied for the modelling of flat plate reactor for water purification. In addition, the optimization of reactor design containing mixing and turbulence promoters has seldom been the topic of reported studies and the determination of optimum process and design parameters still remains a challenge. Consequently a commercially competitive full scale photocatalytic water detoxification system has not yet been developed due to the lack of an efficient solar UV/ visible light absorbing catalyst, poor understanding of the design of the photoreactor and inadequate scale up strategies (Bahnemann, 2004; Trujillo *et al*., 2007). In order to utilize

solar UV and visible light, flat-plate photocatalytic reactors are generally regarded as efficient as they provide high surface area to volume ratio for water treatment. The increased interest in photocatalysis has resulted in a substantial amount of literature in this field, as evident in the numerous review articles published on this topic (Adesina, 2004; Bahnemann, 2004; Ahmed *et al.* 2011a, 2011b). The literature has consistently shown that the overall degradation rate is strongly limited by mass transfer resistance in particular when the TiO_2 catalyst is immobilized on the supporting material or reactor wall. To exploit this difference, several researchers have suggested that the introduction of a baffle which promotes turbulence and mixing would improve the performance of a photocatalytic reactor but this has not been demonstrated yet. Whilst there is a distinct need to explore the specific process steps involved in photocatalysis, there is also a necessity for sound photocatalytic system design and scale-up techniques to enable the prototype reactor for long-term operation (Cox, 2007). The paucity of information in the literature has highlighted the need for CFD simulation of a photocatalytic reactor containing a set of baffles under a variety of arrangements. By addressing the above limitations, this work aims to contribute to the current literature using CFD as a tool to advance our understanding. In order to apply this technique on a large-scale basis, the optimization of reactor design is crucial to minimize the overall treatment cost (Sozzi and Taghipour, 2005). The final focus of this study is to develop a heterogeneous photocatalytic water purification technology for storm and wastewater reuse. In this study, a flat plate photocatalytic reactor has been chosen to optimise its design using computational fluid dynamics (CFD) code FLUENT 6.3. Furthermore, the effects of different turbulence promoters such as baffles and roughness elements under varying flow conditions on the reactor performance were investigated to achieve higher efficiency. CFD allows for modelling simultaneously the hydrodynamics, kinetics and the light intensity distribution within the reactor. Since pollutants degradation rates and local incident radiation are strongly dependent on the reactor hydrodynamics, it is of paramount importance to investigate the role of reactor fluid dynamics on the performance of the reactor. Besides, the existence of dead and dark zones in the reactor may result in reduced performance of the reactor. CFD simulation can provide a better understanding of the flow field, concentration gradient field in the reactor even for complex geometry to improve its performance. CFD analysis suits the needs of photoreactor design, since it eliminates the cost and time required for experimentation in a full scale reactor.

1.3 Objectives and Scopes of the Study

An experimental investigation to evaluate the performance of the flat plate photocatalytic reactor initially designed and developed at QUT, was conducted first. Then a computational model of the reactor was developed and validated with experimental measurements; subsequently the reactor design was optimized, modified and evaluated under various operating conditions to achieve improved efficiency and higher pollutant degradation rate. The main focus was to develop an understanding for the immobilised flat plate photocatalytic reactor for reuse and recycling of storm and waste water.

The specific objectives of the study are divided into four main parts:

Experimental Investigation

- Investigate a flat plate photoreactor and its design to develop an appropriate combination of parameters for efficient pollutant degradation.

Model Development

- Develop a CFD model for the flat plate photoreactor using CFD code FLUENT for the prediction of reactor flow field using various turbulence models and validate CFD simulation with experimental results.
- Evaluate the performance of the flat plate reactor for photocatalytic degradation of model pollutant under various flow conditions.
- Examine the effect of inlet position on the flow field and mass transport of formic acid (FA) in the reactive section of the flat plate reactor.

Optimization of Mixing and Turbulence Promoters

- Understand the role of top and bottom baffles as mixing and turbulence promoters on the hydrodynamic performance of the reactor by simulating the most important hydrodynamic parameters; pressure drop, turbulence characteristics, and wall shear stress.
- Investigate the effect of baffle height, position and spacing on the hydrodynamic performance of the reactor using CFD simulation to optimise the baffle parameters that may potentially enhance reactor performance.

- Compare alternative reactor configuration that combine top baffle and roughness elements in the reactive section to identify reactor designs to enhance hydraulic efficiency by lowering energy consumption.
- Determine the effect of top and bottom baffle on the mass transport of formic acid (FA) in the reactive section of the flat-plate reactor.

Parametric Evaluation

- Evaluate the hydrodynamic parameters on the performance of the reactor.

The above objectives have been achieved using a research approach that includes both CFD modelling and experimental procedures. To simulate pollutant degradation, the combination of the available intrinsic kinetics with rigorous modelling of underlying fluid dynamics is needed to develop an integrated model. The kinetic parameters were obtained from preliminary pollutant degradation experimentation performed at QUT. The governing equations that were employed for CFD modelling of the reactor are the conservation of mass, momentum along with a suitable turbulence model. For the sake of simplicity, this work considered a first order kinetic expression to compute the photocatalytic degradation of a model pollutant, phenol in the flat plate reactor. In order to understand the effect of mixing and turbulence promoters, RNG k-ε model was employed. Using CFD modelling, the detailed local information (flow and hydrodynamic parameters profile) of the simulated system was obtained. This detailed information helps in developing a qualitative understanding of the process and a parameter study can reveal the bottlenecks and the range of applicability of the system. From the parametric studies, reactor design can be optimized for pollutant degradation.

The scopes of this study are divided into three principal components, as illustrated below in Figure 1.1, by splitting of the objectives of the investigation.

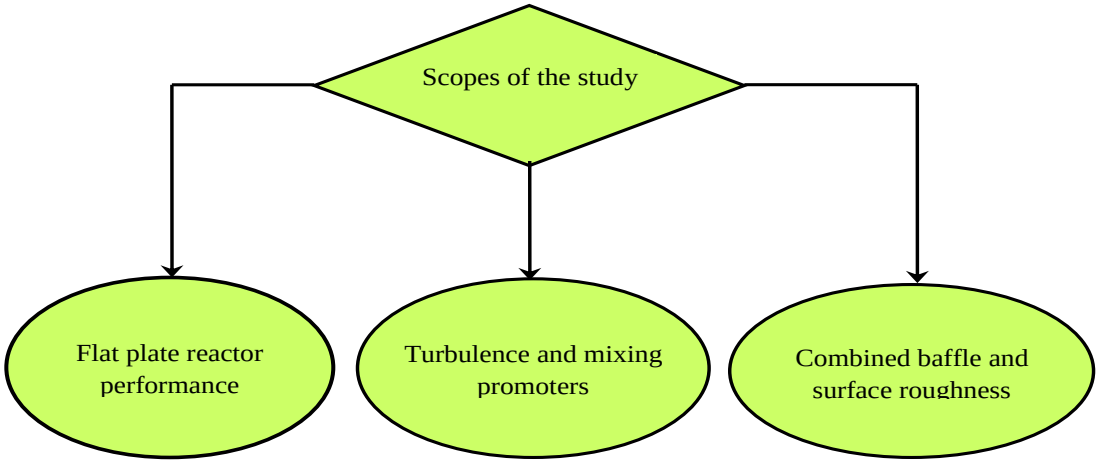

Figure 1.1 Hierarchical diagram of scopes of the study.

1.4 Outline of the Thesis

This thesis includes eight chapters. Chapters 1, 2, 3 and 4 include introduction, literature review, research approach and methodology respectively. Chapters 5, 6 and 8 contain the results and discussion, and conclusion respectively. Contents of the chapters are briefly summarized below.

In chapter 1, an overview of stormwater reuse and the motivation for this study are presented. This chapter also contains the objectives and scopes of the present investigation.

In chapter 2, the literature reviews relevant to the present study are reported. The literature survey covers the stormwater pollutants and treatment options, principle of heterogeneous photocatalytic oxidation process with parameters impacting the efficiency of the process, estimation of kinetic parameters, kinetic modelling of pollutant degradation and computational fluid dynamics modelling of photocatalytic reactor. In light of the available literature, various aspects of reactor design for a complete photocatalytic model are discussed. The gap in the current literature on the modelling of a photocatalytic reactor has been identified where further contributions can be made using CFD simulation. Finally a conclusion that highlights the motivation for this study has been drawn based on the literature survey.

In chapter 3, a detailed background and summary of the recent literature for the most important parameters that influence the performance of a photocatalytic reactor for pollutant degradation are presented.

In chapter 4, the approach and methodology as well as the reactor characteristics are presented in detail. The steps to obtain the experimental data in the flat plate photocatalytic reactor are described in depth. This chapter also discusses the assumption and justification for the development of a CFD model and the resulting observations in terms of the hydrodynamic behaviour of the system. The procedure for validation of a CFD model is described which requires the comparison of model prediction with experimental data to ensure the reliability of CFD simulation.

In chapter 5, a CFD model developed to simulate the flat plate reactor is described. The impact of various turbulence models on the flow pattern has been examined. The validation of simulated results is presented in this chapter. With certain constraints the CFD model has been applied to predict the pollutants degradation and to examine the effect of inlet position on the mass transport of pollutant using the species transport model. The results obtained are discussed in this chapter.

In chapter 6, the CFD modelling that encompasses the influence of top and bottom baffles on the hydrodynamic behaviour of the reactive section of the flat plate reactor are reported. Focus has been placed on the improvement of mixing for a range of baffle heights for both types of baffles. Also the differences in observed flow pattern in the reactive section are compared in terms of the most significant hydrodynamic parameters. The effect of low and high Reynolds number flow on the mass transport of model pollutant has been simulated and discussed.

In chapter 7, a new approach combining the top baffle and roughness elements on the bottom wall have been incorporated and tested using the method described in chapter 6. The CFD modelling has emphasised the computation of local parameters in the reactive section. Attention was paid on the differences in observed hydrodynamic properties in the reactive section for comparative evaluation.

The influence of low and high Reynolds number flow has been investigated. This approach results in a good description of the role of mixing and turbulence promoters in a photocatalytic reactor.

Chapter 8 contains a general conclusion and a summary of the major findings from this study. This chapter finishes with highlighting a number of recommendations for further development of the flat plate photocatalytic reactor for large-scale application.

CHAPTER TWO

LITERATURE REVIEW

2.1 Introduction

In response to the severe scarcity of fresh water in Australia, reuse and recycling of stormwater has received significant attention as it has been thought to be less polluted than real wastewater. Stormwater reuse offers versatile benefits in terms of reducing pollution loads in the nearby water bodies, and alternative sources of water supply for non-potable residential uses. Stormwater quality continues to be a major impediment for its large scale recycling. Urban stormwater contains elevated levels of gross pollutants including litter and course sediments (DEC, 2006). These are likely to present a potential threat to most stormwater reuse schemes through their potential impacts on treatment efficiency measures. From a few selected urban catchments in Brisbane (Goonetilleke *et al.*, 2005), typical primary pollutants in stormwater are reported to be dissolved organic carbon (DOC), suspended solids (SS), nutrients e.g., total phosphorous, total nitrogen during various storm events. Stormwater runoff has been identified as a source of water pollution for many water bodies. During the storm events, washing of road surfaces, parking areas, vehicles, and building materials contribute a wide spectrum of organic contaminants in stormwater runoff which eventually causes the deterioration of receiving waters. Recent studies have reported high level of pollutants in surface water runoff. A comparison of the quality of surface water runoff (Yufen *et al*., 2008) in various locations in the world is given in Table 2.1. Conventional water purification processes such as activated carbon adsorption, precipitation, air stripping, membrane separation and ion exchange have been identified to be inadequate for the removal of toxic and persistent organic pollutants present mostly in stormwater and industrial effluent. Biological systems seem to be a cost effective means for the removal of organic pollutants, however, it has also been shown to be ineffective for the removal of non-biodegradable organic pollutant. In addition, the presence of trace organics poses a detrimental effect on biological systems.

Table 2.1 Comparison of the quality of surface runoff in various locations.

Location	Surface	TSS(mg/L)	COD(mg/L)	BOD_5(mg/L)	TN[a](mg/L)	TP[b](mg/L)
Paris, France	Roof	29.00	31.00	4.00	-	-
Beijing, China	Roof	121.31	177.82	20.63	10.55	0.28
Wuhan, China	Roof	40-60	44.9-54.6	-	4.09-6.04	0.22-0.25
Paris, France	Road	92.5	131	36.00	-	-
Connecticut, USA	Road	15.8-47.8	-	-	0.7-8.0	0.155-0.24
Beijing (campus)	Road	567.17	179.35	17.17	7.4	0.71
Beijing (ring road)	Road	176.05	278.61	14.28	13.62	0.46
Wuhan, China	Road	350-650	60-110	-	4.9-6.04	0.30-0.53

([a]Total Nitrogen, [b]Total Phosphorous)

Most of the conventional treatment processes are based on the separation of pollutants from liquid phase to solid phase. None of them is a destructive process and as a result a further step is needed to handle the wastes. Advanced photocatalytic oxidation (APO) processes, which include both homogeneous photocatalytic oxidation and heterogeneous photocatalytic oxidation, have been introduced for the removal of toxic organic pollutants. Heterogeneous photocatalysis employing UV light and TiO_2 catalyst has gained much interest due to its effectiveness in degrading the toxic organic compounds including the non-biodegradable one to relatively harmless end products such as CO_2, H_2O and inorganic salts. APO technologies can be broadly divided into the following four groups:

a) Vacuum UV (VUV) photolysis

b) UV/oxidation processes

c) Photo-Fenton process and

d) Sensitized APO processes

2.2 Advantages of the Heterogenious Photocatalytic Oxidation Process

The main reason for the interest of photocatalytic processes and specifically the use of titanium dioxide (TiO_2) is the fact that the process can be carried out in ambient conditions that do not require costly oxidants and is less costly, non-toxic, and it can be easily activated by UV light (Al-Qaradawi and Salman, 2002). In this process polluted water stream reacts on the surface of photocatalyst material. It has following advantages:

I) It can deal with toxic and recalcitrant organic pollutants

II) It is an environmental process: complete mineralization of organics with CO_2, water and mineral anions (such as nitrate, sulphate or chloride) are the final products

III) The energy input is low, requiring only UV light, oxygen or air supply and mechanical mixing, while for example, wet-air oxidation has much higher energy and operational costs (EPA, 1998).

(IV) The disinfection process requires no added chemicals (oxidants or biocide) in homogeneous photocatalytic oxidation, a continuous feed of the oxidants is required.

(V) The threshold wavelength for semiconductor photocatalysts is 350-400nm, compared to the homogeneous photocatalysis process (250-300nm), making the use of solar radiation possible.

2.2.1 Steps in the Photocatalytic Oxidation Process

Photocatalytic oxidation process involves a number of steps for the generation of highly reactive hydroxyl radical for the degradation of a wide range of organic contaminants. The heterogeneous photocatalytic degradation process can be divided into the five following steps (Herrmann, 1999):

(1) Transfer of the reactants in the liquid phase to the surface

(2) Adsorption of at least one of the reactants

(3) Reaction in the adsorbed phase

(4) Desorption of the products(s)

(5) Removal of the products from the interface region

The photocatlytic reaction occurs in the adsorbed phase (Step no.3). The only difference with conventional catalysis is the mode of activation of the catalyst in which the thermal activation is replaced by a photonic activation as developed in the next paragraph.

2.2.2 Mechanism of TiO_2 Photocatalysis

In the photocatalytic oxidation process, organic pollutants are destroyed in the presence of semiconductor photocatalysts (e.g., TiO_2, ZnO) an energetic light source, and an oxidising agent such as oxygen or air. As illustrated in Figure 2.1, only photons with energies greater than the band-gap energy (ΔE) can result in the excitation of valence band (VB) electrons which then promote the possible reactions with organic pollutants. The absorption of photons

with energy lower than ΔE or longer wavelengths usually causes energy dissipation in the form of heat. The illumination of the photocatalytic surface with sufficient energy, leads to the formation of a positive hole (h^+) in the valence band and an electron (e^-) in the conduction band (CB). The positive hole oxidizes either pollutant directly or water to produce the hydroxyl radical •OH, whereas the electron in the conduction band reduces the oxygen adsorbed on the photocatalyst (TiO_2). The activation of TiO_2 by UV light can be represented by the following steps.

$$TiO_2 + h\upsilon\ (\lambda < 390nm) \dashrightarrow e^- + h^+ \quad (2.1)$$

$$e^- + O_2 \dashrightarrow O_2^{\bullet-} \quad (2.2)$$

In this reaction, h^+ and e^- are powerful oxidizing and reductive agents, respectively. The oxidative and reductive reaction steps are expressed as,

Oxidative reaction:

$$h^+ + \text{Organic(R)} \dashrightarrow \text{Intermediates} \dashrightarrow CO_2 + H_2O \quad (2.3)$$

$$h^+ + H_2O \dashrightarrow \bullet OH + H^+ \quad (2.4)$$

Reductive reaction:

$$\bullet OH + \text{Organic (R)} \dashrightarrow \text{Intermediates} \dashrightarrow CO_2 + H_2O \quad (2.5)$$

Hydroxyl radical generation by the photocatalytic oxidation process is shown in the above steps. In the degradation of organic pollutants, the hydroxyl radical generated from the oxidation of adsorbed water where it is adsorbed as OH^-, is the primary oxidant; and the presence of oxygen can prevent the recombination of an electron-hole pair. The •OH attacks organic compounds e.g. chlorinated aromatics, aniline and nitrophenols which result in various reaction intermediates depending on the nature of the compounds. The resulting intermediates further react with •OH to produce final degradation products such as CO_2 and H_2O. In the photocatalytic degradation of pollutants, when the reduction process of oxygen and the oxidation of pollutants do not advance simultaneously, there is an electron accumulation in the CB, thereby causing an increase in the rate of recombination of e^- and h^+ (Hoffman *et al*., 1995; Herrmann, 1999).Thus it is of paramount importance to prevent electron accumulation in efficient photocatalytic oxidation. In photocatalysis, TiO_2 is by far the most widely studied system due to its high activity, desirable physical and chemical properties, low cost, and availability. Of three common TiO_2 crystalline forms, anatase and rutile forms have been investigated extensively as photocatalysts. Anatase has been reported to be more active as a photocatalyst than rutile. Similar oxidation pathways to those of TiO_2

are confirmed in ZnO photocatalyst including the formation of •OH radical and the direct oxidation by photogenerated holes, etc. ZnO is reported to be as reactive as TiO_2 under concentrated sunlight, since the band gap energy of ZnO is equal to that of TiO_2, i.e., 3.2eV. Some other metal oxides including CeO_2, SnO_2, WO_3 and CdS have also been examined for organic contaminants degradation (Swarnalatha and Anjaneyulu, 2004; Ji *et al*., 2008, 2009; Lin *et al*., 2008). Different light sources such as UV lamps and solar radiation have been used in the photocatalytic degradation of various organic pollutants dominant in stormwater and wastewater effluent (Bahnemann *et al*., 2007; Lachheb *et al*., 2008).

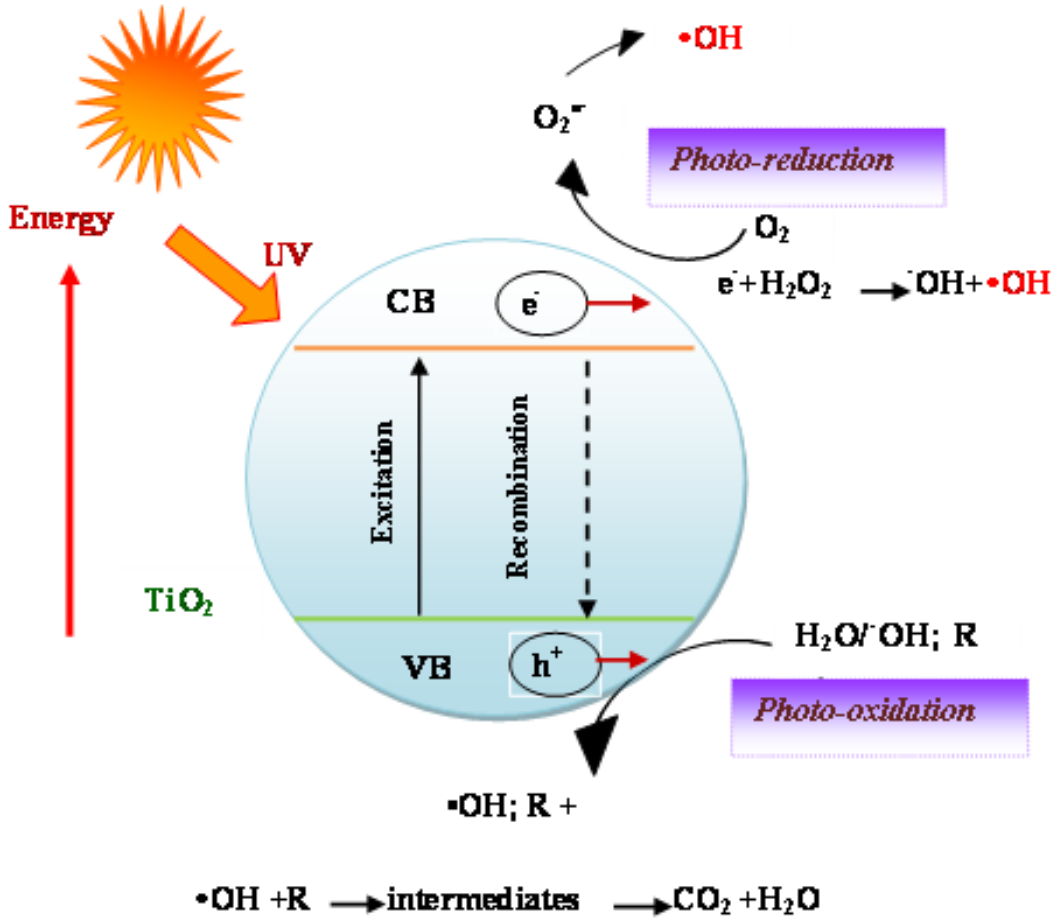

Figure 2.1 Schematic diagram illustrating the principle of TiO_2 photocatalysis.

The most important elements for a photocatlytic system are the catalyst, the light source and the reactor configuration. A number of semiconductors including titania have been investigated to date. Of these solids, WO_3, α-Fe_2O_3, SiO_2, ZnO, and ZnS all show activities lower than that of TiO_2. The band gap energies for various catalysts are shown in Table 2.2.

As a photocatalyst, TiO_2 has been studied mostly because of its high activity, desirable physical and chemical properties and availability. The rutile form has a band gap of 3.0eV and can be excited by light with wavelengths shorter than 414 nm, while the anatase form has a band gap of 3.2 eV and can be excited by light with wavelengths shorter than 387nm (Litter, 1999). Of these crystalline forms, anatase has been reported to be more active as a photocatalyst than rutile.

Table 2.2 Catalyst types with bandgap energy **(**ΔE_{bg}) for photocatalytic activity.

Catalyst Type	ΔE_{bg} **(eV)**
WO_3	2.8
α-Fe_2O_3	3.1
Zns	3.2
ZnO	3.6
TiO_2-Anatase	3.2
TiO_2-Rutile	3.0

A semiconductor photocatalyst for the destruction of water contaminants should possess the following qualities (i) resistant to chemical attack over appropriate range of temperature and pH; (ii) non-toxic; (iii) insoluble in water, and (iv) inexpensive.

2.2.3 Kinetic Model of the Photocatalytic Oxidation Process

In the heterogeneous photocatalytic oxidation process, the primary oxidizer, hydroxyl radical, is a highly reactive and it cannot travel far away from the catalyst surface (Turchi and Ollis, 1990) before reaction occurs. The photocatalytic reactions between hydroxyl radicals and the reactants occur mainly at the catalyst surface. The most favourable condition would be with the reactants adsorbed onto the catalyst surface since the redox reaction requires orbital overlap of the electron donors and acceptors. Moreover, trapping of electrons and holes also requires the presence of adequate oxygen to prevent recombination. Thus, adsorption is one of the significant processes for determining the photocatlytic reaction rate. The photocatalytic degradation rates of organic compounds are often modelled with the Langmuir-Hinshelwood kinetic equation with its two limits: the pseudo-zero order and the first order kinetic model (Turchi and Ollis, 1989, 1990).

In this model, the reaction rate (R_i) is proportional to the fraction of surface (θ) covered by the substrate (Equation 2.6):

$$R_i = -\frac{dC_i}{dt} = k\theta = \frac{kKC}{1+kKC} \qquad (2.6)$$

where C is the substrate concentration (mol/m^3), t is the irradiation time (min), k is the true rate constant (min^{-1}) which depends on experimental conditions and K is the adsorption equilibrium constant (m^3/mol). According to the Langmuir-Hinshelwood (L-H) reaction kinetics model, for dilute solution ($C_0 < 10^{-3}$ M), the reaction is of the apparent first order, whereas the reaction is reduced to the zero order at high concentration ($C_0 > 5 \times 10^{-3}$ M) (Herrmann, 1999).When the substrate concentration is low, the term KC can be neglected. In this case the reaction is essentially an apparent first order reaction and after integration, Equation (2.7) can be simplified in Equation (2.8):

$$\ln(\frac{C^o}{C_t}) = k_{ap}t \qquad (2.7)$$

where k_{ap} is the apparent rate constant (min^{-1}) of a pseudo first-order reaction.

Considering the adsorption of reactant "*i*" in the presence of other reactants, intermediates, inhibitive ions, and the reaction rate of reactant "*i*" can be expressed by a modified Langmuir-Hinshelwood (L-H) equation:

$$R_i = -V\frac{dC_i}{dt} = \frac{AK_oK_iC_i}{1+K_iC_i+\sum_{j\neq i}K_jC_j} \qquad (2.8)$$

In photocatalytic oxidation of organics where oxygen is an electron scavenger, the reaction rate and Langmuir adsorption constants "K_i and K_j" are dependent on the radiation intensity on the catalyst surface, oxygen concentration in the reactive medium, nature of the species *i* , catalyst forms, temperature, and pH (Turchi and Ollis, 1990).

The rate constant, "K_o" can be expressed by the Equation (2.7) below (Chen and Ray, 1998; Turchi and Ollis, 1989; Okamoto *et al*., 1985a, b),

$$K_o = \frac{k_oK_{O_2}C_{O_2}}{1+K_{O_2}C_{O_2}}\frac{I^n}{I^n{}_o} \qquad (2.9)$$

where exponent "n" is dependent, among other factors, on the radiation intensity on the catalyst surface. At low radiation intensity "n" equals to "1" while at high radiation intensity it is 0.5 (Blake *et al.*, 1991; Ollis *et al*., 1991). When the radiation intensity is so high that the limiting factor becomes the transfer of reactants to the reaction sites (i.e., the catalyst surface), an increase in radiation intensity will not result in any increase in reaction rates (Ollis *et al*., 1991). The radiation intensity at which "n" changes from "1" to "0.5" is a function of the redox system being examined (Parent *et al.*, 1996) and has been reported to be between 2 and 170 Wm^{-2} (Reeves *et al*., 1992; Blake *et al*., 1991; Al-Sayyed *et al*., 1990).

Besides the power relationship, the rate coefficient and radiation intensity data can also be fitted into other types of expressions such as (Ray and Beenackers, 1997),

$$K_o = \frac{k_s a I^b}{1 + a I^b} \qquad (2.10)$$

In this equation, *a*, *b*, and k_s are constants. As stated earlier, the reactants need to be provided from the bulk of the liquid to the reaction site, the catalyst surface. This means that at steady state the mass transfer rate of any reactant "*i*", r_{mi}, will be equal to the consumption rate of that reactant due to the reaction:

$$r_{mi} = r_i = k_L (C_i - C_{is}) \qquad (2.11)$$

In general, kinetics are modelled employing the Langmuir-Hinshelwood,L-H, convention. L-H is a simple model for describing surface reactions. Even though the model is not rigorous, it provides an acceptable expression for modelling kinetics on surfaces for many systems. L-H has been used successfully in describing the photocatalysis system (Lea and Adesina, 1998; Adesina, 2004). Competitive adsorption between organic compounds and water and between organic compounds has been reported (Pareek and Adesina, 2003). Multi-site models have been used, but there are rarely adequate data to justify the use of the more complicated rate form. As the complexity of the L-H rate form is increased, the expression acts as more as a curve-fit than a physical model. In order to avoid complicacy during this study, a simple L-H expression or a first order can be used to obtain the photodegradation rate (kinetic parameters).

2.2.4 Radiation Wavelength and Light Intensity

TiO_2 absorbs photons of radiation below the visible range of the light spectrum. Therefore, the generation of electron-hole pair via photoactivation of TiO_2 requires irradiation with light of wavelength less than or equal to 384nm, with an absorbance maximum at approximately 340 nm. Most of the studies reported in the literature have been carried out in the range of wavelengths of 320-380nm and the light that provides the required radiation field can be generated by artificial lamps or by solar radiation (Alfano *et al*., 2000; Cassano *et al.*, 2000). In a photocatalytic reactor, UV-A (320- 380nm) radiation can be obtained by fluorescent low-pressure mercury lamps emitting low-intensity UV-A radiation. Medium pressure mercury lamps have also been used, which emit high intensity UV light in short, medium and long UV spectrums. Nevertheless, short (UV-C; 200-280nm) and medium (UV-B; 280-320nm) UV radiation emitted by the mercury lamp has been reported to be cut off by the photoreactor material with the exception of material which is made of quartz. A number of studies have also been reported to increase the efficiency with UV-C radiation than UV-A for the degradation of certain organic materials (Alfano *et al*., 2000; Demeestere *et al*., 2004). Direct photolysis and the higher probability of trapping of electron-hole pairs with shorter wavelength excitation were thought to be the possible reasons for such an effect. Solar photochemical processes use only high-energy short wavelength photons. Depending on the geographical location, the solar radiation intensity typically range from 15 to 50 Wm^{-2} (Bahnemann, 2004).

The radiation intensity is a common parameter in photocatalytic systems as the catalyst activation and hence the reaction rates are proportional to this intensity. At low radiant values it has been reported that the reaction rate is linearly proportional to the intensity. As this intensity increases the rate becomes square-root dependent, whilst at high radiation intensities the reaction rate is independent of the radiation. Also it is essential to achieve efficient exposure of catalyst to light irradiation. Without photons of appropriate energy content, the catalyst shows no activity (Ray, 1998). The probability for a photon to be absorbed by TiO_2 and utilized in electron-hole pair generation is dependent on its energy level. The UV illumination factor is of utmost important since the amount of catalyst that can be activated determines the water treatment capacity of the reactor.

2.2.5 Oxygen Concentration

The role of oxygen in photocatalytic systems has been widely investigated in the literature. A general stoichiometry for heterogeneous photocatalytic oxidation can be expressed as follows (Hoffman *et al*., 1995),

$$C_xH_yX_z + (X + \frac{y-z}{4})O_2 \xrightarrow{h\gamma} xCO_2 + zH^+ + zX^- + (\frac{y-z}{2})H_2O \qquad (2.12)$$

Given the reaction stoichiometry of this equation, there is no photocatalytic mineralization in the absence of oxygen. Oxygen is needed for complete mineralization and does not compete with other reactives elements during the adsorption on TiO_2 surface since the places where oxidation takes place are different from those of reduction. The use of oxygen in the photocatalytic oxidation process acts as an electron scavenger due to its strong electrophilic nature. The oxygen prevents the recombination of e^-/h^+ by forming superoxide radicals $O_2^{\bullet-}$ which reacts directly. The minimisation of e^-/h^+ recombination enables the system to maintain a charge balance necessary for the photocatalytic redox process. Thus negligible destruction was observed in the absence of oxygen (Herrmann, 1999; Dijkstra *et al*., 2001). The amount of oxygen in solution can be determined by the oxygen partial pressure which has a significant influence on the reaction rate (Bangun and Adesina, 1998). However, air can safely be used on commercial-scale operation instead of pure oxygen, which can substantially decrease the operating costs (Bhatkhande *et al.*, 2002). In chapter 3, detailed descriptions on the role of important parameters that influence the photocatalytic degradation of various organic contaminants are presented.

2.2.6 Configurations of the Photocatalytic Reactor

Numerous classical and novel photocatalytic reactor configurations have been investigated to date. Of these photocatalytic reactors, a few have been patented in recent years, but none has so far been upgraded to pilot scale level. In a photoreactor, the catalyst has to be activated by incident light. The major parameter that is currently assessed with respect to illumination is the amount of illuminated surface per unit volume of reactive liquid (m^2/m^3) inside the reactor. This value has been denoted as kappa, *k*, and determined for various photoreactors by Ray and Beenackers (1998). Based on the arrangement of the light source and reactor vessel, all these reactor configurations can be categorized in the following types.

- **Slurry reactor**: The catalyst (TiO_2) coated surface does not take into account the catalyst specific surface. The efficiency of suspended catalysts has been demonstrated to be superior compared to the immobilized catalyst (Parent *et al.,* 1996). This can be attributed to the enhanced mass transport in suspended form. However, the cost incurred for catalyst recovery makes the slurry system impractical.

- **External type-annular reactor**: This is a classical annular reactor in which a lamp is placed inside the inner tube while the reaction liquid is flowing through the annulus and inside of the outer annulus is coated with catalyst.

- **Immersion type-with classical lamps**: In this reactor, several lamps of equal diameter are coated with catalyst on their surfaces. The lamps are immersed inside the reaction liquid.

- **Annular photoreactor:** In this reactor configuration, the lamp is placed at the centre of the cylindrical vessel. One of the major limitations is the inadequate suspension of photocatalyst inside the reactor. It is an efficient and simple means for continuous operation.

- **Distributive type-with hollow tubes**: The reactor is a rectangular vessel in which light conductors as glass slabs (or rods) coated on their outside surfaces with catalysts are embedded vertically. The lamps together with reflectors are placed on two sides of the reactor while liquid enters and exits from the other two sides. Light rays entering the conductors through one end are repeatedly internally reflected down the length and at each reflection come in contact with the catalyst present around the surface of the conductors (Ray and Beenackers, 1998).

Various photoreactors even those using the same lamp type can have significantly different efficiencies for a particular water and contaminant due to reactor characteristics, such as lamp spacing, lamp configuration (horizontal, vertical, parallel, perpendicular and angled), placing of inlet and outlet piping relevant to lamps, numbers of pipe diameter upstream and downstream of the reactor, baffles and other reactor mixing devices.

2.2.7 Mode of TiO_2 addition in the Photocatalytic Oxidation Process

In photocatalytic degradation using UV/TiO_2 system, one of two modes of TiO_2 application is adopted. There are a) TiO_2 immobilized on support materials e.g., quartz sand, glass, glass wool matrix, ceramic membrane, noble metal etc., and b) TiO_2 suspended in aqueous medium. In terms of technical application, immobilized TiO_2 is preferable compared to suspended TiO_2 since it does not require additional post treatment for the recovery of catalyst particles (Thiruvenkatachari *et al*., 2008) after oxidation stage.

Merits of Immobilized Photoreactor

Over the last few decades, laboratory scale experiments have been conducted using suspensions of extremely small particles of the catalyst for the treatment of aqueous phase (slurry). The small catalytic particles are characterized by a very high specific surface area, but this reactor configuration leads to serious problems in scaling up the process to large-scale plants. In fact, the presence of a fine solid phase gives rise to a rapid fouling of the radiation sources (UV lamps) and to the relevant additional costs due to the separation process (removal of the catalyst). In the last decade, the development of low-cost supported catalysts consisting of photoactive materials deposited on transparent and inert bodies as shown in Table 2.3 improved significantly the feasibility of the process by the use of immobilized reactors. In contrast, post-treatment for the separation of catalyst-water mixture is not required for immobilization systems. However, this type of system may suffer from a range of limitations. Compared to slurry systems, immobilized systems usually possess much a lower catalyst surface area. This is particularly true for conventional photoreactor configurations. Moreover, mass transfer becomes the limiting factor, especially at low pollutant concentrations, under high radiation intensities, or under unfavorable hydraulic conditions (Ollis *et al.,* 1991; Chen *et al.,* 2000). Mass transfer limitations could be minimized through proper design and operation of the immobilized systems (Zhou and Ray, 2003; Dijkstra *et al*., 2001, 2002; Chen *et al*., 2001; Sabate *et al.*, 1991). Moreover, catalyst fouling and regeneration is also a complementary phenomenon resulting from the operation of this type of reactor. Although the findings of photocatalysis seems to be promising for application in real scale, the application of a photocatalytic reactor is limited by the lack of appropriate photoreactor models and design, size limitation as well as the materials of construction for the reactor vessel.

Engineers dealing with this task should choose, for example, UV lamps with optimal size, shape and power. The lamps should also be placed in the reactor with a proper configuration in order to maximize the efficiency of the catalyst. The following section highlights some recent developments in solar photocatalytic reactors for water treatment.

Table 2.3 TiO_2 supported materials in immobilized reactors

Supported Materials	**Reference**
Quartz	Tada and Tanaka, 1997; Fernandez *et al*., 1995
Glass	Ray and Beenackers, 1998; Ohko *et al*., 1997; Zhang *et al*., 1994
Glass wool	Zhang *et al*., 1994
Fibre glass	Serrano and de Lasa, 1997; Pugh *et al*., 1995; Zhang *et al*., 1994 ; Al Ekabi *et al*., 1993
Stainless steel	Ha *et al*., 1996: Fernandez *et al*., 1995, Pacheco *et al*.,1993
Sand	Lee, 1995; Zhang *et al*., 1994; Mathews, 1991
Teflon	Low and Mathews, 1990

2.2.8 Some Pilot-Scale Solar Photocatalytic Reactors

In recent years, there has been a significant amount of research and development in the area of solar photocatalysis. Solar photocatalytic oxidation can be considered as a "Sustainable Technology" as it can use free solar photons and a recoverable, environmentally benign solid TiO_2. In recent years significant progress has been made in the pilotscale solar photocatalytic reactor (Bahnemann, 2004; Malato *et al.*, 2003). Various types of solar reactor have been investigated at pilot scale level. On the basis of the concentration reached in them and the nature of TiO_2 addition, solar reactors can be classified into (I) non-concentrating, low concentration or low temperature systems (up to 150^oC) (II) medium-concentrating, or medium temperature systems (from 150 to 400^oC) (III) high concentrating high temperature systems (over 400^oC) (Malato *et al*., 2004). In the solar photocatalytic reactor, solar radiation is concentrated using a parabolic reflector surface. Compared to the non-concentrating reactor (one sun system), a concentrating reactor requires a smaller volume for the same light-harvesting area.

In addition, these reactors can be run for higher flow rates and pressures thus showing enhanced mass transfer rates (Alfano *et al.*, 2000). On the contrary, the non-concentrating reactors are promising for sunlight capturing as it can reduce the optical losses in the absence of a reflector. Moreover, the direct and the diffuse components of solar radiation can be used through these reactors. This permits their use under unfavourable weather conditions. However, the non-concentrating system suffers from the requirement for low pressure and laminar flow operation and large reactor volumes. Solar reactors have been operated in both continuous and batch mode. In continuous mode, the reactor area and the flow rates must be taken into account in order to achieve enhanced pollutant destruction. As the UV radiation intensity decreases, the flow rates through the solar reactor must be decreased or the number of reactors has to be increased (Alfano *et al.*, 2000). In the batch mode operation, the contaminated water is held in a tank and continuously recirculated through the reactor until the desired pollutant degradation is achieved. Despite the immense potential of solar photocatalysis for water detoxification, there has been limited application of this technology on a commercial or industrial scale. In recent years, several installations based on non-concentrating collectors have been erected at Platforma Solar de Almeria in Spain. Over the last decades, several solar reactors for water decontamination have been tested; the four most used are described briefly below:

- **Parabolic Trough Reactor (PTR):** It has a parabolic shaped reflective concentrating surface (surface covered with reflective polymer film) with the reaction pipe in its focal line. An ideal reflective surface must be highly UV-reflective, weather resistant for long time and cost effective. This reactor is not suitable for photocatalytic application as most of the photons are not used efficiently. Its optical and quantum efficiency is low. TiO_2 is either used as suspension in the tube or fixed onto the surface (Figure 2.2).

- **Compound Parabolic Collecting Reactor (CPCR):** The CPCR reflector consists of two half circular profiles side by side and a parabolic continuation at both outer sides of the circles. The reaction tube is placed in its focal point which is just above the connection of two parabolic profiles Figures 2.3a and 2.3b (Malato *et al.*, 2004). This shape seems to be the best option for solar photocatalytic process. Its optical and quantum efficiency is high because of its ability to use both direct and diffuse solar radiation (Malato *et al*., 2007).

- **Double Skin Sheet Reactor (DSSR):** It consists of a non-concentrating double-skin sheet (PLEXIGLAS) structured box type photoreactor. Its optical and quantum efficiency is higher than PTCs as it can use both direct and diffuse component of solar radiation. The suspension containing the polluted water together with the photocatalyst meanders through the channels in the box (Figure 2.4b).

- **Thin film fixed bed reactor (TFFBR):** It consists of inclined glass plate coated with photocatalyst. The polluted water flows along the inclined surface forming a very thin film (Figure 2.4a). Its construction cost and energy consumption is low.

Figure 2.2 Parabolic trough with two axis solar tracking (left) and single axis solar tracking (right) (Malato *et al.*, 2007).

(a) (b)

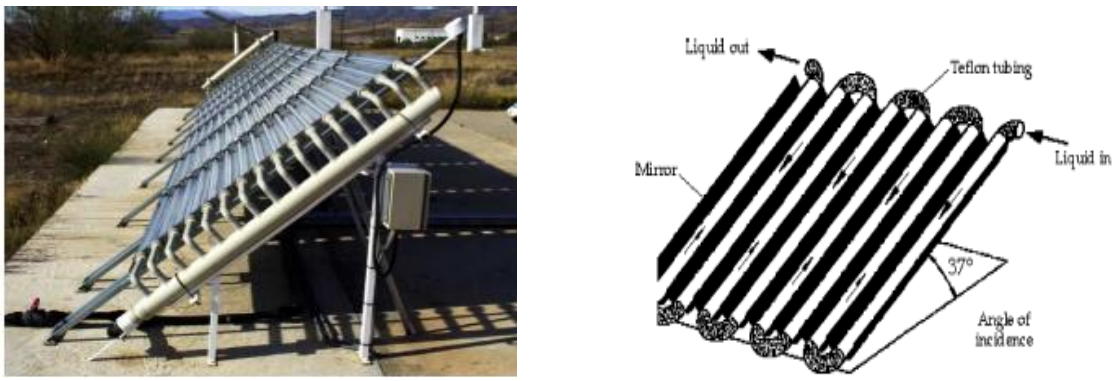

Figure 2.3 CPC reactor at the Plataforma Solar de Almeria (PSA) in Spain (Malato *et al.*, 2002).

a)

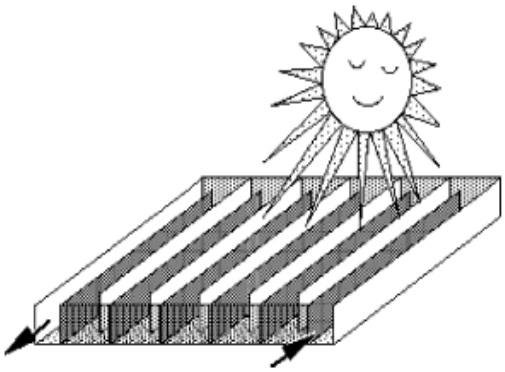

b)

Figure 2.4 TFFBR reactor at the Plataforma Solar de Almeria in Spain (PSA) (a) and b) schematic view of a DSSR reactor (Bahnemann, 2004).

A pilot plant has been built at the site of a textile factory in Tunisia (Menzel Temine) which has been published recently. The reactor can be operated in parallel or with cascade flow and in continuous or recycling mode respectively (Bahnemann, 2004). Site specific treatability studies and the use of pre-treatment steps are crucial for successful application of the solar photocatalysis process (Goswami, 1997). It has been demonstrated that the solar photocatalytic process will be an appropriate technology as the final steps of treatment of biologically or physically treated waste water, and industrial application of this process on a larger scale is in strong demand for cheap photocatalysts with higher activity to be competitive with treatment methods already established in the market (Blanco *et al.*,2007). The present study aims to develop a computational fluid dynamics model for optimization of photocatalytic reactors design starting from basic process data like: the flow rate to be treated, the reaction kinetics and the final conversion required. The following sections deal with aspects of reactor modelling and the previous investigation on reactor modelling using CFD.

2.3 Importance of Hydrodynamics in a Photocatalytic Reactor

An analysis of the light intensity field within the photoreactor is required for the modelling of photocatalytic reactors (Cassano *et al*., 1995). This analysis is related with the modelling of the fluid dynamics and the reaction kinetics, results in integro-differential equations which always requires significant numerical computational efforts. Further improvement of photocatlytic treatment on an industrial scale can be facilitated by the availability of simpler mathematical models that retain the essential elements of a rigorous model and that can be easily used for scale up and design. Due to the low pollutant concentration, thermal energy

balance can usually be neglected from the reaction scheme for the radiation modelling of a photocatalytic reactor (Cassano *et al*., 2000). The development of a photocatalytic reactor model requires the inclusion of a number of sub-models. These are a radiation emission model, a radiation absorption-scattering model, a kinetic model and a fluid dynamic model. A key aspect of the modelling procedure is the calculation of the Local Volumetric Rate of Photon Absorption (LVRPA) at each point of reaction space, which requires solving the radiative transfer equation (RTE) in the reaction space. In practice, the RTE can be simplified by combining a simplified radiation emission model of the light source with a simplified radiation absorption-scattering model in the reaction space and performing a radiation balance in the reaction space. Most of the earlier studies conducted in this regard have focused on the modelling of radiation field for various reactor configurations.

The role of physical effects such as fluid dynamics in a photocatalytic reactors, regardless of its size, is difficult to eliminate from the chemical reaction processes (Jarandehei and Visscher, 2009). They have an influence on the photocatalytic reaction parameters and can complicate the analysis and scale-up of the reactor. The kinetic rate data obtained from experimental units without due considerations to the physical effects can result in an incorrect rate expression and may result in ineffective operation of photocatalytic water purification reactor if used in scale-up. In order to ensure efficient operation of a photocatalytic water treatment system, non-chemical or physical aspects of reactor behaviour that could affect the stability and controllability of the entire unit should be taken into consideration. In addition, little attention has been paid towards the development of a realistic hydrodynamic model for better understanding of fluid flow properties in photocatalytic reactors (Jarandehei and Visscher, 2009). Hence, it is important to make careful studies of interacting mechanisms and to separate their effects from purely chemical processes (Ku *et al*., 2005; Ma and Ku, 2006; Wang *et al*., 2003).

There have been numerous investigations on kinetics of photocatalytic reactions for different operational conditions. However, the effect of fluid flow rate on degradation rates was not tested by some of the researchers which consequently results in the development of kinetic models not necessarily under the kinetically controlled region (Wang *et al*., 2003; Ku *et al*., 2005). Most researchers used simple flow models, plug flow and completely mixed, to account for the effects of mass transfer processes (Demeesttere *et al*., 2004; Imberdorf *et al*., 2006; Ku *et al*., 2005; Bouzaza *et al*., 2006). The hydrodynamic behaviour of most of the

actual reactors differs from these two limiting conditions. This variation may be result of the non-uniformity in flow field, velocity fluctuation due to molecular or turbulent diffusion, by short-passing and channelling of fluid, by the presence of stagnant regions of fluid caused by the internals, reactor shape or by the recycling of fluid within the reactor as a result of agitation (Jarandehei and Visscher, 2009). A realistic hydrodynamic model is important which would be interrelated for more accurate estimation of kinetic parameters and reasonable prediction of the reactor performance as well as better understanding of fluid flow properties. In this regard, a two dimensional mass balance model taking into account the intrinsic kinetics, as well as mass transfer rate processes have been developed (Changrani *et al*., 2000; Lin *et al.*, 2006; Wang *et al*., 2005). While these models have been helpful in providing an understanding of the fluid dynamics, they can rarely be applicable for engineering analysis and design for new equipment with unknown parameters (Jarandehei and Visscher, 2009). Computational fluid dynamics modelling tools can facilitate the reactor engineering tasks with minimal experimentation on pilot scales together with a high degree of reliability. Computational fluid dynamics (CFD) is being increasingly used for the design of new reactors to analyse flow and performance. For simulation of reacting flow systems, the mixing, transport, and production/consumption of chemical species must be solved through species transport equations together with the mass and momentum equations. CFD has been widely applied in several areas of chemical engineering such as fluidization (Cooper and Coronella, 2005; Grace and Taghipour, 2004, Vanderhoef *et al*., 2004) and multiphase flow systems and it has also gained wide interest for simulation of photocatalytic reactors in recent years (Castrillon *et al*., 2006; Mohseni and Taghipour, 2004; Pareek *et al*., 2003; Salvado - Estivill *et al.*, 2007; Sozzi and Taghipour, 2006b ; Tagiphour and Mohseni, 2005; Duran *et al*., 2010a; 2011b).

2.4 CFD Modelling Equations

Computational Fluid Dynamics (CFD) is a well established technique for numerically solving the equations of fluid dynamics over both space and time, including the conservation of mass, conservation of momentum, and conservation of energy. Using appropriate boundary and initial conditions, these governing equations can describe both the physical and chemical changes within a reactor. A CFD model for a photocatalytic reactor can also include the spatial variations of radiation field within the reactor.

The equations that govern the transport of fluid flow include the mathematical statements for conservation of mass, momentum, and energy. For an incompressible fluid, the time averaged equations for the conservation mass, or the continuity equation, can be expressed as,

$$\frac{\partial u_x}{\partial u_x} + \frac{\partial u_y}{\partial y} + \frac{\partial u_z}{\partial z} = 0 \tag{2.13}$$

In Equation (2.13), u_x, u_y, and u_z are the velocity components in the x, y, and z directions, respectively. In case of incompressible flow, the conservation of momentum equations for turbulent flow with no free surface (no gravity term) are expressed as the Reynolds-averaged Navier-Stokes equation (Clark, 1996):

$$\rho \frac{\partial \overline{U_i}}{\partial t} + \rho \overline{U_k} \frac{\partial \overline{U_i}}{\partial x_k} = -\frac{\partial \overline{p}}{\partial xi} + \mu \frac{\partial^2 \overline{U_i}}{\partial x_i \partial xj} - \rho \frac{\partial}{\partial x_j} \left(\overline{u_i u_j} \right) \tag{2.14}$$

where ρ is the density of fluid , U_i is the average velocity in the i-th direction, t is time, p is the average pressure, μ is the molecular viscosity, and u_i is the fluctuating component of velocity in the i-th direction. In Equation (2.14), the first term on the left-hand side of the equation means the local acceleration, the second term on the left means the non-linear convective acceleration, the first term on the right means pressure gradients, the second term on the right describes the viscous forces, and the last term on the right-hand side of the equation represent derivatives of the Reynolds stresses between fluctuating velocity components. In order to correctly account for turbulence, Reynolds stresses are modelled to create a closure of Equation (2.14) since it introduces additional unknowns that outnumber the equations available for solution. Hence, new equations or models must be established such as the two-equation models described in Section 2.5 to numerically solve turbulence problems. The turbulent convective-diffusion equations for reactive species transport can be written by the following equations (Liu and Ducoste, 2006):

$$\rho \frac{\partial C_i}{\partial t} + U_j \frac{\partial C_i}{\partial x_j} = \frac{\partial}{\partial xi} \left(D + D_T \right) \frac{\partial C_i}{\partial x_j} + Ri \tag{2.15}$$

Where C_i is the average concentration of species i, U is the mean velocity, D is the diffusivity coefficient of species, R_i is the reaction term for species i, and D_T is the turbulent diffusivity that is defined as,

$$D_T = \frac{\mu_T}{Sc_T} \tag{2.16}$$

Here μ_T, is the turbulent eddy viscosity and Sc_T is the turbulent Schmidt number in Equation (2.16). By the rearrangement of Equation (2.16), D_T may be defined as the ratio of the eddy diffusivity of momentum (eddy viscosity) to the eddy mass diffusivity. In Equation (2.15), the $D_T\left(\frac{\partial C_i}{\partial x_j}\right)$ term models the effects of the turbulent fluctuations of the concentration and velocity. The reaction that represents the photocatalytic oxidation of any organic pollutant can be used in the turbulent convective-diffusion equation to describe the reactive transport of each species all through the flow domain.

2.5 Turbulence Modelling

The nature of the flow in a typical photocatalytic reactor is turbulent due to the high flow rates required in water treatment facilities and the low viscosity of water. In the turbulent flow regime, the fluid motion is chaotic and random, and the velocity and the pressure change with time at each point in the flow. Visualization of the turbulent flow reveals rotational structures termed as turbulent eddies or vortices with a range of length and time scale. The role of eddies in a photocatalytic reactor is important as they can carry and move contaminants from the bulk of liquid to the catalyst surface. This axial and lateral mixing that result due to the presence of eddies can increase the contaminant mineralization efficiency compared to what could be achieved in a laminar flow condition. In general, as the full-scale photoreactors will operate in a turbulent flow regime, therefore, simulations of a photocatalytic reactor process must incorporate the effect of turbulent mixing on any chemical reactions that occur within these photoreactors. Although the standard k-ε turbulence model is often used for the examination of hydraulics within a flow-through reactor, the incorporation of other turbulent models may provide better characterization of the turbulent behaviour within a photocatalytic reactor. One of the expected outcomes of this study is to achieve better understanding on numerical models for a photocatalytic system analysis. Using experimental measurements, Liu *et al*. (2007) evaluated the accuracy of the turbulence model prediction and was able to assess the impact of the turbulence model selection on UV disinfection performance. The microbial inactivation was shown to have slight sensitivity to the turbulence model selection. Also the sensitivity of effluent microbial inactivation to the turbulence model selection was demonstrated as a function of the UV

operating conditions and the UV response kinetics of the target microorganisms. A similar sensitivity study was also required to be completed for advanced oxidation process, since the proper characterization of the turbulent mixing intensity was reported to be significant for fast competitive chemical reactions typically associated with advanced oxidation process (Alpert *et al*., 2010). The turbulent flow in the photocatalytic reactor could be simulated using three two-equation turbulence models: 1) Standard k-ε, 2) RNG k-ε, and 3) k-ω. While other more complicated turbulence models exist, such as the Reynolds Stress Model or Large Eddy Simulation model, these three two-equation models can provide reasonable and stable results without being numerically intensive. The standard k-ε model was proposed by Launder and Spalding (1974) to solve the turbulence stress closure problem. This model, as described by Wilcox (2004), is shown below and the definitions for different variables are given in Table 2.4:

$$\nu_T = \frac{C_\mu k^2}{\varepsilon} \tag{2.17}$$

$$\frac{\partial k}{\partial t} + U_j \frac{\partial k}{\partial x_j} = \tau_{ij} \frac{\partial U_i}{\partial x_j} - \varepsilon + \frac{\partial}{\partial x_j}\left[\left(\nu + \frac{\nu_T}{\sigma_k}\right)\frac{\partial k}{\partial x_j}\right] \tag{2.18}$$

$$\frac{\partial \varepsilon}{\partial t} + U_j \frac{\partial \varepsilon}{\partial x_j} = C_{\varepsilon 1} \frac{\varepsilon}{\kappa} \tau_{ij} \frac{\partial U_i}{\partial x_j} - C_{\varepsilon 2} \frac{\varepsilon^2}{\kappa} + \frac{\partial}{\partial x_j}\left[\left(\nu + \frac{\nu_T}{\sigma_\varepsilon}\right)\frac{\partial \varepsilon}{\partial x_j}\right] \tag{2.19}$$

$$C_{\varepsilon 1} = 1.44, C_{\varepsilon 2} = 1.92, C_\mu = 0.09, \sigma_k = 1.00, \sigma_\varepsilon = 1.3$$

$$\omega = \frac{\varepsilon}{c_\mu k} \quad , \qquad l = \frac{c_\mu k^{3/2}}{\varepsilon} \tag{2.20}$$

The second closure is the Renormalized Group (RNG) κ-ε model, was developed by Yakhot and Orszag (1986) using techniques from the renormalization group theory. In the RNG κ-ε model, μ_t, κ, and ε variables need to be defined as to the standard k-ε model. However, the RNG κ-ε model modifies coefficients and empirical constants to reduce the higher level of dissipation that is predicted using the standard k-ε model. Thus, equations 2.17, 2.18, and 2.19 are still applicable.

The closure coefficients are replaced by the following (Wilcox, 2004):

$$c_{\varepsilon 2} = \tilde{c}_{\varepsilon 2} + \frac{c\mu\lambda^3(1-\frac{\lambda}{\lambda_0})}{1+\beta\lambda^3} \tag{2.21}$$

$$\lambda = \frac{k}{\varepsilon}\sqrt{2s_{ij}s_{ji}} \tag{2.22}$$

$$c_{\varepsilon 1} = 1.42, \tilde{c}_{\varepsilon 2} = 1.68, C_\mu = 0.085, \sigma_k = 0.72, \beta = 0.012, \lambda_0 = 4.38$$

The third two-equation turbulence model is the k- ω model and was first developed by Wilcox (1988) (as cited in Wilcox 2004) and uses transport equations for k and the Reynolds Mean Stress (RMS) fluctuating vorticity ω. In a later version developed by Wilcox in 1998, in which changes were made to the values of α, β_0, and the dissipation terms (β* and β) and the functions f_β and f_β^* were added, the k- ω (98) model was found to predict the experimental spreading rates reasonably well for all free shear flows, including far wake, mixing layer, and jet flows. The k- ω (98) model is described below (Wilcox, 2004):

$$\nu_T = \frac{k}{\omega} \tag{2.23}$$

$$\frac{\partial k}{\partial t} + Uj\frac{\partial k}{\partial x_j} = \tau_{ij}\frac{\partial U_i}{\partial x_j} - \beta^* k\omega + \frac{\partial}{\partial x_j}\left(\nu + \sigma * \nu_T\right)\frac{\partial k}{\partial x_j} \tag{2.24}$$

$$\frac{\partial \omega}{\partial t} + U_j\frac{\partial \omega}{\partial x_j} = \alpha\frac{\omega}{k}\tau_{ij}\frac{\partial U_i}{\partial x_j} - \beta\omega^2 + \frac{\partial}{\partial x_j}\left[(\nu + \sigma\nu_T)\frac{\partial \omega}{\partial xj}\right] \tag{2.25}$$

$$\alpha = 13/25, \beta = \beta_0 f_\beta, \beta* = \beta^*{}_0 f_\beta, \sigma = 0.5, \sigma^* = 0.5, \beta_0 = 9/125, \beta_0{}^* = 0.09$$

$$f_\beta = \frac{1+70\chi_\omega}{1+80\chi_\omega}, where \chi_\omega = \left|\frac{\Omega_{ij}\Omega_{jk}s_{ki}}{(\beta_0{}^*\omega)^3}\right| \tag{2.26}$$

$$f_{\beta^*} = \begin{Bmatrix} 1 & \chi_k \le 0 \\ \frac{1+680\chi_k{}^2}{1+400\chi_k{}^2} & \chi_k > 0 \end{Bmatrix}, \text{ where } \chi_k = \frac{1}{\omega^3}\frac{\partial k}{\partial x_j}\frac{\partial \omega}{\partial x_j} \tag{2.27}$$

$$\varepsilon = \beta^*\omega k \qquad l = \frac{k^{1/2}}{\omega} \tag{2.28}$$

$$\Omega_{ij} = \frac{1}{2}\left(\frac{\partial U_i}{\partial x_j} - \frac{\partial U_j}{\partial x_i} \right) \tag{2.29}$$

$$s_{ij} = \frac{1}{2}\left(\frac{\partial U_i}{\partial x_j} + \frac{\partial U_j}{\partial x_i} \right) \tag{2.30}$$

Variables that have not been previously defined but that are used in the three turbulence models are defined in Table 2.4. These three models could be used based on their general universality for modelling of uncomplicated turbulent flows. The standard k-ε model is the most popular of the two equation models and performs relatively well for major types of industrial flows. The RNG k-ε model solves the k-ε singularity problem at wall boundaries (where 'k' approaches zero) and reduces the higher level of dissipation that is predicted using the Standard k-ε model. However, the RNG k-ε is not as accurate in predicting free-shear (no wall) flows. The k-ω has been proven to be moderately accurate for boundary layer (i.e., wall bounded) flows with the 1998 revisions, and it also works well for free-shear flows.

Table 2.4 Variables in Turbulence Closure Sub-models

Variables	Name
ν_T	Kinematic eddy viscosity
k	Turbulent kinetic energy
ε	Turbulent energy dissipation
τ_{ij}	Reynolds stress tensor
ν	Kinematic molecular viscosity
ω	Specific dissipation rate (dissipation per unit turbulence kinetic energy)
l	Turbulence length scale
S_{ij}	Mean strain rate tensor
Ω_{ij}	Mean rotation tensor

2.6 Near-Wall Treatment

Turbulent flows are affected to a large extent by the presence of walls. In the near-wall region, the solution variables usually have large gradients, and the momentum and other scalar transports occur most vigorously (Fluent Inc., 2006). Thus successful predictions of wall-bounded turbulent flows require the accurate representation of the flow in the near-wall region. The Standard *k*-ε, Realizable *k*-ε, and RSM models are primarily applicable for turbulent core flows (i.e., the flow in the regions somewhat far from walls). Therefore special consideration is needed for the models to apply them appropriately for wall-bounded flows. Numerous studies have shown that the near-wall region can be largely subdivided into three layers. The innermost layer, termed as the "viscous sub-layer", the flow is almost laminar, and the (molecular viscosity plays a dominant role in momentum and mass transfer). In the outer layer, termed as the fully-turbulent layer, turbulence plays a major role. There is an interim region between the viscous sub-layer and the fully-turbulent layer where the effects of molecular viscosity and turbulence are equally significant. There are two main approaches used to modelling the near-wall region (Fluent Inc., 2006). The semi-empirical formulas called "standard wall functions (SWF)" are used to link the solutions variables in the viscosity affected region (viscosity sub-layer and buffer zone) between the wall and the fully turbulent region. This approach is economical, robust and reasonably accurate for practical industrial flow simulations. It substantially reduces the processing and storage requirements of a numerical model at high Reynolds-number flows. Nonetheless, this approach is inadequate in situations where the low-Reynolds-number effects are persistent in the computational domain. Further, this approach ignores important features of the mass transfer boundary layer if it is deeply rooted within the viscosity sub-layer (Duran *et al*., 2009). These features make the wall function approach unsuitable for modelling wall-mass or heat transfer in liquid flows.

With regard to the non-dimensional wall distance, y^+, a target value of 30 is desired of a mesh for the application of wall functions. This parameter is defined as:

$$y^+ = \frac{\rho\sqrt{\frac{\tau_w}{\rho_w}} \times y_p}{\mu} \qquad (2.31)$$

In Equation (2.31), y_p is the distance from the first computational node *P* to the wall and the subscript w denotes wall properties.

A near-wall flow is said to be laminar if $y^+ \leq 11.63$. If $y^+ \geq 11.63$ the flow is said to be turbulent and the wall function approach is used where the near-wall mean velocity is evaluated via Equation (2.31). The criterion is used to describe the changeover from laminar to turbulent near-wall flow in the buffer layer between the linear and log-law regions of a turbulent wall layer.

$$U^+ = \frac{1}{\kappa}\ln(Ey^+) \qquad (2.32)$$

Where U^+ and y^+ represent a dimensional velocity and near-wall distance, and the values of κ and *E* are set to 0.42 and 9.8 respectively. The above logarithmic wall law is applied at the near-wall cells provided $y^+ > 11.225$ (For lower values of y^+ a linear relationship $U^+ = y^+$ is used).

In the other approach called "enhanced wall treatment (EWT)" modifies the turbulence models to enable the viscosity-affected region to be resolved with a mesh all the way to the wall, including the viscous sub-layer. EWT is a near-wall modelling method that combines a two-layer model with enhanced wall functions. In this approach, the whole domain is divided into a viscosity-affected region and a fully turbulent region. A wall distance based turbulent Reynolds number, Re_y is used to divide the above two regions. *Rey* is determined according to the following relation.

$$\mathrm{Re}_y = \frac{\rho y\sqrt{y}}{\mu}$$

where y is the normal distance from the wall at the cell centres.

In the fully turbulent region, $\mathrm{Re}_y = y\sqrt{k/\nu} \geq 200$, the k-ε models and the RSM model are employed and the eddy viscosity is computed with the usual relationship. In the viscosity-affected near-wall region Rey <200, only the one-equation model of Wolfstein (1969) is employed and the momentum equations and *k* equation are solved.

In the viscous region, the turbulent viscosity, μ_t, is determined using the following relation (Wolfstein, 1969)

$$\mu_{t,2layer} = \rho C_\mu l_\mu \sqrt{k}$$

The dissipation rate in this region is defined by (Chen and Patel, 1988)

$$\varepsilon_{2layer} = \frac{k^{2/3}}{l_\varepsilon}$$

Where l_μ and l_ε are the length scales specified to consider necessary damping effects in the near-wall region in terms of the turbulence Reynolds number, Re_y (Chen and Patel, 1988)

$$l_\mu = C_l y(1-e^{-\mathrm{Re}_y/A_\mu})$$

$$l_\varepsilon = C_l y(1-e^{-\mathrm{Re}_y/A_\varepsilon})$$

In the viscosity affected near-wall region, the turbulent mass flux is determined by the following formula,

$$J_{i,w} = \frac{\mu_{t,2layer}}{Sc_t}\nabla Y_i$$

As part of the enhanced wall treatment in the near-wall region, the turbulent viscosity computed using the two layer formulation described above and is smoothly blended for the outer region, by combining both equations using a blending function (Fluent Inc., 2006).

$$\mu_{t,EWT} = \lambda_\varepsilon \mu_t + (1-\lambda_\varepsilon)\mu_t, 2layer$$

$$\lambda_\varepsilon = \frac{1}{2}[1+\tanh(\frac{\mathrm{Re}_y - \mathrm{Re}_y{}^*}{A})]$$

The constant A denotes the width of the blending function. The blending function, λ_ε is equal to unity in the fully turbulent region when $Re_y \geq 200$. The functional form of λ_ε is designed to ensure a smooth transition around Re_y=200.

$$A = \frac{\left|\Delta \mathrm{Re}_y\right|}{\tanh(0.98)}$$

$$A = 2kC_\mu^{-3/4}$$

In order to extend its applicability throughout the near-wall region, the law of the wall (EWF) is formulated as a single expression for the entire wall region by blending the linear (laminar) and logarithmic (turbulent) laws of the wall using a function suggested by Kader (1981).

The near-wall mesh should be fine enough to resolve the transport equations down to the laminar sub-layer.

$$u^+ = e^{\Gamma} u^+_{lam} + e^{1/\Gamma} u^+_{turb}$$

Where $\Gamma = \frac{a(y^+)^4}{1+by^+}$, a=0.01 and b=5

Further details of turbulence modelling approach can be found in FLUENT Inc., 2006.

2.7 Numerical Simulation Method

The governing equations for fluids flows are based on mass, momentum, and energy balanced principles which are generally articulated in the form of partial differential equations and also expressed by the incompressible Navier-Stokes equations. Among many factors that may interfere the CFD solution results are the discretization of the computational domain (structure and size of the cells), and the type of modelling approach employed and approximation of unknown dependent variables by simplified functions (Ferziger and Peric, 1999) to provide a set of algebraic equations containing only numbers and no derivates that may be solved with any appropriate technique. A quality grid and capable of representing the geometry, is the basis for a reliable accurate simulation. In general, both mesh quality and grid independence of the solution need to ensured (Cengel and Cimbala, 2006). This process of producing a set of numerical equation analogue to the PDEs is called "numerical discretisation". In order to obtain an accurate numerical solution, a discretisation method is employed which approximates the differential equations by a system of algebraic equations which can then be solved on a computer (MOU, 2009). The main techniques that have been employed for discretisation are the finite element method, finite difference method, and the finite volume method.

A. Finite Element Method

The finite element method is mainly used for analysis of stress in structural engineering. This method solves an equation by approximating continuous quantities as a set of quantities at discrete points, often regularly spaced into a so-called grid or mesh. This method is adaptable to problems with great complexity and irregular geometry; they are regarded as a very powerful tool for the solution of important problems in heat and mass transfer, and fluid

mechanics. Furthermore, the availability of fast and inexpensive computers allows problems which are intractable using analytic or mechanical methods to be solved in a straightforward manner using finite element methods. The method divides the solution domain into a finite number of small sub-domains or elements that are connected via nodes. A simple variation of the dependent variables with respect to the location is assumed within each element, and these variations are used subsequently to generate an interpolation function to describe variation of the variables over the whole domain. The variation of a variable within each element is quantified depending on the values of the variable at the end-points of the element, known as the nodes of the element. The equations obtained for each element are then substituted in global matrices, integrated and boundary conditions are imposed on the matrices so that the equations can be solved (Akin, 1994; Brenner and Scott, 1994; Reddy and Gartling, 1994).

B . Finite Difference Method

This method is a commonly employed numerical technique for solving the systems of partial differential equations that govern mass, momentum, and energy balances. The computational domain is approximated using a number of grids of uniformly spaced nodes. At each node, the governing differential equation is approximated by an algebraic expression which is connected to adjacent grid points. Taylor series is used in this method to transform the partial differential equations into a number of linear algebraic equations that describe the derivatives of dependent variables at various grid points (Shaw, 1992). Generally, these algebraic equations are tri-diagonal and they can be easily solved at each node using some elimination method.

C. Finite Volume Method

In CFD codes, the finite volume method is a widely used numerical discretisation scheme due to its ability to accurately ensure the conservation of various properties in a control volume. The main step in the finite volume method is to divide the solution domain into a finite number of small volume cells. This finite volume method solves the partial differential equations that determine the values of the conserved variables averaged across the volume. This approach requires the discretisation of the spatial domain into finite control volumes. The governing differential equations are integrated over each control volume. The resulting

integral conservation laws are exactly satisfied for each control volume and for the whole domain, which is a special advantage of the finite volume method. Each integral term is then transformed into a discrete form, thus yielding discretised equations at the centroids, or nodal points, of the control volumes. This method is somewhat similar to the finite different method but some of its implementations draw on features taken from the finite element method. Like the finite difference method, the numerical equations at a given point depend on the values at neighbouring points. The finite volume method is comparatively advantageous compared with other methods since structured mesh can be used and the boundary conditions can be applied non-invasively. In particular, finite volume methods are powerful for coarse non-uniform grids and in simulation where the mesh moves to track interfaces or shocks.

2.8 Reaction Modelling using CFD

There have been many reports on the experimental evaluation of photocatalytic systems and a variety of pollutants that may be degraded in such systems; these works have not been interpreted into the numerical modelling of corresponding reactive systems. In addition, the recent work into the hydrodynamics and radiation transport has highlighted the increasing interest in CFD as a tool for investigating such aspects of photocatalysis. Furthermore, the application of CFD to model chemical reactions as part of a total photocatalytic system analysis in a wide sense is also inadequate (Cox, 2007). In general, reaction models are divided into two categories: reaction with an infinitely fast chemistry or finite rate chemistry. The infinitely fast chemistry includes reactions that occur on time scales faster than the mixing process and are commonly employed when modelling combustion reactions. This class of reaction has also been further divided into premixed and non-premixed models. For premixed combustion, the turbulent premixed combustion model proposed by Zimont (2000) which models the flame front propagation by solving the scalar transport equation is given below,

$$\frac{\partial}{\partial t}(\rho c) + \nabla.(\rho U c) = \nabla.(\frac{\mu_t}{S_{ct}}\nabla c) + \rho S_c \qquad (2.33)$$

where c is the reaction progress variable, and the source term, ρS_c, was expressed as,

$$\rho S_c = A G_\rho I [\frac{\tau_t}{\tau_c \lambda_{lp}}]^{\frac{1}{4}} |\nabla c| \qquad (2.34)$$

where G is the flame stretch factor, λ_{lp} is the stoichiometric ratio of the leading point composition and τ_t and τ_c are the turbulent and critical time scales respectively. In a non-premixed system, the components enter the reaction system individually and then mix before combustion can take place. This system requires the solving of a scalar quantity representing the mixed fraction, *f*. This simplification avoids the need to model individual species thereby reducing the computational cost. The mixed fraction was given by the following transport equation,

$$\frac{\partial}{\partial t}(\rho f) + \nabla.(\rho U f) = \nabla.(\frac{\mu_t}{\sigma_t}\nabla f) + S_m + S_u \qquad (2.35)$$

where the S_m source term defines the mass transfer only and S_u represents all other user-defined sources.

In finite rate chemistries, which commonly used in non-combustive systems, the method involves the solution to a transport equation for each species mass fraction, which can be given as

$$\frac{\partial}{\partial t}(\rho Y_A) + \nabla.(\rho U Y_A) = \nabla.J_A + R_i + S_i \qquad (2.36)$$

where Y_A is the mass fraction of the component *A*. J_A represents the mass diffusive flux due to any concentration gradient. The reaction term, R_i in Equation (2.16) describes any production or depletion of the component A.

In case of a laminar flow, this flux may be represented as

$$J_A = -\rho D_m \nabla Y_A \qquad (2.37)$$

where D_m is the molecular diffusivity of species A in the mixture. For turbulent flow it is

$$J_A = -(\rho D_t + \frac{\mu_t}{S_{ct}})\nabla Y_A \qquad (2.38)$$

where D_t is the so-called eddy (turbulent) diffusivity for species concentration. With μ_t the turbulent viscosity and Sc_t the turbulent Schmidt number defined as the ratio between the turbulent viscosity and the turbulent diffusion:

$$Sc_t = \frac{\mu_t}{\rho D_t}$$

The value of this dimensionless number typically is close to unity. By reviewing the previous experimental results, Koeltzsch (2000) reported that most authors utilised the values of Sc_t ranging from 0.5 to 0.9. In this study a value of 0.7 was used as suggested in elsewhere (Fluent Inc., 2006; Yimer *et al*., 2000; Spalding, 1971). Several researchers elaborated the model of constant S_{ct} on global quantities of the flow (Rosen and Traegaaedth, 1995), or as algebraic turbulence models (Aravinth, 2000). More accurate predictions of mass and heat transfer were reported using this approach (Wolfstein, 1969; Nelisse *et al*., 2003). Also, more complex models for solving the turbulent mass transfer equation have been recently proposed, like the two-equation model of Sun *et al.* (2005).

The two commonly used methods for evaluating the rate are the laminar-finite rate model and the eddy-dissipation concept model. Mohseni and Taghipour (2004) employed the laminar-finite rate model, which ignores the effect of turbulence on the reaction rate. This model is suitable for modelling a wide range of reactor systems where slow reacting chemistry and small turbulent variation persist. The reaction kinetics are evaluated using the Arrhenius equation or through user-defined kinetics models.

The eddy-dissipation-concept model proposed by Hjertager and Solberg (2005), was mainly developed for a combustion reactor, but may be used for any single step, irreversible reaction, such as given by the equation,

$$A + nB \dashrightarrow (1 + n)\, C \qquad (2.39)$$

This model involves the transport equation for species A mass fraction using Equation (2.12) and for the mixture fraction, *f*. The reaction rate for species *A* is then given by the smallest of the turbulent dissipation rates of all the species (*A*, *B*, and *C*) as given by

$$Y_A = -\alpha\rho\frac{\varepsilon}{\kappa}\min(Y_A, \frac{Y_B}{n}, \beta\frac{Y_c}{1+n}) \qquad (2.40)$$

where α and β are constants.

Mohseni and Taghipour (2004) considered light distribution for modelling the photocatalytic gas phase vinyl chloride oxidation. Assuming a simple first-order rate equation they utilised CFD to model the reaction rates in an annular photocatalyitic reactor. The concentration gradients were shown to decrease radially away from the light source. For modelling an

annular photocatalytic reactor, Pareek et al.(2003) adopted a similar approach using a first order reaction rate model. In his work the rate constant for the CFD simulations was fitted to previous experimental results. Recently Duran *et al*. (2011b) have published a work on the photocatalytic performance of a differential reactor employing a first order reaction rate model considering a constant irradiance at the photocatalyst surface. Under the scope of the current investigation, the reaction kinetics of a model pollutant, evaluated at a laboratory scale has been employed for the modelling of a flat plate reactor, where the flow and irradiance in the reactor are assumed to be uniform. With the inclusion of these kinetic parameters it has been possible to evaluate the performance of the flat plate reactor. The velocity and turbulent profile, which are essential to solve species transport equations, were obtained from the steady state simulation of mass, momentum and turbulence models.

2.9 Previous Studies on Reactor Modelling with CFD

Limited studies have been performed with CFD to simulate a heterogeneous photocatalytic reactor that is employed for water purification. Some studies have been performed to simulate multiphase photocatalytic reactors in bench scale. However, the applied radiation model did not incorporate refraction. Few studies used CFD to evaluate the heterogeneous photocatalytic oxidation of gas-phase pollutants by the UV initiation of a TiO_2 coated surface; however, these researches did not incorporate a radiation model and only described the flux of contaminant toward the TiO_2 - coated surface.

Pareek *et al.* (2003) applied the CFD approach to model a pilot scale annular bubble column photoreactor and analysed its performance for possible industrial wastewater treatment. The Granular Eulerian approach was used to simulate the three phase flow in a photocatalytic reactor. They used CFD combined with a discrete-ordinate radiation transport equation for light intensity distribution and modified k-ε turbulence equations to model a heterogeneous, multi-phase photocatalytic reactor system for the photocatalytic degradation of industrial spent Bayer liquor. The model adequately fitted the experimental data for photodegradation of Bayer liquor.

Mohseni and Taghipour (2004) developed a model to predict the performance of an annular photocatalytic reactor for vinyl chloride (VC) oxidation using CFD. Various surface rate constant values were examined through the comparison of the calculated outlet concentrations from CFD modelling and those obtained experimentally under different

experimental conditions. The value providing the closest agreement between CFD and experimental results was chosen as the reaction rate constant of first order kinetics. They applied the laminar finite rate modelling approach in which the effect of turbulence is ignored. This assumption caused about 10-20% underestimation of the degradation rate. They studied the impact of flow non-uniformities on the reactor performance and suggested some design modifications for improving reactor efficiency.

Pareek *et al*. (2005) evaluated the light intensity distribution in a two-lamp photo-reactor using a finite volume scheme. The irradiated space was divided into a number of finite volumes and angles (directional discretization). Simulations were performed for both homogenous and heterogeneous (with titania catalyst) reactors for incident radiation and local volumetric rate of energy absorption. Model predictions were used to assess the effect of catalyst loading on the light intensity field inside the reactor. Optimal distance between the lamps was reported to be dependent on the optical properties of the photocatalyst. Model predictions match qualitatively with published literature data. Taghipour and Mohseni (2005) conducted CFD modelling of a photocatalytic reactor with surface reaction for TCE oxidation at various reactor lengths, pollutant concentrations, and flow rates in an annular reactor. They also investigated the effect of contaminated air flow thickness on the reactor performance. Though the model did not account for homogeneous reactions such as those initiated by photolysis, it predicted experimental results well except at low TCE concentrations.

Castrillon *et al*. (2006) investigated the aerodynamic behaviour of a photocatalytic reactor for air treatment. They identified several design issues from simulation results and implemented some modifications to uniformize the flow field, mass flow and contact time distributions. Sozzi and Taghipour (2006a) applied the CFD approach to simulate the hydrodynamics of annular UV-reactors for water treatment. Two different reactor configurations U shape and L shape were examined. The influence of three turbulence models on the simulation results was investigated. In general, CFD models showed a close agreement with the experimental data for the majority of the reactor domain and captured the influences of reactor configuration and internal reactor structures on the flow distribution. In another study by Sozzi and Taghipour (2006b) it has been indicated that the integration of fluence rate models and inactivation kinetics with commercial computational fluid dynamics (CFD) could predict the reactor performance by Eulerian and Lagrangian methods for water disinfection.

Salvado-Estivill *et al*. (2007) performed CFD simulation of a flat plate, single-pass, and flow-through photocatalytic reactor for air purification. They studied the effect of UV irradiance (different lamp configuration), flow rate and substrate concentration on trichloroethylene (TCE) conversion. The LH type rate equation considering the effect of UV irradiance was used to model the rate of disappearance of TCE over the catalyst at constant humidity. The CFD model was fitted to the experimental results by adjusting the adsorption constant and the apparent rate constant, until the sum of the residuals between the model and the results was minimized. The CFD model was able to predict the experimental results reasonably.

Trujillo *et al.* (2007) studied the CFD analysis of the radiation distribution in a new immobilized catalyst bubble column externally illuminated photoreactor. The radiative transport equation (RTE) in conjunction with the Navier-Stokes equations were solved to obtain the light incident radiative flux and light absorbed by the immobilized titania as a function of the gas superficial velocity, the angle of inclination, and the separating distance between the plates. The results indicated that gas bubbling considerably increased the incident radiation in the gas-liquid mixture enhancing the radiative flux and the absorbed radiation on the titania-coated plates.

Trujillo *et al*. (2008) studied the enhancement of the surface incident radiation on the walls of an externally irradiated bubble tank photoreactor and modelled by solving the radiation transport equation (RTE) in conjunction with the continuity, momentum and k-ε turbulence equations. CFD simulation results were complemented with actinometric runs to determine the effect of the gas flow rate on the radiation loss by reflection at the surface of the gas-liquid mixture due to bursting of the bubbles. The model assumed the gas-liquid mixture is a semitransparent medium where light is scattered as a result of specular reflection and refraction when the light rays impinge on the air bubbles. The simultaneous solution of the hydrodynamics and radiation transport equation using CFD allowed to establish the relationship between the light scattering coefficient and the bubble size and the gas hold-up. Excellent agreement between the experimental data and CFD model has been demonstrated.

Denny *et al*. (2009) employed CFD coupled with RTE to simulate oxalic acid photo-degradation in a TiO_2 coated glass-bead photoreactor irradiated by end-emitting optical fibre (EEOF) or side-emitting optical fibre (SEOF) bundles. Light irradiance distributions in the photoreactor were modelled for specular, partially specular and diffusive reactor wall

reflectivities with specularly reflective reactor walls best representing the experimental data. However, the developed model demonstrated that at incident radiant power more than ten times greater than the experimental power used, a uniform light distribution gave faster oxalic acid photodegradation with the relative improvement of the SEOF bundle over the EEOF bundle increasing with radiant power. This was attributed to increased electron-hole recombination in photocatalytic surfaces close to the EEOF tip, induced by the increased light irradiance in this region. The model also demonstrated a constant light irradiance profile along the length of a SEIF bundle giving an improved photocatalytic performance when compared to linear or exponentially decaying light profiles.

Denny *et al*. (2010) developed a computational fluid dynamics model coupled with a discrete ordinate radiation model for a channelled optical fibre reactor (COFR) to optimise its channel configuration. The flow field in the COFR was laminar with similar velocity vector distributions in all channels irrespective of their location in the COFR cross-section. The radiation distribution on the TiO_2-coated channel walls was governed by the spatial distance. The ethylene conversion distribution corresponded well with the radiation distribution with channels in the inner and the outer arcs showing the lowest and the highest conversion, respectively. The simulation results agreed well with the experimental data possessing Pearson correlation coefficients of 0.995, 0.997 and 0.997 for variations in the incident radiant power, gas flow rate and initial ethylene concentration, respectively. Six alternate channel configurations were considered for optimising overall ethylene conversion in the COFR with an improvement of up to 33% being achieved.

Duran *et al.* (2010a) developed a CFD model for simulating an immobilized annular (U and L shape) photocatalytic reactors for various flow rates to cover a range of laminar, transitional, and turbulent flow conditions. The evaluation of the CFD model was performed using several hydrodynamic models that incorporated different near-wall modelling approaches. The performance of the model was evaluated in terms of its capability for predicting the photocatalytic degradation rate of benzoic acid as a model compound. Regardless of the flow rates and turbulence models evaluated, the main patterns and local distributions of the analysed variables (velocity, mass transfer coefficient, surface reaction rate, and external effectiveness factor) were somewhat similar. The overall reaction rate in these systems was shown to be limited by the rate of mass transport. Hence, identifying areas of low mass transfer, and finding alternatives for increasing the transport of species toward those

photocatalyst-coated areas was indicated to result in an increase of the degradation rate achieved in the photoreactor. The U-shape annular reactor configuration showed a low mass transfer area in the top region of the reactor, toward the outlet port. The use of internal baffles that generate fluid turbulence toward that region was suggested to improve the local mass transfer coefficient. Incorporating external mass transfer promoters into the design of such reactors were evaluated using two common promoters: repeated ribs on the photocatalyst-coated wall and static delta wing mixers by Duran *et al*. (2011a). The reactor with repeated ribs presented a 53% higher apparent reaction rate and an increase of only 1% in the pressure drop when compared with the plain reactor. The reactor with the delta wings presented only 8% increase in the apparent reaction rate. The better performance of the repeated ribs over the delta wings was due to the fact that ribs produce turbulence very close to the wall, exactly where mass transfer is taking place. In contrast, delta wings generate turbulence mainly in the core flow.

2.10 Role of Turbulence and Mixing Promoters in a Photocatalytic Reactor

Although recent studies have shown very promising results, no research has been performed that investigates the sensitivity of both the turbulence model selection and the use of baffles on UV initiated photocatalytic reactor simulations. In addition, none of the previous studies utilized the model to investigate whether the simulations were able to predict changes in the reactant degradation or formation of products due to changes in water quality and reactor configurations (Alpert *et al*., 2010). The reaction occurs at the liquid-solid interface, and mass transfer from the bulk of the liquid to the catalyst surface plays an important role in the overall rate of pollutant destruction. However, immobilization of TiO_2 on the support materials also creates its own problems. There are two common problems that can occur from this arrangement (Periyathamby and Ray, 1999). The overall pollutant destruction is limited by the accessibility of the catalyst surface to the photons and the reactants and a significant influence of the external mass transfer particularly at low flow rate, because of the increasing diffusional length of the reactant in the bulk solution to the catalyst surface (Zhou and Ray, 2003). The performance of immobilized photocatalytic reactors was shown to be strongly limited by the rate of mass transfer of the contaminants to the catalyst coating (Duran *et al*., 2010a). The degradation of phenol by using TiO_2 supported on glass fibres becomes slower

and slower during repeated experiments (16 cycles of 90 min). This effect was related to the adsorption of by-products on the photocatalyst surface (Brezova *et al*., 1995). Introducing turbulence enhances fluid mixing in the immobolized reactor, thereby improving conversion (McMurray *et al*., 2004). However, if turbulence is generated only by increasing the flow rate, the residence time of the pollutant in the reactor will decrease and the extent of conversion will decrease subsequently (Duran *et al.,* 2011b). In a recent study using a Taylor Coute Votex reactor, external mass transfer resistance has been eliminated by promoting mixing in the bulk solution which is created by flow instability.

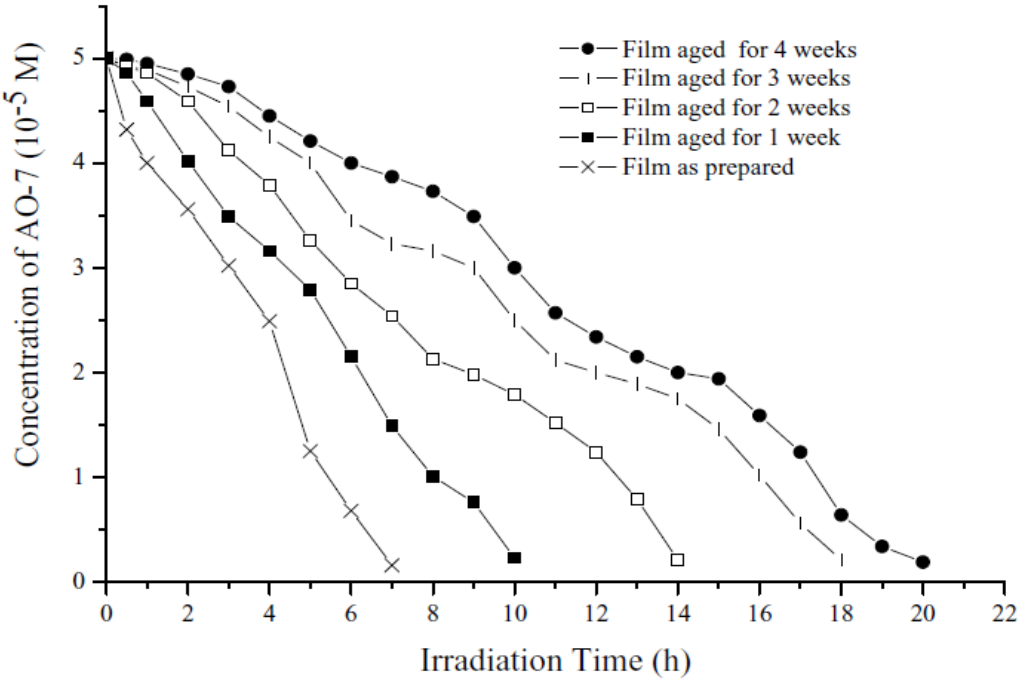

Figure 2.5 Effect of TiO_2 film aging on the photocatalytic decolorization of Acid orange (AO-7) (Rao *et al.,* 2004).

The formation of vortices has been reported to enhance the performance of the photocatalytic reactor through the utilization of the flow instability (Dutta and Ray, 2004; Kabir and Ray, 2003; Mehrotra and Ray, 2003). During the process of photo degradation, depending on the nature of the compounds, some relatively stable intermediates may be formed, particularly when the parent compounds are of large molecular weight, and these intermediates may even be more toxic than the original compounds. These intermediates can form a deposit on the TiO_2 coated layer and may affect the performance of the reactor. The short-term use of immobilized TiO_2 on pumice stone, organic fibres or "polymer" film was reported to have

good results (Rao *et al*., 2004) However, the long-term use of immobilized TiO_2 caused a significant decrease in the photocatalytic efficiency for the decolourization of dyes in wastewater as shown in Figure 2.5. This was attributed to the fouling of the catalyst by the by-products of degradation during the photocatalytic degradation process. In a pulsed baffled tubular photocatalytic reactor, increased reaction rates were observed with increasing mixing intensity when TiO_2 was coated onto spherical polystyrene beads (Fabiyi and Skelton, 2000). Enhancement of fluid mixing in the reactor by means of internals features such as baffles or by any means helps to remove adsorbed intermediates from the catalyst surface and creates available active sites for further reaction, and thereby increases the region of constancy of the overall rate for the pollutants (Periyathamby and Ray, 1999; Sengupta *et al.*, 2001; Dutta and Ray, 2004). New contaminants with higher degradation requirements increase the importance of reactor hydrodynamics. Thus understanding the role of mixing and turbulence promoters in a photocatalytic reactor is of paramount importance for the design and optimization of the reactor that require effective mixing and transport of species, momentum and energy. The magnitude of the turbulent kinetic energy determines the quality and the efficiency of many industrial mixing processes (Liu *et al*., 2006). Therefore, the local turbulent dissipation rate,ε, is one of the fundamental parameters for the process designer.

2.11 Research Needs

From the literature review it is quite evident that the development of treatment systems based on heterogeneous photocatalysis is an area of major technical importance. Most of the earlier studies focused on the degradation of various substances, reaction mechanism, and kinetics, activities of different catalysts and effects of a few selected environmental conditions. An immobilized photocatalytic water purification method is an attractive treatment option compared to the slurry type reactor. In the slurry type reactor, TiO_2 is usually applied in aqueous suspension, but the reactor configurations lead to serious problems in scaling the process to large size plants such as fouling of radiation source and relevant additional costs due to catalyst recovery. Over the last decades, low-cost supported catalysts consisting of photoactive material deposited on the transparent and inert bodies has improved significantly its feasibility for recalcitrant organics degradation (Alexiadis and Mazzarino, 2005). During the process of photo degradation, some relatively stable intermediates may be formed on the catalyst surface depending on the model compounds, particularly when the parent compounds are of large molecular weight, and these intermediates may even be more toxic than the

original compounds (Parent *et al*., 1996). Improving fluid mixing in the reactor by means of internals such as baffles was indicated to remove adsorbed intermediates from the catalyst surface and result in fresh active sites available for further reaction, and thereby increasing the region of constancy of the overall rate for the pollutants (Periyathamby and Ray, 1999; Sengupta *et al*., 2001; Mehrotra and Ray, 2003; Dutta and Ray, 2004 ; Duran *et al*., 2010a).

Therefore it is of utmost importance to optimize the fluid mixing and the residence time of the pollutant within the reactor through introducing internals and selecting suitable reactor configurations.

For the reactor design and scale-up, the optimisation of the system features is important to achieve sustainable investment. Due to the complexity of the systems and the interaction of many parameters, the simulation of photoreactors for design optimisation is crucial for the successful application in water purification. Research with potential use in the development and scale-up of energy efficient reactor systems is still scarce. A commercial competitive full scale photocatalytic water detoxification system has not yet been generally accepted due to the lack of efficient solar UV light absorbing catalyst, poor understanding of the design of the photoreactor and inadequate scale-up strategies (Bahnemann, 2004). Computational fluid dynamics (CFD) has become an affordable engineering tool to simulate and optimize reactor design with the enhanced performance of computational resources and the fast development of simulation software. CFD is widely used and shows great viability for the design optimization of chemical reactors. CFD modelling has been applied successfully to determine the photoreactor hydrodynamics as well as photoreactor performance based on integrated models. Kamimura *et al*.(2002) integrated reactor hydrodynamics, radiation distribution and UV reaction kinetics to simulate UV reactor performance (Kamimura *et al*., 2002; Sozzi and Taghipour, 2006b). A CFD model can provide detailed information on flow field characteristics that can aid in identifying hydraulic based reasons for variation in reactor performance.

2.12 Conclusions from the Literature Review

Limited pilot scale results indicated that photocatalysis could be as cost-effective as other best available water treatment technologies. Current state of the art suffers from inadequate scale-up strategies and poor understanding of reactor hydrodynamics and design. Thus more work on the reactor modelling is still required to elucidate the complete history of all fluid

elements flow through the reactor. Recent studies on the modelling of photoreactor have demonstrated very promising results. There have been a few works on the CFD modelling of UV reactor for wastewater disinfection (Sozzi and Taghipour, 2006; Janex *et al.,* 1998), however, the CFD modelling of photocatalytic reactors for water purification has been done much less extensively (Pareek *et al.*, 2003; Taghipour and Mohseni, 2005; Duran *et al*.2010a, 2010b). In this regard, most of the work has focused on a single aspect of photocatalytic reactive system, namely the solution of the radiation transport equation (RTE) in a variety of reactor configurations (Cassano *et al*., 1995; Raupp *et al*., 2001; Pareek *et al.,* 2003, 2004; Castrillon *et al*., 2006; Trujillo *et al*., 2007, 2008; Denny *et al*., 2009). Of equal importance is the investigation of the fluid dynamics of the photocatalytic reactors and the impact of reactor geometry (Castrillon *et al*., 2006). The influence of hydrodynamics on the performance of photoreactor has been widely acknowledged suggesting the significance of detailed flow field information for the design and optimisation of photoreactors (Sozzi and Taghipour, 2007). In addition, the minimisation of catalyst fouling due to the adsorption of organics in wastewater and the deposition of degradation by-products on the immobilised TiO_2 surface is crucial to ensure the long-term operational stability of a prototype photocatalytic reactor (Rao *et al*., 2004). These findings highlight the necessity for further research on this aspect of the photocatalytic reactor to minimize the accumulation of organics and degradation by-products on the TiO_2 catalyst surface.

The use of repeated ribs as a turbulence promoter in the wall of an immobolised photocatalytic reactor has been demonstrated to improve the performance of an annular reactor (Duran *et al*., 2011a). In terms of solar UV and visible light utilization, the flat plate photocatalytic reactor is usually considered as commercially efficient. There have been no systematic investigations on the hydrodynamic performance of a flat plate photocatalytic reactor in wastewater remediation. None of the earlier studies have emphasised the influence of modelling approach (turbulence models) and the role of turbulence and mixing promoters on the CFD simulations of a flat plate photocatalytic reactor which merits further investigation. The models that have been developed using simplified mass balance equations provide useful but insufficient information about the system. In addition, a lot of simplifications are required to be made in the development of those models and consequently they provide a solution which is inadequate for this purpose (Jarandehei and Visscher, 2009).

To address the gap in the current literature, this study aims to investigate the hydrodynamic performance of a flat plate photocatalytic reactor using CFD code FLUENT with a particular emphasise on the role of turbulence and mixing promoters on the performance of photocatalytic reactor.

CFD has become an efficient tool for the detailed analysis of the hydrodynamic behaviour of the photocatalytic reactor coupled with mass and momentum transfer in various reactor geometries (Kamimura *et al*., 2002; Sozzi and Taghipour, 2007). It can also simulate concentration gradient of chemical species throughout the reactor. Modelling of a photocatalytic reactor using CFD code could provide detailed local information (velocity field, distribution of turbulence characteristics, wall shear stress and concentration profile) of the simulated system. The detailed information obtained from simulation can provide a qualitative understanding of the process and a parametric study can reveal the bottlenecks and the range of applicability of the system (Jarandehei and Visscher, 2009).

CHAPTER THREE

INFLUENCE OF PARAMETERS ON THE PHOTOCATALYTIC DEGRADATION OF ORGANIC POLLUTANTS

3.1 Introduction

Hetereogenous photocatalytic oxidation (HPO) process employing catalysts such as TiO_2, ZnO etc., and UV light has demonstrated promising results for the degradation of persistent organic pollutants, producing more biologically degradable and less toxic substances (Garcia *et al*., 2006, 2008; Vora *et al*., 2009). This process largely depends on the in-situ generation of hydroxyl radicals under ambient conditions which are capable of converting a wide spectrum of toxic organic compounds including a non-biodegradable one into relatively innocuous end products such as as CO_2 and H_2O. In HPO process, the combined action of semiconductor photocatalyst, an energetic radiation source and an oxidizing agent governs the destruction of recalcitrant organics. Moreover, the process can be driven by solar UV and visible light. Near the earth surface, the sun produces 0.2-0.3 mol photons $m^{-2}h^{-1}$ in the range of 300-400nm with a typical UV flux of 20-30 Wm^{-2}. This suggests that the sunlight is an economically and ecologically sensible light source (Goslich *et al*., 1997). As a result, development of an efficient photocatalytic water purification process for large scale applications has received substantial interest but it still remains a challenge. Although heterogeneous photocatalysis appeared in numerous forms, photocatalytic degradation of pesticides and phenolic compounds has recently been most widely investigated. However, low quantum efficiency due to inefficient visible light harvesting catalyst (Adesina, 2004), the design of photoreactor (Mukherjee and Ray, 1999), the recovery and reuse of titanium dioxide (Adesina, 2004) the generation of toxic intermediates (Konstantinou and Albanis, 2003; Moctezuma *et al*., 2007), as well as concern about catalyst deactivation (Legrini *et al*., 1993) are reported to be the major drawbacks. Results reported here indicate that the photocatalytic degradation of pesticides and phenolic compounds is largely dependent on the solution pH, types of catalyst and composition, organic substrate type and concentration, light intensity, catalyst loading, ionic composition of waste water, types of solvent, oxidant concentration, and calcination temperature (Sakthivel *et al*., 2003). Understanding the

impacts of various parameters on the photocatalytic degradation efficiency is of paramount importance from the design and the operational points of view when choosing a sustainable and efficient technique for the treatment of waste water. This chapter aims to present an overview of recent studies on the TiO_2 photocatalytic oxidation process with particular emphasis on the role of important operating parameters on the photocatalytic degradation of pesticides and phenolic compounds together with recent achievements. In order to utilize the solar UV and visible light spectrum more efficiently, numerous research groups have contributed to the development of more stable and powerful visible-light photocatalysts leading to the degradadtion of various organic pollutants. Recent advances in TiO_2 and ZnO photocatalysis for pesticide and phenol degradation using metal, non-metal and ion doping is also highlighted in this section. The existing limitations and future research needs to utilize TiO_2 photocatalysis for water treatment is also discussed.

3.2 Influence of Types and Composition of Photocatalysts

The photocatalytic activity of TiO_2 depends on surface and structural properties of the semiconductor such as crystal composition, surface area, particle size distribution, porosity, band gap and surface hydroxyl density. Particle size is of primary importance in heterogeneous catalysis, because it is directly related to the efficiency of a catalyst through the definition of its specific surface area. A number of commercially available catalysts have been tested for the photocatalytic degradation of various organic compounds in an aqueous environment. Table 3.1 presents the specification and characteristics of some commercial TiO_2 samples. The photocatalyst titanium dioxide Degussa P-25 has been widely used in most of the experimental conditions; other catalyst powders, namely, Hombikat UV100, PC 500, PC10, PC 50, Rhodia and Travancore Titanium Products (TTP), India, were also used for degradation of toxic organic compounds (Bahnemann *et al*., 2007; Singh *et al*., 2004, 2007b; Erquez and Pichat, 2006). P-25 contains 75% anatase and 25% rutile with a specific BET surface area of $50m^2/g$ and a primary particle size of 20 nm. Hombikat UV 100 consists of 100% pure and smaller anatase with a specific BET surface area of $250m^2/g$ and a primary particle size of 5 nm. The photocatalyst PC 500 has a BET surface area of $287m^2/g$ with 100% anatase and primary particle size of 5-10nm and TiO_2 obtained from TTP, India has a BET surface area of $9.82m^2/g$. It has been demonstrated that the degradation rate of dyes proceeds much more rapidly in the presence of P-25 as compared to other photocatalysts. The efficiency of photocatalysts was shown to follow the order: P-25> UV100> PC500> TTP for

the degradation of various pesticides and herbicides derivatives (Singh *et al.*, 2003, 2004, 2007a, 2007b, Rahman and Muneer, 2005a, 2005b; Qamar and Muneer, 2005). The differences in the photocatalytic activity are likely to be related to the differences in the BET surface, impurities, lattice mismatches or density of hydroxyl groups on the catalyst's surface, since these factors could affect the adsorption behavior of a pollutant or intermediate molecule and the life time and recombination rate of electron-hole pairs (Bahnemann *et al*., 2007; Singh *et al*., 2007a, 2007b, 2007c; Rahman and Muneer 2005a, 2005b; Qamar and Muneer 2005; Muneer and Bahnemann, 2002).

Table 3.1 Specification and Characteristics of TiO_2 Samples.

Sample	Specific surface area BET (m^2/g)	Crystal size (nm)	Composition	Ref.
P-25	50	21	75% Anatase, 25% Rutile	Singh *et al.*, 2007b
PC 500	287	5-10	100% Anatase	Singh *et al.*, 2007b
UV 100	250	5	100% Anatase	Singh *et al.*, 2007b
TTP	9.82	N/A	N/A	Singh *et al* ., 2007b
PC 10	10	65-75	100% Anatase	Erquez and Pichat, 2006
PC 50	54	20-30	100% Anatase	Erquez and Pichat, 2006
Rhodia	150	N/A	100% Anatase	Erquez and Pichat, 2006

N/A= Not available

Swarnalatha and Anjaneyulu (2004) compared the photocatalytic efficiency of P25, TiO_2 (Merck), ZnO, CdS and WO_3 for photocatalytic degradation of 1×10^{-4} M 2,6-dinitrophenol (2,4-DNP). In the presence of UV light (254nm) and 4g/L catalyst dose, the degradation rate was shown to follow the order: P25> ZnO> TiO_2 (Merck)> CdS> WO_3. The observed low activity of CdS and WO_3 is related to its smaller band gap. In comparison to UV 100, P-25 was reported to be efficient for the degradation of prometryn (Evgenidou *et al.*, 2007). The photocatalytic activity of Degussa P-25 was reported to be higher due to slow recombination between electron and holes whereas Hombikat UV 100 has a high photoreactivity due to fast interfacial electron transfer rate. The higher photoactivity of P-25 has been attributed to its crystalline composition of rutile and anatase. It was postulated that the smaller band gap of rutile absorbs the photons and generates electron-hole pairs. Then the electron transfer takes place from the rutile CB to electron traps in anatase phase (Hurun *et al.*, 2003). Thus it inhibits the recombination and allows the hole to move to the surface of the particle to react (Hurun *et al*., 2003). Poulios and Kositzi (2006) studied the photocatalytic oxidation of

methomyl by comparing the efficiency of P-25, ZnO and UV-100. Under the conditions investigated, the order of the photocatalytic dissolved organic carbon (DOC) reduction of methomyl was reported to be: P-25>ZnO>UV100. The photocatalytic degradation of vanillin is demonstrated in the order: P-25> UV100> ZnO (Qamar and Muneer, 2009). Under the tested conditions, the photocatalytic degradation of 4-Chlorophenol (4-CP) was shown to follow the order: P25> PC10> PC50> PC500> Rhodia (Erquez and Pichat, 2006). Salah *et al.* (2004) compared the efficiency of three commercial catalysts P-25(20nm), A1(160nm) and A2(330nm) available in anatase form, and ZnO for the degradation of phenol. After 5h reaction, the order of the efficiency was shown to follow ZnO>P-25>A1>A2. Valenzuela *et al*. (2002) compared the photocatalytic activity of ZnO, Fe_2O_3 and $ZnFe_2O_4$ for the degradation of phenol. After 100 min irradiation, the observed degradation from the samples calcined at 800^{o}C was shown to follow the order: TiO_2 P-25> $ZnFe_2O_4$> ZnO> Fe_2O_3.

3.3 Influence of Substituent Group

Lapertot *et al*. (2006) investigated the influence of the halogen substituent on the photocatalytic degradation of the *p*-halophenols by comparing their apparent rate constants. The observed order was found to decrease in the order as follows: *p*-fluorophenol≈*p*-chlorophenol≈phenol >*p*-bromophenol >*p*-iodophenol. This was related to the electron density on the aromatic ring, which varies with the halogen substituent. In suspended form, Lachheb *et al*. (2008) reported that in comparison to PC 500, P-25 was more efficient for the degradation of phenols and poly nitrophenols(4-NP, 2,4-DNP,2,4,6-TNP) in the presence of either artificial or solar light. The photocatalytic degradation of the tested compounds were shown in the following order: 2,4,6-TNP> 2,4-DNP> 4-NP> phenol. However, they observed a different order: phenol <4-NP <2, 4-DNP <2, 4, 6-TNP for PC 500 supported on Ahstrom paper 1048. The difference was related to the variation in adsorption behaviour. The photocatalytic degradation of phenol and ortho-substituted phenolic compounds was shown to follow the order: Guaiacol> 2-chlorophenol= Phenol>Catechol (Peiro *et al.*, 2001). Kusvuran *et al*. (2005) studied the photocatalytic degradation of 2,4,6-trimethylphenol (TMP), 2,4,6-trichlorophenol (TCP), 2,4,6-tribromophenol (TBP), 2,4-dimethylphenol (DMP), 2,4-dichlorophenol (DCP)and 2,4-dibromophenol (DBP). Under the conditions tested, degradation of these tri-substituted phenols is found to be in the following order: TCP> TBP> TMP. and the degradation of di-substituted phenols is shown to be in the order: DCP> DBP>

DMP. Under the experimental conditions, Baran *et al*. (2008) indicated that the pattern of photocatalytic degradation of Acid Black1 (AB1), Acid Orange 7(AO7), and Basic Orange 66 (BO66) dyes (C_o=0.1mM) follows the order: BO66 > AO7> AB1. This was attributed to the variation in adsorption behaviour due to different chemical structures.

3.4 Influence of Light Intensity and Wave Length

Light intensity determines the extent of light absorption by the semiconductor catalyst at a given wavelength. The rate of initiation of photocatalysis, electron-hole formation in the photochemical reaction is strongly dependent on the light intensity (Cassano and Alfano, 2000). Light intensity distribution within the reactor invariably determines the overall pollutant conversion and degradation efficiency (Pareek *et al*., 2008). Consequently the dependency of pollutant degradation rate on the light intensity has been studied in numerous investigations of various organic pollutants while in some cases the reaction rate exhibited a square root dependency on the light intensity, others observed a linear relationship between the two variables (Terzian and Serpone, 1991). Ollis (1991) reviewed the effect of light intensity on the organic pollutant degradation rate. It has been reported (Ollis, 1991; Al-Sayyed *et al*., 1991; Hermann, 1999) that the rate was proportional to the radiant flux Φ for Φ < 25mW/cm^2, above 25mW/cm^2, the rate was shown to be varied as $\Phi^{1/2}$, indicating a too high value of the flux and an increase of the electron-hole recombination rate. At high intensity, the reaction rate is independent of light intensity. This is likely because at low intensity reactions involving electron-hole formation are predominant and electron-hole recombination is insignificant. Wong and Chu (2003) studied the photocatalytic degradation of alachar using three different UV lamps at 254,300 and 350nm. Of the three UV wavelengths used, the highest photocatalysis quantum yield was obtained at 300nm.

The degradation rate constant of chlorsulfuron was reported to increase from 0.074 min^{-1} to 0.28 min^{-1} when the radiant flux increases from 6.9 mW/cm^2 to 33.8 mW/cm^2 (Freshno *et al*., 2005). In the case of pyridaben degradation, a linear relation between reaction rate *k* and radiant flux was reported to exist for the range of radiant flux studied from 2.8 to 8.8 mW/cm^2 (Zhu *et al*., 2005). Under the tested conditions, they also noticed that photocatalytic degradation of pyridaben was more efficient at $\lambda \geq 300$nm than at $\lambda \geq 360$nm irradiation.

The degradation rate of atrazine in an immobilized reactor was independent of UVA (λ_{max}=365nm, I=3.28×10^{-8} Einstein cm^{-2}s^{-1}) and UVB (λ_{max}=313nm, I=2.0×10^{-8}Einstein cm^{-}

$^{2}s^{-1}$) irradiation, however, the maximum apparent quantum yield under UVB was higher compared to UVA irradiation (McMurray *et al*., 2006). Para *et al*. (2004) indicated the dependence of atrazine degradation rate on the intensity of incident light from the Suntest solar simulator. Photocatalytic degradation rate constants of Imazapyr were indicated to be directly proportional to the radiation intensity from 0 to 25 mW/cm^2 (Carrier *et al*., 2006). A faster degradation was obtained with intensity at 90mW/cm^2 as compared to a light intensity of 50mW/cm^2. Similar trends have been indicated for the degradation of carbofuran (Mahalakshmi *et al*., 2007), cyromazine (Gutailler *et al*., 2001) with increase in irradiation light intensity from 16 to 64W. Vulliet *et al*. (2003) studied the effect of photon flux on the photocatalytic degradation of sulfonylurea herbicides. The reaction rate was shown to be proportional to the incident photon flux when photons flux $\leq 4.2\times10^{-16}$ photons s^{-1}. The degradation rate was reported to vary as the square root of the radiant flux until 12.6×10^{-16} photons s^{-1}. Sleiman *et al*. (2007) observed that the first order rate constant of iodosulfuron degradation is directly proportional to the photon flux when flux is below 10^{16} photon s^{-1}cm^{-2}. At high photon flux, the rate constant was shown to vary as the square root of flux. It has been indicated that the build-up of electron-hole pairs within the photocatalyst is smaller than the oxidizable organic substrate concentration and hence a linear rate law was observed at low fluxes whereas the photocatalytic degradation efficiency was shown to be limited to the electron-hole recombination which is predominant at flux above 10^{16} photon s^{-1}cm^{-2}. Kaneco *et al*. (2009) investigated the effect of irradiance on the solar photocatalytic destruction of thiram with various light intensities on sunny and cloudy days. The degradation efficiency increased rapidly with increase in the light intensity up to 0.4mW/cm^2, and above the intensity the efficiency increased gradually. The solar photocatalytic degradation efficiency of bishphenol A (BPA) is reported to increase rapidly with increase in the light intensity up to 0.35mW/cm^2, and then the efficiency increased gradually (Kaneco *et al*., 2004).

Venkatachalam *et al*. (2007a) compared the mineralization efficiency of 4-CP using the lamps of wavelength 365nm and 254nm over TiO_2. The mineralization rate at 365nm is reported to be slightly higher than at 254 nm.The observed lower degradation rate at 254 nm was attributed to the partial absorption and wasting of light at 254nm by 4-CP itself. Pourata *et al*., (2009) tested the effect of light intensity (5.3-17.5Wm^{-2}) on the photooxidative removal of bentazon and achieved the highest removal at 17.5Wm^{-2}. Chiou *et al*. (2008) reported the effect of UV light intensity (20-400W) on the photocatalytic degradation of

phenol. The degradation rate constants with a light intensity of 20, 100, and 400W are shown to be $8.3x10^{-3}$, 0.012 and $0.031min^{-1}$, respectively. Under the conditions tested, an acceptably good linear correlation exists between the apparent first order rate constant and light intensity. The studies reviewed here suggested that the effect of light intensity on the photocatalytic degradation rate must be determined to ensure successful application of photocatalytic oxidation system.

3.5 Influence of Pollutant Initial Concentration

Successful application of photocatalytic oxidation system requires the investigation of the dependence of photocatalytic degradation rate on the substrate concentration (C_o). Table 3.2 summarizes a variety of pesticides and phenolic compounds studied under various initial concentrations. The photocatalytic degradation rate of phosphamidon was shown to increase with the increase in initial concentration from 1×10^{-4} to 4.5×10^{-4}M (Rabindranathan *et al.*, 2003). However, at concentration of 6×10^{-4}M, the rate slows down considerably. Similar trends have been observed for the photocatalytic degradation of triclopyr and daminozid (Qamar *et al.*, 2006), carbofuran (Mahalakshmi *et al.*, 2007), propham and tebuthioron (Muneer *et al.*, 2005), Indole -3-acetic acid and Indole-3-buteric acid (Qamar and Muneer, 2005), methamidophos (Wei *et al.*, 2009), methyl parathion (Kim *et al.*, 2006), 4-chlorophenol (Venkatachalam *et al.*, 2007). Using ZnO, Pardeshi and Patil (2009) tested the effect of initial concentration (50-300ppm) on the photocatalytic degradation of resorcinol under solar light. The degradation efficiency in 7h decreases from 100 to 43.8% as the Co increases from 100 to 300 ppm. Consistently similar results have been reported for degradation of phenol (Pardeshi and Patil, 2008), thiram (Kaneco *et al.*, 2009), lindane (Senthilnathan and philip2010), dimethoate (Chen *et al.*, 2007), diazinon and erioglaucino (Daneshvar *et al.*, 2006, 2007), Bentazon (Pourata *et al.*, 2009), 2-chlorophenol (Barakat *et al.*, 2005). The photocatalytic degradation of 4-nitrophenol (4-NP) was shown to decrease from 100 to 40.9% as the initial concentration increases from 0.02 to 0.1g/L (Parida *et al.*, 2006). Parida and Parija (2006) examined the effect of initial substrate concentration (2-25g/l) on the photocatalytic degradation of phenol under sunlight, visible and UV light, respectively. With the increase in the substrate concentration, the degradation efficiency decreased from 100% to 60% under solar irradiation. Under UV light, the degradation was reported to

decrease from 94% to 52% with increasing initial concentration. The degradation was found to decrease from 95% to 50% under visible light.

Table 3.2 Influence of initial pollutant concentration on the photocatalytic degradation of various pollutants.

Pollutant	Light source	Photocatalyst	Co range, mM	Optimum Co, mM	Ref.
Phosphamidon	UV	TiO_2	0.1-0.6	0.45	Rahman and Muneer, 2005b
Acephate	UV	TiO_2	0.7-1.0	1	Rahman *et al*., 2006
Diphenamid	UV	TiO_2	0.1-0.6	0.6	Rahman *et al*., 2003
Phenol	Solar	ZnO	0.027-0.32	0.027	Pardeshi and Patil, 2008
2,4-dinitrophenol	UV	ZnO	0.05-0.09	0.09	Vora *et al*., 2009
Carbofuran	UV	TiO_2	0.023-0.113	0.09	Mahalakshmi *et al*., 2007
Thiram	Solar	TiO_2	4.2×10^{-4}-16.6×10^{-4}	4.2×10^{-4}	Kaneco *et al*., 2009
Indole-3-acetic acid	UV	TiO_2	0.2-0.6	0.3	Qamar and Muneer, 2005
Indole-3-buteric acid	UV	TiO_2	0.18-0.6	0.3	Qamar and Muneer, 2005
Lindane	Visible	N-TiO_2	$3.45x10^{-5}$-$2.07x10^{-4}$	$3.45x10^{-5}$	Senthilnathan and Philip, 2010
Dimethoate	UV	TiO_2	0.0195-0.49	0.0195	Chen *et al*., 2007
Isoproturon	Solar	TiO_2	0.25-.75	0.75	Haque and Muneer, 2003
Triclopyr	UV	TiO_2	0.25-1.0	0.75	Qamar *et al*., 2006
Daminozid	UV	TiO_2	0.50-1.5	0.75	Qamar *et al*., 2006
Diazinon	UV	ZnO	0.003-0.005	0.003	Daneshvar *et al*., 2007
Methamidophos	UV	Re-TiO_2	0.1-0.5	0.1	Zhang *et al*., 2009
2-chlorophenol	UV	Co-TiO_2	0.097-0.583	0.097	Barakat *et al*., 2005
Resorcinol	Solar	ZnO	0.05-0.272	0.05	Pardeshi and Patil, 2009
Erioglaucine	UV	TiO_2	0.006-0.02	0.006	Daneshvar *et al*., 2006
Bentazon	UV	TiO_2	0.02-0.062	0.02	Pourata *et al*., 2009
Propham	UV	TiO_2	0.25-1.3	0.75	Muneer *et al*., 2005
Prophachlor	UV	TiO_2	0.2-1.35	1.35	Muneer *et al*., 2005
Tebuthioron	UV	TiO_2	0.25-1.5	1.0	Muneer *et al*., 2005

As indicated in several investigations that as the concentration of the target pollutant increases, more and more molecules of the compound are adsorbed on the surface of the photocatalyst. Therefore, the reactive species (•OH and $\bullet O_2^-$) required for the degradation of the pollutant also increases. However, the formation of •OH and $\bullet O_2^-$ on the catalyst surface

remains constant for a given light intensity, catalyst amount and duration of irradiation. Hence, the available OH radicals are inadequate for pollutant degradation at higher concentrations. Consequently the pollutant degradation rate decreases as the concentration increases (Bahnemann *et al.*, 2007). In addition, an increase in substrate concentration can lead to the generation of intermediates, which may adsorb on the surface of the catalyst. Slow diffusion of the generated intermediates from the catalyst surface can result in the deactivation of active sites on the photocatalyst and result in a reduction in the degradation rate. In contrast, at low concentration, the number of catalytic sites will not be limiting factor and the rate of degradation will be proportional to the substrate concentration, in accordance with apparent first-order kinetics (Hermann, 1999). Priya and Madras (2006) tested the effect of initial concentration (10-76ppm) on the photocatalytic degradation of 2,4-dinitrophenol in the presence of combustion synthesized TiO_2 and P-25. The highest degradation was observed at 76ppm. Similar trends have been reported for the photocatalytic degradation of acephate (Rahman *et al*., 2006), 2,4-DNP (Vora *et al.*, 2009), isoproturon (Haque and Muneer, 2003),diphenamid (Rahman *et al*., 2003) and propachlor (Muneer *et al*., 2005). This is in accordance with the Langmuir-Hinshelwood (L-H) law. Several investigations have described the dependence of the photocatalytic degradation rates on the concentration of various phenols and dyes using the L-H kinetics model (Mathews 1988, 1990; Mills and Morris, 1993). The L-H model is used to describe the dependence of the observed reaction rate on the initial solute concentrations (Turchi and Ollis, 1990).

3.6 Influence of Catalyst Loading

A number studies have indicated that the photocatalytic degradation rate initially increased with catalyst loading and then decreases at high values because of light scattering and screening effects. The tendency toward agglomeration (particle-particle interaction) also increases at high solids concentration, resulting in a reduction in catalyst surface area available for light absorption and hence a drop in the photocatalytic degradation rate. Although the number of active sites in solution will increase with catalyst loading, a point appears to be reached where light penetration is to be compromised because of excessive particle concentration. The trade off between these two opposing phenomena results in an optimum catalyst loading for the photocatalytic reaction (Adesina, 2004). A further increase in catalyst loading beyond the optimum will result in non-uniform light intensity distribution, so that the reaction rate would indeed be lower with increased catalyst dosage.

Table 3.3 shows the influence of catalyst loading on the photocatalytic degradation of various organic compounds. Singh et al. (2007a) examined the effect of catalyst concentration using three different TiO_2 powders on the degradation of phenoxy acetic acid (PAA) and 2,4,5-trichlorophenoxy acetic acid (2,4,5-TCPAA). P-25 was reported to be more efficient as compared to other TiO_2 powders at all the employed concentrations for the degradation of PAA and the order of efficiency was P-25>UV100>PC500. The degradation rate was shown to increase with the increase in catalyst loading up to 1g/L and, on further increase in catalyst loading, the degradation rate lead to a decrease for all catalysts. Similar trends were also observed for the degradation of 2,4,5-TCPAA and pyridaben as well as photocatalytic degradation of thiram. Under the conditions tested, Garcia and Takashima (2003) observed an optimum TiO_2 concentration of 8g/L for the degradation of imazaquin. The degradation rate was found to increase with increasing catalyst concentration up to 3 g/L and on subsequent addition of catalyst leads to the leveling off of the degradation rate. Similar results have been reported for photocatalytic degradation of thiram (Kaneco *et al*., 2009), tebuthiron (Muneer *et al.*, 2005), Atrazine (Bahena *et al.*, 2008).

Using ZnO and solar light, the photocatalytic degradation rate of 4-Nitrophenol (4-NP) was observed to increase up to 0.6g/L and then levelled off as the ZnO concentration increases to 0.8g/L (Parida *et al*., 2006). An optimum concentration of P-25 was reported to be 0.1g/L under the conditions examined for the photocatalytic degradation of prometyrin (Evgenidou *et al*., 2007). Wei *et al*. (2009) indicated that the degradation of methamidophos increases with catalyst concentration from 2.0 to 12.0g/L and further increase in TiO_2 results in reduced degradation. An increase in the amount of catalyst provides an increased number of active sites for adsorption; however, the simultaneous increase in the solution opacity inhibits the penetration of the photon flux. Kuo *et al*. (2010) observed that under visible light (400nm) irradiation, the photocatalytic degradation rate constants of BPA were 0.44 and 1.89 h^{-1} for 0.5 g/L and 2 g/L TiO_2, respectively. However, further addition of TiO_2 (≈3.0 g/L) was reported to result in reduced degradation due to reduced visible light penetration. Under the conditions investigated, the optimum concentrations of TiO_2 and ZnO were found to be 3 g/L and 4 g/L respectively for efficient removal of 4-fluorophenol (Selvam *et al.*, 2007).

Table 3.3 Influence of catalyst loading on the photocatalytic degradation of various pollutants.

Pollutant	Light source	Photocatalyst	Catalyst dose range , g/L	Optimum dose, g/L	Ref.
Erioglaucine	UV	TiO_2	0-0.35	0.3	Daneshvar *et al*., 2006
Diazinon	UV	ZnO	0.5-4.0	3.0	Daneshvar *et al*.,2007
Glyphosate	UV	TiO_2	1.0-9.0	6.0	Shifu and Yunzhang, 2007
Thiram	Solar	TiO_2	0-0.3	0.20	Kaneco *et al*., 2009
Trichlorfon	UV	TiO_2	5.0-10.0	8.0	Liu *et al*., 2009
Phorate	UV	TiO_2	0.1-1.0	0.5	Wu *et al*., 2009a
Tebuthioron	UV	TiO_2	0.5-7.5	5.0	Muneer *et al*., 2005
2,4,5 TCPAA	UV	TiO_2	0.5-5.00	3.00	Singh *et al*., 2007a
Phenol	UV/Visible	Fe^{3+}-TiO_2	0.4-1.0	0.5	Nahar *et al*., 2006
2,4-dinitrophenol	UV	ZnO	1.0-3.0	3.0	Vora *et al*., 2009
Propham	UV	TiO_2	0.5-5.0	5.0	Muneer *et al*., 2005
Terephthalic acid	UV	ZnO	0.2-3.0	2.5	Shafaei *et al*., 2010
Beta-cypermethrin	UV	RuO_2-TiO_2	2.0-6.0	5.0	Yao *et al*., 2007
Methamodiphos	UV	Re-TiO_2	2-12	1.0	Zhang *et al*., 2009
Triclopyr	UV	TiO_2	0.5-5.0	2.0	Qamar *et al*., 2006
Methyl orange	Solar	SO_4^{2-}-TiO_2	0-2.5	2.5	Parida *et al*., 2008
Picloram	UV	TiO_2	0.2-2.0	2.0	Rahman and Muneer, 2005
Floumeturon	UV	TiO_2	0.5-3.0	3.0	Rahman and Muneer, 2005
Carbofuran	UV	TiO_2	0.025-0.125	0.1	Mahalakshmi *et al*., 2007
Turbophos	UV	TiO_2	0.1-2.0	0.5	Wu *et al*., 2009b
Carbendazim	UV	TiO_2	0-0.09	0.07	Saien and Khezrianjoo, 2008
Imazapyr	UV	TiO_2	0.315-2.5	2.5	Pizarro *et al*., 2005
Resorcinol	Solar	ZnO	0.5-3.5	2.5	Pardeshi and Patil, 2009

In the presence of solar light, the highest photocatalytic degradation of phenol was observed at 2.5g/l of ZnO (Pardeshi and Patil, 2008). In the presence of ZnO, Pardeshi and Patil (2009) tested the effect of catalyst loading (0.5-3.5g/L) on the solar photocatalytic degradation of resorcinol. The degradation of resorcinol was shown to increase with increase in ZnO up to 2.5g/L, further increase in photocatalyst amount showed negative effect due to increased turbidity of the suspension. In the presence of B/Ce-codoped TiO_2, the optimum catalyst loading was observed to be 4.26g/L for the photocatalytic degradation of dicofol, cyfluthrin

and fenvalerate in visible light irradiation (Lifen *et al*., 2009). Using C-doped TiO_2, Xiao *et al*. (2008) demonstrated the effect of catalyst loading (0.5-4.0 g/L) on the solar photocatalytic degradation of methylene blue in the order 1.0>2.0>4>0.5 g/L. They related the reported lower degradation at high catalyst loading with high turbidity due to C-doped TiO_2 nanopartciles. Using 036 mol % Co-doped TiO_2, Barakat *et al*. (2005) tested the effect of catalyst loading (0.005-0.03 g/L) on the photocatalytic degradation of 2-CP. The degradation reached a maximum value of 93.4% with catalyst dosage of 0.01g/L. A further increase in the catalyst dosage slightly decreased the degradation efficiency. This suggests that the amount of photocatalyst to be used should maintain a balance between these two opposing effects. In order to ensure efficient absorption of photons and to avoid excess catalyst, photocatalytic reactor should be operated at optimum catalyst loading.

3.7 Influence of Medium pH

Characteristics of organic pollutants in wastewater differ greatly in several parameters, particularly in their speciation behaviour, solubility in water and hydrophobicity. While some compounds are uncharged at common pH conditions typical of natural water or wastewater, other compounds exhibit a wide variation in speciation (or charge) and physico-chemical properties. At pH below its pKa value, an organic compound exists as neutral state. Above this pKa value, organic compound attains a negative charge. Some compounds can exist in positive, neutral, and negative forms in aquous solution. This variation can also significantly influence their photocatalytic degradation behaviour. Wastewater pH varies significantly and can play an important role in the photocatalytic degradation of organic contaminants since it determines the surface charge of the photocatalyst and the size of aggregates it forms (Bahnemann *et al*., 2007; Haque *et al*., 2006; Qamar *et al*., 2006; Singh *et al*., 2007a; Rahman *et al*., 2006) . The surface charge of photocatalyst and the ionization or speciation (pKa) of an organic pollutant can be profoundly affected by the solution pH. Electrostatic interaction between semiconductor surface, solvent molecules, substrate and charged radicals formed during photocatalytic oxidation strongly depends on the solution pH. In addition protonation and deprotonation of the organic pollutants can take place depending on the solution pH. Sometimes protonated products are more stable under UV-radiation than its main structures (Saien and Khezrianjoo, 2008). Therefore the pH of the solution can play a key role in the adsorption and photocatalytic oxidation of pollutants.

The ionization state of the surface of the photocatalyst can also be protonated and deprotonated under acidic and alkaline conditions respectively as shown in the following reactions:

$$pH<P_{zc} \quad TiOH + H^{+} \dashrightarrow TiOH_2^{+} \qquad (3.1)$$

$$pH>P_{zc} \quad TiOH + OH^{-} \dashrightarrow TiO^{-}+H_2O \qquad (3.2)$$

The point of zero charge (P_{zc}) of the TiO_2 (Degussa P-25) is widely investigated/ reported at pH~6.25 (Zhu *et al.*, 2005). While under acidic conditions the positive charge of the TiO_2 surface increases as the pH decreases (Equation 3.1); above pH 6.25 the negative charge at the surface of the TiO_2 increases with increasing pH. Moreover, the pH of the solution affects the formation of hydroxyl radicals by the reaction between hydroxide ions and photo-induced holes on the TiO_2 surface. The positive holes are considered as the major oxidation steps at low pH, whereas hydroxyl radicals are considered as the predominant species at neutral or high pH levels (Shifu and Gengyu, 2005; Mathews, 1986). It would be expected that the generation of •OH are higher due to the presence of more available hydroxyl ions on the TiO_2 surface. Thus the degradation efficiency of the process will be logically enhanced at high pH. To elucidate the effect of pH on the photocatalytic degradation of organic compounds and adsorption on the TiO_2 surface, numerous investigations (Singh *et al*., 2007a, 2007b, 2007c; Rahman and Muneer, 2005; Qamar and Muneer, 2005; Muneer and Bahnemann, 2002) have been carried out. The degree of electrostatic attraction or repulsion between the photocatalyst's surface and the ionic forms of organic molecule can vary with the change in solution pH, which can result in enhancement or inhibition on the degradation of organic pollutants in the presence of TiO_2. Table 3.4 shows the effect of pH on the photocatalytic degradation of various organic compounds. Wu *et al*. (2009b) indicated that degradation rate of turbuphos (neutral solute) decreased with a decrease in pH, and it proceeded much faster under alkaline pH. The observed behaviour is ascribed to the hydroxylation of catalyst surface due to the abundance of OH^- ions in alkaline conditions. Similar observation has also been made for the degradation of methamidophos (Wei *et al*., 2009), carbofuran (Mahalakshmi *et al*., 2007) and thiram (Kaneco *et al*., 2009). However, the degradation rate of methamidophos was nearly independent of solution pH when Re-doped TiO_2 was used as the photocatalyst (Zhang *et al*., 2009). A significant variation in the degradation of carbendazim (pKa=4.5) has been shown in the pH range of 3-4.5 compared to 7-9 (Saien and Khezrianjoo, 2008).

In contrast, acidic or alkaline medium favours the degradation of glyphosate (Shifu and Yunzhang, 2007), and chlorphenapyr (Cao *et al*., 2005). A decreasing trend has been observed for the photocatalytic degradation of PAA and 2,4,5-TCPAA in the pH range 3-9 (Singh *et al.*, 2007a). The degradation of imazaquin was also shown to decrease in the pH range 3-11 (Garcia and Takashima, 2003). The observed trends were attributed to the unfavourable electrostatic repulsion between the negatively charged surface of the catalyst and OH^- which decreases the degradation efficiency at higher pH (Qamar *et al*., 2006).

Table 3.4 Influence of pH on the photocatalytic degradation of various pollutants.

Pollutant	Light source	Photocatalyst	Tested pH range	Optimum pH	Ref.
Atrazine	Solar	TiO_2	2.0-9.99	4-5	Parra *et al*., 2004
Diazinon	UV	ZnO	3.5-11.3	5.2	Daneshvar *et al*., 2007
Erioglaucine	UV	TiO_2	2.4-12.2	2.4	Daneshvar *et al*., 2006
Phorate	UV	TiO_2	4.0-8.0	8.0	Wu *et al*., 2009a
Dimethoate	UV	TiO_2	2.04-11.05	11.05	Chen *et al*., 2007
Propham	UV	TiO_2	3.0-11.0	5.0	Muneer *et al*., 2007
2,4-DCP	Visible	N-TiO_2	5.14-9.01	5.87	Xing *et al*., 2009
Turbophos	UV	TiO_2	3.0-8.0	8.0	Wu *et al*., 2009b
Beta-cypermethrin	UV	RuO_2-TiO_2	2.4-10.8	6.42	Yao *et al*,. 2007
Terepthalic acid	UV	ZnO	8.0-11.0	9.0	Shafaei *et al*., 2010
Propachlor	UV	TiO_2	3.0-11.0	3.0	Muneer *et al*., 2005
Methamodiphos	UV	Re-TiO_2	4.0-10.0	6.0	Zhang *et al*., 2009
4-chlorophenol	UV	WO_3-TiO_2	4.0-10.	4.0	Lin *et al*., 2008
Methylparathion	UV-A	Bi^{3+}-TiO_2	2.0-10.0	2.0	Rengaraj *et al*., 2005
Thiram	Solar	TiO_2	2.5-11.4	8.0	Kaneco *et al*., 2009
Isoproturon	Solar	TiO_2	3.0-10.0	7.0	Sharma *et al*., 2009
o-cresol	Visible	Pt-TiO_2	3.0-11.0	9.0	Chen *et al*., 2007
2,4-dinitrophenol	UV	ZnO	2.0-8.0	6.0	Vora *et al*., 2009
4-CPAA	UV	TiO_2	3.0-9.0	3.0	Singh *et al*., 2007b
Carbofuran	UV	TiO_2	4.0-9.0	7.0	Mahalakshmi *et al*., 2007
Carbendazim	UV	TiO_2	3.0-9.0	9.0	Saien and Khezrianjoo, 2008
Monocrotophos	UV	La-ZnO	8.0-10.0	10.0	Anandan *et al*., 2007
Resorcinol	Solar	ZnO	4.0-10.	9.0	Pardeshi and Patil, 2009

The higher degradation rate of diuron (Sayeh *et al.*, 2007), propham and prophachlor (Muneer *et al.*, 2005) was observed at pH values 3-5, whereas the degradation rate was moderately influenced by the solution pH and increased slightly at pH 11. Under the conditions tested, Zhu *et al.*, (2005) reported a significant increase in the degradation rate of pyridaben at pH below 4. However, the degradation rate constant decreases gradually upon increasing pH from 6 to 11. Alkaline medium favours the the photocatalytic degradation of trichlorfon (Liu *et al.*, 2009). The photocatalytic degradation of metamitron in ZnO suspension was higher in acidic conditions compared to alkaline conditions (Minjin *et al.*, 2009). Under visible light irradiation, Xing *et al.* (2009) studied the photocatalytic degradation of 100 mg/L 2,4-dichlorophenol(2,4-DCP) using P-25, TiO_2 and N-TiO_2 prepared in different conditions for a pH range 5.14-9.01. Compared to pure TiO_2 and P-25, the photocatalytic activities of N-TiO_2 are reported to be significantly higher for all the tested pH values. As the pH increases, the photocatalytic activity also increases at first and then decreases. The highest degradation was observed at pH 5.87 when N/Ti ratio is 2.0 and H_2O/Ti ratio is 1:76. Anandan *et al.* (2007) reported that the degradation rate of monocrotophos (MCP) was significantly favoured in alkaline pH (8-10) compared to acidic pH when La-doped ZnO was used as the photocatalyst. Nonethless, the degradation rate was reported to decline above pH 10 due to the neutral state of MCP. Lin *et al.* (2006) indicated that the degradation rates of pentachlorophenol (PCP) using four metal (Au, Ag, Cu, Pt) doped-TiO_2 are shown to be higher at pH 3 than that obtained at pH 7. At pH 3, the degradation efficiency of four metal-doped TiO_2 is shown to follow the order: Au >Ag >Pt > Cu. In acidic solution, the positive surface charge of TiO_2 strongly attracted the negatively charged PCP since its pKa value is at pH 4.74. This leads to an increase in its degradation.

Using 1% Au-TiO_2 prepared by photoreduction method, Iliev *et al.* (2007) tested the influence of Au loading pH on the photocatalytic destruction of oxalic acid. The photonic efficiency was shown to increase from 0.79 to 1.87% with increasing pH from 3 to 7 and then it decreases to 1.67% as the pH increases to 9. For all the pH values (3-9) tested, the BET surface area is shown to decrease from 18 to 4 m^2/g and the average particle size is observed to be decreased from 18 to 4 nm. Under visible light (λ=410nm) irradiation, the photocatalytic degradation rate constants of BPA at pH 4, 7 and 10 were shown to be 0.44, 0.31 and 0.10 h^{-1}, respectively (Kuo *et al.*, 2010). Since the pKa value of BPA is 9.6–10.2,

the electrostatic interactions between the TiO_2 surface and BPA resulted in higher adsorption and degradation at pH 4.0. In the presence of 0-1.5wt% Pt deposited TiO_2 and visible light irradiation, Chen *et al*. (2007) noticed that the degradation of o-cresol increases as pH value increases from 3 to 9. Furhther increase in pH to 10, results in a decrease in the degradation rate due to increased repulsion between TiO_2 surface and o-cresol which reduces adsorption of o-cresol on TiO_2.Venkatachalam *et al*. (2007a) indicated that the photocatalytic degradation of 4-CP was higher at pH 5 compared to alkaline pH. The reported higher degradation in the acidic pH is related to the enhanced adsorption of 4-CP on the TiO_2 surface. In the acidic pH, minimization of electron-hole recombination is an important factor for the enhanced degradation of 4-CP. The photocatalytic degradation of 4-NP was reported to increase 92% at pH 6.0 and then decreased with increasing pH until 7 (Parida *et al*., 2006). This was related to negative charges of ZnO surface which hinders the degradation of 4-NP at pH 7. Using sulphate-modified TiO_2, the influence of pH on the photocatalytic degradation of methyl orange (MO) was reported to be pH 2> pH 4> pH6 >pH 8 in visible light (Parida *et al.,* 2008). Using C-doped TiO_2, the effect of pH (3-10) on the solar photocatalytic degradation and adsorption of methylene blue was demonstrated to be pH10> pH7> pH3 (Xiao *et al*., 2008). Using 0.036 mol %Co-doped TiO_2, the effect of pH (4-12) on the photocatalytic degradation of 2-CP was shown to be pH12> pH11> pH9> pH7> pH4 (Barakat *et al*., 2005). In the presence of TiO_2 and ZnO, the influence pH on the photocatalytic degradation of 4-fluorophenol was observed to be pH7> pH9> pH4 (Selvam *et al.,* 2007). The results summarized here indicate that a suitable pH control strategies should be implemented for an efficient photocatalytic water purification process.

3.8 Influence of Interfering Substances

Since wastewater composition can vary with time, the basic understanding of the effect of organic and inorganic constituents present in wastewater on the performance of photocatalytic systems is crucial to ensure operational stablility of a prototype photocatalytic water purification process. A number of studies demonstrated that water components like calcium, magnesium, iron, zinc, copper, bicarbonate, phosphate, nitrate, sulfate, chloride, and dissolved organic matters can affect the photocatalytic degradation rate of organic pollutants since they can be adsorbed onto the surface of TiO_2 (Abdullah *et al*., 1990; Parent *et al*., 1996). Depending on the solution pH, they can also compete with the target pollutant for the active sites. The adsorption of water components can reduce the formation of $^{\bullet}OH$ radicals.

Although hydroxyl radical scavenging by the anions bicarbonate, phosphate, nitrate, sulfate, and chloride resulted in corresponding anion radicals, they have lower oxidation potential. Consequently all these reactions can influence the overall rate of photocatalytic oxidation. In order to elucidate the UV shielding effect from water turbidity, Giri *et al*. (2010) tested the influence of inorganic solids (kaolin, bentonite and silica gel) on the photocatalytic degradation of 2,4-dichlorophenoxy acetic acid (2,4-D) using TiO_2 fibre module for a range from 0 to 1.0 g/l. In the absence of solids, 2,4-D removals due to photocatalytic oxidation are shown to be about 53% after 2h reaction. However, the removals were reported to decrease the lowest values (≈41%, 14% and 38%) for 3.0g/L kaolin, 0.5g/L bentonite and 0.5g/L silica gel in the same period. The apparent zero order reaction rate also showed the strong inverse correlation between solid concentration (0-0.5g/l) and 24-D removal in case of bentonite and silica gel, nonetheless, this was not observed for kaolin particles. Chen *et al*. (2010) examined the effect of humic acid (HA) (0 to 25mg/l) as possible photosenitizer on the photocatalytic mineralization of dimethoate. Upon 60 min irradiation, the mineralization efficiency is shown to increase from 63.73 % and 78.88% as the HA concentration increases from 0 to 5mg/L. Further increase in HA led to a decrease in photocatalytic efficiency. This was attributed to the reduced light transmittance due to the excessive HA in reactive solution and the competitive adsorption of HA for the active sites on the catalyst surface. They also tested the effect of CH_3COCH_3 concentration (0 to1.0 % (v/v) on the dimethoate mineralization at neutral pH. The mineralization rate appears to decrease from 36.73 to 9.23% with increasing CH_3COCH_3 concentration due to the competition of dimethoate for the reactive site. Under the conditions examined, the influence of Fe^{3+}, Cu^{2+}, Zn^{2+}, HCO_3^- and NO_3^- on the extent of mineralization is shown to increase with increasing ions concentration and reached a maximum level at optimal concentrations. In contrast, the mineralization of dimethoate was observed to be strongly inhibited by Cl^- and Cr^{3+} ions.

Rabindranathan *et al.* (2003) studied the effect of Cl^-, PO_4^{3-}, and NO_3^- on the photocatalytic degradation of phosphamidon. In the presence of 1.5×10^{-4} M of the tested anions, no significant effect was observed under the conditions examined. However, the degradation rate was reported to be inhibited by these anions at high concentration which was attributed to the competition of ions for active sites on the TiO_2 surface. The order of inhibition of three anions on the degradation rate is shown as $PO_4^{3-}>Cl^->NO_3^-$. Shifu and Yunzhang (2007) tested the effect of SO_4^{2-},Cl^-, Br^-,Na^+,K^+,Mg^{2+}, Ca^{2+}, Zn^{2+},Co^{2+} and Ni^{2+} on the photocatalytic

degradation rate of glyphosphate. No discernible effect was observed when trace amount of these anions were added to the solution. The degradation of glyphosate was reported to increase with the addition of 0.05mM Fe^{3+} and 0.01mM Cu^{2+} in solution. The scavenging of electrons by metal ions and subsequently preventing the recombination of electron-hole pairs, favours the formation of •OH and O_2^{2-} on the TiO_2 surface. In the presence of SO_4^{2-}, Cl^-, Br^-, Fe^{3+} and Cu^{2+}, similar results have been observed for the degradation of methamidophos (Wei *et al*., 2009). Shifu and Gengyu (2005) examined the effect of Cu^{2+},Zn^{2+} and Na^+ on the photocatalytic degradation of MCP and phorate. No discernible effect was observed with the addition of small amount of Zn^{2+} or Na^+. However, the degradation efficiency of tested compounds are shown to increase when 0.05 mM/dm^3 Cu^{2+} was added to the solution. Further Cu^{2+} addition results in reduced catalytic efficiency due to the predominance of $[Cu(H_2O)4]^{2+}$. In the presence of Cu^{2+} and Ni^{2+} ions (0.04-0.31 mM/L), the degradation efficiency of imazapyr was reported to decrease by factors of 4 and 2 for the cooper and nickel respectively (Carrier *et al*., 2006). Mahmoodi *et al*. (2007) investigated the effects of Cl^-, NO_3^-, and SO_4^{2-} on the photocatlytic degradation of diazinon and imidaclorpid respectively. The observed inhibitive effect on the degradation of the tested pollutants is shown to follow the order: $SO_4^{2-} < NO_3^- < Cl^-$. The detrimental effect of the tested anions is attributed to their competition for the active sites on the TiO_2 surface and catalyst deactivation which subsequently, decrease the degradation rate. A major drawback from the high reactivity and non-selectivity of •OH is that it also reacts with non-target compounds present in the background water matrix.This results in a higher •OH demand to accomplish the desired degree of degradation (Parent *et al*., 1996). Wu *et al*. (2009b) examined the effect of nitrate and chloride anions on the photocatalytic degradation of turbophos and phorate. Significant inhibition on the degradation efficiency has been reported due to the presence of anions. As explained in several studies (Mahmoodi *et al*.,2007; Wu *et al*., 2009b) that inhibition is due to the reaction of positive holes and hydroxyl radicals with anions that behaved as radical (h^+ and •OH) scavenger resulted in longer turbophos removal. Mijin *et al.* (2009) studied the effect of NaCl, Na_2CO_3 and Na_2SO_4 salts on the photocatalytic degradation of metamitron in ZnO suspension. The effects of salt addition are shown to be in the order: $CO_3^{2-} > SO_4^{2-} > Cl^-$. Negligible inhibition was observed when the concentration of NaCl was 20mM.

Dissolved organic matter (DOM), ubiquitously present in storm and wastewater effluent also plays an important role in regard to pesticide degradation. Lin and Lin (2007) observed that the presence of humic acid caused a significant retardation on the photocatalytic degradation of 4-chlororphenol. The observed retardations of humic acids was related to the inhibition (surface deactivation), competition and light attenuation effects. Moreover the presence of humic acid in the reaction mixture has been reported to significantly reduce light transmittance, and therefore the photooxidation rate. Zhu *et al*. (2005) examined the effect of water content (0-50%) on the initial reaction rates of photocatalytic degradation of pyridaben. The initial reaction rate was shown to follow the sequence: acetonitrile/H_2O (80/20)> (90/10> (70/30)> (60/40)> (95/5)> (50/50)> (100/0). This order was indicated to be related to hydroxyl radials generated and the solubility of pyridaben in various cases. Kundu *et al.* (2005) studied the effects of various solvents on the photodegradation of 2,4-dichlororphenoxy acetic acid in 10% aqueous methanol and 10% aqueous acetonitrile. The photodegradation was also studied in two different micellar environments such as aqueous 10^{-2}M Cetyltrimethyl ammonium chloride (CTAC) micelle (cationic) and aqueous sodium dodecyl sulphate (SDS) anionic micelle (10^{-2}M). Under 45 min irradiation, the degradation was varied in the range of 16-57%. The degradation of 2, 4-D in the CTAC micelle was observed to be higher and it was more than two times as obtained with other conditions.

The effect of transition metal ions on the degradation of 4-flurophenol was shown to be in the order of Mg^{2+}>Fe^{3+}>Fe^{2+}>Cu^{2+} and the inhibition of inorganic anions on the degradation of 4-FP was demonstrated to be CO_3^{2-}>HCO_3^->Cl^->NO_3^->SO_4^{2-} (Selvam *et al*., 2007). Naeem and Feng (2008) reported that the order of anions inhibition on the photocatalytic degradation of phenol is Cl^->SO_4^{2-}>NO_3^->CO_3^-. At certain level, Fe^{3+} is reported to improve the degradation rate whereas Ca^{2+}, Cu^{2+}, and Mg^{2+} hinder the degradation process. The effect of surfactants (0.05mM/L) on the degradation rate was observed to be sodium dodecyl benzene sulphate (SDBS) > sodium dodecyl sulfonate (AS)>sodium dodecyl sulphate (SDS). The presence of anions is reported to alter the ionic strength of the solution, which influences the catalytic activity and the photocatalytic degradation. Marinas *et al*. (2001) studied the influence of humic acids on the photocatalytic degradation of formetanate (FMT). In the presence of humic acid, the degradation rate was shown to decrease due to the competition between FMT and humic acids for active sites on the catalyst surface. The photocatalytic degradation of 2,4-dichlorophenoxy acetic acid and 4-chloro-2-methylphenoxy acetic acid

was reported to be inhibited by 70% and 80% due to the presence of 1.4×10^{-2} mol/L ethanol (Djebbar *et al.*, 2006). Inorganic anions, such as phosphate, sulphate, nitrate, and chloride, have been reported to limit the performance of solar based photocatalysis (Parent *et al.*, 1996).

3.9 Influence of Oxidants/electron Acceptor

The electron/hole recombination is one of the main drawbacks in the application of TiO_2 photocatalysis as it causes waste of energy. In the absence of suitable electron acceptor or donor, recombination step is predominant and thus it limits the quantum yield. Thus it is crucial to prevent the electron-hole recombination to ensure efficient photocatalysis. Molecular oxygen is generally used as an electron acceptor in heterogenous photocatalytic reactions. Addition of external oxidant/electron acceptors into a semiconductor suspension has been shown to improve the photocatalytic degradation of organic contaminants (1) by removing the electron-hole recombination by accepting the conduction band electron; (2) increasing the hydroxyl radical concentration and oxidation rate of intermediate compound; and (3) generating more radicals and other oxidizing species to accelerate the degradation efficiency of intermediate compounds (Singh *et al.*, 2007a, 2007b, 2007c, Rahman and Muneer, 2005a, 2005b; Qamar and Muneer, 2005; Muneer and Bahnemann, 2002). Since hydroxyl radicals appear to play an important role in the photocatlytic degradation, several researchers have investigated the effect of addition of electron acceptors such as H_2O_2, $KBrO_3$, and $K_2S_2O_8$ on the photocatlytic degradation of various pesticides and herbicides (Bahnemann *et al.*, 2007; Singh *et al.*, 2003, 2004; Rahman *et al.*, 2006, Wei *et al.*, 2009) to enhance the formation of hydroxyl radicals as well as to inhibit the electron/hole (e^-/h^+) pair recombination. In all cases the addition of oxidants has resulted in higher pollutant degradation rate compared to the molecular oxygen. In most of the cases, the order of enhancement is $UV/TiO_2/BrO_3^->UV/TiO_2/S_2O_8^{2-}>UV/TiO_2/H_2O_2$. The enhancement of degradation rate is due to reaction between BrO_3^- and conduction band electron (Singh *et al.*, 2007a, 2007b, 2007c; Rahman and Muneer, 2005a, 2005b). This reaction reduces the recombination of electron-hole pair.

$$BrO_3^- + 6e^-_{CB} + 6H^+ \dashrightarrow Br^- + 3H_2O \qquad (3.3)$$

$S_2O_8^{2-}$ can generate sulphate radical anion ($SO_4^{\bullet-}$) both thermally and photolytically in aquous solution. $SO_4^{\bullet-}$ then reacts with H_2O to produce •OH radicals.

$$S_2O_8^{2-} \dashrightarrow 2SO_4^{\bullet-} \qquad (3.4)$$

$$SO_4^{\bullet-} + H_2O \dashrightarrow {}^{\bullet}OH + SO_4^{2-} + H^+ \qquad (3.5)$$

With the addition of H_2O_2, the enhancement of degradation is due to the increase in the hydroxyl radical concentration as shown by Equation (3.6) and (3.7);

$$H_2O_2 + e_{CB}^- \dashrightarrow {}^{\bullet}OH + OH^- \quad (3.6)$$

$$H_2O_2 \dashrightarrow {}^{\bullet}OH + {}^{\bullet}OH \quad (3.7)$$

The degradation efficiency of UV/TiO_2/oxidant process is slightly more in acidic medium than in basic medium. Wei *et al.* (2009) examined the effect of H_2O_2, $KBrO_3$ and $K_2S_2O_8$ addition on the photocatalytic degradation of methamidophos by varying the amount of oxidant concentration. The optimum concentrations of the oxidants were 0.8mM/L, 4.0mM/L and 0.8mM/L for H_2O_2, $KBrO_3$ and $K_2S_2O_8$ respectively. Of the oxidants studied, $K_2S_2O_8$ was demonstrated to be most effective for the degradation of methamidophos. $KBrO_3$ was shown to be more efficient acid as compared to H_2O_2 for improving the degradation rate of tebuthiuron, propachlor, chlortoluron, thiram (Bahnemann *et al.*, 2007), PAA and 2,4,5-TCPAA (Sing *et al.*, 2007a), terbacil and 2,4,5-tribromoimidazole (Muneer and Bahnemanna, 2002), imazapyr (Carrier *et al.*, 2006),dimethoate (Chen *et al.*, 2007) , Glyphosphate (Shifu and Yunzhang, 2007). The reduction of bromated ions by electrons does not lead directly to the formation of hydroxyl radicals, but rather to the formation of other reactive radicals or oxidizing agents, e.g. BrO_2^- and HOBr (Singh *et al.*, 2007a). Moreover, bromated ions by themselves can act as oxidizing agents.

In contrast H_2O_2 was reported to be efficient for propham, prophachlor (Muneer *et al.*, 2005) and triclopyr, daminozid (Qamar *et al.*, 2006), dicamba and floumeturon (Rahman and Muneer, 2005). Both H_2O_2 and $K_2S_2O_8$ were shown to be equally effective for prometryn degradation at an optimum concentration of 2mM (Evgenidou *et al.*, 2007). However, the degradation rates were also demonstrated to decrease at high concentration. This behaviour has been related to the modification of TiO_2 surface by H_2O_2 adsorption and scavenging of the photogenerated holes and reaction with hydroxyl radicals. The effect of oxidants on the degradation of 4-flurophenol was shown to be in the order of IO_4^->BrO_3^->$S_2O8_2^-$>H_2O_2> ClO_3^- (Selvam *et al.*, 2007). Park *et al.* (2009) studied the effect of H_2O_2 concentration (from 0-3.0mM) on the photocatalytic degradation of benomyl.Under the conditions investigated (C_o=3.2mg/l, TiO_2=2.0g/l, I_{UV}=6.525mW/cm^2), the degradation rate constant of benomyl are shown to vary from 0.0208 min^{-1} to 0.0235 min^{-1}. Under the conditions tested, the effect of oxidant addition on the photocatalytic degradation of trichlorfon is shown to be in the order: $K_2S_2O_8$>$KBrO_3$>H_2O_2 (Liu *et al.*, 2009).This trend may be attributed to the generation of

highly reactive intermediate radicals $SO_4^{\bullet -}$ from $K_2S_2O_8$ and oxidizing agents such as, BrO_2 and HOBr from $KBrO_3$etc.

3.10 Influence of Mode of Application: Suspended vs Immobilized System

The efficiency of suspended catalysts (TiO_2) has been demonstrated to be superior compared to the immobilized catalyst (Parent *et al.,* 1996). This can be attributed to the enhanced mass transport in suspended form. However, the cost incurred for catalyst recovery makes the slurry system impractical. In contrast, the immobilized catalyst would be easier to handle but will likely be more costly due to fouling and deactivation of catalyst. The reasons for the deactivation include (a) generation of reaction by products which cause the loss of active sites on the surface, and (b) fouling which changes the catalyst surface by blocking pores. The stability and the photoreactivity of the catalyst are strongly influenced by the amount of hydroxyl groups. As the reaction proceeds, the density of hydroxyl groups on the catalyst surface decreases, consequently the activity of the catalyst drops. The experimental results (Dutta and Ray, 2004) indicated that strongly adsorbed intermediates occupied the active sites on the catalyst surface and led to the loss of photocatalytic activity. Therefore, more efforts should be focused on to eliminate the intermediates that occupy the active sites of the catalyst and regenerate the hydroxyl radicals. Comparable photodegradation kinetics of atrazine has been obtained when TiO_2 was used in suspended and immobilized systems (Parra *et al.,* 2004). Pizaro *et al.* (2005) evaluated the photocatalytic degradation of imazaphyr using powdered and supported catalytic system for titania P-25 and PC-500. In the case of powdered titania, 76.5µmol-1 of imazaphyr was completely degraded with P-25 after 30 min irradiation. In contrast, only 45% conversion of imazaphyr was achieved with PC-500. However, when a mixture of PC-500 and P-25 with a ratio 1:1 was used as the catalyst composition; imazaphyr disappeared practically at the same rate as the pure P-25. In the case of three supported catalysts, the conversions of same amount of imazaphyr after 4 hours irradiation were 82, 89 and 21.4% for P-25,P-25+PC-500 and PC-500 respectively.

Madani *et al.* (2006) studied the photocatalytic degradation of diuron in the presence of paper-supported TiO_2 catalysts. Regardless of the nature of TiO_2 (P-25 or PC500 or their equimolar mixture deposited on paper NW 10), the photocatalytic degradation rate of diuron was similar to the results obtained with suspended powders. The efficiency of PC 500

deposited on NW10 paper was comparable to that obtained with unsupported PC 500. In contrast, P-25/NW10 showed two times lower efficiency compared to P-25 powder. Using supported and suspended TiO_2, the degradation rate of chlortoluron was compared under identical (2.8g/L) TiO_2 loading and other experimental conditions (Lhomme *et al*., 2008). TiO_2 supported on non-woven paper appeared to be an efficient photocatalyst for degrading and mineralizing chlortoluron. Photocatalytic degradation of methyl parathion, dichlorvos and lindane in aqueous medium were investigated with suspended and immobilized system (Senthilnathan and Philip, 2009). The rate constant of methyl parathion and dichlorvos was reduced by 50% when the initial concentration increased by 10 times. In contrast, the rate constant of lindane was decreased by almost 30%. As the pesticide concentration increases, the adsorption of pesticide on the active sites of catalyst surface increases. Hence, competitive adsorption of OH^- for the same sites decreases, thus reducing the formation of •OH. Under the conditions examined, at low concentration of pesticides, there was no significant variation in degradation rates obtained in suspended and immobilized TiO_2 systems. Recently, there has been growing interest for the development of photocatalyst supported on various materials e.g glass and alumina beads, zeolites (Shankar *et al*., 2006; Sharma *et al*., 2008a, 2008b). Sahnkar *et al*. (2006) indicated that 1wt %TiO_2 supported on HY zeolite was reported to be efficient for the photocatalytic degradation of 2,4-dichlorophenoxyacetic acid compared to bare TiO_2. This effect was associated with the improved adsorption and efficient delocalisation of photogenerated electrons by zeolite support.

Sharma *et al*. (2008a) studied the photocatalytic degradation of isoproturon in a TiO_2 immobilized over mesoporous SBA-15 composite system using solar light. 10 wt%TiO_2/SBA supported system was reported to show higher photocatalytic activity compared to bare TiO_2. This was attributed to the synergistic effect resulted from the adsorption of isoproturon over mesoporous material facilitating the degradation. In addition to isoproturon, the composite was shown to be efficient for the degradation of imidaclorapid and phosphamidon in wastewater. Similar observations have been made for the degradation of isoproturon in a 10wt% TiO_2 supported on Al-MCM-41 composite (Sharma *et al*., 2008b).This was related to the delocalization of electrons which come from TiO_2 excitation and inhibits electron and hole recombination. The dispersion of TiO_2 over mesoporous materials to eliminate particle-particle aggregation and light scattering by TiO_2, which provides complete harvesting of solar

light. Zhao *et al*. (2009a) reported the enhanced degradation efficiency for a composite TiO_2 supported on NaY zeolite (Specific surface area=659 m^2/g, particle size=0.65nm) for the degradation of omethoate under the optimal conditions. A composite of 5wt % TiO_2 and porous nano silica was reported to be efficient compared to TiO_2 for the degradation of imidaclorpid and phosphamidon in wastewater (Sharma *et al*., 2009).

3.11 Influence of Calcination Temperature

A range of techniques have been employed to prepare nanocrystalline TiO_2 powder for catalytic purposes including sol-gel method, solvo-thermal process, reverse micellar, hydrothermal method and electrochemical methods. Of these methods, the sol-gel process is regarded as a promising alternative due to its low sintering temperature, versatility of processing and homogeneity at molecular level. The structure and size of TiO_2 crystallites significantly depends on calcination temperature. Thermal treatment of TiO_2 gels at higher temperature promotes phase transformation from thermodynamically metastable anatase to more stable and condensed rutile phase. As dehydration occurs during heat treatment, crystallites grow to dimensions larger than those of the original particles. Table 3.5 shows the influence of calcination temperature on photocatalytic degradation of various organic contaminants.Using ZnO thin films, Aal *et al*. (2009) examined the effect of calcination temperature (350-550^oC) and time (1-2h) on the photocatalytic degradation of 2,4,6-trichlorophenol. The growth of ZnO nano-structure was found to be dependent on calcination time and temperature. Optimum ZnO nano-fibres is observed to be formed uniformly after 2h oxidation at 550^oC. Zhao *et al*. (2009a) showed that the optimum temperature for the photocatalytic degradation of omethoate was found to be 550^oC. Under the conditions investigated, a sharp decrease in the degradation rate at 650^oC has been related to the over growth of the TiO_2 crystal size and the presence of a rutile phase in the TiO_2 crystal. Amadelli *et al*. (2008) tested the effect of calcination temperature (100-500^oC) on the time required for mineralization of 4-CP using 0.2%Co-TiO_2 (prepared by the incipient impregnation method) and TiO_2. The best result was obtained for the sample calcined at 400^oC for 30 minutes; however, heating over 2h at this temperature did not result in any appreciable changes in surface area and anatase/rutile phase ratio. Co-TiO_2 is shown to be more active than the pure TiO_2 for all treatment temperatures. Song *et al*. (2009) investigated the effect of titania films with different nanostructures of nanorods (NR), sol-gel film (SG),

nanotubes (NT) and nanoparticle aggregates on the photocatalytic degradation of rodamine B (RB) , methylene blue (MB) and methyl orange (MO). In the case of RB degradation, the observed order was reported to be NR>DP>SG>NT, while the order was shown to be NR>SG>DP>NT for the degradation of MB. However an order of NT>DP>SG>NR was found for the degradation of MO. Using 0.50wt% Pt-TiO_2, Chen *et al*. (2007) tested the effect of calcination temperature (150-750^oC) on the photocatalytic degradation of o-cresol under visible light. The reaction rate constant was reported to decrease as the calcination temperature increases from 150 to 750^oC. This was related to the decrease in surface area as the calcination temperature increases for the above range.Using C-doped TiO_2, the complete solar photocatalytic degradation of MB (Co=10mg/L) was observed at 600^oC in 80 min irradiation due to stronger absorption of the C-doped TiO_2 in 300-500nm range (Xiao *et al*., 2008). Pardeshi and Patil (2009) tested the effect of calcination temperature (400-900^oC) on the solar photocatalytic degradation of resorcinol using ZnO. ZnO calcined from 400^oC to 550^oC showed about 100% degradation with in 7h even if the ZnO particle size increases from 31.8nm to 51.9 nm. This was related to the uniform ZnO crystallite growth rate up to 550^oC, which gives ZnO of same morphology. After 550^oC the degradation efficiency was observed to decrease with increase in calcination temperature. This may be due to the increase in ZnO crystallite size with calcination temperature which leads to a decrease in number of active sites of photocatalyst for adsorption of substrate molecules. Using C-doped TiO_2 prepared by sol-gel method, Park *et al*. (2009) tested the effect of calcination temperature (100-500^oC) on the photocatalytic degradation of 4-CP under visible light (λ>420nm) irradiation. Maximum degradation was obtained at 250^oC. Further increase in calcination temperature above 300^oC results in a dramatic fall in the visible light activity, indicating that the incorporation of the lattice carbons is hindered at higher temperatures. Sirisaksoontorn *et al*. (2009) studied the efficacy of N-doped TiO_2 for the degradation of phenanthrene under visible light. Using the N-doped TiO2 (size=8.84nm, BET= 253.7m^2/g) calcined at 400^oC; nearly 80% degradation was observed in 8h irradiation. In contrast, less than 10% degradation was obtained using either N-doped TiO2 (BET=74m^2/g) calcined at 500^oC or P25 (49.2m^2/g). The higher activity of the N-doped TiO2 calcined at 400^oC was attributed to its smaller particle size and the greater number of active sites due to larger surface area. The N-doped TiO_2 showed the anatase-to-rutile phase transformation at the calcination temperature range of 400–700^oC.

Table 3.5 Influence of calcination temperature on the photocatalytic degradation of various pollutants

Pollutant	Light source	Photocatalyst	Range of calcination	Optimum calcination temperature	Ref.
Omethoate	UV	TiO_2	350-650°C	550°C	Zhao *et al*., 2009b
Beta-cypermethrin	UV	RuO_2-TiO_2	400-700°C	500°C	Yao *et al*., 2007
Methamidophos	UV	Re-TiO_2	400-800°C	700°C	Zhang *et al*., 2009
4-chlorophenol	Visible	C-TiO_2	100-500°C	250°C	Park *et al*., 2009
4-chlorophenol	Visible	Co-TiO_2	100-500°C	400°C	Amadelli *et al*., 2008
o-cresol	Visible	Pt- TiO_2	150-750°C	150°C	Chen *et al*., 2007
Phenol	UV	TiO_2	400-900°C	800°C	Tian *et al*., 2009
Methylene blue	UV	C-TiO_2	500-800°C	600°C	Xiao *et al*., 2008
Phenanthrene	Visible	N-TiO_2	400-700°C	400°C	Sirisaksoontorn *et al*., 2009
4-chlorophenol	UV	Zr^{4+}-TiO_2	105-1100°C	900°C	Lukac *et al*., 2007
Rhodamine B	Solar	TiO_2	300-800°C	700°C	Wang *et al*., 2008
Phenol	UV/Visible	I-TiO_2	400-600°C	400°C	Hong *et al*., 2005
Phenol	Visible	N-TiO_2	350-500°C	400°C	Wang *et al*., 2005
2,4,6-TCP	UV	ZnO	350-550°C	550°C	Aal *et al*., 2009
Resorcinol	Solar	ZnO	400-900°C	550°C	Pardeshi and Patil, 2009

Wang *et al*. (2005) investigated the effect of calcination temperature (350-500°C) on the photocatalytic activity of N-doped TiO_2 for the degradation of phenol in visible (λ>400nm) light.The amount of mineralization was reported to be 24.1% at 350°C and 35.6% at 400°C in 120min respectively. In contrast, N-doped TiO_2 calcined at 500°C and P25 did not significantly change the total organic carbon value. The high photocatalytic activity at 400°C is partially due to the smaller particle size and higher adsorption area toward the organic substrate as well as the intense absorption in the visible light range and a red shift in the band gap transition of the doped TiO_2 samples. Tian *et al*. (2009) tested the effect of calcination temperature (400-900°C) on the photocatalytic activity of biphase TiO_2 synthesized by hydrothermal process and ammonia post treatment for the degradation of phenol (50mg/L). Under the conditions examined, the sample calcined at 800°C showed the highest activity due to large surface area, high crystallinity and separation rate of charged carriers, and heterojunction microstructure between anatase and brokite. The sample calcined at 900°C showed reduced activity due to the excessive decrease of surface area and the growth of sample particles. Using the Re-doped and undoped TiO_2, Zhang *et al*. (2009) studied the effect of calcination temperature on the degradation of methamidophos. For both catalysts, the degradation efficiency was shown to increase for the calcination temperature from 400°C

to 600^{o}C.This effect was ascribed to the growth of crystallization and the elimination of photocatalyst amorphism due to temperature increment. However, the degradation efficiency was reported to decrease with further increase in temperature (>600^{o}C) due to crystal development. Doped nano-TiO_2 was reported to have better photocatalytic activities until 700^{o}C due to the presence of Re and the resulting inhibition on crystal growth. Bessekhouad *et al*. (2004) studied the effect of alkaline (Li, Na, K) doped TiO_2 prepared by sol-gel route and impregnation method on the photocatalytic degradation of benzamide. The crystallinity levels of catalysts are found to be largely dependent on both the nature and the concentration of alkaline. The best crystallinity is obtained for Li-doped TiO_2 and is lowest for K-doped TiO_2. For a given alkaline concentration, the catalyst prepared by the impregnation technique was shown to be more efficient than those prepared by the sol-gel route. The half life of benzamide was two to four times higher compared to undoped TiO_2. The half-life of benzamide obtained with 5% Li-doped TiO_2 was comparable to P-25. The half-life of benzamide with 1% K-doped TiO_2 was shown to be lower than that of P-25. 1% Na-doped TiO_2 prepared by impregnation method is reported to better than P-25. Using hydrothermal assistant sol-gel method, An *et al*. (2008) tested the effect of the calcination temperatures (350-650^{o}C) on the photocatalytic activity of mesoporous TiO_2 for the degradation of 2,4,6-tribromophenol (TBP). XRD analysis indicated that a sample calcined at 350^{o}C possesses a high BET surface area of 142 m^2/g and the observed BET surface area was reduced to 49m^2/g when the calcination temperature was increased to 550^{o}C.The BET surface area was 7m^2/g when the sample calcinated at 650^{o}C, which was attributed to the complete, collapsed mesoporous structure. In addition, the degradation of 2,4,6-TBP was reported to increase as the calcination temperature increases from 350 to 550^{o}C and then sharply decrease when the sample calcination temperature further rises to 650^{o}C. This was due to the increase in crystalline size from 9.8 to 18.4 nm and the resulting decrease in BET surface area from 142 to 49 m^2/g and completely collapsed mesoporous structure at 650^{o}C.

Gorska *et al*. (2009) tested the influence of calcination temperature (350^{o}C-750^{o}C) on the photocatalytic degradation of 0.21mM phenol under UV (250<λ<400nm) and visible (λ>400nm) light irradiation. Using P-25 sample calcined at 350^{o}C, the highest amount of phenol degradation was shown to be 80% in 60 min in the visible light. In addition to the largest BET surface area (205.8m^2/g) and the smallest crystallite size (8.4nm) and average pore diameter (8.3nm) of TiO_2, this effect was attributed to the efficient absorption of light

vis region due to the existence of largest amount of carbon in aromatic C-C bonds (10.1 at%). In contrast, the photocatalyst calcinated at 450^{o}C was reported to have the highest activity in UV light. Under visible light irradiation, Wawrzyniak *et al.* (2006) studied the effect of calcination temperature (100-800^{o}C) on the photocatalytic degradation of phenol and two azo dyes (reactive Red, direct Green) by N doped-TiO_2. The highest amount of phenol was degraded at 700^{o}C. For the degradation of both azo dyes, the highest degradation was achieved at 500^{o}C and 600^{o}C respectively. Using N-doped TiO_2 and visible light, the maximum amount of phenol degradation was achieved at 600^{o}C and no variation was observed at 700^{o}C and 800^{o}C (Silveyra *et al.*, 2005). Lettman *et al.* (2001) observed that about 30% 4-CP (C_o=0.25mM) was degraded after 100 min irradiation (λ>400) in using a catalyst obtained by hydrolysis, followed by calicnation at 250^{o}C for 3h. Using a carbon doped TiO_2 prepared by $TiCl_4$ hydrolysis in tetrabutylammonium hydroxide (calcination at 400^{o}C, 1h), 70 % TOC reduction of 0.25mM 4-CP was reported by Sakthivel *et al.*,(2004). The highest photocatalytic degradation of phenol using 2%-Au/TiO_2 was observed at 275^{o}C in solar light (Sonawane and Dongare, 2006). Using ZnO upon solar irradiation, the photocatalytic degradation of 4-NP increases from 52.9 % to 74.4% as the calcination temperature increases from 110 to 300^{o}C due to higher surface area and lower crystallite sizes (Parida *et al.*, 2006). Under visible light irradiation, Gorska *et al.* (2009) reported that about 60% phenol was degraded after 60 min in the presence of C-doped TiO_2 calcined at 350^{o}C. Under visible light, Li and Liu (2008) examined the photocatalytic activity of N-F codoped TiO_2 prepared by acid catalysed hydrolysis for the degradation of phenol over a range of calcination temperature 600-900^{o}C. The sample with 1:0.1 ratio of TiO_2 to NH4F showed maximum degradation at 700^{o}C and the complete degradation is shown to achieve within 60 min whereas only 15.5% and 13.0% phenol were degradated with pure TiO_2 and P-25 in 100 min. The activity of N-F codoped TiO_2 was also higher than the bare TiO_2 and P-25 in UV light. N-F codoping can improve dispersion of TiO_2 by inhibit particle size agglomeration, and retard phase transformation.

Lukac *et al.* (2007) examined the effect of annealing temperature (105-1100^{o}C) on the photocatalytic activity of Zr-doped TiO_2 for the degradation of 4-chlorophenol. The samples annealed between 800 and 900^{o}C are more efficient than the standard photocatalyst P-25. The optimum size of the Zr doped anatase crystallites is 69.2 and 86.5 nm obtained at 875 and 900^{o}C, respectively. The photocatalyst annealed at 900^{o}C was reported to have 1.5 times

higher degradation rate compared to P-25. At 900^{o}C, the sample is shown to have 87 wt. % of anatase and 13 wt. % of rutile. Using I-doped TiO_2 with anatase phase, Hong *et al*. (2005) investigated the effect of calcination temperature (400-600^{o}C) on the photocatalytic degradation of phenol under UV and visible light irradiation (λ>400nm). Of the temperatures tested, I-doped TiO_2 calcined at 400^{o}C shows significantly higher photocatalytic activity compared to undoped TiO_2 nanoparticles (P-25 and pure TiO_2). Using N-F codoped TiO_2 prepared by sol-gel approach, Meng *et al.* (2009) tested the effect of calcination temperature (400-700^{o}C) on the photocatalytic degradation of methylene blue in visible light (>410nm) irradiation. The sample (BET=42 m^2/g) calcined at 500^{o}C showed better photocatalytic efficiency. The phase transformation from anatse to rutile was hindered due to codoping with N and F.

3.12 Influence of Doping and Mixed Semiconductor

The light that TiO_2 can utilize is limited to UV fraction of the entire solar spectrum. A number of approaches have been suggested to enhance the photocatalytic activity of TiO_2 in the visible light. Modification of TiO_2 surface is one of the promising routes to enable TiO_2 sensitive to visible light for its use in water purification. Metal ion doping and co-doping with non-metals can improve trapping of the photo excited conduction band electrons at the surface whereby minimizing charge carrier recombination (Iwasaki *et al*., 2000; Abramovic *et al*., 2007, 2009; Rockafellow *et al*., 2009; Tryba, 2008; Dvoranova *et al*., 2002; Sanchez and Lopez, 1995; Kato *et al*., 2005). Successful doping can result in enhanced efficacy of the photocatalyst system. Several dopants used e.g Sn (Fresno *et al*., 2005) Ag and Pd (Liqiang et al., 2006), Re (Zhang *et al*., 2009), Bi^{3+} (Rengaraj *et al*., 2005), V^{5+}, Mo^{6+} and Th^{4+}(Devi *et al*., 2009a, 2009b; Devi and Murthy, 2008), Pt^{6+} (Katsumata *et al*., 2009) were shown to enhance photocatalytic activity substantially for the systems examined. However, the photoactivity of the metal-doped TiO_2 photocatalyst significantly depends on the dopant ion nature and concentration, preparation method and operating conditions (Dvoranova *et al*., 2002). Both positive and negative results have been reported from doping with metal ions. It is desired that the deposition of metal ions on TiO_2 can modify the photoconductive properties by increasing the charge separation efficiency between electrons and holes, and also by acting as a trap for electrons, inhibiting volume and surface recombinations of electron and hole that reduce the photoefficiency of TiO_2 photocatalyst (Sanchez and Lopez,

1995). The increase in charge separation efficiency will enhance the formation of both free hydroxyl radicals and active oxygen species (Kato *et al*., 2005). In contrast, the photocatalytic activity of metal doping is impaired by thermal instability and the recombination of photogenerated electrons and holes (Borous *et al*., 2007).The amounts of doping concentration along with a summary of the pesticides degraded using doped catalyst are shown in Table 3.6.

3.12.1 Influence of Metal Doping

Modification of TiO_2 through metals is increasingly being considered for maximizing its photocatalytic efficiency. The exerted effects depend on selected metal and content, type of TiO_2 used, nature of organic pollutants, and the photoreactor medium. Rengaraj *et al*. (2005) reported that the highest degradation and mineralization of methylparathion was achieved in the doping range of 0.7-1.5% Bi^{3+}. At the highest doping level (2%), the reduced degradation efficiency was ascribed to the formation of Bi^{3+} clusters, rather than a homogeneous distribution and lower crystallinity. Anandan *et al*. (2007) compared the photocatalytic activity of la-doped ZnO with pure ZnO and TiO_2 for the degradation of monocrotophos (MCP) Of the catalysts investigated, the efficiency of 0.8wt% La-doped ZnO was 2.5 and 1.5 times higher compared to pure ZnO and TiO_2 catalyst for the degradation of MCP both at wave lengths 254 and 365 nm respectively. In addition to high roughness and porous surface, this effect was attributed to a strong absorption of OH- ions on the surface of ZnO due to a large number of oxygen vacancies. Devi *et al*. (2009a) examined the effects of V^{5+}, Mo^{6+} and Th^{4+} doping into TiO_2 matrix for the degradation of chlorpyrifos under UV/solar irradiation. Undoped TiO_2 showed the highest rate constant (3.1×10^{-2} min^{-1}) compared to all the doped TiO_2 samples under UV light. This may be due to the fact that mid band gaps created by the dopants may serve as site for recombination. The optimum dopant concentration of all catalysts was found to be 0.06%. Of all the catalysts, 0.06% Th^{4+}doped-TiO_2 showed enhanced photocatalytic activity compared to all other catalysts under solar light due to (i) the large surface area, (ii) large shift in the bandgap,(iii) higher concentration of surface adsorbed water and hydroxyl groups (iv) effective separation of electrons and holes. The larger shift in the absorption band (460 and 482nm) to visible region increases the efficiency of the photocatalysts to absorb more photons under solar light. Devi *et al.* (2009b) tested the efficacy of TiO_2 doped with Th^{4+},V^{5+}, and Mo^{6+} for the photocatalytic degradation of

imidachloprid under solar light. The dopant amount of each metal ion ranged from 0.02% to 0.1%. Th^{4+}(0.06%)-TiO_2 showed enhanced activity and its efficiency was 2.8 times higher compared to P-25 under solar light compared to all the other catalysts studied. Due to the presence of Th^{4+}, the band gap of TiO_2 was reported to lower 2.5 and 2.6 facilitating solar light absorption. Detrapping of the trapped charge carriers depends on electronic configuration and the oxidation state of the dopants. Fresno *et al*. (2005) compared the photocatalytic activity of Sn-doped TiO_2 with P-25 TiO_2 for the degradation of chlorsulfuron. Sn-doped TiO_2 was reported to show higher photocatalytic activity in comparison to undoped TiO_2 due to incorporation of Sn^{4+} into the TiO_2 lattice. Devi and Murthy (2008) investigated the effectiveness of Mo^{6+} doped-TiO_2 for the photocatalytic degradation of tebuconazole under UV and visible light. In the presence of UV light, the undoped catalyst showed higher activity than the doped catalyst. However, 0.06% Mo^{6+}doped-TiO_2 showed enhanced photocatalytic activity under visible light irradiation. In the presence of TiO_2-Ag, Yan *et al.* (2005) indicated that the degradation rates of dimethomorp were 71.5% compared to 45.5% with pure TiO_2 in under 5 days sunlight.

Table 3.6 The influence of dopant concentration on photocatalytic activity of photocatalyst.

Pollutant	**Light source**	**Photocatalyst**	**Doping (%)**	**Optimum doping (%)**	**Ref.**
Diuron	UV	Pt-TiO_2	0-2.0	0.2	Katsumata *et al*., 2009
Monocrotophos	Solar	La-ZnO	0-1.0	0.8	Anandan *et al*., 2007
2,4-DCAA	Visible	CeO_2-TiO_2	0-10.0	5.0	Galindo *et al*., 2008
Methylparathion	UV	Bi^{3+}-TiO_2	0-2.0	1.5	Rengaraj *et al*., 2005
4-chlorophenol	Visible	N-TiO_2	0.21-0.45	0.45	Sun *et al*., 2009
Clopyralid	Visible	Fe^{3+}-TiO_2	0.13-1.48	1.27	Šojić *et al*., 2010
Mecoprop, MCPP	Visible	Fe^{3+}-TiO_2	0.13-1.48	0.13	Šojić *et al*., 2010
o-cresol	Visible	Pt-TiO_2	0-1.0	0.5	Chen *et al*., 2007b
Lindane	Visible	Ag-TiO_2	0-2.5	1.5	Senthilnathan and Philip, 2010
Lindane	Visible	Cr-TiO_2	0-2.5	2.0	Senthilnathan and Philip, 2010
Beta-cypermethrin	UV	RuO_2-TiO_2	0.1-0.8	0.3	Yao *et al*., 2007
Methamidophos	UV	Re-TiO_2	2.0-6.0	5.0	Zhang *et al*., 2009
Oryzalin	Solar	Th-TiO_2	0-0.1	0.06	Devi and Murthy, 2009
Acetamiprid	UV	Ag-TiO_2	0-0.12	0.75	Cao *et al*., 2008
Chlorsulfuron	UV	Sn-TiO_2	0-0.2	0.11	Freshno *et al*., 2005
Phenol	UV	Ag-ZnO	0-1.0	0.75	Liqiang *et al*., 2006
Phenol	UV	Pd-ZnO	0-1.0	0.5	Liqiang *et al*,. 2006

Cao *et al*. (2008) examined the efficacy of Ag-doped TiO_2 for the photocatalytic degradation of acetamiprid for a range of Ag content (0-0.12). At low level doping (0.02-0.06), anatase grain sizes decreased and the specific surface areas of TiO_2 increased. Ag dopant was found to accelerate the transformation of TiO_2 from anatase to rutile phase. At high level doping (0.08-0.12), particle size aggregation was reported to increase. The photocatalytic degradation rate constant was reported to increase rapidly when the Ag content ranged from 0.02 to 0.06 and then decreased slowly as the Ag content increased from 0.06 to 0.12. Shifu and Gengyu (2005) studied the SiO_2 content on the photocatalytic activity of TiO_2.SiO_2 beads for degradation of MCP. The optimum content of SiO_2 was reported to be 0.2. Devi and Krishnamurthy (2009) compared the photocatalytic degradation efficiency of diclofop-methyl using TiO_2 and $BaTiO_3$ under UV light irradiation. $BaTiO_3$ is shown to be more efficient than TiO_2 in the presence of ammonium persulfate. Rengaraj and Li (2006) tested the photocatalytic activity of Ag-TiO_2 prepared by ultrasonic assisted sol-gel method for the photocatalytic degradation of BPA. The presence of Ag in TiO_2 is reported to improve the degradation of BPA. Compared to pure TiO_2, the efficient electron-hole separation in Ag-TiO_2 was observed to increase the BPA degradation.

Liqiang *et al*. (2006) investigated the effect of Ag and Pd doping (0-1.0wt %) on the photocatalytic degradation of phenol using ZnO nanoparticles. The Ag and Pd modified ZnO was shown to have enhanced activity compared with pure ZnO because the modified ZnO can promote the adsorbed O_2 capturing photoinduced electrons to produce $\bullet O_2$. Under the studied conditions, the optimum amount of doping was observed to be 0.75wt.% and 0.5 wt % for Ag and Pd respectively. The surface hydroxyl content of 0.5% Pd-ZnO is reported to be larger than that of 0.5% Ag-ZnO, which is responsible for the higher activity than 0.5% Ag- ZnO. At pH 9, Chen *et al*. (2007) tested the effect of Pt dosage (0.04-1.5wt %) on the photocatalytic activity of TiO_2 for the decomposition of 9mg/L o-cresols under visible light. The band gap energies were observed to be 3.11eV for pure TiO_2 and 2.95eV for 1.5 wt% Pt/TiO_2. More than 90% o-cresols were shown to be decomposed by 0.50wt % Pt-TiO_2.The degradation rate constants of o-cresol for the 0.50wt% Pt-TiO_2 was 4.8 times than that obtained with pure TiO_2. The presence of Ti^{3+} prevents the recombination of e^-/h^+ due to the formation of Schottky Barrier between platinum and TiO_2. Amadelli *et al*. (2008) investigated the influence of cobalt (Co) addition (0.05-0.5%) on the performance of TiO_2 for the degradation of 1mM 4-CP with visible light (λ>450 nm). Under the conditions tested,

0.2% Co-doped TiO_2 is shown to be efficient. After 30 min irradiation, 0.5%Co-TiO_2 calcined at 400^oC showed superior activity compared to undoped TiO_2 for the degradation of BPA and 4-CP in visible light (λ>420nm; λ>450nm) irradiation. Lin *et al*. (2006) investigated the activity of four metals (Ag, Au, Pt, and Cu) doped TiO_2 for the photocatalytic degradation of pentachlorophenol (PCP). All four metals doped TiO_2 samples showed strong visible light (400-800 nm) absorption and enhanced activity due to reduced e^-/h^+ recombination and smaller particle size which increases surface areas. The surface areas of TiO_2, Ag-TiO_2 and Au-TiO_2 are reported to be 78.3, 84.6, and 86.0 m^2/g, respectively.The effect of metal contents on the photocatalytic efficiency was observed to follow the trend 0.1>0.5>1.0 wt%. The quantum yields of PCP degradation ranged from 9.9×10^{-3} to 13.6×10^{-3}. Iliev *et al*. (2010) studied the photocatalytic activity of TiO_2, Au/TiO_2, N-doped TiO_2 and Au/N-doped TiO_2 synthesized by sol–gel method for the degradation of oxalic acid under UV, visible and combined UV–visible light irradiation. The average size of the TiO_2 and N-doped TiO_2 is 20 nm and the average size of Au/TiO_2 and Au/N-TiO_2 is ≈5 nm. In the UV light, the rate constants of oxalic acid by the studied samples follow the order Au/N-TiO_2> Au/TiO_2>N-TiO_2>TiO_2. In the visible light, the rate constants of oxalic acid by the studied samples follow the order Au/N-TiO_2> N-TiO_2>>Au/TiO_2> TiO_2. The rate constants using Au/N-TiO_2 are shown to be 0.085 and 0.012 mmol L^{-1} min^{-1} in UV and visible light respectively. Using N-TiO_2 and Au/N-TiO_2, nearly similar degradation rate constants are noticed in UV and UV-visible light. They reported that the absorption edge of TiO_2 was shifted from 340 nm in UV to 450nm in visible region. Venkatachalam *et al*. (2007b) tested the effect of Zr^{4+} doping (0.5-5.0 mol % Zr^{4+}) in TiO_2 matrix for the photocatalytic degradation of 4-CP using sol-gel method. The photocatalytic activity of 3.0 mol% Zr^{4+}-doped TiO_2 was shown to be superior compared to nano TiO_2 and P-25 due to enhanced adsorption of 4-CP over the catalyst surface and the smaller particle size.

Kim *et al*. (2005) tested the efficacy of TiO_2 doped with 1.0 wt% transitions metals such as Fe, Cu, Nd, Pd and Pt for the dgerdation of 4-CP. After 240 min irradiation, the extents of degradation are shown to be about 90%, 75% and 65% for Pt-TiO_2, Pd-TiO_2 and pure TiO_2 respectively. This is related to the suppression of electron/hole recombination due to trapping of electrons. However, the Fe and Cu (1.0 wt%)-doped TiO_2 shows lower degradation efficiencies compared to pure TiO_2. The reduction of Cu^{2+} by photo-generated electrons may compete with the formation of superoxide anion-radicals and consequently may reduce the

formation of peroxidic species, destroying phenol molecules. They also studied the effect of Pt and Pd contents (0-3.0 wt%) on the photocatalytic degrdataion of 4-CP and the optimum doping level was reported to be 2 wt% under the conditions examined. Zaleska *et al*. (2008) tested the photocatalytic activity of TiO_2 modified with boric acid for the degradation of phenol under UV and visible light, respectively. The use of boric acid as a boron source resulted in lower photocativity of obtained B-TiO_2 than pure TiO_2 under UV light. All the tested TiO_2 powders with boric acid series have almost the same photactivity under visible light. Naeem and Ouyang (2009) studied the effect of Fe^{3+} doping (0-3.0 mol% Fe^{3+} on the photocatalytic activity of TiO_2 for the degradation of phenol under UV light. Fe^{3+}-doped TiO_2 was reported to possess the anatase structure with a range of crystal size 8-11nm. The highest degradation efficiency was found at 0.5mol% Fe^{3+}-doped TiO_2. In visible light irradiation, about 60% methyl orange (C_o=150mg/L) was degraded in 4h with SO_4^{2-}-modified TiO_2 compared to only 33% with pure TiO_2 ,which was due to increased BET surface area, smaller crystallite size and increased number of reaction sites (Parida *et al*., 2008). Following 2h calcination at 600^{o}C, photocatalytic activity of La-doped TiO_2 was ranked in the order 1>1.5>3>0.5>5>0 mol%La for phenol degradation (Liqiang *et al*., 2004).

Venkatachalam *et al*. (2007c) compared the photocatalytic activity of 0.5-3.0 mol%Mg^{2+} and 1-3.0mol % Ba^{2+}-doped TiO_2 synthesised by the sol-gel technique for the degradation of BPA. The band gap values of Mg^{2+} and Ba^{2+}-doped TiO_2 were reported to be higher compared to pure TiO_2.The degradation of BPA was found to be higher for metal doped TiO_2 than both pure nano TiO_2 and P-25. This was related to the enhanced adsorption of BPA over the catalyst surface and the decrease in particle size due to Mg^{2+} and Ba^{2+} loadings. The pure TiO_2 nanoparticles gave both anatase and rutile phases together, but the metal ion in TiO_2 gave only anatase phase. Fan *et al*. (2009) compared the efficacy of N-Fe co-doped TiO_2 prepared by the sol-gel method for the degradation of methylene blue (MB) with TiO_2 under solar light. After 90 min irradiation, the degradation was observed to be about 80% with N-Fe co-doped TiO_2 compared to 45 % with pure TiO_2. This was attributed to the shifiting of the absorption edge in co-doped smaple.Under visible light (>380nn) irradiation, Zhu *et al*. (2006) tested the photocatalytic activity of Fe^{3+}-doped TiO_2 for the degradation of 2, 4-DCP. After 7h reactions, the average photonic efficiencies were reported to be 8.36×10^{-6} and 5.12×10^{-6} for 0.15 Fe^{3+}-TiO_2 and P-25 respectively. This was related to small crystal size, high specific surface rea, mesoporous structure, surface chemisorbed water and hydroxyl groups. In visible

light irradiation, Silva *et al*. (2009) noted an optimum Ce content of 0.6 %(w/w) in TiO_2 matrix in the enhanced degradation of 4-CP. In addition to the retardation of phase transformation, this behaviour was related to the shift of the TiO_2 absorption edge towards longer wavelengths, by reducing the band gap of original material. Kim *et al*. (2008) studied the photocatalytic degradation of 4-CP using anatase, rutile, Ni 8-wt%-doped TiO_2 powders (anatase and rutile) under UV and visible light irradiation. Under UV and visible light irradiation, the effectiveness of Ni 8 wt%-doped TiO_2 (234 m^2/g) was much higher than that of other powders (100-150 m^2/g). Adan *et al*. (2007) investigated the effect of Fe^{3+} doping (0.4-5.1 wt %) on the photocatalytic degradation of phenol. The photocatalytic activity was shown to be enhanced following doping with Fe^{3+} up to ca.1wt%. Doping above ca.3wt% did not result in any enhancement of the catalytic activity. Jin and Shiraishi (2004) tested the photocatalytic activity of Pd, Cu and Pt deposited TiO_2 either individually or simultaneously for the degradation of 2,4-DNP(Co=8mg/L). After 180 min, nearly complete degradation was achieved with the metals doped TiO_2 whereas only 81.25% degradation obtained with bare TiO_2. The pattern of degradation was ranked in the order: Pd/TiO_2> $Pd\text{-}Cu/TiO_2$>$Pd\text{-}Cu\text{-}Pt/TiO_2$>$Cu/TiO_2$>$TiO_2$. Wang *et al*. (2007) studied the synergistic effects of Cu^{2+} and F^- ions on the photocatalytic degradation of phenol. The degradation rate constanst (*k*) was shown to be 0.010 min^{-1} in the absence of Cu^{2+} and F^-. The addition of 0.4 mmol L^{-1} Cu^{2+} increases *k* by 40% and the addition of 5 mmol L^{-1} F^- improves *k* by ca. 120%, and the co-addition of 0.4 mmol L^{-1} Cu^{2+} and 5 mmol L^{-1} F^- enhancess *k* further by ca. 310%. The observed synergistic effect of Cu^{2+} and F^- ions was attributed to the surface modification of photocatalyst by adsorbed Cu^{2+} and F^- ions.

3.12.2 Influence of Non-metals Doping

The metal doping can result in thermal instability of doped TiO_2, electron trapping by metal centres, and requirement of expensive ion-implantation facilities. Recent investigations indicate that the desired band gap narrowing of TiO_2 can be better achived by employing non-metal elements such as N, F, S and C. Such modified TiO_2 showed stronger absorption in the visible region owing to band gap narrowing and enhanced the degradation of organic pollutants under visible light irradiation, especially under solar light. The photocatalytic activity of anatase crystal phase N-doped TiO_2 for the degradation of mecoprop and (4-chloro-2-methylphenoxy) acetic acid (Co=2.7mmol/dm^{-3}) under visible light (400-800nm) irradiation was reported to be 1.5 times higher compared to P-25 (Abramovic *et al.*, 2009).

Carbon doped TiO_2 was reported to be efficient for the degradation of phenol (Co=30 mg/L) under visible light (λ>420nm) irradiation due to the shifting of absorption edge to a lower energy level (Lee *et al.*, 2008). Anandan *et al.* (2009) compared the performance of IO_3^- doped TiO_2 with pure TiO_2 for the degradation of MCP (Co=40mg/L) at wavelengths 254 and 365nm. The degradation rate constant of IO_3^-doped TiO_2 (1 wt%) was shown to be nearly three times higher than pure TiO_2. However, the rate constant and relative photonic efficiencies for the degradation of MCP were smaller at 365nm compared to 254nm due to enhanced electron-hole recombination at wavelength 365nm. The enhanced photocatalytic activity of IO_3^- doped TiO_2 was related to the IO_3^-doping which serves as an electron trap during the photocatalytic reaction, eventually suppressing the recombination of electron-hole pairs. In addition, the high activity of IO_3^-doped TiO_2 was strongly dependent on the particle size, shape, surface area, formation of mixed phases, and distribution of iodine particles on titanium surfaces. At wavelengths 254 and 365nm, the relative photonic efficiencies of 1wt% IO_3^- doped TiO_2 systems were shown to be 2.5 and 2.0 times greater than pure TiO_2. Under UV (365nm) and visible light (> 400nm) irradiation, Senthilnathan and Philip (2010) studied the photocatalytic degradation of N-doped TiO_2 prepared by the sol-gel method using triethylamine, urea, ethylamine and ammonium hydroxide for the degradation of 3.44×10^{-4} mmol lindane. The band gap energies of all N-doped TiO_2 samples (1:0.8, 1:1.2, 1:1.6 and 1:2.0 ratio) were lower compared to P-25 and anatase TiO_2 and the absorption of light in the range 400 to 600nm was stronger after nitrogen doping. In addition, the absorption increases with increasing doping concentration from 1:0.8 to 1:2.0. In comparison to urea, ammonium hydroxide and ethylamine, triethylamine doped TiO_2 showed greater photocatalytic activity since it forms a stable organo titanium complex which plays a very important role on the stability of the nano-particles and avoids the growth and aggregation of the particles (Yu *et al.*, 2007). Using P-25 and anatase TiO_2, degradation of 5.17×10^{-4}mmol lindane was shown to be 100% under UV light, whereas only 13.24% and 20.68% degradation was reported in visible light. However in the presence of N-doped TiO_2, 37.5% and 100% of degradation of lindane was observed under UV and visible light, respectively.

Under visible light (λ≥ 400 nm), Cheng *et al.* (2007) tested the photocatalytic activity of carbon-modified TiO_2 for the degradation of 0.15mM 4-CP. C-doped TiO_2 is shown to have large surface area. The first order rate constant for the C-TiO_2 and P-25 are observed to be 6.1×10^{-3} and 1.0×10^{-3} min^{-1}, respectively. Huang *et al.* (2006) reported that N-F co-doped

TiO_2 showed higher photocatalytic activity for p-chlorophenol under visible light irradiation (400-500nm). Under the conditions examined, the degradation efficiency was shown to be 1.75, 1.25 and 1.5 times higher compared to P-25, N-doped TiO_2 and F-doped TiO_2 respectively. This behaviour was ascribed to a synergistic effect of surface acidity, and doped N and F atoms. Xing *et al.* (2009) showed that N-doped TiO_2 synthesized by ammonium nitrate and ammonia as a nitrogen sources showed maximum photocatalytic activity for the degradation of 2,4-DCP (Co=100mg/L) within 5h of irradiation under visible light. Similar study using N-doped TiO_2 was reported by Cong *et al.* (2007) with 2,4-DCP (Co=100mg/L) and rhodamine B (Co=20mg/L) under visible light and complete degradation was achieved within 5h and 1h irradiation respectively. Huan *et al*. (2007) tested the decomposition of 4-CP (Co=13mg/L) using N-doped TiO_2 under visible light and achieved 63.5% degradation within 6h irradiation. Kun *et al.* (2009) examined the photocatalytic activity of phenol (Co=0.5mmol/L) under visible light with N-doped TiO_2 and found that acid treated N-TiO_2 showed higher catalytic activity in 2h irradiation.

Under visible light, Ananpattarachai *et al*. (2009) investigated the photocatalytic efficacy of N-TiO_2 prepared with different nitrogen dopants for the degradation of 2-CP. The photocatalytic activity of all N-doped TiO_2 ranked in the following order: TiO_2/diethanolamine> TiO_2/triethylamine > TiO_2/urea > un-doped TiO_2. After 50 min irradiation, 2-CP removal was 66% for TiO_2 doped with diethanolamine whereas only 3% and 14% 2-CP removal was obtained with P-25 and undoped TiO_2 respectively. This increase is related to the strong absorption in the visible light region and a red-shift in the bandgap transition of the doped TiO_2 with nitrogen dopant.Under visible light ($\lambda \geq 420$nm) irradiation, Šojić *et al*. (2010) studied the photocatalytic degradation of herbicides mecoprop (MCPP), 4-chloro-2-methylphenoxy acetic acid (MCPA) and clopyralid(CP) using Fe^{3+} or N-doped TiO_2. Rutile TiO_2 doped with Fe^{3+} showed lower photocatalytic activity for the degradation of MCPP and MCPA. In contrast, the rate of CP degradation is shown to increase with increase in the Fe^{3+} content up to 1.27 at.%. When N-doped anatase TiO_2 was used, the rate of degradation of all three herbicides was higher compared to that obtained using undoped anatase TiO_2. In all the cases the photocatalytic efficiency of undoped anatase TiO_2 was higher compared to that of the undoped rutile form. Rengifo-Herrera and Pulgarin (2009) tested the photocatalytic activity of N,S co-doped and N-doped commercial anatase TiO_2 powders for the degradation of phenol under simulated solar irradiation. Undoped P-25 was

shown to have the highest photocatalytic activity. N,S co-doped powders showed similar photocatalytic activity as undoped TKP 102(Tayca) while N-doped TKP 102 was less active photocatalyst due to N impurities on the TiO_2 acting recombination centres. Wang *et al.* (2005) compared the photocatalytic degradation of phenol in the presence of N-doped TiO_2 and P-25 under visible and sunlight irradiation. The photocatalytic activity of the N-doped TiO_2 with anatase phase is shown to be higher than that of the P-25 under visible light irradiation. P-25 exhibits higher photoactivity for the degradation of phenol compared to N doped-TiO_2.

3.13 Evaluation of Energy Efficiency

In heterogeneous photocatalytic water purification processes, the generation of photons driven by UV and solar light for catalyst activation is the significant part of the total cost for the operation of the system. The evaluation of the treatment costs is, at this time, one of the aspects that need more attention. In order to select a purification system for storm and wastewater reuse, a number of important factors; including economics, economy of scale, regulations, effluent quality goals, safe operation, and robustness should be taken into consideration. While all these factors are important, economics is often paramount. Simple figures-of-merit that provide a direct link to the electric-or solar-energy efficiency of an advanced oxidation process (AOP), have been recommended for comparison by IUPAC. Several researchers (Wu *et al.*, 2009a, 2009b; Daneshvar *et al.*, 2006, 2007) evaluated the energy efficiency of the photocatlytic water purification system for degradation of various organic contaminants in water. Bolton *et al.* (2001) defined the figures-of-merit "electrical energy per mass" (E_{EM}) for use in the zero-order kinetic regime and "electrical energy per order" (E_{EO}) for use in the first-order kinetic regime for low and high contaminant concentrataions respectively in AOPs. Daneshvar *et al.*, (2007) evaluated the E_{EO} for the photocatalytic degradation of the insecticide diazinon. In the case of photocatalytic (particle size 14 nm) process, the E_{EO} value was reported to be 1075.3kWh/m^3 compared to only 20,000kWh/m^3 in photolysis system. Wu *et al.*, (2009a) indicated that the photocatalytic degradation of pesticide turbufos could be efficiently achieved with an E_{EO} value of 71kWh/m^3. Wu *et al.*, 2009b reported that phorate could be treated easily and effectively using UV/TiO_2 system with an E_{EO} value of 96kWh/m^3 order. Using P25 and rutile TiO_2, the E_{EO} values for the photocatalytic degradation of eriglaucine are reported to be 175.44 and 10,000.00 kWh/m^3 respectively (Daneshvar *et al.*, 2006). Bandala and Estrada (2007)

compared the four different solar collectors based on figures-of-merit for the photocatalytic degradation of oxalic acid and carbaryl when the incident solar radiation was 1000W/m^2. Under the conditions tested, compound parabolic collector (CPC) and V trough collector (VTC) systems were demonstrated to be efficient for the degradation of both pollutants.The flat tubular (FT) collector has been reported to be inefficient probably due to its poor radiative flux distribution.The capital cost of a solar collector is proportional to its area and hence figures-of-merit based on the solar collector area are considered appropriate. The E_{EO} determination is essential, however, the costs associated with chemicals and capital outlays should also be considered to gain an overall picture of the process economics.

3.14 Conclusion

The role of various operating parameters on the photocatalytic degradation of various pesticides and phenols has been explored in this chapter. TiO_2 has been suggested to be an efficient and viable photocatalyst for the degradation and mineralization of various toxic organic pollutants such as pesticides and phenolic compounds in water in the presence of UV, visible or solar light and oxygen. The reported results also suggest that various operating parameters such as photocatalyst type, light intensity, pollutant types and initial concentration, catalyst amount, initial pH of the reaction medium, catalyst application mode, oxidizing agents/electron acceptors, and the presence of ionic components in solution can significantly influence the photocatalytic degradation rate of pesticides and phenols. Optimizing the degradation parameters is crucial from the perspective of efficient design and the application of photocatalytic oxidation process to ensure sustainable operation. It is evident from the current literature that TiO_2 photocatalysis has potential for the degradation of various organic pollutants. However, there is still a need to find out the practical utility of this technique on a commercial scale. In addition, more work is required on the modeling of the photoreactor to optimize its design for pollutant degradation. In the literature, there is currently limited information on the modeling of photoreactor to optimize its performance. Recent research has demonstrated the applicability of computational fluid dynamics (CFD) for modelling of photocatalytic reactors. It shows promise in its flexibility to vary parameters for optimisation of reactor design. This study focuses on the computational fluid dynamics modeling of a flat plate reactor to optimize its design and to predict its performance.

CHAPTER FOUR

APPROACH AND METHODOLOGY

This chapter presents the systematic approach and methodology which has been used for collecting the data from the lab-scale flat plate photocatalytic reactor. The concepts and fundamentals of Computational Fluid Dynamics (CFD), which is the major tool of investigation are briefly described for obtaining the data analysed in this thesis. In addition, it explains the procedure employed for numerical modelling, simulation and validation. Lastly, the necessary steps to obtain an efficient numerical solution using the systems of equations are presented. The approach and methodology of the study has been divided into three parts;

Part 1: Experimental design, procedures investigation and data collection
Part 2: Numerical modelling, simulation and model validation
Part 3: Optimization of reactor design and configuration

4.1 Experimental and Reactor Design

A prototype flat plate reactor developed and constructed at QUT under an ARC project is used in this study. The principal components of the reactor are shown in Figure 4.1. Among the various types of reactor, the configuration as depicted in Figure 4.1 was selected, because of its simplicity to easily change the TiO_2 films to be tested in the reactor. In this reactor, TiO_2 films are deposited on glass slides (220 x 100 x 3.5 mm) and the glass slides are placed in the recess in the bottom part of the reactor. The upper part, instead, holds the quartz window that allows the 254nm light to reach the surface of the titania to be activated and is machined to obtain a 1mm × 98 mm channel where the contaminated fluid can flow over the catalyst. The lower part was machined in PVC while the upper part was made of stainless steel AISI316; the stainless steel has been chosen for the upper part due to its extended exposure to UV light and its ability to achieve higher precision in the machining. The two main parts of the reactor were joined together with M3 screws. Simple holes were machined in the upper part while metal inserts were placed

in the bottom part in order to ensure a precise and durable connection on the joint. Water tightness is ensured with the use of an O-ring in a specifically designed recess.

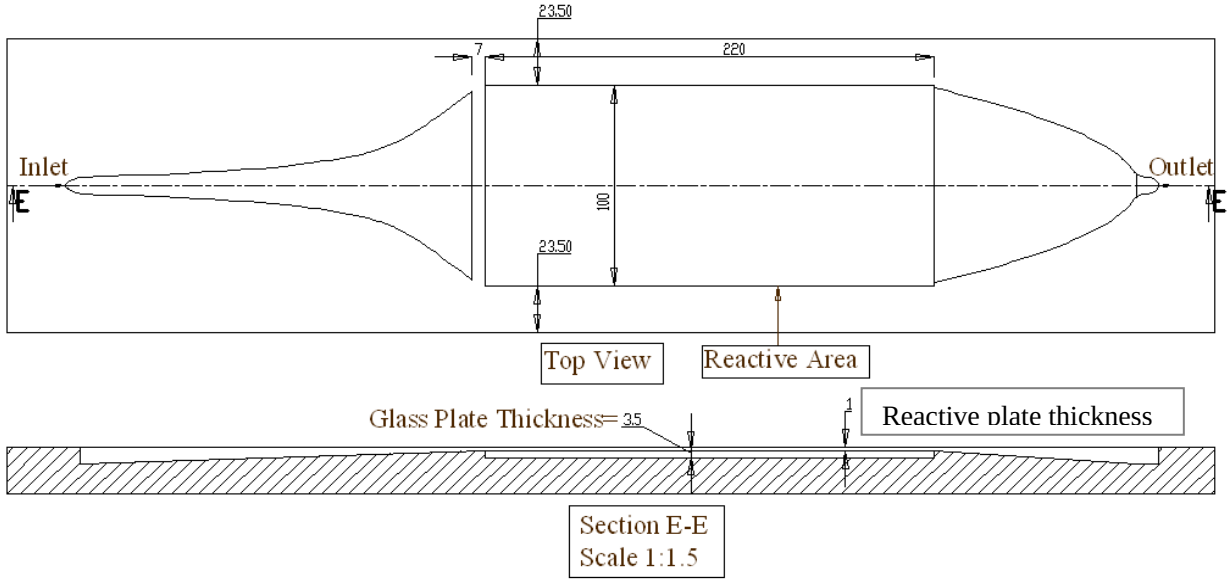

Figure 4.1 Reactor components and dimensions (mm) of the flat plate reactor.

The reactor inlet and outlet was carefully designed in order to eliminate any possible dead zones inside the reactor thereby creating an even flow within the reactive volume (Capel, 2008). The effect of inlet and outlet position on the flow in the reactive volume was verified for different possible flow velocities. These velocities are considered in the experimental runs. A few simple dye tests were performed by Patrick Capel, a Mechanical engineering student at QUT in order to verify the design and develop an appropriate working head pressure for the system. The reactor is illuminated externally with a suitable light system to obtain an even light distribution and the necessary control over the light intensity. The system consists of a light box where the reactor can be enclosed to limit its exposure to UV light and a parabolic reflector. The box is composed of a main part which is capable of supporting the reflector at different adjustable heights and a lid. The reflector and reactor assembly is shown in Figure 4.2. An exploded view of top and bottom flange with a cross-section of the reactive area can be seen in Figure 4.3. The box is made of aluminum. The lamp reflector is composed by the thermoformed acrylic with CVD aluminum to ensure high reflectivity, two side parts that hold both tombstones for the lamp and the parabolic diffuser, and two metal supports to hold the diffuser in the box. Parabolic diffusers are commonly used for the illumination of the reactors where a low light intensity is required; they usually allow a maximum of two lamps and two diffusers over the reactor's window. If a higher intensity is required an array of

lamps can be used over the quartz window and a simple linear model can be used to optimize the distance to be kept from the quartz window to obtain a uniformly distributed intensity.

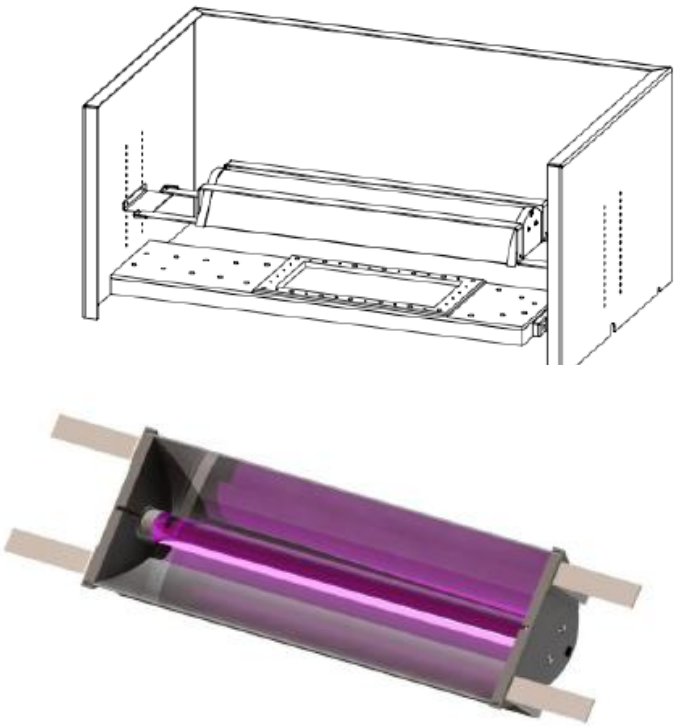

Figure 4.2 Parabolic reflector and reactor assembly (top) and reflector (bottom) respectively.

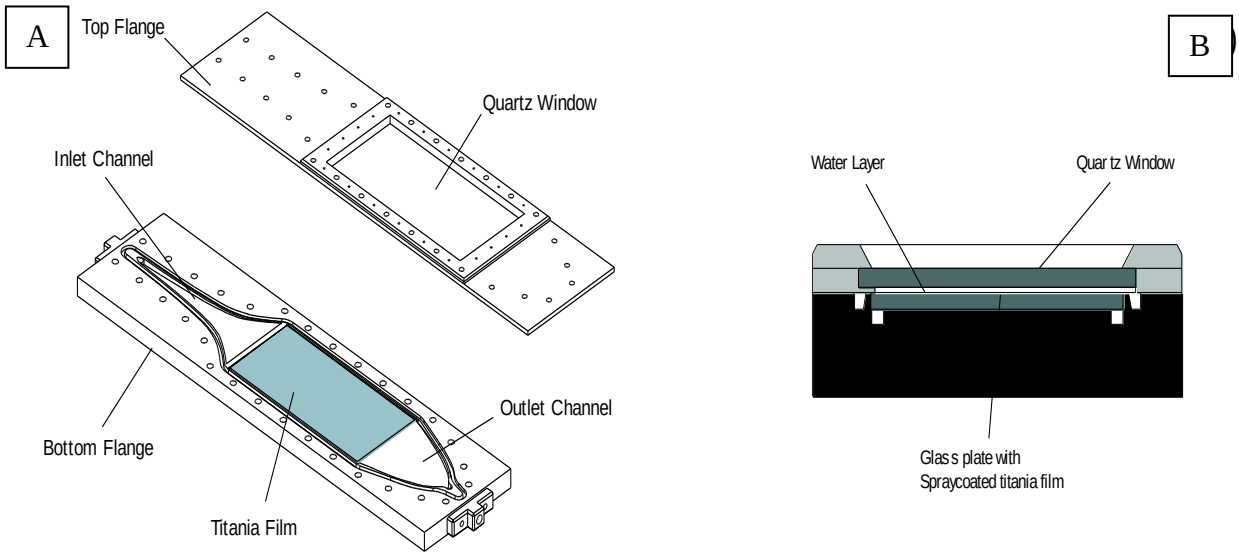

Figure 4.3 Reactor geometry. A) exploded view of top and bottom flange; B) Cross section of the reactive area (Vezzoli *et al*., 2011).

4.2 Experimental Set up and Procedures

The reactor system consists of a "pulse free" ismatec gear pump, 1/4 inch stainless steel tubing to avoid any leaching and contamination of the solution, safety valves, pressure gauge, 5L beaker and a magnetic stirrer. It is very important to maintain a sufficient level of oxygen in order to ensure complete oxidation. The oxygen can be provided through bubbling air into the beaker from a cylinder. A schematic diagram of the experimental set-up, which is basically a batch recirculation system, is shown in Figure 4.4. The experimental system of the flat plate reactor consists of a set of fluorescent UV lamps, whose dominant emission was at 254 nm wavelength. The reactive flat plate is made of a 3.5mm thick glass slide which was coated with TiO_2 catalyst. The reactive plate with an area of 220 mm x 100mm was exposed to UV light during the experimentation.

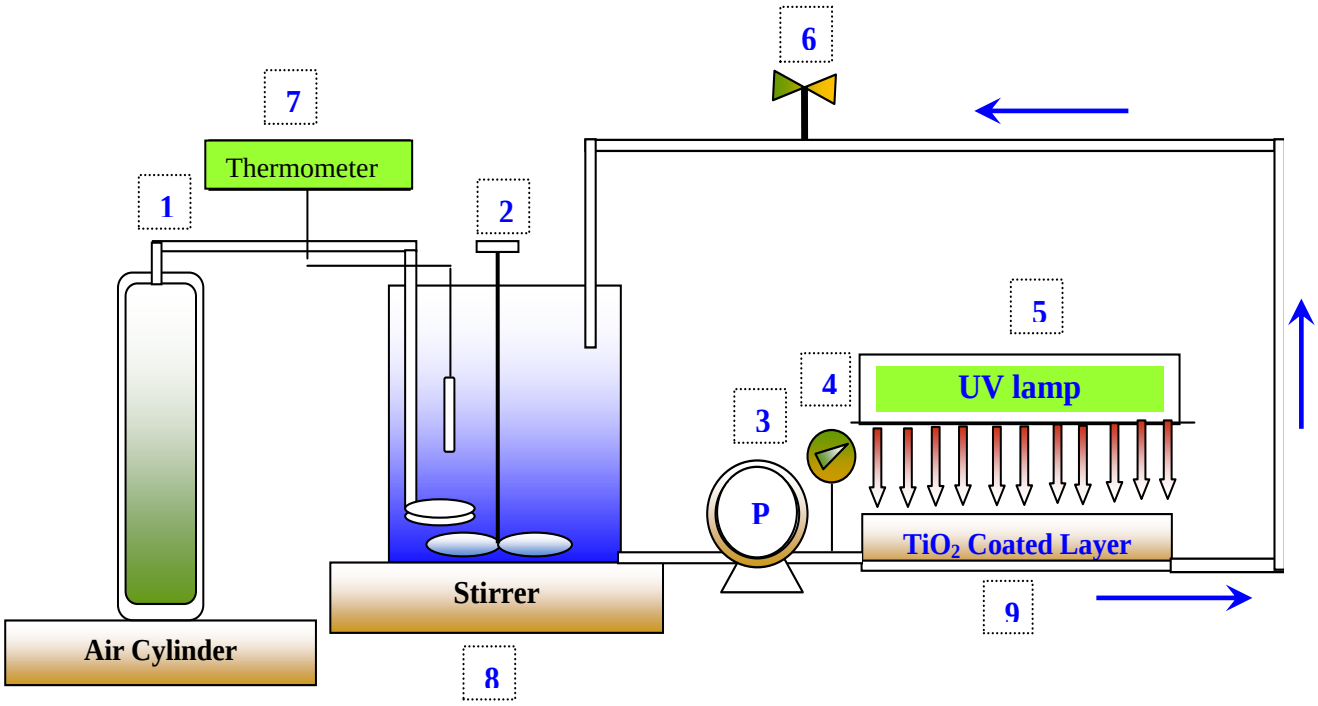

Figure 4.4 represents the schematic of experimental set up of the reactor system. (1) Air supply cylinder, (2) 5L feed tank, (3) Gear pump, (4) Inlet pressure gauge and safety valve, (5) parabolic reflector (6) Outlet Valve, (7) Thermometer (8) Magnetic stirrer (9) Flat plate reactor.

Contaminated water from the feed tank (No.2) in Figure 4.4 was pumped to the photoreactor through the inlet and flows over the illuminated reactive area in the form of a liquid film. Feed water flow rate to the reactor was maintained by a pressure regulator. In order to eliminate the formation of vortices in the feed tank at higher flow operation, a suitable amount of feed water was treated in all the experiments. In order to obtain the reaction rate constants of the flat plate reactor under various flow rates, it was operated for a certain time period where the solution was recirculated to the liquid reservoir (feed tank). The temperature and the flow rate of the feed water were continuously recorded using a thermostat and flow meter, respectively. The experiments were repeated several times to ensure consistent results.

In this study, phenol (C_5H_5OH) a simple aromatic heterocyclic organic compound was chosen as the model pollutant to test the efficiency of the flat plate reactor. To evaluate the performance of the photocatalytic reactor, several operating parameters can be varied; they are flow rate of the feed water, the initial concentration of the pollutants and the UV light intensity. In order to investigate the influence of these parameters, the reactor was allowed to run in the dark in steady state conditions for 20-30 minutes in each case before sampling by covering the entire experimental set up. Samples from the feed water tank were withdrawn from the reactor effluent at a suitable time interval for an experimentation run. In the experiments, the feed water in the tank was aerated by filtered compressed air at 3 L/min via a diffuser to supply adequate oxygen. Reaction rates are strongly influenced by the light intensity. Depending on the light intensity, reaction rates can follow a first order or half order relation with the light. To determine the order of the reaction precisely, light intensity needs to be measured accurately. Two procedures are generally followed to measure the light intensity; actinometry (Kuhn *et al*., 2004) and through the use of a radiometer (spectrophotometer). Chemical actinometry was employed as it is a relatively simple and accurate method for radiation measurement. The irradiation intensities at fixed position over the reactors considered when lamps are switched on was measured at a wavelength of 254 nm at the start of the experiments. The average intensities in the three cases were determined from the irradiation profiles obtained at these locations. A photo-diode was put at a fixed location to monitor the light intensity at the illuminated area at a predetermined time interval during the experiments. The temperature of the feed water was measured every 20 minutes using a thermometer.

4.3 Catalyst Coating Method

The TiO_2 catalyst was coated on a 3.5 mm thick glass slide. The used plates were degreased using a reagent grade H_2O_2 solution and rinsed several times with deionized water. They were then etched using dilute nitric acid to provide a better surface for catalyst adhesion, and were washed carefully with distilled water before drying (Chan *et al*., 2001). Spray coating deposition method was used to immobilize TiO_2 catalyst on the glass plates. TiO_2 solution was prepared by adding the desired amount of TiO_2 powders into analytical reagent grade ethanol. The solution was then sonicated for an hour to obtain a homogeneous suspension. A magnetic stirrer was employed to constantly agitate the suspension during the coating process. In the spray coating method, the TiO_2 solution can be applied on the glass slides. After each coat, the coating was dried in an incubator for more than two hours. The incubator dry cycle was repeated up to eight times to produce successively thicker catalyst layers. After drying at ambient conditions, the reactive slide was heated at 400^oC for several hours in an oven to ensure the stability of TiO_2 coating to mechanical attrition.

4.4 Experimental and Data Collection

Typical experimentation conditions obtained from the test runs in the flat plate reactor at QUT are summarized in Table 4.1. Moreover, the optimum operating conditions have been determined from the preliminary test runs. A set of experiments designed for various operating conditions was conducted in order to examine the effectiveness of the proposed method to describe the photocatalytic degradation of a model organic pollutant, phenol. A range of phenol concentrations such as 20, 40 and 80 ppm, corresponding to about 15.3, 30.6 and 61.3ppm of TOC in solution, combined with four different irradiation conditions, 70.6, 57.9, 37.1 and 20.4 W m^{-2}, were studied using a photocatalytic plate of approximately 4.8μm thickness. A set of five photocatalytic plates were investigated to determine the effect of film thickness on the reaction rate. The average thicknesses of the plates, estimated via SEM imaging, corresponded to 0.52, 1.21, 2.24, 4.77 and 7.01 μm. Each of the experimental runs of the photocatalytic reaction lasted for 3.5 hours. In order to obtain the kinetic parameters and the rate expression for the flat plate reactor, laboratory experimentation with wastewater containing a representative model pollutant (phenol) was performed for different initial

pollutant concentrations and operating conditions (Vezzoli *et al.*, 2011). Using the approach in Figure 4.5, the kinetic data obtained from the degradation of phenol are shown in Table 4.2

Table 4.1 Typical Experimental Operating Conditions

Applied Pressure (KPa)	Air flow rate (L/min)	Flow rate (L/min)	Pump running speed
70	3.00	0.5	10%
103	3.00	1.0	13%
145	3.00	2.0	21%

Optimum Operating Conditions: Applied pressure= 70 KPa, Stirring speed= 300 rpm, Lamp power=15 Watt, Light Intensity= 2.9 mw/cm^2, Optimum lamp height from the Quartz plate =107 mm.

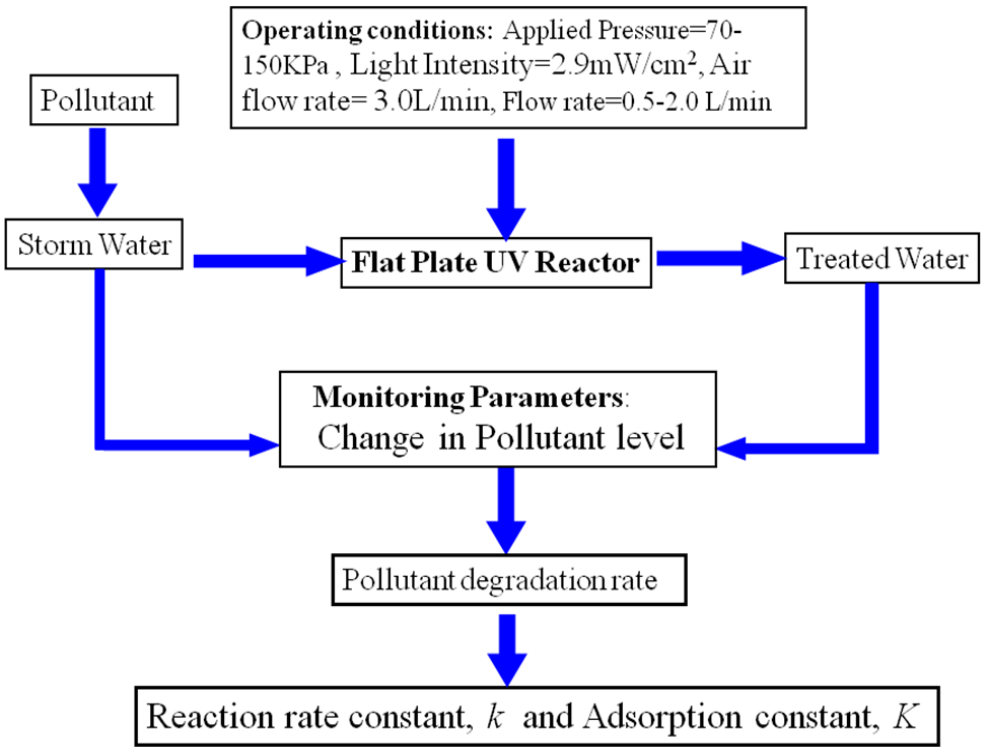

Figure 4.5 Schematic approach to obtain experimental kinetic data.

The parameters in the reaction rate equations (k_{ph}= phenol reaction rate constant, K_{ph}= adsorption equilibrium constant, k_I, K_I= constants for intermediates) were determined using the experimental data collected from the twelve experimental runs. The results for the kinetic parameters obtained from the experimental runs, together with the 95% confidence intervals, are reported in Table 4.2 (Vezzoli *et al.*, 2011).

Table 4.2 True kinetic parameters

Parameter	Value	95% CI	Unit
k_{ph}	0.5226	0.028	mmol m^{-1} s^{-1} W^{-1}
K_{ph}	8.5 x 10^{-4}	1 x 10^{-4}	m^3 $mmol^{-1}$
k_I	0.120	0.0088	mmol m^{-1} s^{-1} W^{-1}
K_I	2.2 x 10^{-3}	3 x 10^{-4}	m^3 $mmol^{-1}$

The geometric dimensions of the proposed TiO_2- coated reactive section with different arrays of top and bottom baffles and roughness elements are shown in Table 4.3 for Case 1, Case 2 and Case 3. The position and the number of baffles in the reactive section were chosen to explore the optimum condition for improved mixing with minimal pressure drop for the three cases thereby eliminating the dead zones and short circuiting. As shown in Figure 4.6, the existing reactive section of the flat plate reactor was replaced by the three different configurations to form a size identical to the original reactive section of the reactor for simulation runs. These three configurations have been chosen to promote mixing and to minimize the catalyst fouling due to the deposition of degradation by-products within the reactive section and to eliminate the mass transfer limitation which is a major barrier in an immobilized reactor (Dijkstra *et al*., 2002, Sengupta *et al*., 2001; Mehrotra and Ray, 2003).

4.5 Numerical Modelling, Simulation and Validation

In the first stage, the hydrodynamic investigation of the flow field in the flat plate photocatalytic reactor was simulated using three two-equation turbulence models: 1) standard κ-ε, 2) RNG κ-ε, 3) Realizable κ-ε and 3) κ-ω 4) Reynolds Stress Model (RSM) as described in chapter 2. The goal of using multiple sub-models is to determine the CFD model sensitivity to the turbulence sub-model selection. While other more complicated turbulence model exist, such as the Large Eddy Simulation (LES) model, the three two-equation models

were chosen for this study since they are widely applied in many engineering applications and provide reasonable and stable results without being numerically intensive (Alpert *et al*., 2010).

Table 4.3 Geometric dimension of the reactive section used in CFD simulation runs.

Overall Geometric Dimensions of TiO_2 coated plate for CFD simulation			
Parameter	**Case 1**	**Case 2**	**Case 3**
Length, mm	200	200	200
Height, mm	15	15	15
Depth, mm	1.5	1.5	1.5
No. of baffles and location	1 bottom	7 top	4 top+5-roughness elements
Baffle length, mm	1.5-7.5	3-10	5
Catalyst layer thickness, μm	4.8	4.8	4.8
Reynolds number	2150, 7500	2150,7500	2150,7500

Case 1: Bottom baffle

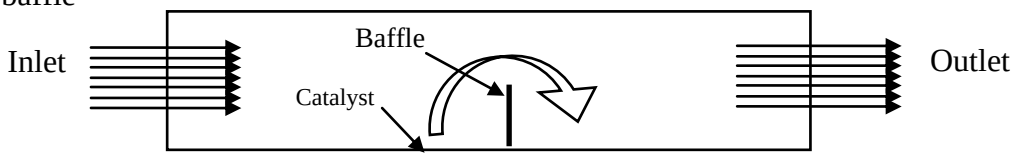

Case 2: Top baffle

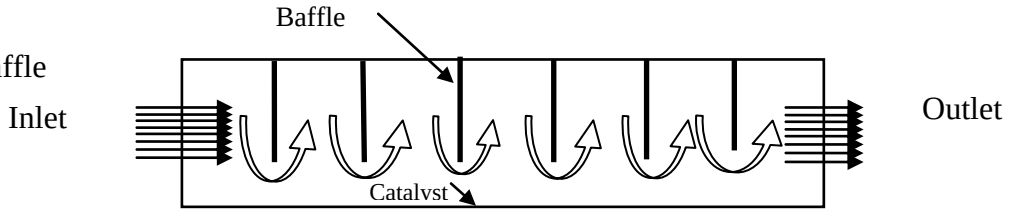

Case 3: Combined baffle and bottom roughness element

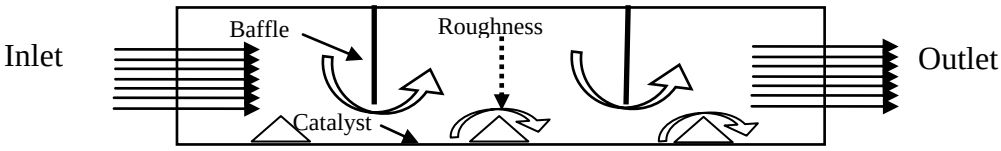

Figure 4.6 The proposed geometry of reactive area for Case 1, Case 2 and Case 3 in CFD simulation runs.

In the second stage, the flow fields in the reactive section were obtained for Case 1, Case 2 and Case 3 using a RNG *k*-ε model. Simulations were also performed at the same operating conditions for the reactive section without the baffles for comparison purposes. In order to gain an insight about the mass transfer performance of the proposed cases, the fluid flow model was coupled with the species transport model to obtain an integrated model in FLUENT. Similarly, the kinetic parameters obtained from the phenol degradation were used for the surface chemical reaction modelling together with the fluid flow model. For the sake of simplicity, this work considers the first order kinetic expression as the rate expression to model the photocatalytic degradation of phenol in the flat plate reactor. This integrated model was implemented for predicting pollutant degradation profile for the flat plate reactor operating at various hydrodynamic conditions to investigate the role of fluid dynamics in the photocatalytic reactor. Performance of the flat plate reactors for model pollutants degradation under different flow rates was analysed and compared to predict the role of hydrodynamics using CFD simulation. Using the CFD simulation, detailed local information (flow field and concentration profile) can be obtained which provides a qualitative understanding of the process to explain better the reactor behaviour.

4.6 Steps in CFD Modelling

Computational fluid dynamics (CFD) is based on the solution of the equations of fluid flow the Reynolds Averaged Navier-Stokes equation (RANS) and turbulence transport equations over a region of interest, with specified (known) conditions at the boundaries of that region. The CFD software Fluent 6.3 was chosen for this study. Using this software, the region of interest was divided into small elements, called control volumes. The governing equations were discretised and solved iteratively for each control volume. As a result, an approximation of the value of each variable at specified points throughout the domain could be obtained. In this way, a full picture of the behaviour of the flow field in the reactor could be derived.

Simulation Technique

CFD simulations of the flat plate reactor together with the proposed configurations for the reactive section were performed in 2D. The fundamental governing equations of fluid flow and turbulence transport equations were solved to model the single phase fluid flow in the flat plate and the proposed reactive configurations. Simulation was performed using the CFD

code “FLUENT 6.3.26” which is based on the finite volume method. The steps in CFD simulation that was used to set up and solve the problems are summarized below.

1) Geometry and mesh development in GAMBIT
2) Define boundary conditions
3) Solver approach
4) Post processing of results

Geometry and Mesh Development

The first step to any numerical integration solution technique consists of defining a computational domain and dividing the domain into discrete sections. This is referred to as discretization. The reactor consists of three parts; (i) reactor inlet (ii) reactive (TiO_2 coated) area (iii) reactor outlet. In CFD modelling, discretization of the reactor was accomplished through dividing the whole solution domain into smaller computational domains through meshing. Using GAMBIT software which is the pre-processor of FLUENT, the computational domain was created and the grid was generated. GAMBIT has the ability to generate both structured and unstructured grids ensuring representation of flow boundaries using various inbuilt algorithms incorporated in it.

Boundary Conditions

In this study, for simulation of the photoreactor, the fluid phase was considered as single phase that is incompressible; density and viscosity are assumed to be constant, because the fluid flow in the computational domain is essentially single phase flow. In addition, the walls were treated as adiabatic and no-slip wall conditions were specified for the velocity at the walls. Reactor inlet was assumed to be as velocity inlet. A uniform mean axial velocity (that corresponds to a measured flow rate) at a constant pressure was defined as the reactor inlet. In addition, the turbulence parameters (turbulence intensity and hydraulic diameter) were specified using the intensity and hydraulic diameter method as per the guidelines in FLUENT 6.3. At the outlet, pressure outlet with fully developed uniform flow was assumed using pressure outlet boundary conditions.

Solution Approach

In the CFD code FLUENT, discretization of RANS and turbulence transport equations was carried out using finite volume method (FVM) to convert the partial differential equations into linear algebraic equations. A non staggered grid arrangement was employed where all variables are stored in geometrical cell centres of control volumes (CV). The whole set of equations was solved in steady state. The equations were solved by CFD code in each cell of the computational domain. The code stores the discrete values at the centre of the cell. However, these values need to be interpolated from the centre of the cell to the face values which can be achieved via discretizing schemes. The details on the schemes can be obtained from FLUENT Inc. (2006) version 6.3. However, the schemes can be changed for the simulations purposes. In order for the solution to progress smoothly algorithm requires under relaxation parameters to update the solution after each iteration. The under relaxation parameters were maintained at default values as suggested in FLUENT manuals for most of the simulations. The numerical simulation approach is shown in Figure 4.7.

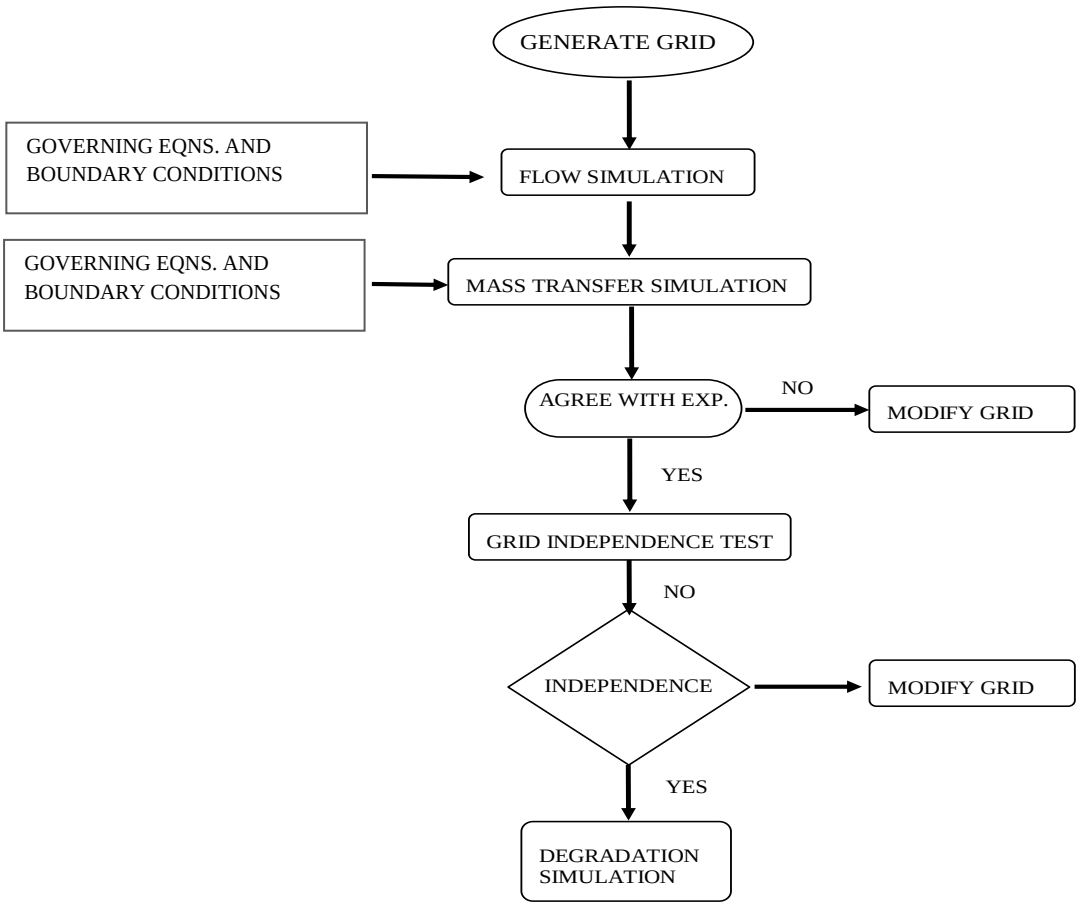

Figure 4.7 A schematic flow chart for numerical simulation.

Grid Sensitivity Test

In any numerical solution technique, judging convergence is of major importance. In this study, the sensitivity of solution to the number of grids was performed until a grid-independent solution was attained to verify whether an increase in the grid size (finer discretization) would have a significant impact on the simulation results.

4.7 Model Validation

Validation of a numerical model consists of comparing the computed results with experimentally measured results. This is generally considered to be a clear-cut approach to ensure the reliability of simulation results. Although a lot of experimental investigations are available in the current literature, the geometric configurations analysed in the reported studies often vary considerably from the cases examined in this study, such that a strict quantitative validation is not possible with literature data and only a qualitative comparison can be made. In this study, data predicted using CFD simulation are validated against the experimental measured velocities under various flow rates obtained for different applied pressures in an incremental order from the test runs in the flat plate photocatalytic reactor. These flow rates correspond to four different inlet velocities of 0.663m/s, 1.32m/s, 1.98m/s and 2.65m/s. In an effort to validate the CFD code, the CFD predictions can also be compared with empirical relation in terms of friction factor, mass transfer coefficient at low and high Reynolds numbers.

In order to further our validation, the simulation results of benzoic acid (BA) mass transfer from the catalyst coated surface was compared with the results obtained from the experimental runs in the flat plate reactor. The validation was based on BA concentration of the reactor outlet under similar operating conditions for a given inlet pollutant concentration. A range of hydrodynamic conditions which correspond to flow rates 2.0-6.0 L/min were employed to simulate the benzoic acid concentration at reactor outlet. The experimental mass transfer coefficients of benzoic acid (k_{mBA}) were determined using the flat plate reactor equipped with an aluminum plate coated with benzoic acid. The coatings on the plate were done by dipping them into molten benzoic acid. The operation of the system involves a flow of clean water into the reactor causing the dissolution of the slightly soluble acid into the bulk fluid.

Based on the stagnant film model (Sherwood *et al*., 1975) the mass balance over a liquid film can be represented by the equation:

$$\frac{dC_{BA}}{dt} = k_{mBA}a(C_{bBA} - C_{sBA}) \qquad (4.1)$$

Using a mass balance system according to equation (4.1), the average mass transfer coefficients of the system were determined under different hydrodynamic conditions (800 < *Re* < 2200) at 25°C (Vezzoli *et al*., 2011).

The fitting of experimental values of k_{mBA} for different Reynolds number to a power law, $k_{mBA}=aRe^{b}$ was found to give the following relation (Vezzoli *et al*., 2011)

$$k_{mBA} = 9.763 \times 10^{-7} Re^{0.65} \qquad (4.2)$$

The mass transfer coefficients of formic acid can be estimated from the experimental mass transfer coefficients of benzoic acid determined for the same flat plate reactor and applying the following relation:

$$k_{c,FA} = k_{c,BA}\left(\frac{D_{m,FA}}{D_{m,BA}}\right)^{2/3} \qquad (4.3)$$

Where $D_{m,FA}$ (1.49×10^{-6} m^2/s) and $D_{m,BA}$ (9.32×10^{-10} m^2/s) are the molecular diffusion coefficients of formic acid and benzoic acid, respectively. The above equation (4.3) is commonly used in the open literature and is based on the general dependence of mass transfer coefficients, with the diffusion coefficient to the power of 2/3 (Perry and Green, 1997).

4.8 Optimization of Reactor Design

The optimization of the flat plate reactor was performed through CFD simulation of reactor performance for pollutant degradation by investigating the effects of various parameters such as inlet pollutant concentration and feed water flow rates. In the case of TiO_2 immobilized photoreactors, the pollutant degradation is strongly related to geometrical factors which enhance the external mass transfer and degradation efficiency in the system. However, little research has been conducted in this area (Duran *et al*., 2011a). Accordingly, CFD simulation

was also conducted for the proposed reactor configurations with various arrangements of baffles and roughness elements as turbulent and mixing promoters (Case 1, Case 2 and Case 3) to predict the role of baffles and surface roughness on the hydrodynamic performance of the reactor and to identify the reactor design for improved reactor efficiency.

4.9 Evaluation of Criteria

A number of parameters have been used for evaluation of the hydrodynamic performance of the photocatalytic reactor under investigation for the reported cases. Of them, pressure drop (Δp), turbulent kinetic energy (κ), wall shear stress (τ_w), and turbulent dissipation rate (ε) as well as % contact loss due to boundary layer separation are considered in this study. In addition, the mixer efficiency in a reactive module depends on its ability to provide strong mixing with a reasonable pressure drop. To characterize the mixing performance of a mixer, knowledge of the turbulence kinetic energy dissipation rate is necessary (Kaci *et al*., 2009). Baldyga and Bourne (2003) proposed the dissipation of turbulence kinetic energy as a measure of mixing efficiency, since it determines the turbulent activity at small scales (almost Kolmogorov scale) of the flow.

A dimensionless parameter η (Equation 4.4) based on the ratio of the turbulence kinetic energy dissipation rate in the baffled reactor ε_M to the turbulence kinetic energy dissipation rate in an empty module ε_D was used to describe the mixing efficiency gain (Kaci *et al*.,2009):

$$\eta = \varepsilon_M / \varepsilon_D \qquad (4.4)$$

where ε_M is determined using a standard k–ε turbulence model and represents the time-averaged turbulence kinetic energy dissipation rate in the baffled reactor. ε_D is obtained by applying the same method to the turbulent flow in an empty reactor.

CHAPTER FIVE

Computational Fluid Dynamics Modelling of a Flat Plate Photocatalytic Reactor

5.1 Introduction

Heterogeneous photocatalysis using a semiconductor TiO_2 photocatalyst and ultraviolet light is an emerging and promising technology for water treatment (Adesina, 2004; Herrmann, 2005). The irradiated TiO_2 promotes oxidization and reduces species that are capable of reacting with organic molecules, resulting in many cases to complete mineralization with the production of CO_2 and water (Castrillon *et al*., 2006). Over the last decade, the application of a photocatalytic water treatment system has been demonstrated significantly and offers several advantages over traditional methods particularly in the area of water pollution abatement. The application of this technology has not been commercially exploited yet due to the lack of proper models and simulation tools for predicting and analysing the performance of full-scale systems. Developing models for predicting the behaviour of heterogeneous photocatalytic reactors is complicated (Duran *et al*. 2011b). The complex interactions among transport processes, reaction kinetics, and radiation absorption result in a strong coupling of physicochemical phenomena (Periyathamby and Ray, 1999). Yet, understanding the detailed flow field in a reactor is of paramount importance for the design and optimization of a photocatalytic reactor for water purification (Sozzi and Taghipour, 2006a, 2006b), as, to give one instance, the optimization of a reactor system often leads to significant savings in energy and construction costs. Such optimization requires accurate models of the flow structure within the reactor.

In order to elucidate or model the reactor hydrodynamics, the governing equations for the conservation of flow mass and momentum must be solved in the discretised computational domain using a numerical (e.g. finite volume) method. This calls for proper definition and incorporation of suitable turbulence models for the reactor hydrodynamics. Different approaches can be taken to modelling turbulent flows. Simplified models have been established for modelling photoreactor hydrodynamics using fully developed laminar flows and fully mixed conditions.

While these models have been demonstrated to be valuable under restricted conditions, their application to the more common non-uniform flows on an industrial scale is not clear (Sozzi and Taghipour, 2007). Recent research has demonstrated the applicability of computational fluid dynamics (CFD) to the modelling of photocatalytic reactors. CFD shows promise in its flexibility to vary parameters for the optimization of reactor design and the scale-up of reactive systems. CFD has also been used successfully for the simulation of photocatalytic reactors for air treatment (Mohseni and Taghipour, 2004; Taghipour and Mohseni, 2005).The flow field of water in two reactor geometries, representing annular reactors in general, was simulated by CFD (Sozzi and Taghipour, 2006a). Their investigation highlighted the effect of two main modelling parameters (discretization of volume and a turbulence model) on the numerical solution for both those reactor geometries, and the results were compared with experimental measurements. In terms of solar UV and visible light utilization, flat-plate photocatalytic reactors are usually seen as commercially efficient as they provide high surface area to volume ratio for water treatment. CFD modelling of scaled-up reactors would give a very useful insight into the performance of a photoreactor prior to the final experimental validation by reducing experimental effort and fabrication costs at the pilot-scale level. Using various turbulence models, this chapter presents the results obtained from the simulation of a flat plate reactor developed at QUT under various flow conditions. The performance of the reactor for photocatalytic degradation of a model pollutant has been simulated and reported for various flow rates. In addition, the influence of reactor inlet positions on the flow field and mass transport of a pollutant in the reactive section has been examined under various reactor inlet positions.

5.2 CFD Modelling Governing Equations

In this study, the fluid is assumed to be Newtonian, incompressible, isothermal, non-reactive with constant properties, and under steady state the Reynolds-averaged Navier-Stokes modelling approach involves solving the following time-average equations to simulate the single phase flow in the flat plate reactor (Ranade, 2002). The continuity equation is given below;

$$\frac{\partial \rho}{\partial t} + \nabla \cdot \left(\rho \vec{u}\right) = 0 \qquad (5.1)$$

The following momentum equation governing the flow in the reactor is solved throughout the entire domain. The momentum equation depends on the volume fraction of all phases through the properties and is given by;

$$\frac{\partial}{\partial t}\left(\rho\vec{u}\right) + \nabla\cdot\left(\rho\vec{u}\vec{u}\right) = -\nabla p + \nabla\cdot\tau \qquad (5.2)$$

Where the over bar indicates a time-averaged value, $\vec{u}$ is the velocity vector (m/s), p is the pressure (Pa), τ is the viscous stress tensor, ρ is the density (kg/m^3) and μ is the viscosity (Pa.s).

The modelling of photocatalytic chemical reaction for phenol (C_6H_5OH) degradation involved solving the hydrodynamic model comprising the continuity equation (conservation of mass, Equation (5.1) and momentum conservation Equation (5.2) together with the species transport equation. The transport equation for each species can be given by ;

$$\frac{\partial(\rho Yi)}{\partial t} + \nabla.(\rho\vec{u}Yi) = -\nabla.\vec{J}_i + R_i^s \qquad (5.3)$$

Where J_i is the diffusion flux of species i and R_i is the net rate production of species i due to chemical reaction. The concentration of reactants and final products in each control volume of the grid is expressed in terms of mass fraction, Yi.

5.3 Hydrodynamic Models

A hydrodynamic model is a set of semi-empirical equations used to determine the turbulent transport terms and thus close the system of RANS equations to obtain the mean flow field properties and the Reynolds stresses. Many models have been developed for application in practical engineering. The most common of these implemented in commercial CFD codes are described below:

a) **Standard k-ε Model**

The k-ε models are the simplest of the two-equation models and were proposed by Launder and Spalding (1974). Standard k-ε is a semi-empirical model based on the solution of transport equations for the turbulent kinetic energy (k) and the turbulent dissipation rate (ε). Standard k-ε is robust, economical, and provides reasonable accuracy for predicting a wide range of turbulent flows (Sozzi and Taghipour, 2006) but they are only applicable in fully turbulent flows. However, the flows in the complex systems such as sudden changes in the mean strain rate, streamline curvature, secondary motions, and flow separation cannot be

accurately predicted by this model. All of these give rise to additional interactions between the mean strain rate and the Reynolds stresses. It is likely to estimate turbulence generation inaccurately for the cases where the mean flow is highly accelerated or decelerated (Fluent Inc., 2006).

b) **Realizable k-ε Model**

The Realizable k-ε model (Shih *et al*., 1995) is a modification of the standard k-ε model. This model contains a new formulation for the turbulent viscosity and an extra term in the dissipation rate, ε equation to satisfy the mathematical constraints on the Reynolds stress, which is consistent with physics of turbulent flow. It can accurately predict the spreading the rate of both planar and round jets. It is also likely to provide enhanced performance for flows which include rotation, boundary layers separation under adverse pressure gradients and recirculation (Fluent Inc., 2006). A realizability constraint is featured on the predicted stress tensor. It can produce non-physical turbulent viscosities in situations when both rotating and stationary fluid zones are present in the computational domain. Excessive levels of turbulence generation in the regions of large mean strain can be avoided, which may occur in impinging flows.

c) **Reynolds Stress Model**

In Reynolds Stresses Models (RSM), an alternative to the Boussinesq hypothesis, is used to close the system of RANS equations which is referred to as the second-order closure model (Launder and Spalding, 1974). This approach solves the exact transport equations for the Reynolds stresses based on the Navier-Stokes equations which addresses most of the problems adequately and performs well where turbulence is largely anisotropic. It ignores the isotropic eddy-viscosity assumptions and can provide reasonable accuracy for many flows in complex systems for instance; it can selectively augment or damp the stresses due to curvature effects, swirling flows, buoyancy and flows which involve strong acceleration/retardation. Due to seven additional partial differential equations, this model requires sufficiently fine meshes which render it computationally expensive caused by the significant increase in storage and run time and thus difficult to implement. As a result it has not received wide application in industrial flow calculation.

d) **κ-ω Model**

The k-ω model developed by Wilcox (2004) is another two-equation empirical model which incorporates modification for low-Reynolds number effects and shear flow spreading. This

model is based on the computation of the turbulent kinetic energy (k) and the specific dissipation rate (ω) which can be represented as the ratio of the turbulent dissipation rate to the turbulent kinetic energy. While there have been a few investigations on the CFD modelling of photoreactors for water disinfection, the detailed numerical modelling of the flat plate photocatalytic reactor suitable for water treatment has not been demonstrated in the open literature. Here the effect of grid number on the CFD results in a current reactor configuration is studied and the influence of five different turbulence models is also assessed.

5.4 Reactor Geometry

A 2D computational domain of the reactor employed in the CFD modelling is illustrated in Figure 5.1. The reactor consists of three parts: inlet, reactive area and the outlet. A parabolic diffuser was designed for the region between the inlet and the reactive area (100×220mm) of the reactor. The width of both the inlet and the outlet was set at 4mm. This configuration was selected to reduce the flow separation and to minimize the presence of dead and recirculating zones within the reactor (Capel, 2008). The shape of the reactor outlet was selected to reduce the amount of construction material and to simplify the manufacturing complexity of the device. The reactor geometry was constructed using GAMBIT 2.3.16 (Fluent Inc.) and was discretized to a sufficiently large number of 5,13,537 cells for CFD simulation purposes.

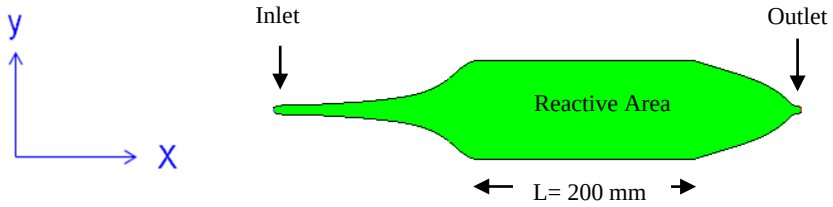

Figure 5.1 Top view of the 2D computational domain

5.5 Solver Approach

To limit computational power requirements, a 2D pressure-based segregated solver with a first order unsteady formulation was used for the single phase fluid flow modelling. Geo-Reconstruct, a time-dependent with the geometric reconstruction interpolation scheme in FLUENT was employed for the time-accurate transient behaviour of the numerical solution and a 2nd order up-wind differencing scheme was used to overcome numerical diffusion. The pressure-velocity coupling scheme was resolved with a SIMPLE algorithm.

This scheme allows for an improved convergence (Fluent-Inc., 2006). Pressure was discretized with a PRESTO scheme because of its strong convergence capability.

5.6 Boundary Conditions

For the purposes of simulation, a no-slip boundary condition was specified at the side walls. At the inlet and the outlet, VELOCITY-INLET and PRESSURE-OUTLET boundary conditions were imposed respectively. The initial velocity was assumed to be 0.663 and 1.326 m/s respectively. The pressure at the outlet was specified to be 101,325 Pa. The hydraulic diameter of the inlet and outlet of the flat plate reactor was set at 4mm. The turbulence intensity (TI) was specified with a value close to 5%. For BA concentration modelling, a no-slip boundary condition was imposed at all the walls. Also, zero diffusive flux of species was specified at the wall, except for the walls coated with benzoic acid, where a constant concentration of 3.4×10^{-3} (mass fraction) was fixed. This concentration corresponds to the saturation concentration of BA in water at 298 K. For the photocatalytic degradation of phenol, separate boundary conditions were applied which is given in section 5.8.5.

5.7 Grid Independence

The influence of quadrilateral mesh on the CFD results was studied for a number of mesh sizes. A more accurate solution can be expected when the mesh size is sufficiently refined; however, the finer the mesh, the more time is required for computations. Therefore, a suitable mesh size should be chosen that will enable an accurate solution being obtained within a reasonable time. At the same time, it is essential that the solution obtained should be mesh independent (FLUENT-Inc., 2006). To obtain the simulation results independent of mesh sizes and to eliminate the effect of mesh quality, initial simulations were conducted for a variety of resolutions to determine whether an increase in the mesh size (finer discretization) would have a significant impact on the results. The study was performed by decreasing the cell size until a grid independent solution that generates constant results for the centre line velocity of the flat plate reactor. The parameters used in simulation for the reactor geometry were kept constant all through the study with the exception of mesh size. In this study, the effect of mesh sizes on the accuracy of the CFD simulation results was evaluated by performing simulations at three different grid resolutions which correspond to interval sizes 0.17 mm, 0.27 mm and 0.37 mm, respectively.

The numbers of elements with three grid resolutions are listed in Table 5.1 for Grid 1, Grid 2 and Grid 3 (termed as fine, medium and coarse) respectively.

Table 5.1 Grid independence test

Grid	Interval Size, m	Cell Number	Face Number	Node Number
Grid 1	0.00017	12,15,432	2434164	1218733
Grid 2	0.00027	5,13,537	1029152	515616
Grid 3	0.00037	2,82,893	567303	284411

Figure 5.2 shows the simulation results for the centre line velocity profile of the flat plate reactor that was obtained using three different mesh densities. The results obtained with the coarse mesh (Grid 3) demonstrate little deviation (0.8m-0.19m from inlet) compared with those that correspond to other two resolutions (medium and fine). However, the predictions with medium and fine grid resolutions are close to each other.

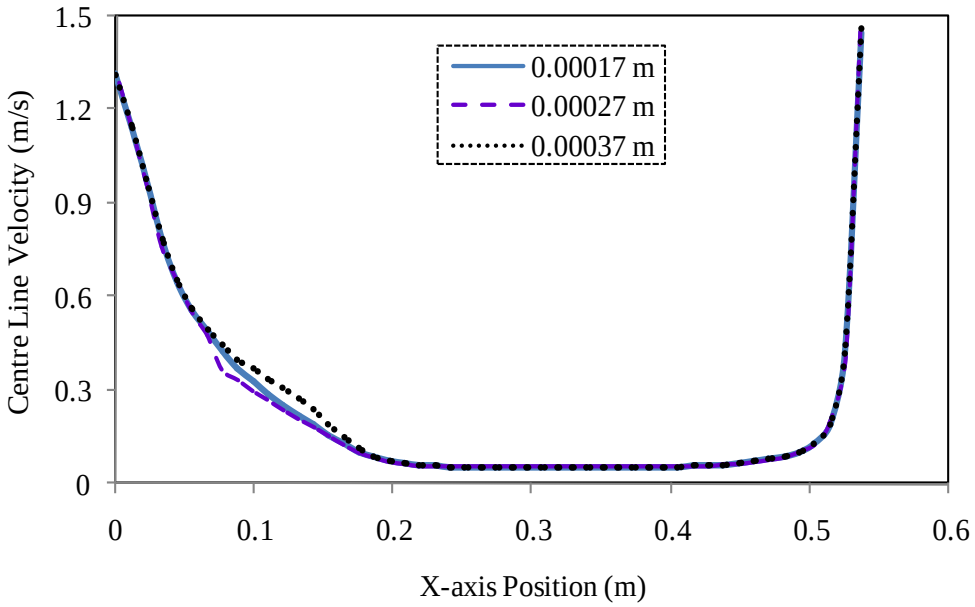

Figure 5.2 Influence of mesh density on the centre line velocity.

Under the simulation conditions (inlet velocity=1.32 m/s) the results shows that there was only an insignificant difference in the predicted velocity profile with three mesh densities. A likely reason for this difference is that uniform flow rates were defined for the reactor inlet boundary conditions; nonetheless, in practical situations, the flow rates can vary across the

inlet surfaces. Further reduction of mesh size did not improve the accuracy of the modelling much. Thus, a mesh size of 5,13,537 was adequate to ensure the mesh-independent results and was selected for the rest of study.

5.7.1 Mesh Quality

The parameter Equi-Angle Skew is used to evaluate the mesh quality (0 is best quality and 1 is worst). This parameter was found to be smaller than 0.5 for all the cells investigated in this study. The value distribution of this parameter is:

- 6.26 % of the meshes were of quality ranging from 0.3 to 0.5 (average quality);
- 10.07% of the meshes were of quality between 0.1 and 0.2 (good quality);
- 83.67% of the meshes were of quality ranging from 0.0 and 0.1 (high quality).

5.7.2 Convergence Considerations

In order to ensure an adequate convergence criterion, a series of simulations for different stop-criterion values that range from 10^{-3} to 10^{-6} was carried out. Beyond a convergence criterion of 10^{-4}, no noticeable changes were observed in continuity equation, velocity field or turbulence quantity; consequently this value was assumed as the convergence criterion.

5.7.3 Wall Treatment

Using k–ε models, the simulations of the flat plate reactor were carried out with near-wall treatments, a wall-function model and a near-wall-treatment model, whereas the RSM simulation was computed with the two-layer approach only. The near-wall treatment is not needed in either standard κ–ω and SST κ–ω models because these models take into account the near-wall effects. However, the standard κ–ω and SST κ–ω models were computed with both meshes built for wall functions and the two-layer model. The detailed discussion on the wall treatment approaches has been provided in literature review, in chapter 2.

5.8 Results and Discussion

5.8.1 Comparison of Experimental Measurement and CFD Prediction

To validate the numerical results some experimental measurements were done as discussed in section 4.7 (chapter 4). A comparison between the simulated and experimental results for the Realizable k-ε model for four different inlet velocities such as 0.663m/s, 1.32m/s, 1.98 m/s

and 2.65 m/s is shown in Figure 5.3a. Under the conditions tested, a good level of agreement between the measured and predicted values was found (Figures 5.3a). The relative variation between the measured and the simulated data was below 5% indicating that the model provides a good overall description of the reactor behaviour.

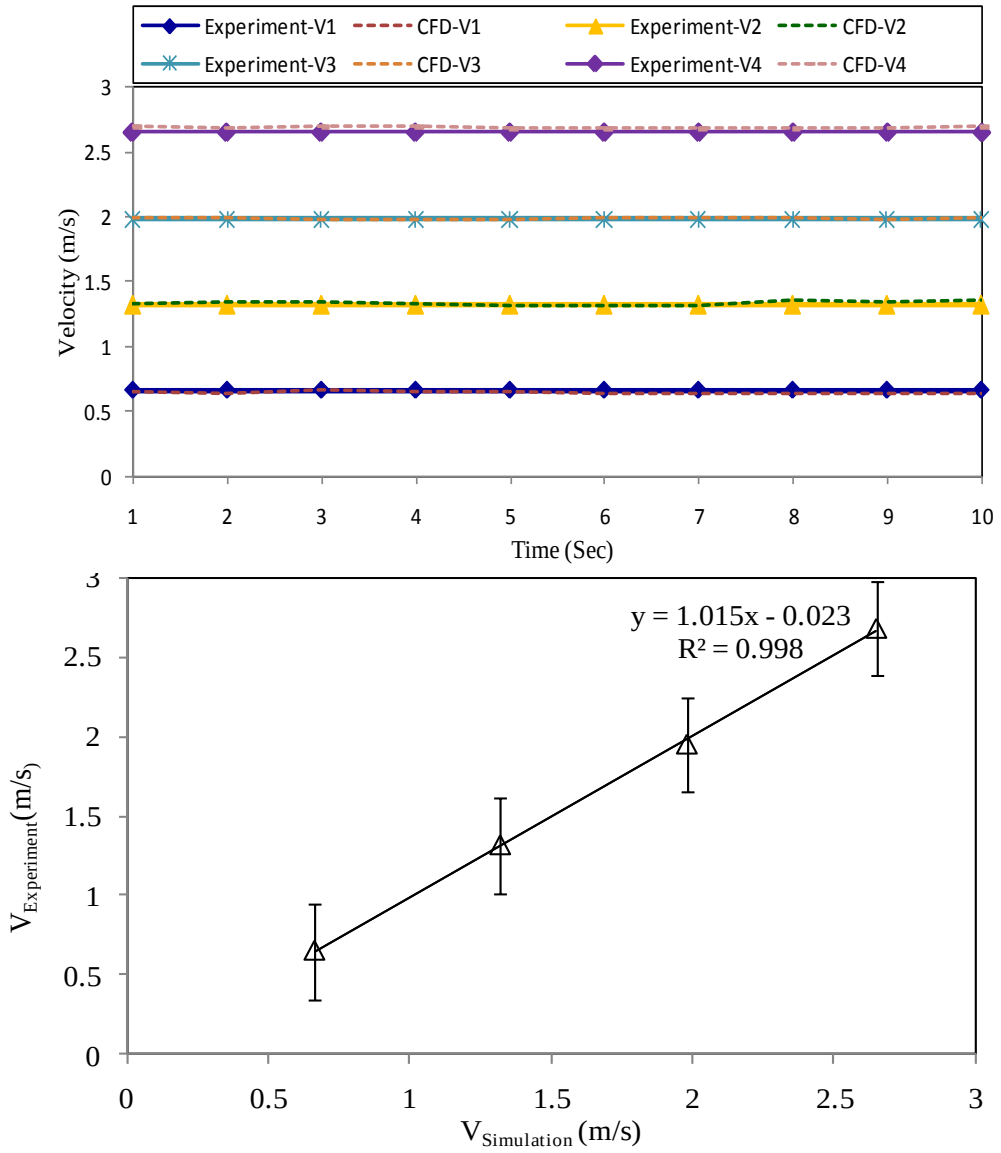

Figure 5.3a Comparison between experimental and CFD prediction.

In the simulation, the errors might be derived from several sources such as geometry meshing, numerical treatment of initial boundary conditions, and incomplete iterations. With regard to geometry meshing, a grid-independency test was performed to select the optimal number of grids, thus related influences (such as truncation errors) can be ignored. As indicated in Figure 5.3b, the simulated benzoic acid (BA) concentration of the reactor outlet

was observed to be closely comparable with the experimentally measured values for various feed water flow conditions.

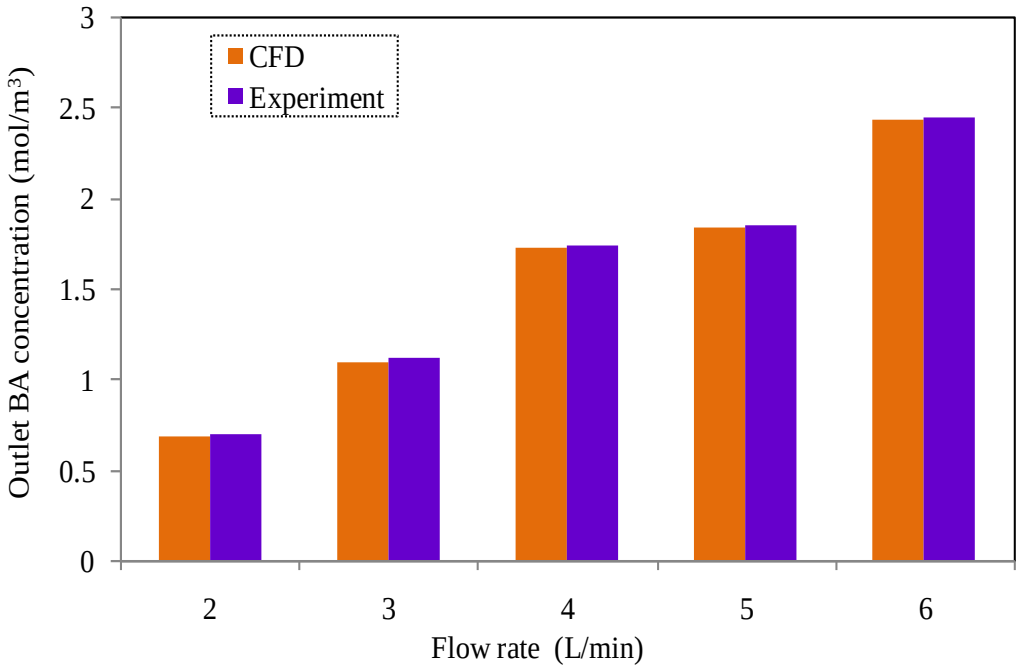

Figure 5.3b Comparison between experimental and CFD prediction of outlet benzoic acid.

5.8.2 Inlet Velocity Profile in Different Flow Rates

Using the Realizable k-ε model, simulations of fluid velocity vectors at the reactor inlet are shown in Figure 5.4 for inlet velocities of 0.663 and 1.32 m/s respectively. The prediction of the reactor zone was different under the conditions simulated. The turbulence model predicted some degree of swirling after the fluid left the entry point. For both inlet velocities, the velocity vectors showed higher magnitudes at the entrance region of the inlet, especially at the 0.02 to 0.03m locations. Beyond that point, the velocity vectors decreased in magnitude and approached more uniform values. It can be seen that the magnitude of the velocity vectors ranges from 0.52 to 0.744 m/s in the central zone along the horizontal axis when the inlet velocity is 0.663m/s. At the inlet, two recirculation zones can also be observed in Figure 5.4a. However, the magnitude of the velocity vectors varies from 1.07 to 1.32 m/s in the vicinity of the reactor inlet for an inlet velocity of 1.32m/s. The highest magnitude of velocity occurs in a smaller region of the reactor inlet compared to the lower velocity (0.663 m/s). These differences in inlet velocity can have an influence on the fluid flow pattern in the subsequent sections of the reactor as will be explained later. Although the data not shown

here, there were not appreciable differences among the flow fields predicted by the RSM and k-ω turbulence models. The magnitude of the predicted velocity obtained from the RSM and k-ω turbulence models ranged from 1.07 to 1.22 m/s at the entrance region under similar simulated conditions. However, at 0.025m from the reactor inlet, the magnitude of the velocity appears to decrease from that measured at the inlet to 0.579 - 0.664 m/s for all turbulence models studied. This is probably related to the gradual expansion of the reactor inlet; the fluid particles spread gradually towards the side walls of the reactor inlet section. The flow field becomes almost uniform for the entire inlet zone of the reactor.

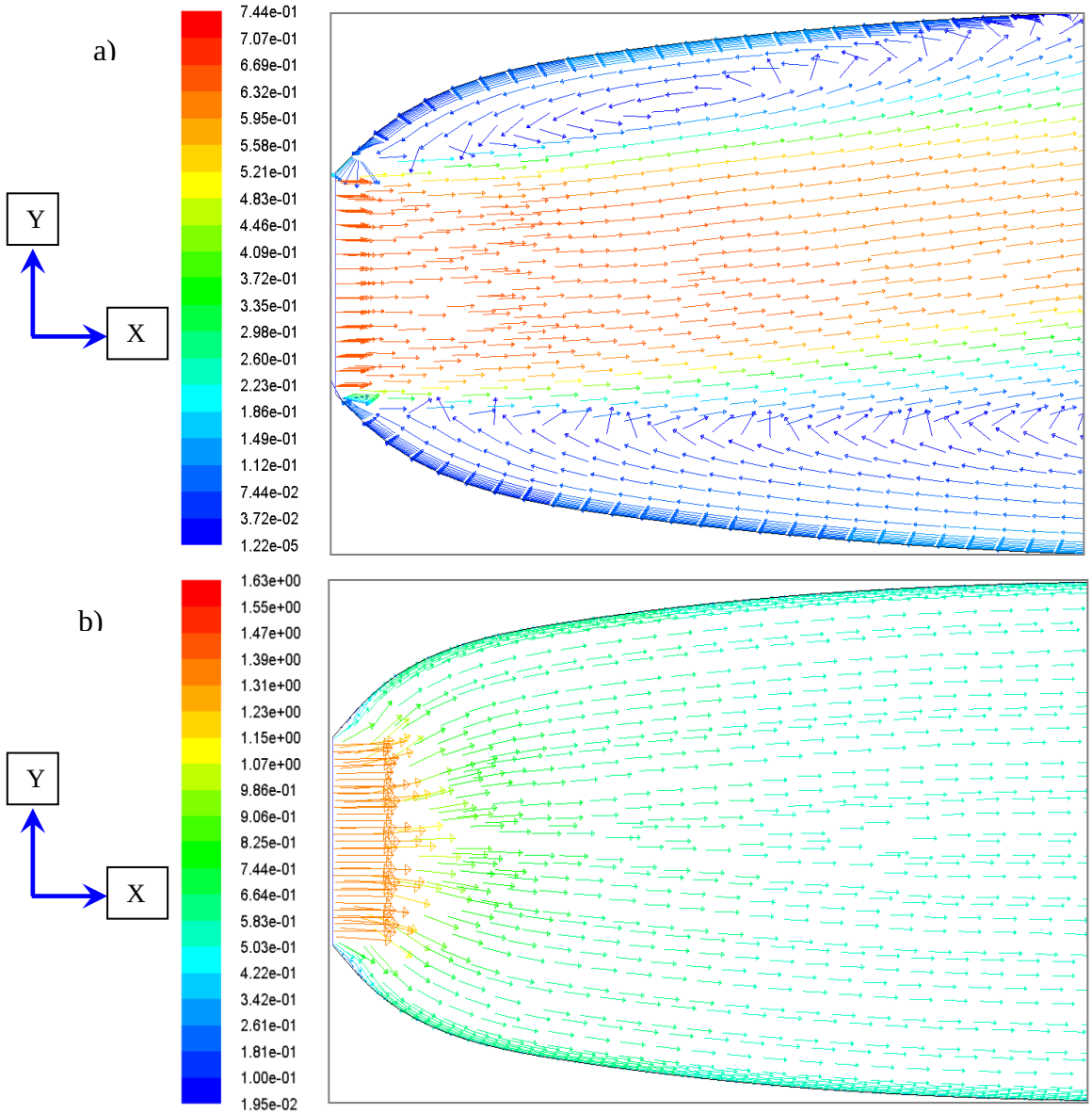

Figure 5.4 Inlet velocity vectors (ms^{-1}) simulated using the Realizable k-ε model a) V_{inlet}=0.663 m/s and b) V_{inlet}= 1.32 m/s respectively.

5.8.3 Outlet Velocity Profile in Different Flow Rates

Figure 5.5 shows the calculated flow fields of the reactor outlet that were predicted using a Realizable k-ε turbulence model. The Figure also depicts clearly how the velocity field changes as the water approaches the outlet. The main features of these flow fields are the formation of uniform velocity regions, which occupy the major part of the outlet zone. The first part is directed to the upper side of the outlet section, flowing parallel to the side walls and exiting via the outlet.

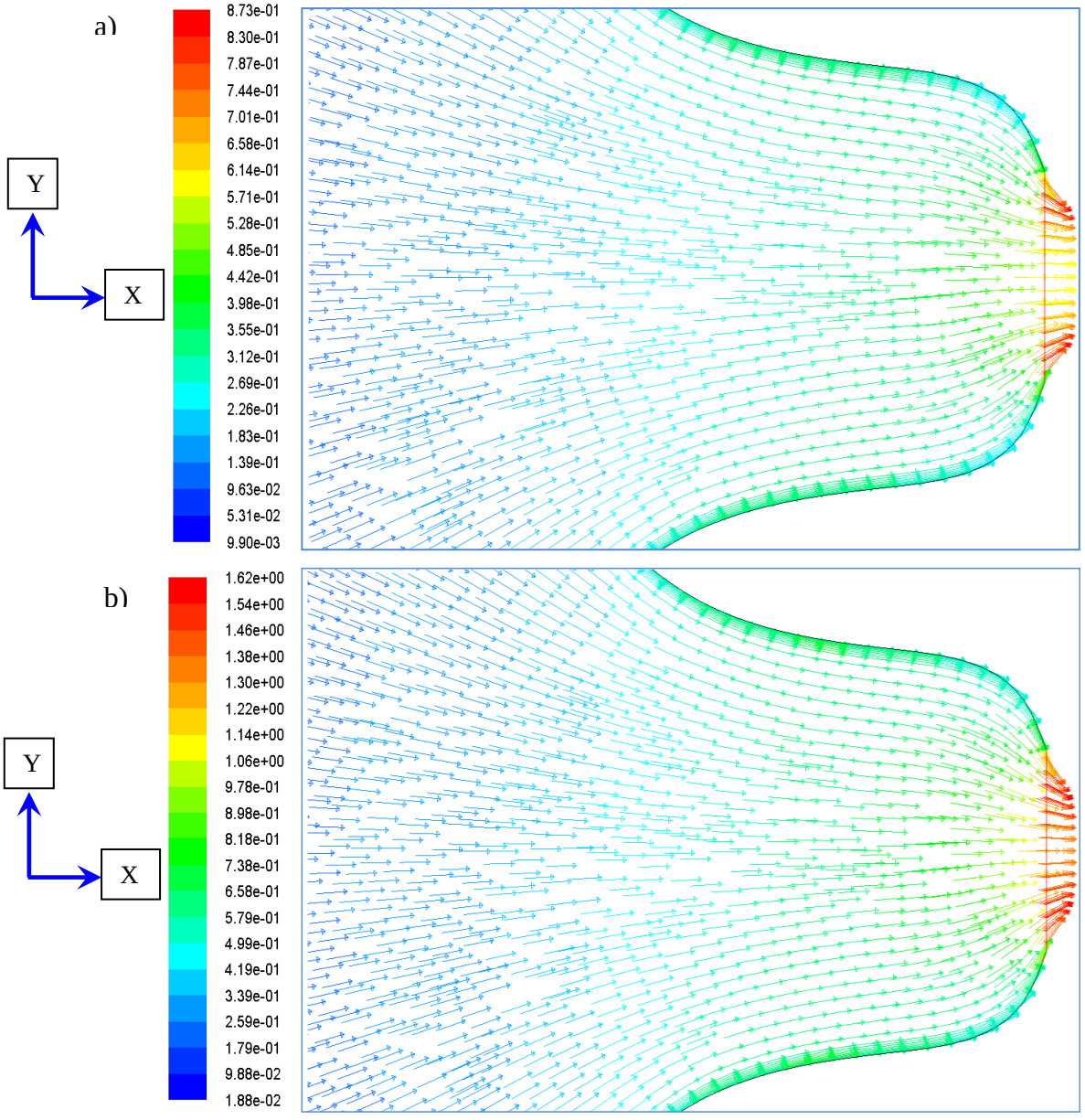

Figure 5.5 Outlet velocity vectors (ms^{-1}) simulated using Realizable k-ε model a) V_{inlet}=0.663 m/s and b) V_{inlet}= 1.32 m/s respectively.

The velocity vectors tend to form a clockwise rotation in the vicinity of the exit section. In contrast, the velocity vectors in the lower side of the outlet section are directed towards the anti-clockwise. A gradual variation in the magnitude of the velocity is seen at the position 0.5 to 0.535m from the exit edge. Regardless of the other turbulence models used (data not reported), the magnitude of the predicted velocity varies slightly at some locations before the exit. The maximum magnitudes obtained from the three turbulence models vary from 1.3 to 1.38 m/s at the outlet section under the conditions simulated. However, nearly 0.025m from the reactor outlet, the velocity magnitude appears to be around 0.659 to 0.499 m/s for the turbulence models studied. A uniform flow seems to prevail in the entire outlet region of the reactor. As the fluid particles strike on the side walls and move from the wider reactive area to the narrower outlet section, they tend to stream in line from the side walls to the central outlet zone and attain higher velocities at the constricted section.

5.8.4 Influence of Turbulence Model Selection

Figure 5.6 represents the simulated velocity vector fields using various turbulence models (Standard *k*-ε, Realizable *k*-ε , and Reynolds stress model) obtained at the same flow rate and in the experimental conditions (inlet velocity 1.32m/s) which corresponds to *Re*=5290. The inlet region is a more challenging zone since it can cause flow separation and the spreading of flows in the subsequent sections. These three turbulence models were used for comparison purposes. Similar patterns of velocity vectors were observed in the velocity fields computed using different turbulence models. For example, all the simulations predicted similar vortices in the region close to the entrance. For the Standard k-ε model, the predicted velocity vectors with varying magnitudes were almost parallel throughout the reactor. Irrespective of the turbulence models used, velocity vectors of higher magnitudes existed in the entrance section compared to the adjacent zones of the reactor inlet. At the entrance zone, the maximum simulated velocity was found to be 1.47 to 1.63 m/s for the S k-ε, Realisable k-ε and RSM models respectively. In the region close to the inlet, the velocity vectors spread gradually and attain a constant uniform flow towards the reactive section. In the central zone, the velocity was observed to be around 0.91 m/s. At the beginning of the reactive area, there are two small vortices where the velocity vectors tended to swirl.

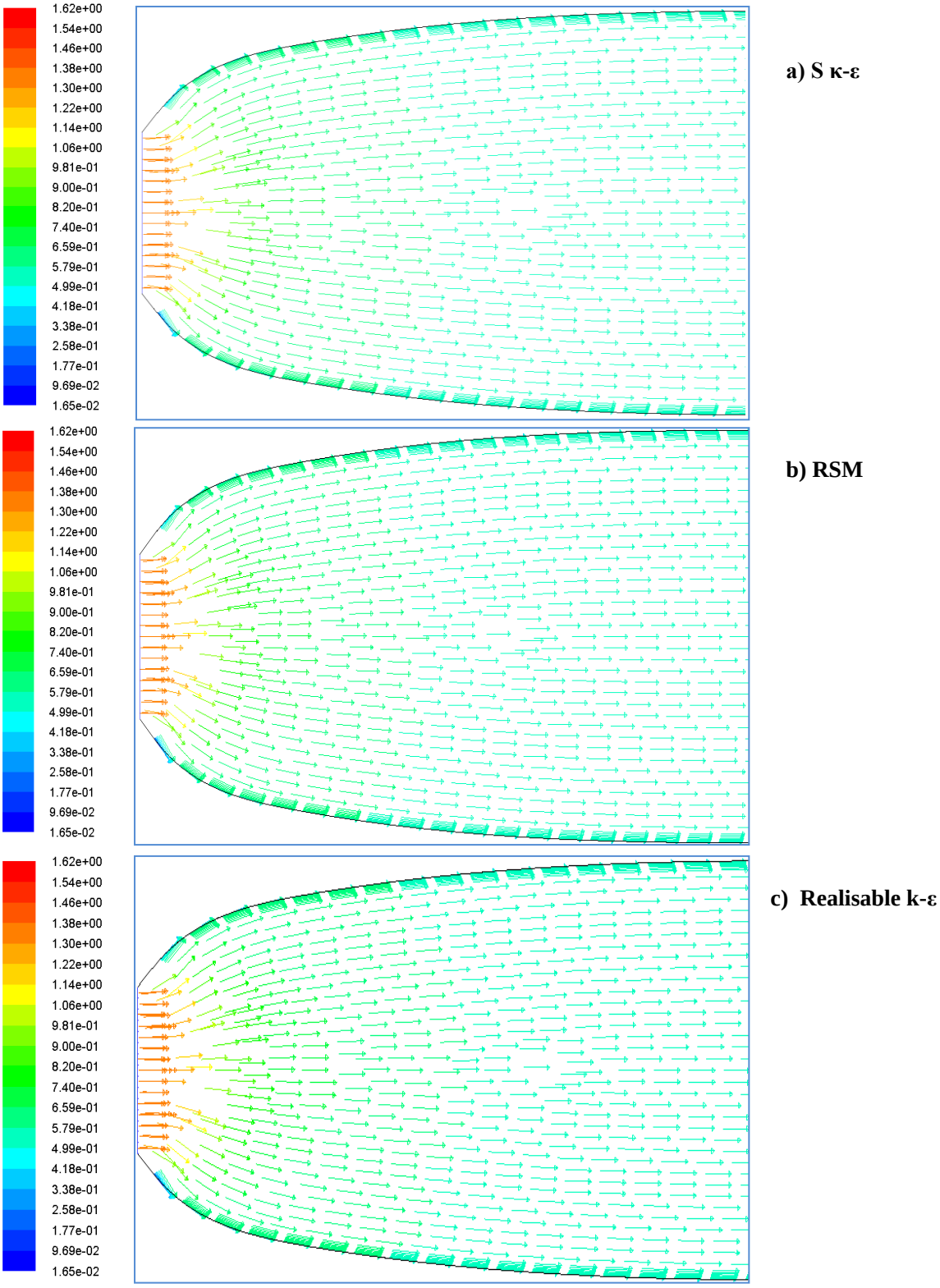

Figure 5.6 Inlet velocity (ms^{-1}) vectors prediction for models at *Re*=5360 a) Standard κ-ε, b) RSM and c) Realisable κ-ε.

The results presented here suggest that the three turbulence models show promise for predicting velocity vector fields and may be deemed sufficiently accurate for the study undertaken here. Using five turbulence models, the axial velocity components obtained for a distance of 50mm from the inlet are compared in Figure 5.7 and all turbulence models show an excellent match with each other in terms of axial velocity. In Figure 5.8, the stream function contours along the flat plate reactor obtained using the Realisable k-ε, RNG k-ε RSM and S k- ε turbulence models for *Re*= 5290 are shown. The CFD simulation results displayed no significant differences among the turbulence model predictions under the conditions simulated. Similar flow patterns were found when using the other turbulence models such as k-ω SST and Realizable k-ε and other flow rates. As Figure 5.8 shows, the distribution of local stream lines along the reactive zone of the reactor is more uniform than that at the reactor inlet and outlet. This might be related to the configuration of the inlet and outlet. The predicted stream function contours indicate higher magnitudes of flow persisting through the upper part of the reactor compared to the lower part.

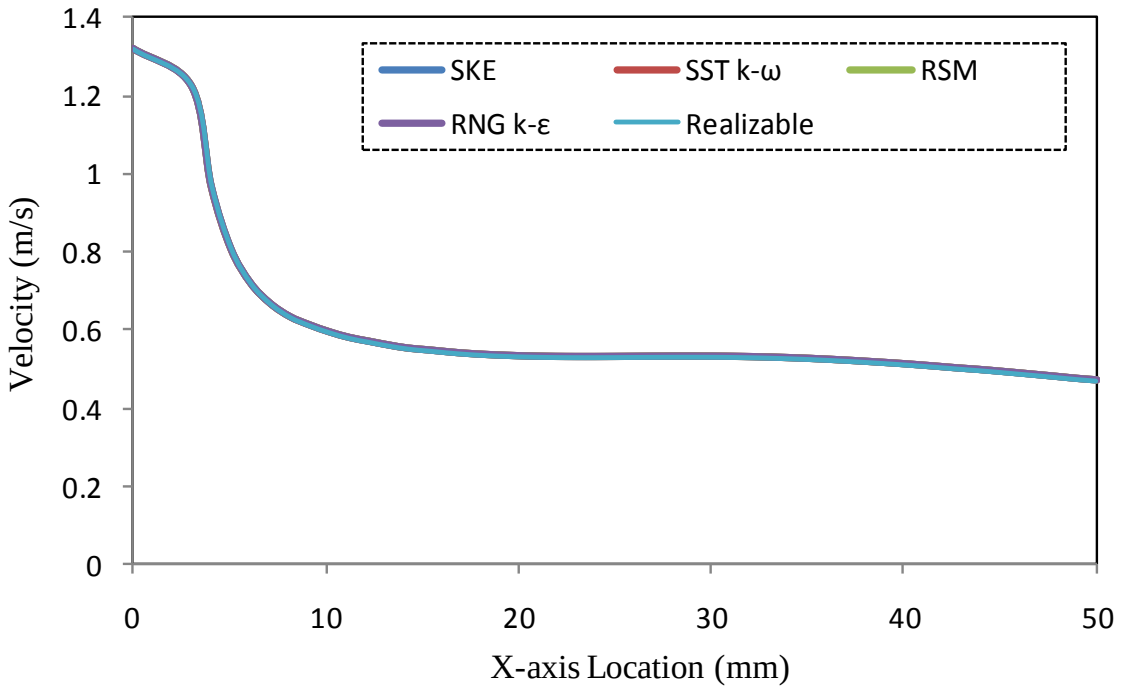

Figure 5.7 Effect of turbulence model on axial velocity profile for a distance of 50mm from the inlet for inlet velocity=1.32m/s.

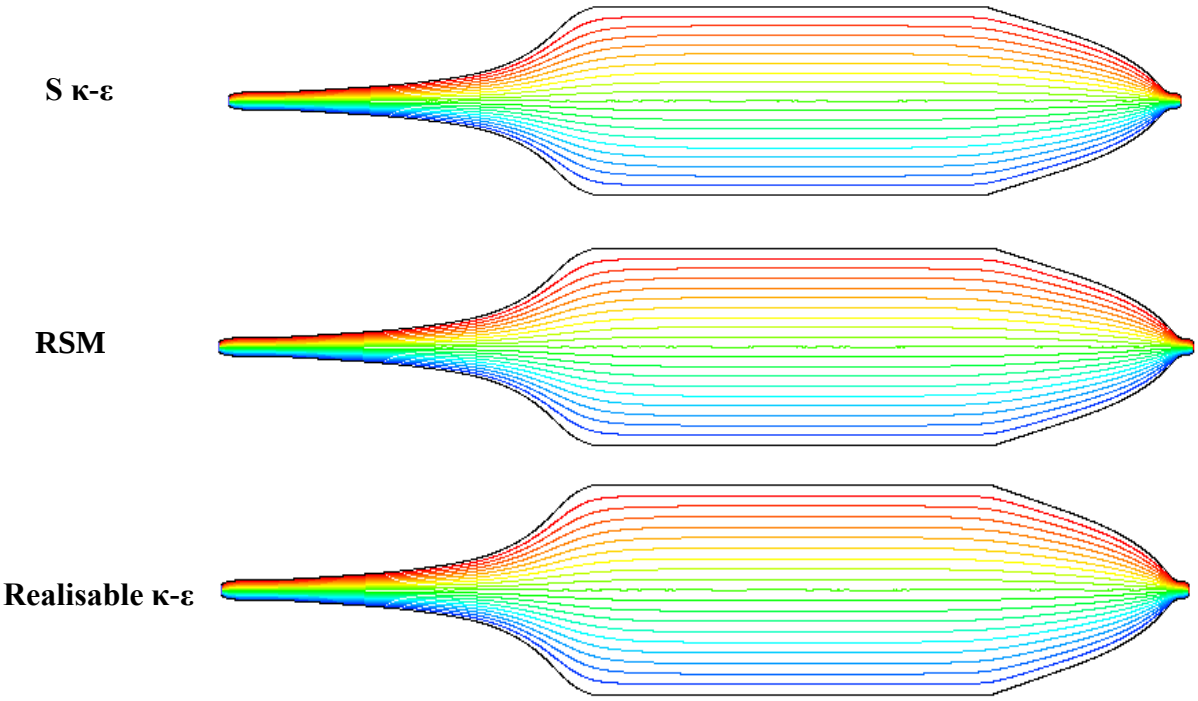

Figure 5.8 Stream function contours predicted using a) Realisable κ -ε, b) RSM and c) S κ-ε turbulence model for an inlet velocity 1.32 m/s.

5.8.5 Photocatalytic Degradation of Phenol in the Reactive Section of the Flat Plate Reactor

In order to analyse the performance of the flat plate reactor, a 3D domain of the reactive section with a dimension of 25mm × 50mm ×3mm was selected for CFD simulation which is shown in Figure 5.9. The geometry was discretised into a large number of 468750 hexhedral cell to obtain a mesh independent results. In addition, phenol was taken as model pollutant since traces of this contaminant is commonly present in wastewater streams. The initial concentration of phenol was assumed to be around 100 ppm, the dissolved oxygen concentration was kept constant at saturation (8 ppm at 25^{o}C) and no CO_2 was present initially. A no-slip boundary condition was specified at all walls (top and bottom including the sides). Moreover, zero-diffusive flux of species was defined at all walls except for the bottom one which was considered to be coated with photocatalyst TiO_2, where the following boundary condition was specified.

$$J_i = n.\, R_i^S \qquad (5.4)$$

Here n is a unit vector normal to the surface and R_i^S is the rate of production and depletion of species i from the catalyst coated surface by chemical reaction.

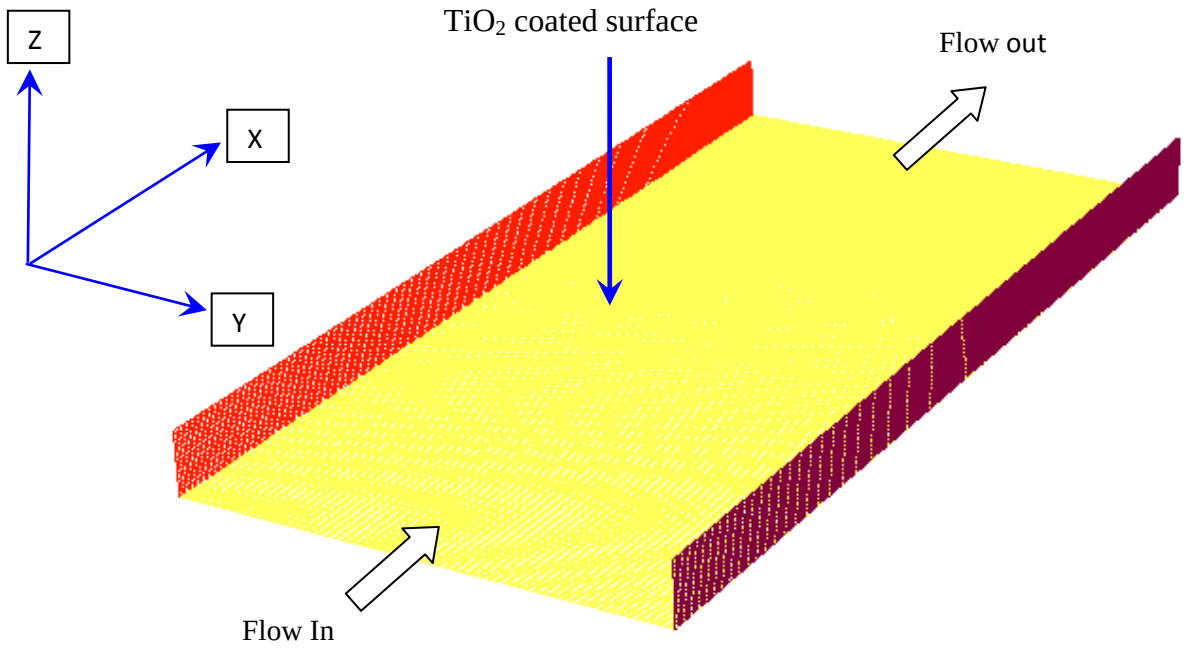

Figure 5.9 Schematic diagram of 3D-reactive domain used in phenol degradation simulation (top cover not shown).

A specific reaction rate ($0.17 min^{-1}$) was assumed for the photocatalytic phenol degradation simulation. Based on a linear emission model, the radiation intensity on the catalyst surface of the flat plate reactor was determined. The average value of irradiance computed for the reactive area was 44.5 W/m^2. A good uniformity in light intensity with variations less than 2.3% was found over the catalyst surface (Vezzoli *et al.*, 2011). The irradiance over the photocatalyst surface was assumed to be constant. The hydrodynamic system was considered to be constant and equal to that of water as phenol concentration is very low. Under the experimental condition in the flat plate reactor at Queensland University of Technology, the surface photocatalytic degradation of phenol was observed to follow the pseudo first-order kinetics with regard to the concentration of phenol and UV irradiance. Under isothermal condition, the photocatalytic oxidation of phenol (C_6H_5OH) was chosen as model reaction which can be represented by the following reaction,

$$C_6H_5OH+7O_2 \dashrightarrow 6CO_2+3H_2O \qquad (5.5)$$

The "laminar finite rate" model available in FLUENT which ignores the effect of turbulent fluctuations on reaction rates was used for reaction modelling since its application is well documented in the literature for photocatalytic reactor modelling (Duran *et al.*, 2010a; 2010b). The photocatalytic degradation rates of phenol obtained from experimental investigation are displayed in Table 4.2 in chapter 4. The contours of molar concentration of phenol for the photocatalytic degradation in the flat plate reactor for various inlet velocities are shown in Figures 5.10A, 5.11A, and 5.12A. A close scrutiny of these figures reveals that the distribution of phenol concentration decreases as the contaminated stream passes along the catalyst coated reactive slides. Under the conditions simulation performed, several small peaks in the transversal profile of phenol contours were also noticed along the catalyst coated plates for lower inlet velocities. However, the observed peaks disappeared gradually as the inlet velocities increases from 0.1m/s to 0.85m/s. Also Figures 5.10B, 5.11B and 5.12B show that the production of CO_2 increases as part of phenol in the pollutant stream is converted into CO_2. It indicates that the degradation of phenol is slower at the entrance region of the catalyst coated plate compared to the end region. Under the simulated conditions, a large gradient in the phenol concentration was observed along the axial direction for the lowest inlet velocity.

At the lower inlet velocity, the polluted stream will have long contact time with the photocatalyst surface in the reactor for its degradation (Duran *et al*., 2011b). However, the contaminated stream may not be degraded effectively at the higher fluid flow since a comparatively smaller gradient in phenol concentration was observed at high fluid velocity (Jarandehei and Visscher, 2009). The results presented here suggest that the residence time can play a key role on the photocatalytic degradation of organic pollutant in the flat plate photocatalytic reactive system. It appears in particular that the reaction mainly occurs only at the catalyst coated surface for all inlet velocities examined because of the contact of pollutant with the catalyst surface. Thus it is of paramount importance to enhance the fluid and catalyst contacting by improving mixing and turbulence in the reactive section for a sustainable photocatalytic system. However, increasing turbulence by increased flow rates does not appear to be a suitable approach since it reduces the photocatalytic degradation rate as evidenced from Figures 5.10 to 5.12. The reported results indicate the necessity to understand further the role of mixing and turbulence promoters in the flat plate reactor which has been presented in Chapter 6.

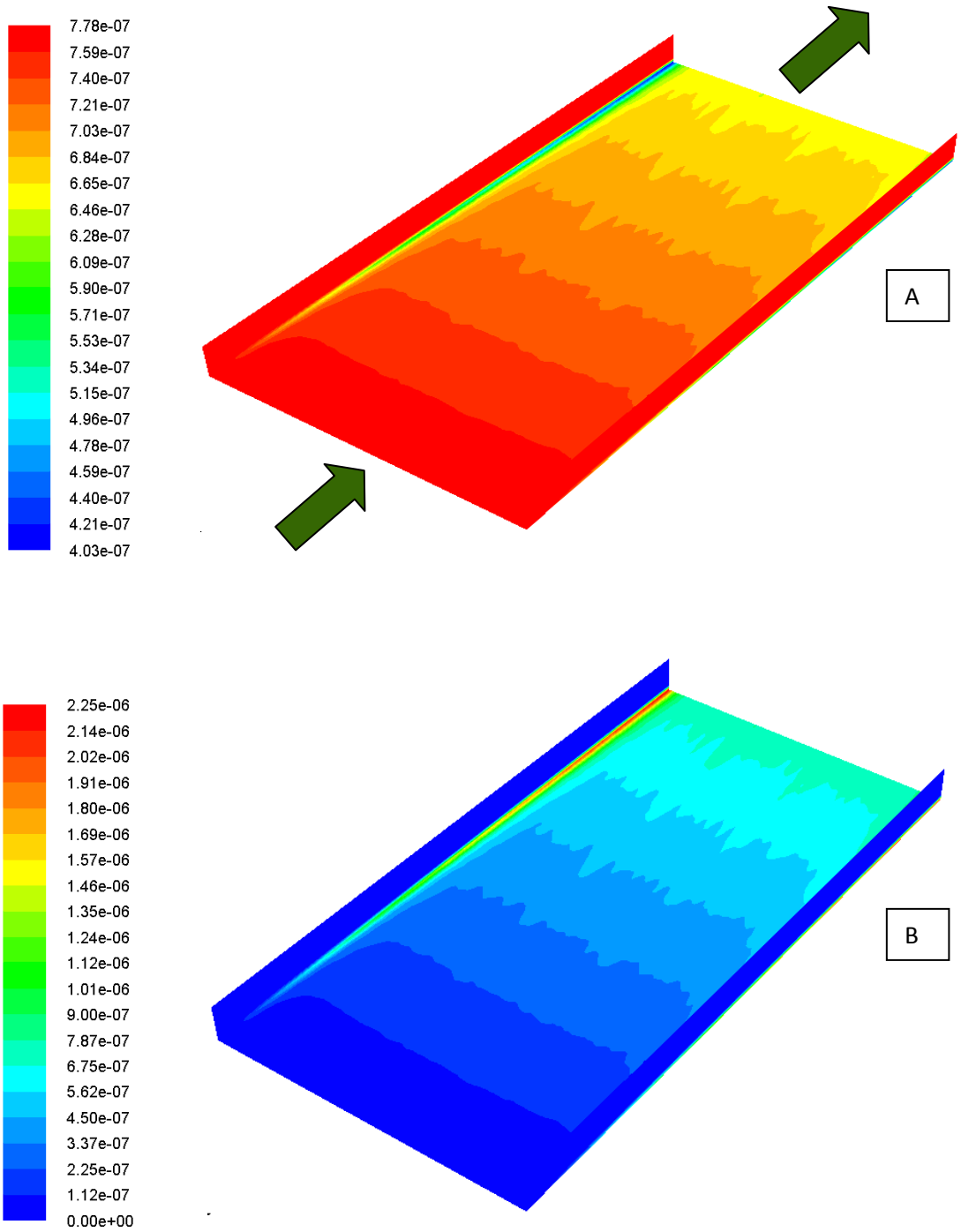

Figure 5.10 Contours of molar concentration of A) phenol (kmol m^{-3}) and B) CO_2 (kmol m^{-3}) at the TiO_2 coated surface of the reactor for an inlet velocity of 0.1m/s.

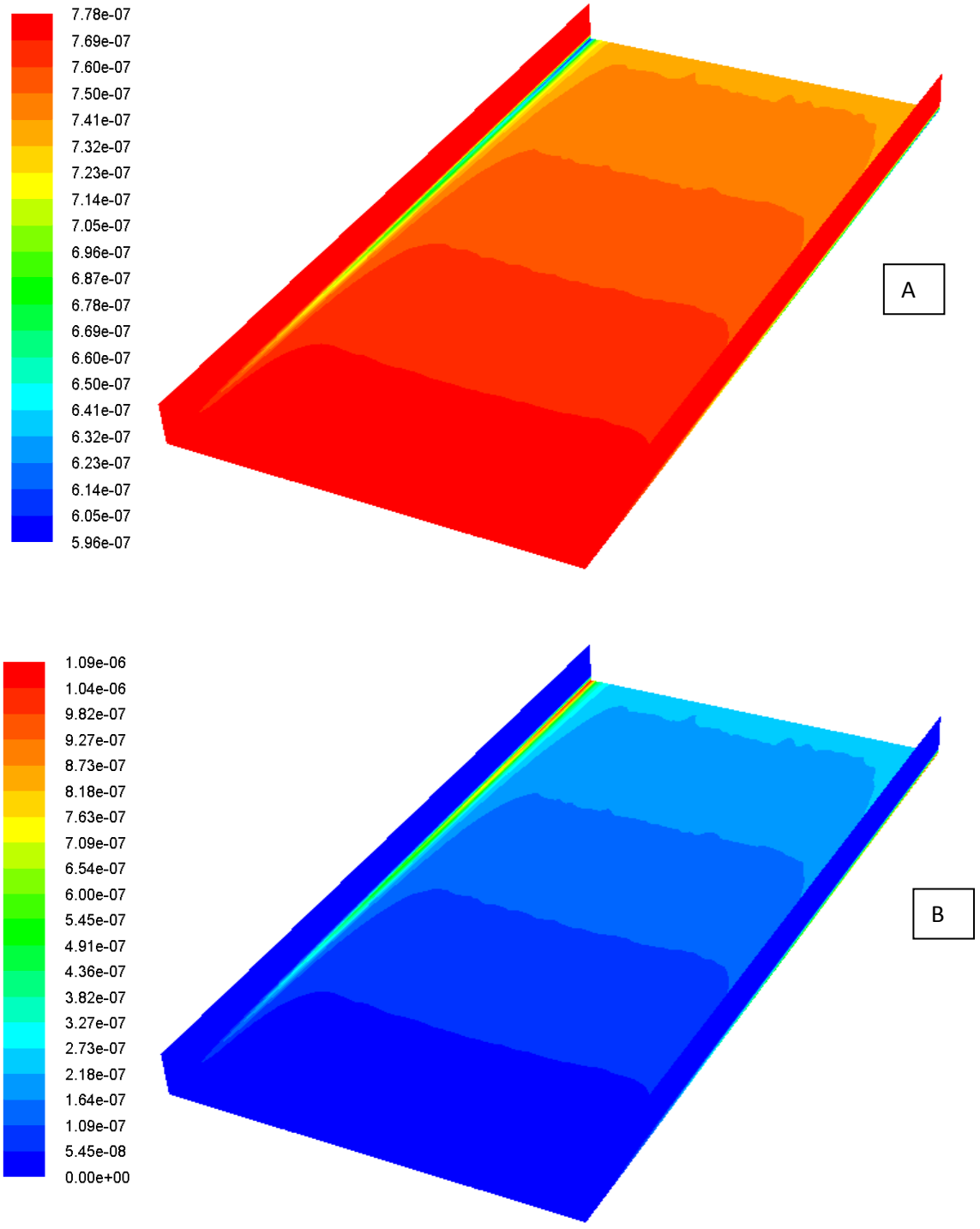

Figure 5.11 Contours of molar concentration of A) phenol (kmol m^{-3}) and B) CO_2 (kmol m^{-3}) at the TiO_2 coated surface of the reactor for an inlet velocity 0.35m/s.

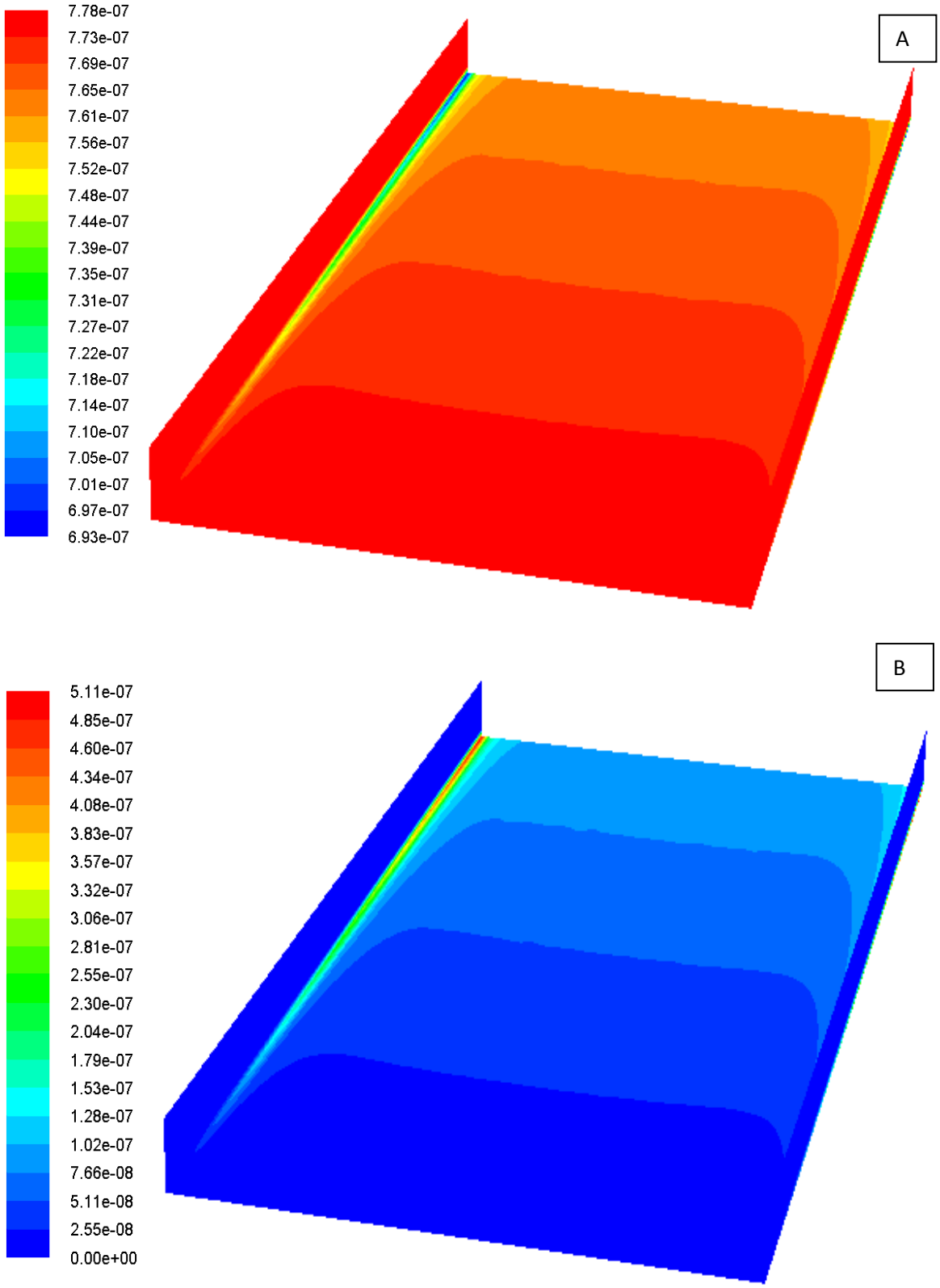

Figure 5.12 Contours of molar concentration of A) phenol (kmol m^{-3}) and B) CO_2 (kmol m^{-3}) at the TiO_2 coated surface of the reactor for an inlet velocity 0.85m/s.

5.8.6 Influence of Inlet Positions on Flow and Mass Transport

The position of the inlet opening can play a crucial role in hydrodynamic performance and fluid mixing in a photocatalytic reactor. In order to identify the optimal position of the inlet, several tests with an inlet velocity of 0.5m/s in which the inlet opening to the reactive section was varied were conducted in FLUENT. The height of the inlet opening was specified to be 50% of the reactor height (H) and its position was assumed to be at the top, bottom and mid-height of the reactor inlet as shown in Figure 5.13. Figure 5.14 represents the simulated stream lines in the reactive section in a two dimensional coordinate system computed at *Re*=3750. With respect to the inlet position, the predicted local stream lines patterns differed considerably over the span of the reactive section. For clarity, it can be seen that a recirculation region spanning nearly 33% of the reactive length (Figure 5.14b) occurred when the inlet opening was positioned in the upper half of the inlet. By contrast the recirculation region became shorter once the opening was placed in the bottom half of the inlet (Figure 5.14a). No discernible recirculation region was found, when the inlet opening was positioned at the mid-height or top-bottom position of the inlet with a similar opening height (Figure 5.14c). However, some degree of stream line distortions can be seen in Figure 5.14d.

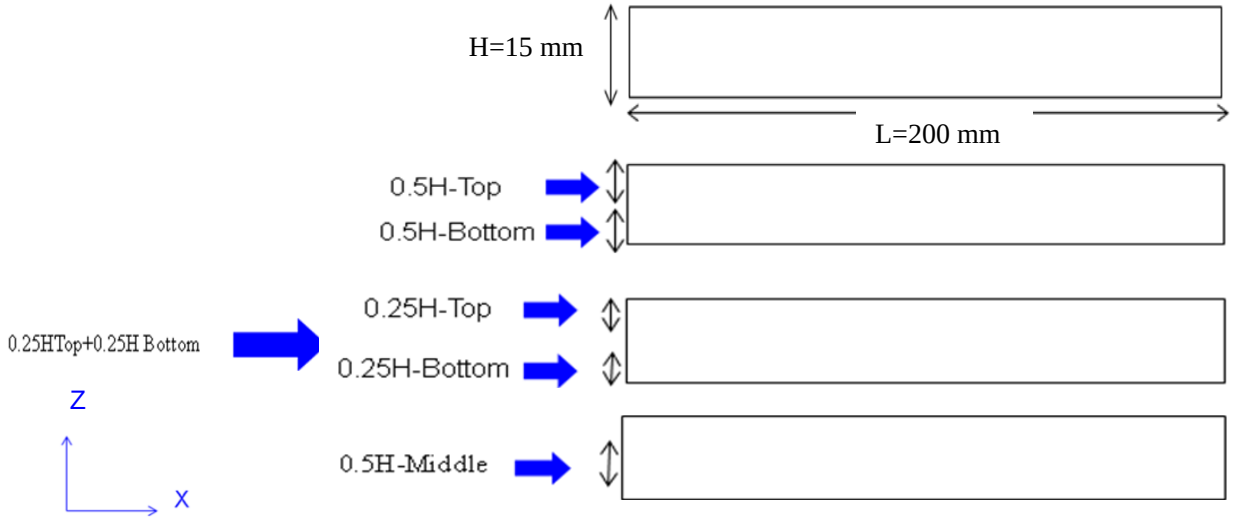

Figure 5.13 Schematic diagram of reactive section and inlet opening positions.

With respect to the inlet position, the predicted patterns of local velocity magnitude at *Re*= *3*750 differ considerably over the span studied. From Figure 5.15, it can be seen that a low velocity region with a magnitude of 2.52×10^{-2} m/s spanning nearly 0.02m to 0.05m at the bottom wall occurred when the inlet was positioned in the lower half of the inlet height (H).

In contrast a strong recirculation region can be observed once the inlet was positioned in the upper half of the inlet height (H). As shown in Figure 5.15c, two distinct low velocity regions ranging about 0.05m from the inlet are found at above and below the inlet when positioned at mid-height. A few scattered discernible recirculation regions were found (Figure 5.15d), when the inlet was positioned at top-bottom position of the inlet with the same opening height.

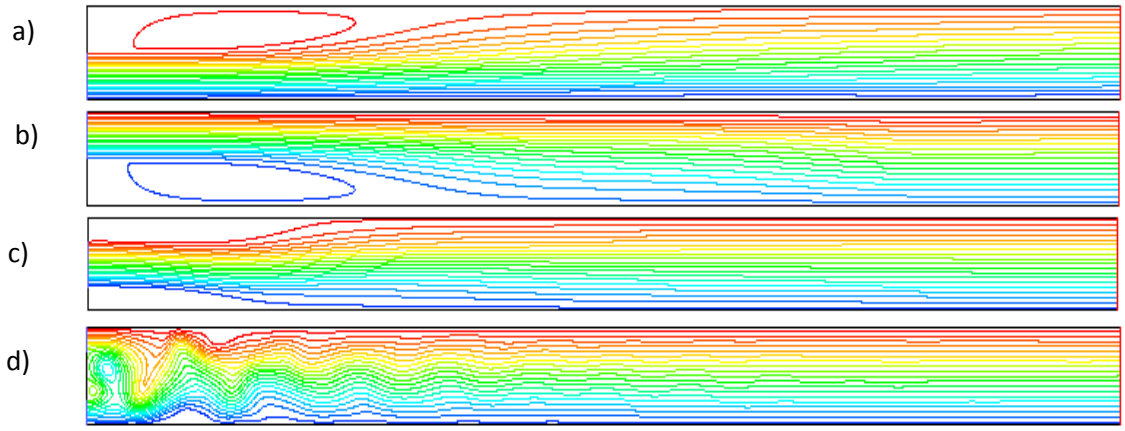

Figure 5.14 Influence of inlet positions a) bottom (0.5H), b) top (0.5H), c) middle (0.5H) and d) top plus bottom (0.5H) on local stream functions.

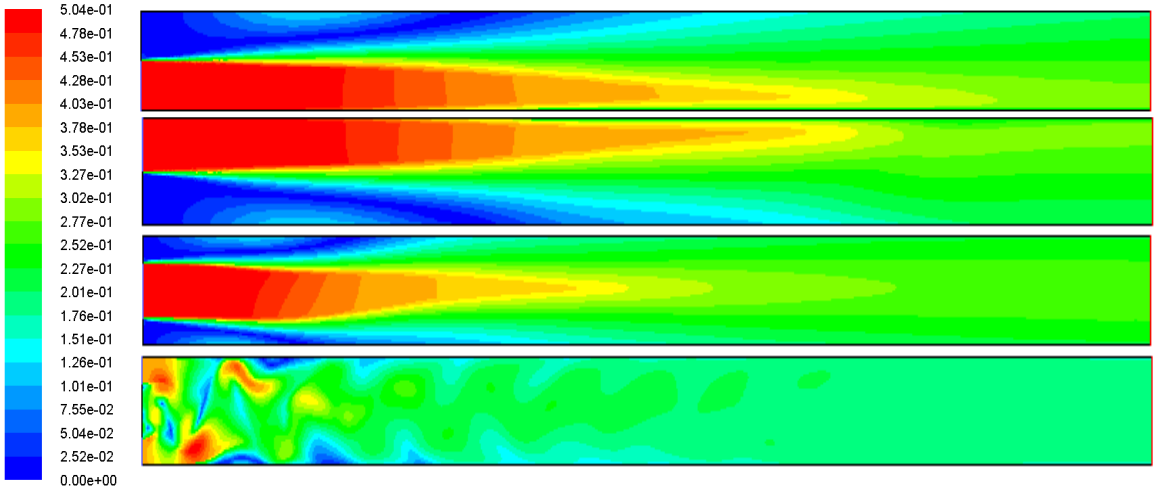

Figure 5.15 Influence of inlet positions a) bottom (0.5H), b) top (0.5H), c) middle (0.5H) and d) top plus bottom (0.5H) on velocity field respectively.

In order to examine the role of inlet positions on the FA mass transport, several runs were performed to compute the concentration field by varying the position of the inlet at bottom, top, mid, and top-bottom for Reynolds numbers 1875 and 3750 respectively. Under both

simulation conditions (Inlet FA mass fraction=0.0034), it can be seen in Figure 5.16 that a lower concentration of FA has been predicted over the reactive segment when the inlet opening was positioned in the bottom half of the inlet for both Re=1875 and 3750 respectively. At *Re*=1875, the low concentration zone spans over 50% of the reactive length in Figure 5.16 (upper). This can be attributed to the laminar nature of the fluid flow and that mixing occurs mainly by molecular diffusion. In contrast, the extent of the low concentration zone is significantly reduced when *Re* approaches 3750 due to the turbulent diffusion. Significant reduction in FA concentration distribution was found, when the inlet opening was positioned at the top, mid-height or top-bottom position of the inlet with a similar opening height at *Re*=1875. By contrast the distribution of FA concentration was enhanced considerably for the inlet opening positioned at the top, mid-height or top-bottom position of the inlet with same height at *Re*=3750 in Figure 5.16 (lower). The pattern of observation can be attributed to the recirculation zones occurring in the reactive section under the conditions simulated.

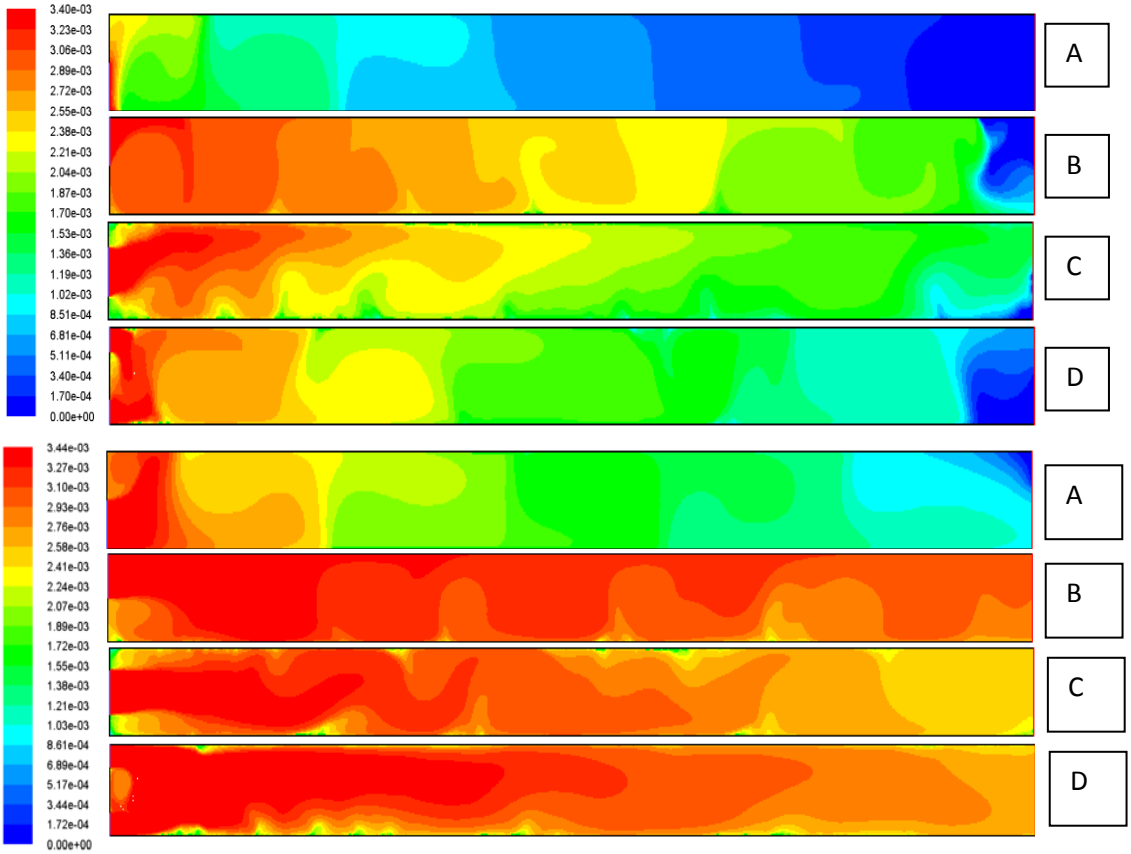

Figure 5.16 Influence of inlet positions A) bottom (0.5H), B) top (0.5H), C) middle (0.5H) and D) top plus bottom (0.5H) on formic acid mass fraction computed at *Re*= 1875 (upper figure) and *Re*= 3750 (lower figure) respectively.

On the basis of the recirculation zone due to the inlet opening positions either in the top or in the bottom half of the inlet, it can be concluded that they are more suitable compared to the inlet opening positioned in the middle half or top-bottom position. However, at low and high flow conditions, the inlet opening positioned in the bottom half of the inlet does not seem to be better for mass transport of FA.

5.9 Conclusion

In this chapter, the fluid flow structure of a flat plate photocatalytic reactor was investigated using CFD code FLUENT. The simulation results show the computed flow features for inlet and outlet components of the reactor under different flow regimes. The effect of inlet positions on the flow and mass transport of formic acid in the reactive module has been examined which provides significant insight for the efficient design of the flat plate reactor. Also the effectiveness of a photocatalytic reactor for pollutant degradation was observed to depend on the reactor's hydrodynamics. The results reported here suggest the importance of fluid mixing in the reactor since the reaction takes place only at the fluid-catalyst interface. Also the continuous contact of pollutant and catalyst surface is necessary to advance the photocatalytic system efficiently. The use of baffles to promote mixing and turbulence in the immobilised flat plate reactor is of utmost importance to enhance the pollutant mass transport to the catalyst surface and to obtain the overall reaction rate independent of mass transfer limitation. Improved mixing can result in well-formed vortices which are useful to increase the pollutant-catalyst contacting and reaction yield as well as to minimise the deposition of degradation by-products on the catalyst surface. In this regard, a new approach using various baffles and roughness elements in the reactive section of the reactor have been investigated in chapter six and seven respectively to understand better the interplay of the parameters such as baffle height, position, spacing and mass transport of pollutant under low and high flow conditions that influence the performance of the photocatalytic reactor.

CHAPTER SIX

EFFECT OF TURBULENCE PROMOTERS IN THE PHOTOCATALYTIC REACTOR

6.1 Introduction

The application of photocatalytic water treatment processes using a catalyst and an energetic light source has received significant attention due to its effectiveness in degrading and mineralizing the organic contaminants in wastewater. The use of a catalyst in suspended form makes the photocatalytic water treatment system impractical. To avoid the subsequent catalyst removal from the treated water, the supporting materials are coated with catalyst. However, when the catalyst is immobilized on supported materials, its photocatalytic efficiency is shown to decrease due to the deposition of degradation by-products on the catalyst surface (Rao *et al*., 2004). Moreover the catalyst surface can be fouled due to the adsorption of higher levels of pollutants in water. As a result the light penetration through the bulk liquid medium to the catalyst surface can be strongly inhibited and may reduce the overall effectiveness of the photocatalytic reactor. In order to ensure long-term operational stability of the reactor, the thickness of the deposited layer on the catalyst surface should be minimized using suitable strategies. Mixing of chemical reactants is a fundamental and common operation in an efficient chemical reactor. Further, the inadequate mixing in an immobilized reactor can result in low mass transfer of pollutant from the bulk of the liquid to the photocatalyst surface which lowers the efficiency of the immobilized photocatalytic reactor (Periyathamby and Ray, 1999; Dutta and Ray, 2004). The degree of optimum mixing mostly depends on the relative distribution of mean and turbulent kinetic energy. Improving turbulence using internal elements such as baffles is indicated to enhance the pollutant mass transfer in the immobilized photocatalytic reactor (Mehrotra and Ray, 2003). To the author's knowledge, very limited information on this aspect of the photocatalytic system is available in the current literature. The photocatalytic oxidation process relies on four essential stages; mixing, mass transfer, reaction, and separation by pollutant destruction. Since mixing plays a crucial role in the operation of a photocatalytic reactor and conditions the subsequent processing steps, this area has received substantial attention from both the fundamental and

the application point of view (Kaci *et al*., 2009). Two types of reactors namely batch reactors and continuous reactors are usually used in photochemical reactions. As a batch reactor, the application of a stirred tank has several disadvantages such as excessive fluid stagnation and non-homogeneous mixing, huge energy consumption to operate, and large device dimensions (Kaci *et al*., 2009).

By contrast, the use of baffles in a photocatalytic reactor can act as a continuous static mixer which offers several advantages such as reduction of overall device dimensions, reduced energy consumption by replacing moving parts, better process control, shorter residence time and improvement of reaction selectivity. Mixing enhancement by releasing turbulence in the low mass transfer region in an annular type phtotoreactor was recently discussed by Sengupta *et al*. (2001) and Duran *et al.* (2009, 2010a). They indicated that the degradation of pollutant was significantly limited by mass transfer resistance in an immobilized photocatalytic reactor. These results have highlighted the need for further research on this aspect of a photocatalytic reactor to generate vortices by a local flow instability mechanism, which considerably increases mixing. The design of the photocatalytic reactor is mostly based on the assumptions of uniform residence time and flow field. These assumptions, however, are not realistic and neglecting the reactor hydrodynamic phenomena, which would occur in the reactor, may result in an inefficient design. Several methods are employed to improve the hydraulic efficiency of the reactor while minimizing the extent of the stagnant zones. The use of a suitable baffle configuration has been indicated in earlier studies. Nonetheless the use of baffles without optimization would result in a reactor with worse performance than the reactor without a baffle. These make it essential to investigate the suitable height and position of the baffles in the reactor. While there have been a few investigations on the CFD modelling of photoreactors for water disinfection, modeling of reactor hydrodynamics for wastewater treatment under various baffle arrangements has not been addressed adequately. In addition, investigation has focused upon devising optimum reactor design for pollutant degradation which is becoming an important research area (Castrillon *et al*., 2006). CFD shows promise in its flexibility to vary parameters for the optimization of reactor design. CFD simulation allows for the accessing of such local parameters of turbulence mechanism as turbulent kinetic energy, turbulence energy dissipation rate and others that are difficult to control experimentally in complex geometries. In this chapter, the influence of top and bottom baffles as mixing and turbulence promoters in the reactive module of the flat plate

reactor on the hydrodynamics performance are investigated, which has recently attained considerable attention due to its ability to generate large-scale stream-wise vortices, enhancing mass and momentum-transfer phenomena and turbulent energy dissipation in the flow over those of the simple un-baffled one. Using CFD code FLUENT several test runs were performed to predict the distribution of significant hydrodynamic parameters in the reactive section for various baffle arrangements and the results obtained are discussed herewith.

6.2 CFD Modelling Governing Equations

In this section, the governing equations and assumptions for the modelling of fluid flow in the reactive module are discussed. The flow field encountered in this study is represented by the Reynolds averaged, Navier-Stokes equation for mass and momentum conservation. In this study, the following governing equations are solved with the considerations that the fluid (water) is Newtonian, isothermal, incompressible, non-reactive and has constant physical properties. The reactor flow field is assumed to be under transient and turbulent steady state conditions. Using the assumptions described above and the Reynolds-averaged Navier-Stokes (RANS) turbulence modelling approach (Ranade, 2002), the CFD modelling involves the numerical solution of the continuity equation (6a), Reynolds-averaged Navier-Stokes equation (6b) and time-average conservation of species equation (6c) by a finite volume technique which are expressed as

$$\frac{\partial(\rho)}{\partial t} + \nabla.(\rho\bar{u}) = 0 \tag{6a}$$

$$\frac{\partial}{\partial t}(\rho\nabla) + \nabla.(\rho\overline{uu}) = -\nabla\bar{P} - \nabla.\tau \tag{6b}$$

$$(\rho\bar{U}\bar{m}_k + \rho\overline{um'}_k) = -\nabla.\bar{J}_k \tag{6c}$$

Where the over bar indicates a time-averaged value, ρ is the density (kg/m^3), U (m s^{-1}) is the velocity of fluid, P (Pa) is the pressure, and τ is the viscous stress tensor, m_k is the mass fraction of species k, J_k is the diffusive flux of species k, and u and m_k are fluctuating flow velocity and mass fraction of species k, respectively. In order to consider turbulence correctly, Reynolds stresses are modelled to achieve closure of Equation (6b).

A turbulence model is a set of semi-empirical equations used to determine the turbulent transport terms and thus close the system of RANS equations and solve them in order to obtain the mean flow field properties and the Reynolds stresses. By applying this computational method, a variety of fluid flow properties can be determined. The most common of these are included in commercial CFD codes: i) the Spalart-Allmaras model, ii)) the k-ε model with variants including: the Renormalization Group (RNG) k- ε model , realizable k-ε model , the k-ω model iii) Reynolds stress model (RSM) and iv) the Large Eddy Simulation (LES) model. Unfortunately, none of the turbulent models is universal; indicating that although few of the turbulent models work well for some flows others may not be suitable for general turbulent flow fields where flow separation and reattachment phenomena are dominant. Of the available models, six classical turbulence models namely the mixing length, standard *k–ε*, RNG *k–ε*, realizable *k–ε*, are widely used in many engineering applications (Launder and Spalding, 1974). In order to simulate more complex flows especially in a flow channel containing different barriers, the RNG *k–ε* model is reported to be more effective compared with other k–ε models due to its accuracy for solving eddy activities at relatively low Reynolds numbers (Cao *et al*., 2001). In contrast to the Reynolds stress and algebraic stress models, the RNG k-ε model also requires lower computational time. Using a rigorous statistical technique i.e renormalization group, this model was derived which is similar to the standard *k–ε* model developed by Launder and Spalding (1974). This model uses additional terms in its ε equation that substantially improves its accuracy for rapidly strained flows. In light of standard k-ε model, the RNG k-ε model provides an analytical formula for the effective viscosity that accounts for the low Reynolds number. The use of these features requires the appropriate treatment of the near-wall region. These features enable the RNG k-ε model to be more accurate and reliable for a wider range of flows which include strong streamline curvature, vortices and rotations. In this study, depending on the inlet velocity, the RNG k-ε model was chosen from the available models for CFD simulation. The model provides the following transport equations for *k* and *ε* as

$$\frac{\partial}{\partial t}(\rho k) + \frac{\partial}{\partial x_i}(\rho k u_i) = \frac{\partial}{\partial x_j}\left[\left(\mu + \frac{\mu_t}{\sigma_k}\right)\frac{\partial k}{\partial x_j}\right] + P_k - \rho\epsilon \tag{6.4}$$

$$\frac{\partial}{\partial t}(\rho \epsilon) + \frac{\partial}{\partial x_i}(\rho \epsilon u_i) = \frac{\partial}{\partial x_j}\left[\left(\mu + \frac{\mu_t}{\sigma_\epsilon}\right)\frac{\partial \epsilon}{\partial x_j}\right] + C_{1\epsilon}\frac{\epsilon}{k}P_k - C_{2\epsilon}^{*}\rho\frac{\epsilon^2}{k} \tag{6.5}$$

$$C_{2\varepsilon}^{*} = C_{2\varepsilon} + \frac{C_{\mu}\eta^{3}(1-\eta/\eta_{0})}{1+\beta\eta^{3}}$$

In this model, Boussinesque approximation has been used to relate the Reynolds stresses with turbulent viscosity (μ_t) and mean velocity graident. In Equations (6.4) and (6.5), $P_k = \mu_t S^2$ or $P_k = -\rho\overline{u_i' u_j'}\frac{\partial ui}{\partial xi}$ is the production term of turbulent kinetic energy due to mean velocity gradient, where S is the modulus of mean rate-of-strain tensor, defined as

$$S = (2SijSij)^{1/2}$$

The turbulent viscosity (μ_t) is the effective viscosity of the fluid due to turbulence and is calculated using the following relationship,

$$\mu_t = \rho C_{\mu}\frac{\kappa^2}{\varepsilon}, C_{\mu} = 0.0845$$

The values of model constants are: $C_{1\varepsilon}$=1.42, $C_{2\varepsilon}$=1.68, η_0=4.38 and, β=0.012 . $\eta = Sk/\epsilon$

6.3 Geometry of Reactive Module

A 2D computational domain of the reactor used in CFD modelling is illustrated in Figure 6.1. The reactor consists of three parts: inlet, reactive area and outlet. This configuration was designed to reduce the computational time and to minimize the presence of dead and recirculating zones within the reactor (Capel, 2008). The reactor outlet was designed to reduce the amount of construction material and to simplify the manufacturing complexity of the device. For simulation purposes, dimensions of the reactive module being 15 mm in height and 200mm in length were considered for the reactive region between the inlet and the outlet of the reactor. The hydraulic diameter of the inlet and outlet was specified to be 15 mm. A set of six top baffles having 12mm, 10mm, 7.5mm, and 5mm heights was fixed at 0.125L, 0.25L, 0.375L, 0.5L, 0.675L, 0.75L and 0.875L respectively. The reactor geometry was constructed using GAMBIT 2.3.16, (Fluent Inc., 2006) and was discretized to a sufficiently large number of 3,47,809 cells to ensure a grid independent solution. The finer computational grids have been employed near the baffles and walls by utilizing the fixed size function, where intense fluctuations of velocity and shear stress may exist. The reactive section with a bottom baffle (lower one) is illustrated in Figure 6.1. This configuration was selected to reduce the computational time and to minimize the storage requirement (Ahmed *et al.*, 2011c).

The finer computational grids have been employed near the baffles and walls by utilizing the fixed size function, where intense fluctuations of velocity and shear stress may exist.

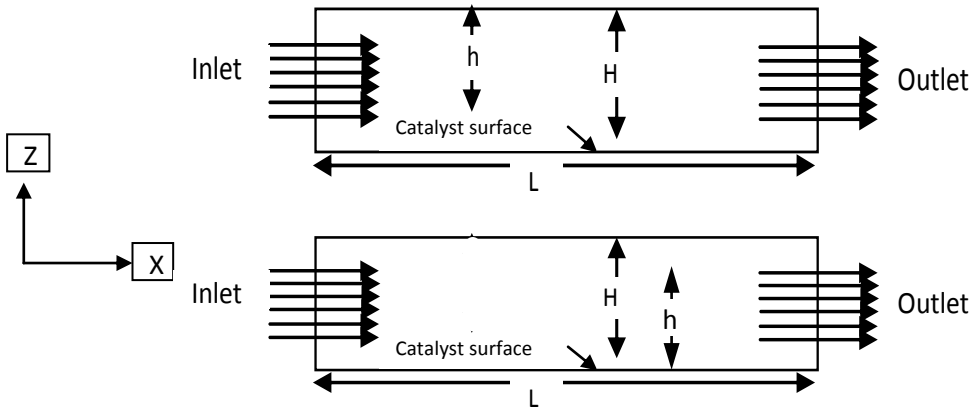

Figure 6.1 Schematic diagram of the reactive module with top (upper figure) and bottom (lower figure) baffle, h= baffle height, H= reactor depth, L= reactive module length.

6.4 Solution Strategies

To reduce computational power requirements, a 2D pressure-based-segregated solver with a first-order steady state formulation was employed for the single phase modelling. A second-order up-wind differencing scheme was used to overcome numerical diffusion. The pressure-velocity-coupling scheme was resolved with a SIMPLE algorithm. This scheme allows for an improved convergence. Pressure was discretized with a PRESTO scheme because of its strong convergence capability. To ensure the convergence of the numerical solution, the scaled residuals were monitored to a criterion of at least 10^{-4} for the continuity and momentum variables and κ-ε as well as 10^{-6} for concentration. In addition, the variation of velocity magnitude at one point of the computational domain located in an area of high velocity gradients was used as an indicator of convergence. Assuming that the very low concentrations of FA did not affect the velocity field within the reactor, the CFD model was solved in two steps. Firstly, equations of continuity (6.1) and motion (6.2) were solved for obtaining the flow field across the computational domain. Then, the velocity values were kept ‘‘frozen” and the equation of conservation of species (6.3) were solved using the converged flow solution (Duran *et al.*, 2009; Ahmed *et al.*, 2011c). This solving strategy minimizes computation time and brings stability to the solution.

6.5 Boundary Conditions

For simulation, a no-slip boundary condition was used at the bottom wall and the top surface was modelled as a wall. Also this boundary condition was applied for the top and bottom baffles. At the inlet and the outlet, VELOCITY-INLET and PRESSURE-OUTLET boundary conditions were imposed respectively. The hydraulic diameter of inlet and outlet was fixed at 15 mm. The inlet velocity was assumed to be 0.15m/s and 0.5 m/s respectively and the operating pressure at the reactor outlet was specified at 50,000 Pa. The direction of the flow was defined normal to the boundary. The turbulence intensity (TI) was set with values close to 5%. At the outlet, a fully developed flow condition was assumed. Formic acid (FA) was chosen as a model compound to test the influence of top and bottom baffle height on the mass transport of FA. At the inlet a constant concentration of 0.0034 (mass fraction) was specified and zero-diffusive flux was specified for the top wall.

6.6 Grid Independence

In order to ensure the numerical solutions is mesh independent, a series of tests using different mesh sizes have been conducted prior to the actual simulations. The wall velocity profiles at 2 mm above the bottom wall of the reactive section for three different global mesh sizes of 0.1, 0.2 and 0.3 mm are compared in Figure 6.2.

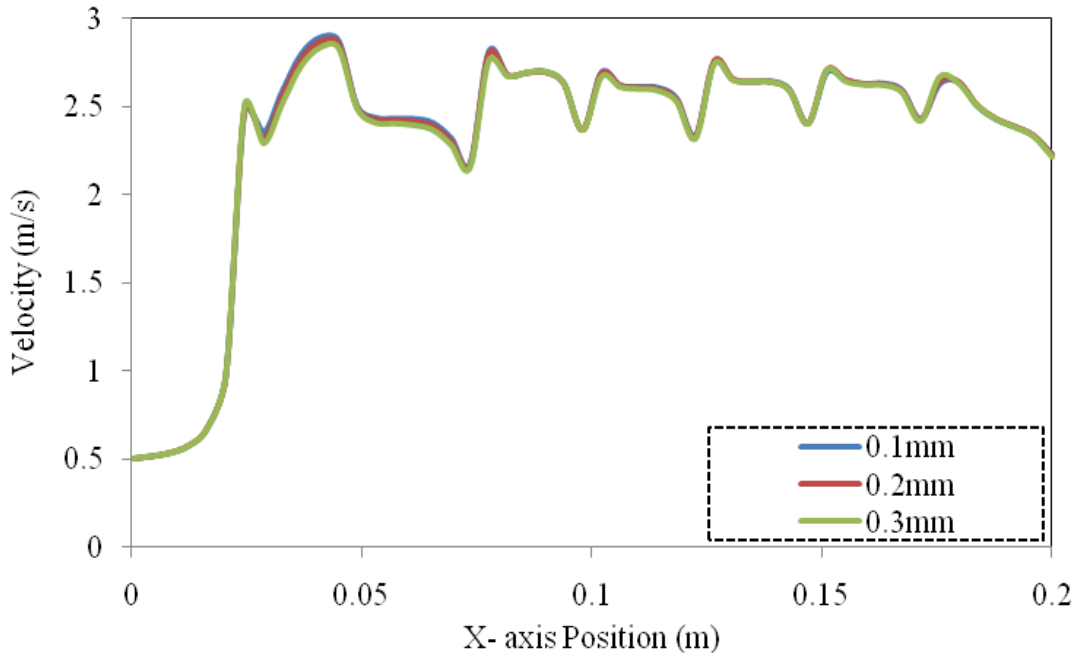

Figure 6.2 Influence of mesh size on the velocity at 2mm inside from the catalyst coated layer.

The three mesh sizes that were tested included a total of 34189, 54183,105637 quadrilateral cells respectively. A negligible difference was observed among the velocity profiles obtained by the grids used. Additionally, the simulated hydrodynamic parameters were found to be consistent across the mesh sizes tested. Thus the remaining simulations were performed with a mesh having a maximum element size of 0.1mm.

6.7 Results and Discussion

6.7.1 Influence of Top Baffle Height on Flow Field

Improving the efficiency of the reactor using static devices is a cost-effective approach for water treatment. Numerous attempts have been made to improve the flow conditions using two approaches: manipulating the inlet structure, and installation of solid or perforated walls or baffles in the reactor. Without any mechanical parts, the construction of baffled channels in water treatment plants is considered to be more reliable and economical and requires less maintenance. A number of investigations have indicated that the use of baffles in a reactor will improve the performance of mass transfer resistance by improving mixing when the catalyst is immobilized in a reactor (Sengupta *et al*., 2001; Mehrotra and Ray, 2003; Duran *et al*., 2010a). As the flow pattern in a reactor depends on the position of the inlet, the medium and outlet baffles, the optimization of baffle height and position is important for the improved hydrodynamic performance of the reactor. In order to identify the optimal height and positions, several test runs using a set of baffles have been conducted at various locations. The simulated baffle height was assumed to be 20%, 33%, 50% and 67% of the reactor height (H) and its effect on the flow field was examined by positioning them at 0.125L, 0.25L, 0.375L, 0.5L, 0.625L, 0.75L and 0.875L respectively. Figure 6.3 shows the local stream lines obtained using various baffle heights. From this figure, it can be seen that a recirculation zone is formed at the inter-baffle region for each baffle position and the size of the dead zones appears to be diminished as the height of the baffle decreases. As the existence of the recirculation zone and its extent in a reactor is coupled with the baffle height and location, optimal design of the baffle should be based on the above effects to minimize the formation of circulation zones and to ensure uniform flow structure. In this regard, choosing the optimum number of baffles is one of the practical aspects to avoid the formation of dead zones within a reactor. This observation is discussed in subsequent sections.

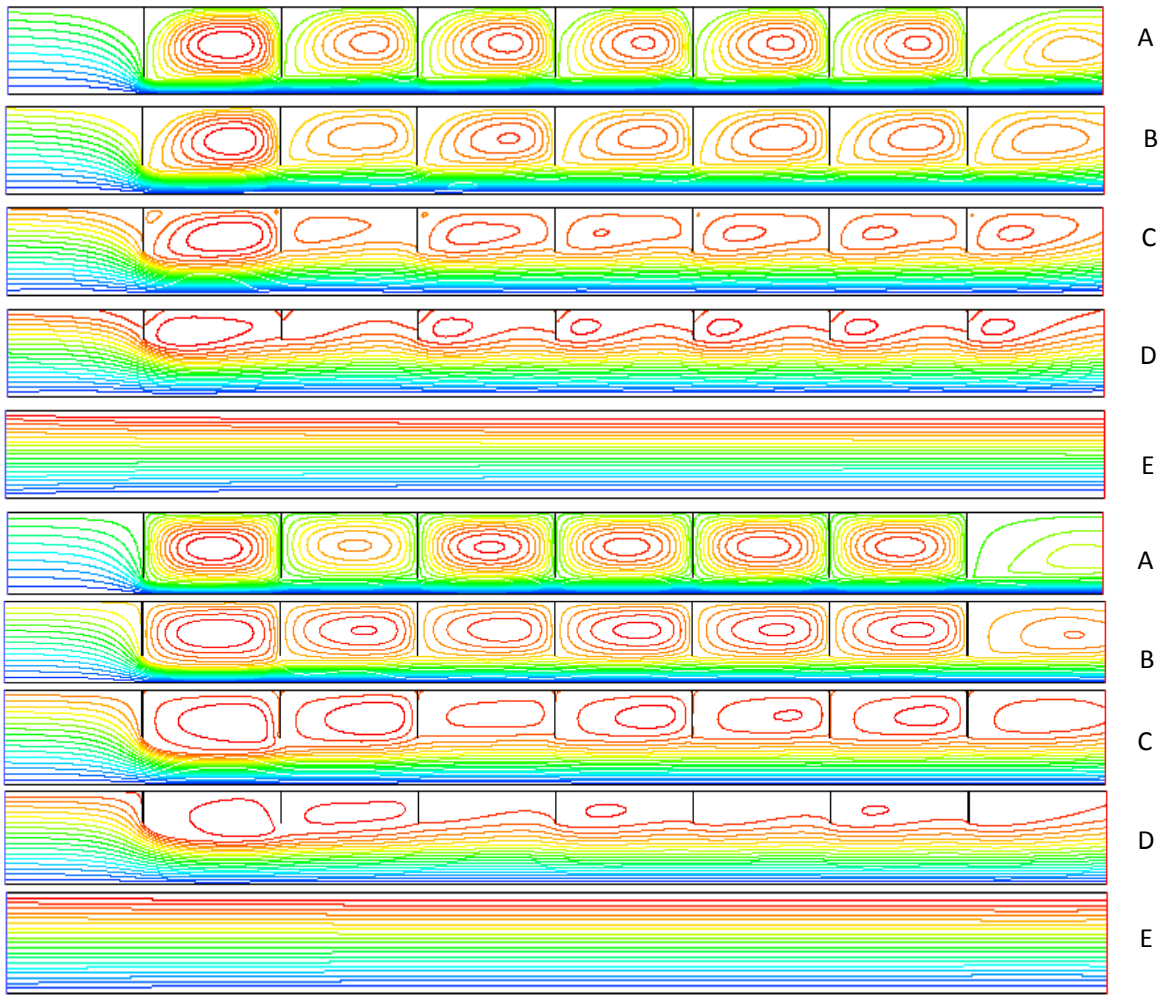

Figure 6.3 Effect of top baffle height on local stream functions with an inlet velocity of 0.15m/s (top figure) and 0.5m/s (bottom figure) for A) 12mm, B) 10mm, C) 7.5mm, D) 5mm baffle and E) plain reactor respectively.

In order to gain an insight to the flow field of the reactive section, simulations have been performed using the baffles having the stated five heights at six different positions for an inlet velocity of 0.5 m/s (*Re*=7500) and 0.15m/s (*Re*=2150). Figure 6.4 shows the contours of velocity field over the reactive length for the set of baffles positioned at 0.125L, 0.25L, 0.375L, 0.5L, 0.625L, 0.75L and 0.875L respectively. It indicates that the common features are the core flow regions and the recirculation regions. When flow is under the baffle, the fluid passes from the upstream to the reactor bottom and approaches into the constricted section to produce a strong shear layer at the baffle tip. For all the baffles simulated, the magnitude of maximum wall velocities varies considerably depending on the liquid height.

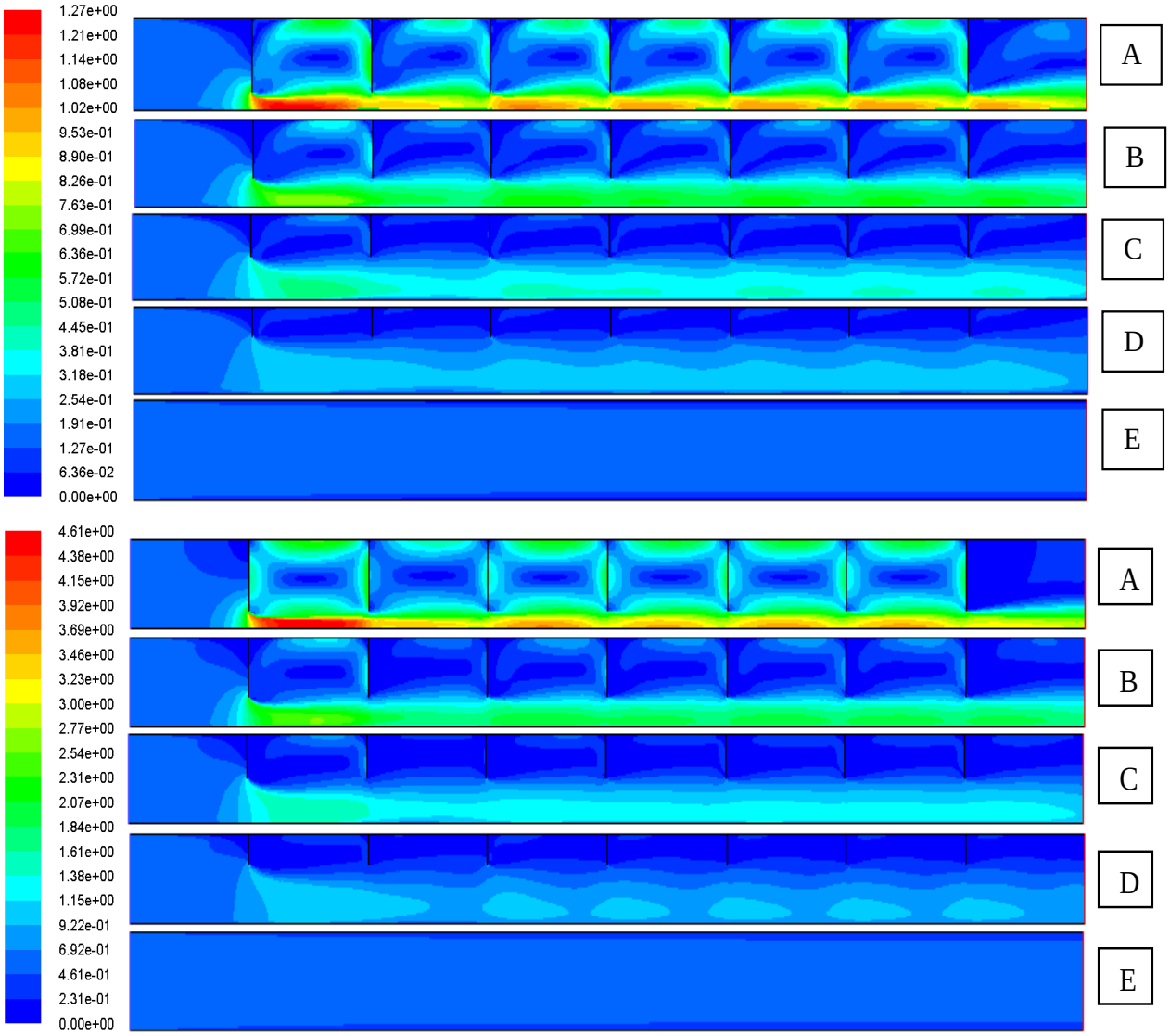

Figure 6.4 Effect of top baffle height on velocity contours (ms^{-1}) with an inlet velocity of 0.15m/s (top figure) and 0.5m/s (bottom figure) for A) 12mm, B) 10mm, C) 7.5mm, D) 5mm baffle and E) plain reactor respectively.

For the 12mm baffle height, the highest velocity magnitude appears to be around 4.61 m/s which was observed at 0.02m to 0.04m from the inlet position. This might be associated with the reduction in cross sectional area and an increase in the kinetic energy of fluid. In contrast a low velocity region can be seen to persist for all cases at the inter baffle regions and upstream and downstream of the first and last baffle respectively. This flow behaviour seems to prevail until the reattachment point which can be attributed to the occurrence of flow reversal. The spanning of recirculation increases the degree of interfacial distortion with a larger interfacial area between fluids which can result in substantial improvement in fluid

mixing. A velocity region with a magnitude of 0.465 m/s seems to present between the above stated regions. Unfortunately, no measured data are currently available to verify the predicted results. However, the overall prediction of velocity vector fields is as good as can be expected. Similar observations have been made for the baffles measuring 10mm, 7.5mm, and 5mm height respectively.

6.7.2 Influence of Top Baffle Height on Turbulence Characteristics

The contour plots of turbulent kinetic energy (TKE) and turbulent energy dissipation rate for different baffle heights (12mm, 10mm, 7.5mm, 5mm) and plain reactor respectively are displayed in Figure 6.5a, 6.5b and 6.6a, 6.6b for *Re*=7500 and 2150 respectively. For simulation, the baffles with variable heights were fixed at 0.125L, 0.25L, 0.375L, 0.5L, 0.625L, 0.75L and 0.875L from the inlet of the reactive section respectively. The highest value of TKE predicted by the RNG k-ε turbulence model can be seen on the inter-baffle region when the baffle height is 12mm. A large turbulent kinetic energy zone is also found for 10mm baffle height which spans a region close to the main flow and it yields a strong influence through turbulence intensity.

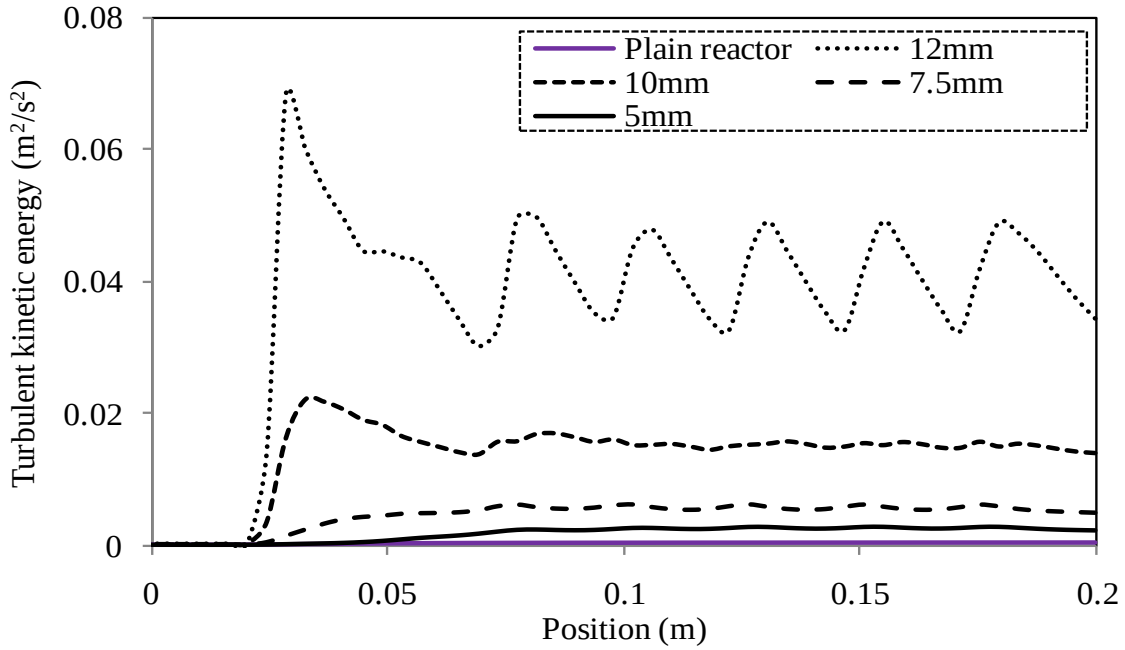

Figure 6.5a Effect of top baffle height on turbulent kinetic energy (m^2/s^2) distribution for *Re*=2150.

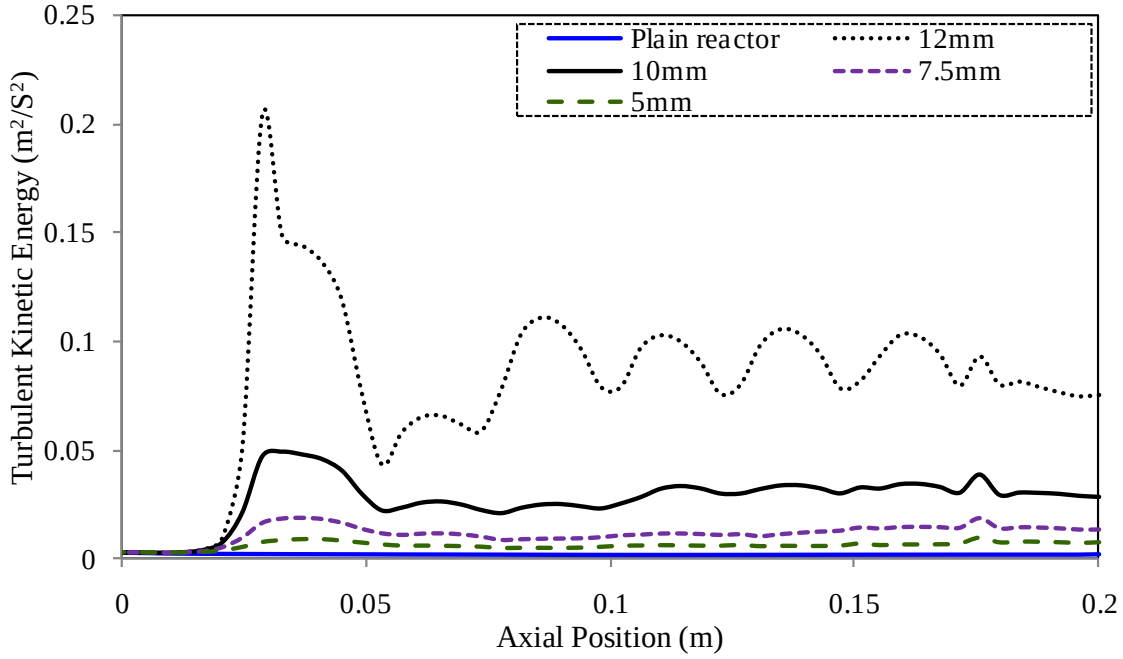

Figure 6.5b Effect of top baffle height on turbulent kinetic energy (m^2/s^2) distribution for *Re*=7500.

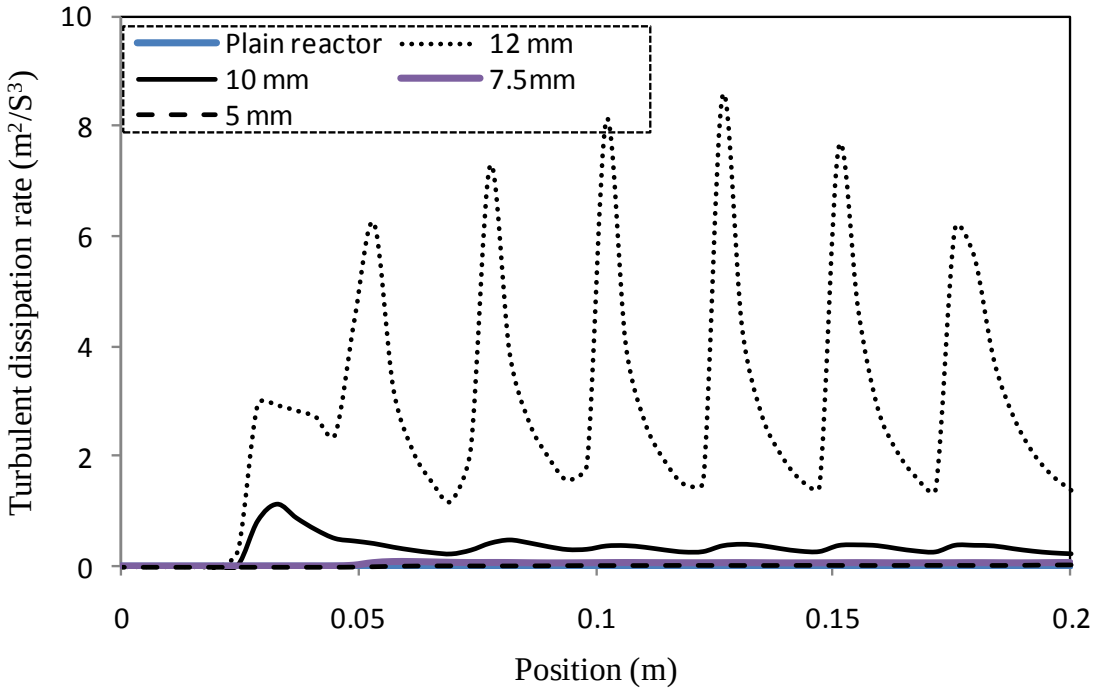

Figure 6.6a Effect of top baffle height on turbulent dissipation rate (m^2/s^3) distribution computed at *Re*=2150.

However, the turbulence intensity is observed to be very low at adjacent and downstream of the each baffle location in the reactive module. In contrast a turbulent kinetic energy zone having the lowest magnitude is predicted in the reactive module in the absence of baffles

which is indicated as plain reactor in Figures 6.5a and 6.5b respectively. At the same time, the turbulence dissipation rate was found to be higher for 12 mm top baffle. As expected the presence of an array of baffles in the reactor module causes frequent changes in flow direction and intense velocity fluctuations (data not shown). This phenomenon leads to high local flow turbulence and improves the fluid mixing thereby it will tend to enhance the mass transfer of pollutants from the bulk of the hydrodynamic solution to the catalyst surface.

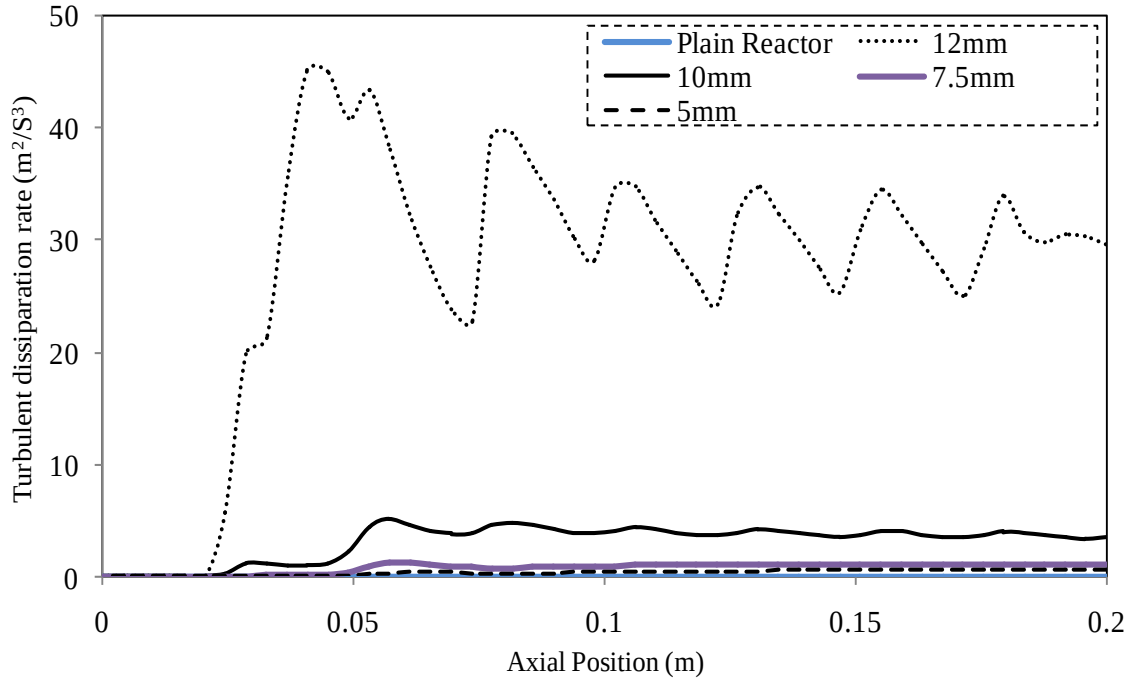

Figure 6.6b Effect of top baffle height on turbulent dissipation rate (m^2/s^3) distribution computed at *Re*=7500.

6.7.3 Influence of Top Baffle Height on Wall Shear on Catalyst Coated Surface

The presence of an array of baffles in the reactive section induces a rapid fluctuation of wall velocity on the catalyst surface which results in a fluctuation of wall shear stress. Generally, the highest value of local wall shear stress occurs in certain positions where velocity fluctuation is high. As illustrated in Figure 6.7, the fluctuation tendency of wall shear stress is similar to that observed for wall velocity (data not reported) for both *Re*=7500 and 2150. As a result, the trough and peak values of wall shear stress periodically appear in the positions where the corresponding values of wall velocity occur. The periodic peak and trough phenomenon was reported to cause a mass transfer enhancement on the permeable wall

surface (Cao *et al*., 2001). For the 12mm baffle height with 0.5m/s inlet velocity, the peak and trough values of wall shear stress were approximately 12 and 9 Pa, respectively, and with an average value of more than 10.5 Pa, which is much higher than that in a smooth reactor (about 0.25 Pa). In the case of 10mm baffle, the highest amount of wall shear stress was found to be around 6 Pa and the minimum amount of wall shear is observed to be 3 Pa.

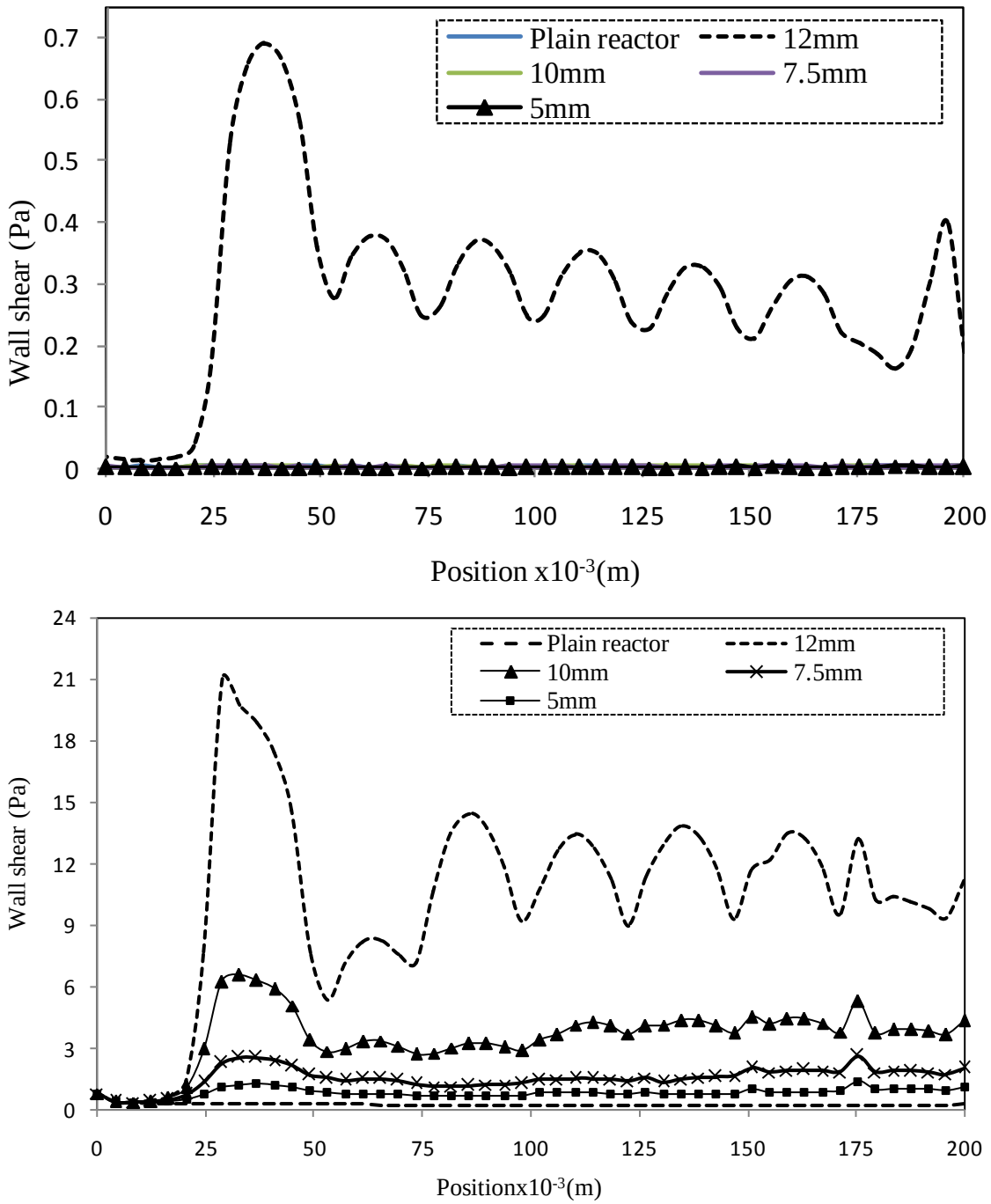

Figure 6.7 Effect of top baffle height on wall shear stress of catalyst coated layer for *Re*=2150 (top figure) and 7500 (bottom figure) respectively.

As to the 7.5mm baffle, the average value of wall shear stress is 2.0 Pa, which is also higher, compared to a plain section. In each case, the magnitude of wall shear stress was found to be smaller before the position of the first baffle. This could be associated with the variation in fluid flow cross-section. In contrast, the highest value of wall shear stress was found to be 0.7 Pa for an inlet velocity of 0.15m/s. No variation was observed for 10mm, 7.5mm and 5mm baffle height for 0.15m/s inlet velocity. There are two peaks of wall shear stress that spans from 25mm to 50mm in the reactive section for both flow conditions. This observation may be attributed to the higher wall velocities as can be seen in Figure 6.4. Higher wall shear stress was reported to significantly promote the back transfer of small solute away from the permeable wall surface to the bulk stream due to shear induced diffusion (Zydney and Colton, 1986). Consequently, for the baffled reactor, the thickness of the deposited layer formed by the degradation by-products of pollutants on the photocatalyst surface will be less than that in the case of a plain reactor which will likely to be more efficient for long-term reactor operation.

6.7.4 Influence of Top Baffle Height on Pressure drop across the Reactive Section

The amount of pressure drop along the reactive section obtained for various baffle heights is shown in Figures 6.8a and 6.8b. In the case of the baffled reactor, when fluid passes each baffle, it always undergoes a sudden drop of static pressure, which corresponds to the velocity fluctuation and eddy formation. The amount of pressure drop along the channel has been determined from the difference of static pressures between the inlet (x = 0 m) and the outlet (x = 0.2 m). Using an inlet velocity of 0.5 m/s and an outlet pressure of 50 KPa, the computed pressure drops along the channel are found to be approximately 10 KPa, 3KPa and 1 KPa and 0.5 KPa for baffles with 12mm, 10mm, 7.5mm and 5mm heights respectively. On the contrary, for an inlet velocity of 0.15 m/s and an outlet pressure of 50 KPa, the calculated pressure drops along the channel are determined to be approximately 1.75KPa, 0.5KPa and 0.2 KPa and 0.12 KPa for baffles with 12mm, 10mm, 7.5mm and 5mm heights respectively. Apparently, no pressure drop was observed in the absence of baffles as can be seen in Figures 6.8a and 6.8b. The larger pressure drop may lead to an increase in additional energy costs. The higher pressure drop along the reactive section containing baffles causes the frequent change in flow direction and intensifies velocity fluctuation, which will considerably increase the frictional loss of the fluid flow.

In addition, the eddy formed behind the baffles also results in an increased energy loss due to the simultaneous turbulent energy dissipation.

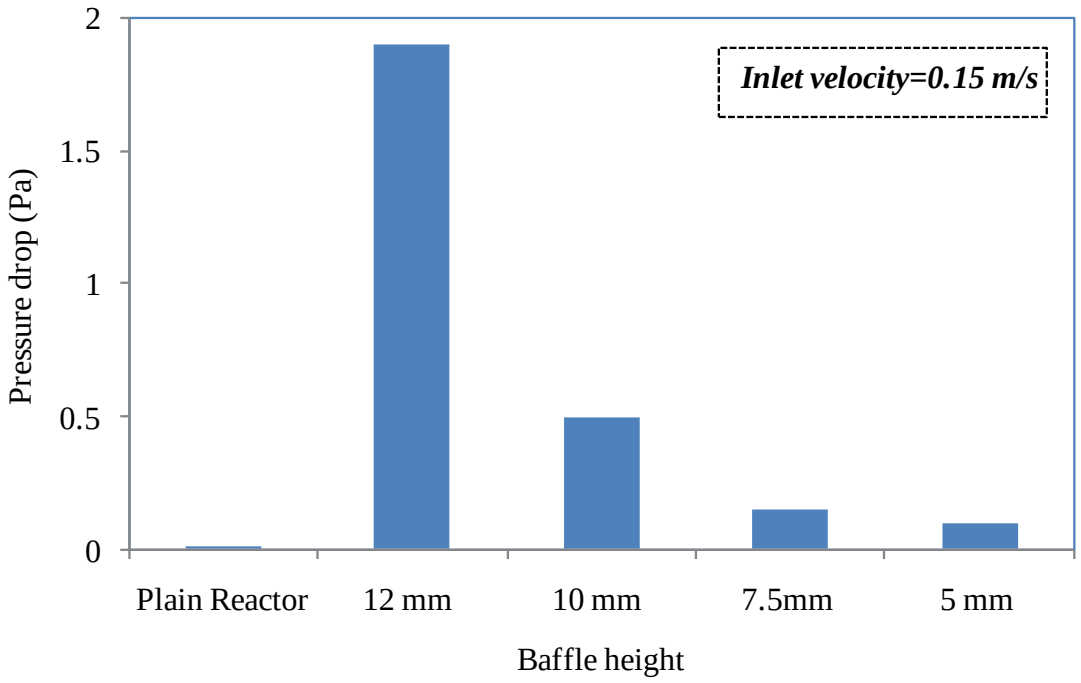

Figure 6.8a Effect of top baffle height on pressure drop for *Re*=2150.

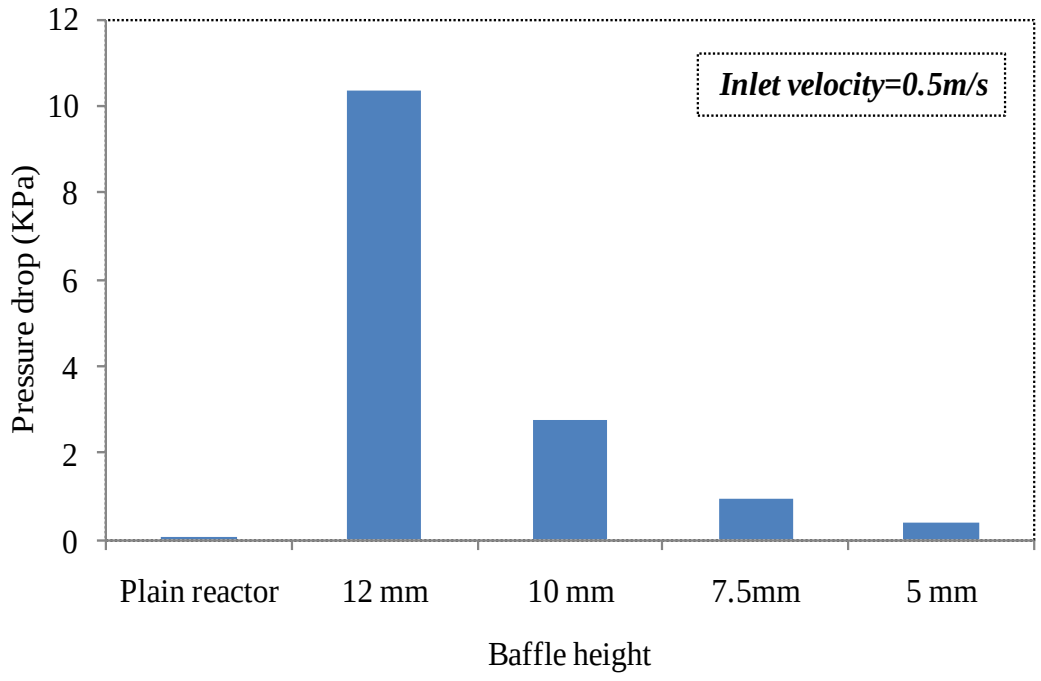

Figure 6.8b Effect of top baffle height on pressure drop for *Re*=7500.

6.7.5 Influence of Top Baffle Height on Mass Transport of Formic acid

Figure 6.9 shows the contours of the mass fraction of formic acid at the photocatalyst surface as computed using the RNG k-ε hydrodynamic model at Reynolds number 2150 and 7500 respectively. For *Re*=2150, it can be observed that the concentration of FA along the photocatalyst-coated surface decreases as it approaches the exit end for all the baffle heights studied. The FA concentration at the photocatalyst surface decreases significantly for the plain and 5mm reactive module. Two low concentration zones are formed at the end of 7.5mm and 12mm modules under the conditions simulated. Higher concentration of FA is present in the upper half region for 0.5L from the inlet of the reactive section. In these zones, higher concentration regions are found to be the consequence of higher fluid velocity gradients. This condition was verified by examining the velocity field in the reactive section.

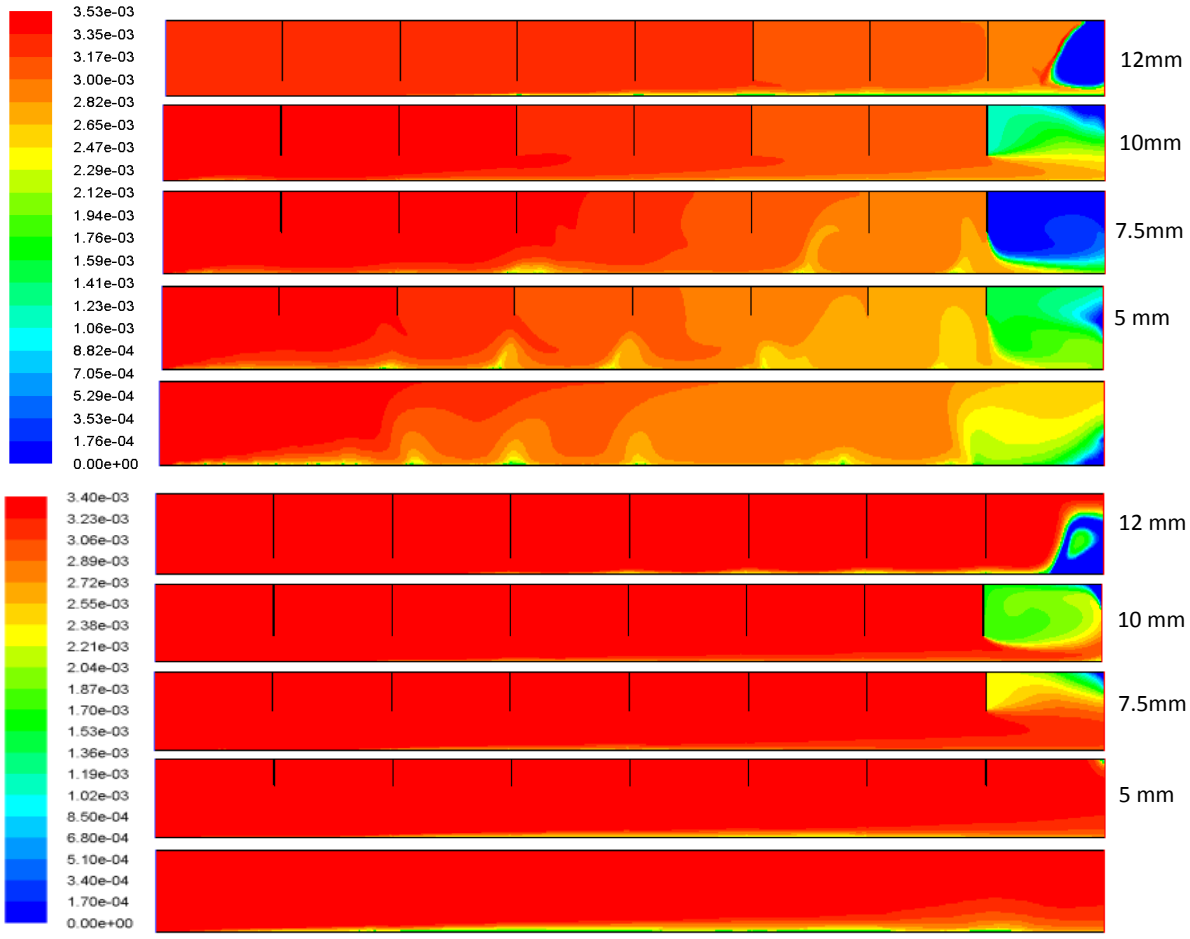

Figure 6.9 Contours of mass fraction of formic acid at the photocatalyst surface as computed at *Re*=2150 (top figure) and 7500 (bottom figure) respectively.

By analysing the velocity field in the system, it was observed that the recirculation zones that formed at the inter-baffle region induced high velocity gradient regions in the flow distribution. However, at *Re*=7500, two low concentration regions can be seen at the downstream of the end baffles for 12mm and 5mm baffles in the reactive module respectively. This observation can be associated with the formation of a low velocity zone. A strip of low concentration can also be observed at the bottom of the plain reactive module which can be attributed to the presence of low TKE. Comparatively the range of the low concentration zone is smaller at turbulent flow conditions than that in laminar flow conditions.

6.7.6 Influence of Top Baffle Spacing on Distribution of Wall Shear Stress on Catalyst Surface

The influence of baffle spacing was numerically studied by considering an identical baffle with 11.5 mm height for an inlet velocity of 0.5m/s. Figure 6.10 represents the effect of baffle spacing on the distribution of wall shear stress along the reactive module on the catalyst coated surface. Obviously, the baffle spacing markedly influences the wall shear stress distribution, since it determines the required number of baffles when the length of reactive section is constant.

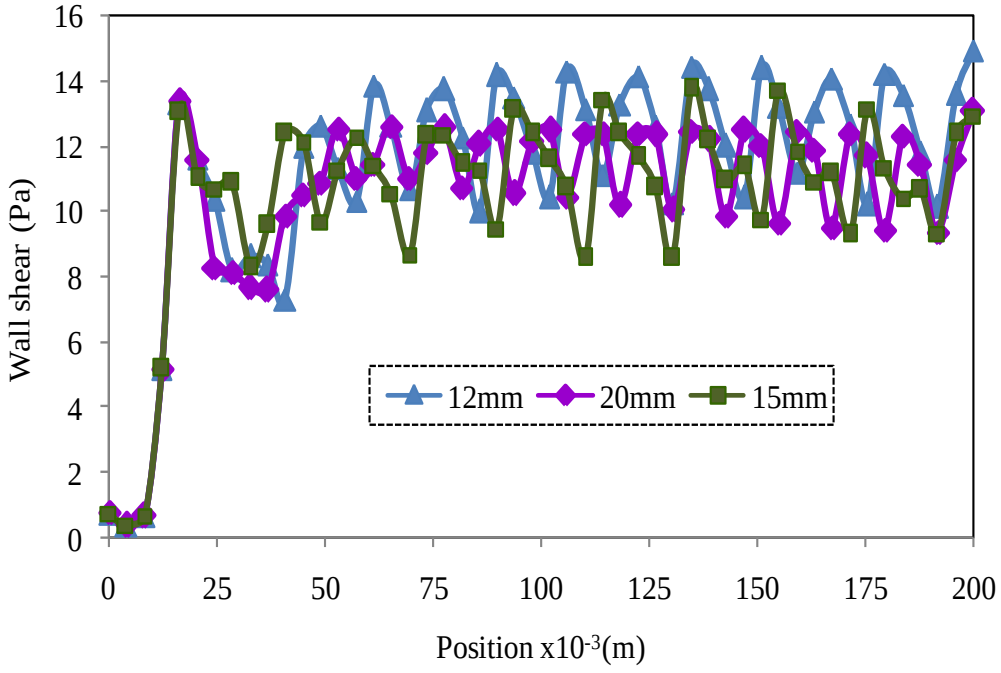

Figure 6.10 Effect of top baffle spacing on distribution of wall shear stress on catalyst surface.

For the reactive length of 200 mm, when the simulated baffle spacing was 12, 15 and 20 mm, the required numbers of baffles were 16, 13 and 10 respectively. Consequently the average values of wall shear stress for the corresponding three cases were found to be 12, 14 and 13.5 Pa respectively. It is evident from Figure 6.10 that the average value of wall shear stress decreases with the increase in baffle spacing, thus a similar trend is observed for the respective pressure drop. A summary of hydrodynamic parameters obtained with top baffles for various heights computed at *Re*=2150 and 7500 is presented in Table 6.1. The values of the parameters computed at *Re*=7500 was significantly higher than at *Re*=2150. No % loss of contact can be seen for both flow conditions.

Table 6.1

A summary of hydrodynamic parameters for top baffles with different heights.

Parameters		**Inlet velocity=0.15m/s (Re=2150)**				**Inlet velocity=0.5m/s (Re=7500)**			
		12mm	**10mm**	**7.5mm**	**5mm**	**12mm**	**10mm**	**7.5mm**	**5mm**
Pressure drop (KPa)		1.9	0.52	0.2	0.1	15.1	4	1.05	0.4
Turbulent kinetic energy (m^2/S^2)	*Max.*	6.8×10^{-2}	2.72×10^{-2}	0.019	7.47×10^{-3}	6.14×10^{-1}	0.23	0.121	7.87×10^{-2}
	Min.	3.01×10^{-10}	3.32×10^{-10}	1.87×10^{-11}	2.19×10^{-10}	8.24×10^{-10}	1.27×10^{-2}	3.75×10^{-9}	3.6×10^{-9}
Wall shear,τ_w (Pa)	*Max.*	0.7	2	1.5	1	22.5	6	3	1.5
	Min.	0.25	0.25	0.1	0.05	13	2	1.5	0.5
	Avg.	0.3	1	0.5	0.45	10	3.5	2	0.72
Turbulent dissipation rate (m^2/S^3)	*Max.*	3.0	2.77	0.783	0.21	7.0	3.5	5	2
	Min.	1.75	0.461	0.157	2.98×10^{-2}	1.75	0.75	0.45	0.25
% Contact loss		0	0	0	0	0	0	0	0

6.7.7 Influence of Bottom Baffle Position on Flow Field

Enhancing the efficiency of the reactor using non-mechanical devices is an economical approach for water treatment. Attempts have been made to improve flow conditions using two approaches: manipulating the inlet structure, and installation of solid or perforated walls or baffles in the reactor. The construction of baffled channels in water treatment plants with no mechanical parts is thought to be more reliable, requires less maintenance and minimizes

cost. Several investigations have indicated that the introduction of baffles in a reactor would improve the performance of mass transfer resistance by promoting mixing when a catalyst is used in an immobilized reactor (Periyathamby and Ray, 1999; Dutta and Ray, 2004; Sengupta *et al*., 2001). Since the performance of the reactor flow field depends on the location of the inlet, medium and outlet baffles, the determination of the optimal baffle position is crucial for the improved hydrodynamic performance of the reactor. In order to identify the optimal location, several numerical simulations have been conducted by placing a baffle with 5mm height at three different locations. The baffle height was considered to be 30% of the reactor depth (H) and its effect on the local stream lines was tested by positioning it at 0.125L, 0.25L, and 0.5L respectively. Figure 6.11 represents the stream lines pattern obtained with simulation for inlet velocities of 0.15m/s and 0.5m/s respectively. From this figure, it can be seen that a recirculation zone is formed at the downstream of each of the baffle location and the size of the recirculation zones appears to be sensitive to the position of the baffle and the inlet velocities of the reactor. For a given baffle position, the size of the re-circulation zone is larger at high Reynolds number flow compared with one that formed at low Reynolds number flow.

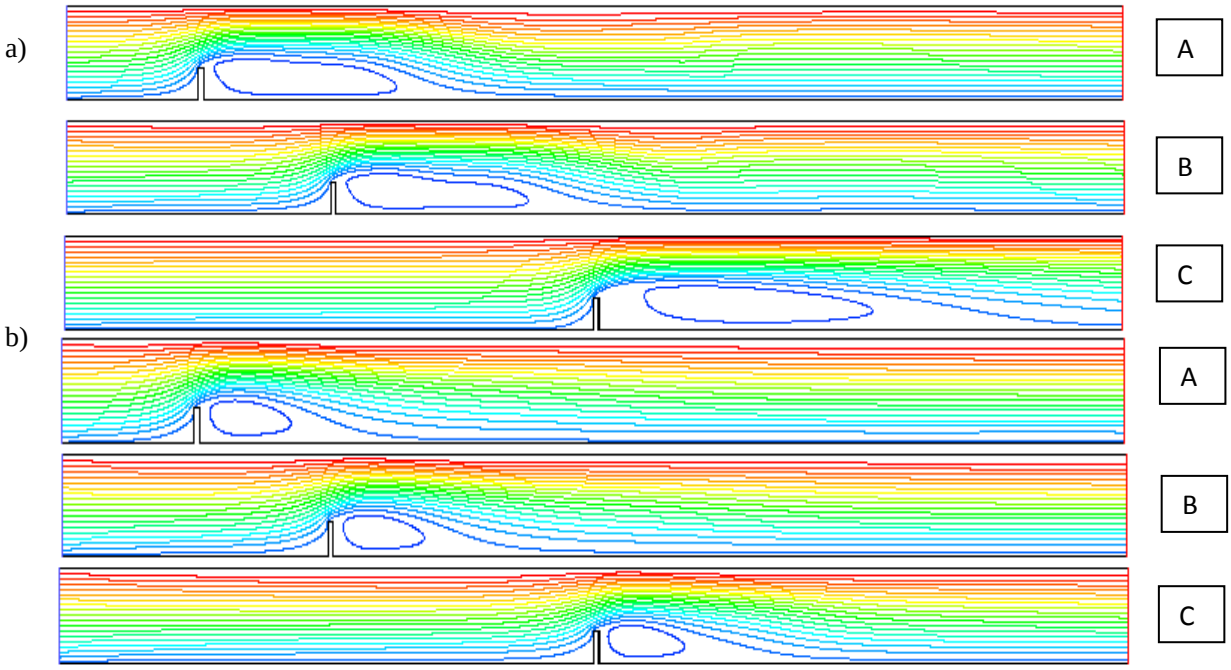

Figure 6.11 Effect of bottom baffle positions on local stream function contours computed at *Re*=7500 (a) and *Re*=2150 (b) for A) 0.125L B) 0.25L C) 0.5L respectively.

Because the presence of recirculation zone and its size in a reactor is related with the baffle height and location, optimal design of baffles should be undertaken to avoid the formation of circulation zones and to ensure uniform flow structure. In this regard, choosing the optimum number of baffles is one of the practical strategies to minimize the formation of dead zones within a reactor. This observation is discussed in the following sections. In order to gain an insight about the fluid flow structure of the reactive section, simulations have been carried out by placing a 0.17H mm baffle at three different locations for an inlet velocity of 0.5 m/s (*Re*=7500). Figure 6.12 shows the velocity profiles over the reactive length for the baffle positions at 0.125L, 0.25L and 0.5L respectively. It is seen that the common features of flow structure are the core flow regions and the recirculation regions. When the fluid particles flow over the baffle, the fluid movement from the upstream channel bottom wall into the contraction creates a strong shear layer at the baffle tip.

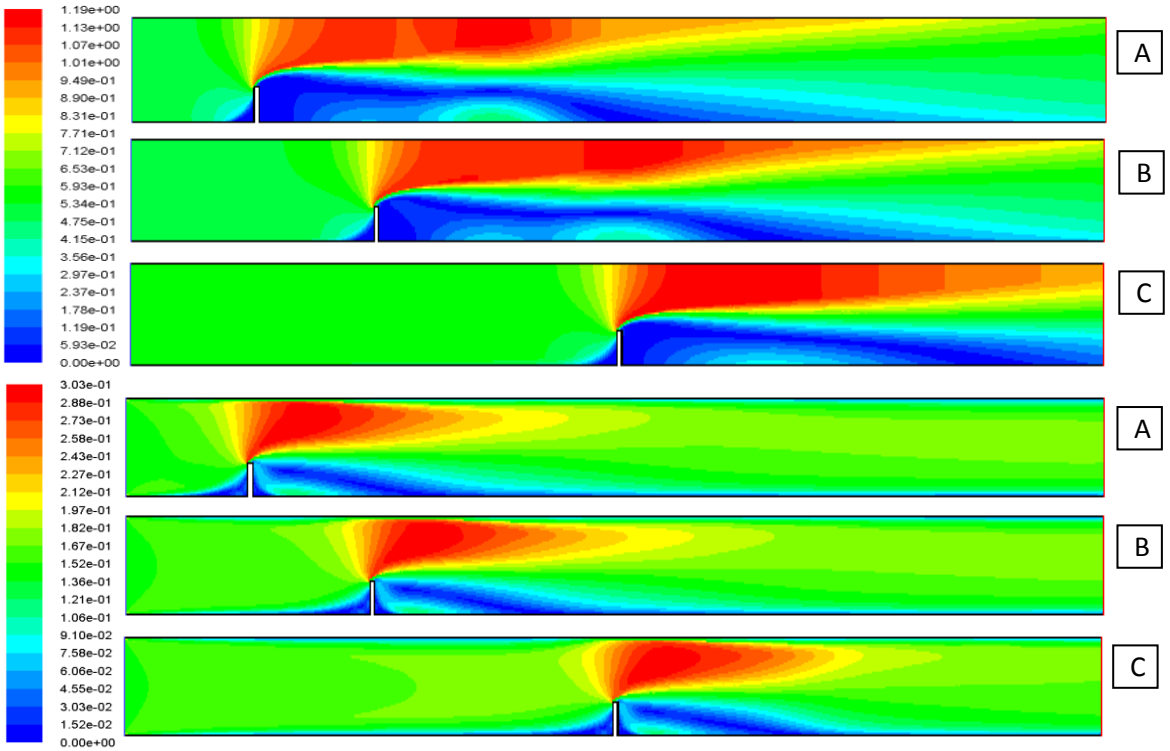

Figure 6.12 Velocity contours (ms^{-1}) for bottom baffle position at A) 0.125L B) 0.25L C) 0.5L for *Re*=7500 (top figure) and *Re*=2150 (bottom figure) respectively.

For the baffle at 0.125L, the maximum velocity magnitude appears to be around 1.19 m/s which was observed for a region at the top of the baffle. This might be coupled with the reduction in cross section area and an increase in the kinetic energy of fluid. In contrast a region of low velocity is also observed to persist at and adjacent to the downstream of the

baffle. This flow behaviour seems to prevail until the reattachment point which can be attributed to the occurrence of reverse flow. A velocity region with a magnitude of 0.566 m/s seems to exist between the above stated regions. Unfortunately, no measured data are available to verify the simulated results. However, the overall pattern of velocity vector fields are as good as can be expected. Similar observations have been made for the baffles positioned at 0.25L and 0.5L respectively.

6.7.8 Influence of Bottom Baffle Height on Flow Field

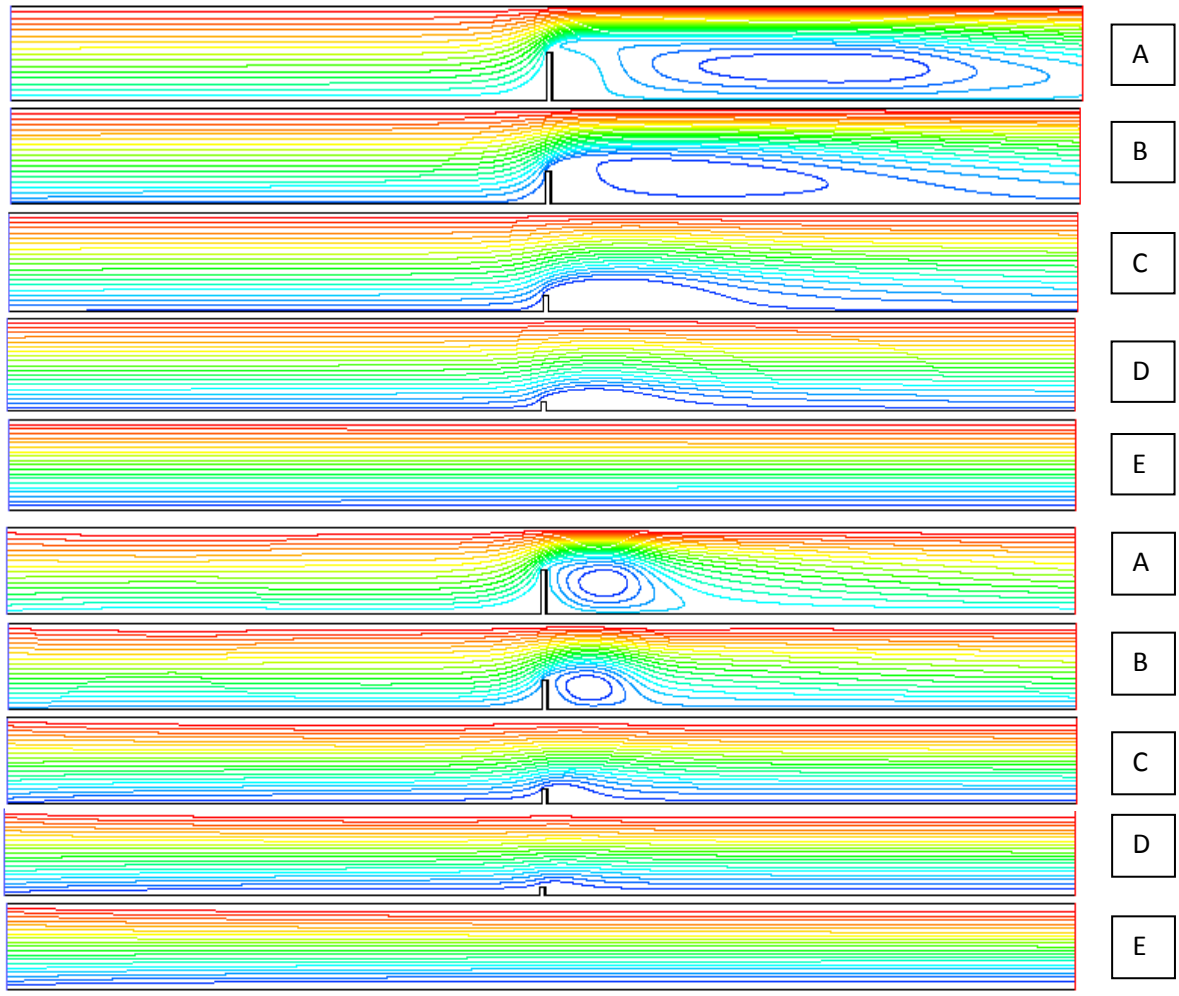

Figure 6.13 Effect of bottom baffle height A)7.5mm,B)5mm, C) 2.5mm, D) 1.5mm , E) Plain reactor on local stream functions for Reynolds number 7500 (top figure) and 2150 (bottom figure) respectively (baffle positioned at 0.5L from inlet).

The influence of baffle height on the local stream lines in reactive section are depicted in Figure 6.13 for a flow rate which corresponds to a Reynolds number of 7500. In simulation,

the position of the baffle is assumed to be fixed at 100 mm from the inlet and the baffle height was varied for a range from 1.5mm to 7.5mm. It can be seen that the extent of the recirculation region increases from 50mm to 100 mm as the baffle height increases from 1.5mm to 7.5mm.

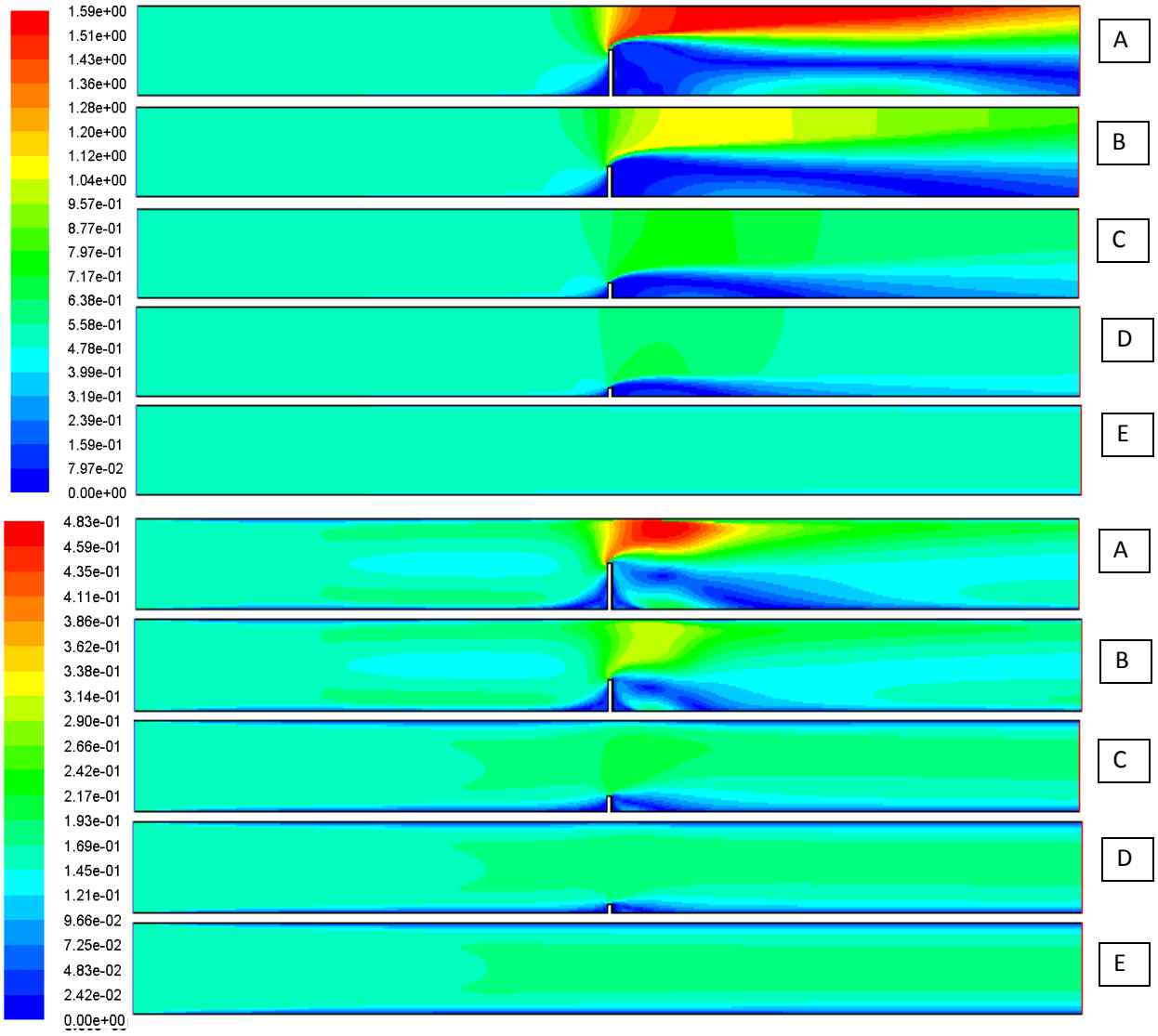

Figure 6.14 Effect of bottom baffle height A) 7.5mm, B) 5mm, C) 2.5mm, D) 1.5mm , E) Plain reactor on local velocity field (ms^{-1}) for Reynolds number 7500 (top) and 2150 (bottom) respectively (Baffle positioned at 0.5L from inlet).

As shown in Figure 6.14, the magnitude of highest velocity for the 7.5mm baffle height was determined to be 1.59m/s at Re=7500. Nonetheless, the amount of stream line distortion for lower Reynolds number flow was observed to be limited from 25mm to 45mm under the conditions simulated. At Re=2150, the computed maximum velocity was around 0.458 m/s

for 7.5mm baffle. For a given flow rate and location, it is well established that the friction factor will increase as the flow blockage ratio (baffle height to reactor height) increases in a flow channel. Higher magnitudes of velocity vectors are found to exist at the baffle tip for all tested baffle heights which could be associated with the smaller cross-sectional area at baffle top. Results reported here suggest that for a particular position, optimization of baffle height is essential to ensure a zone free from short-circuiting. In order to ensure adequate mixing in a reactor, optimum number of baffles should also be tested which will be discussed in the following section.

6.7.9 Influence of Bottom Baffle Aspect Ratios on Turbulent Kinetic Energy

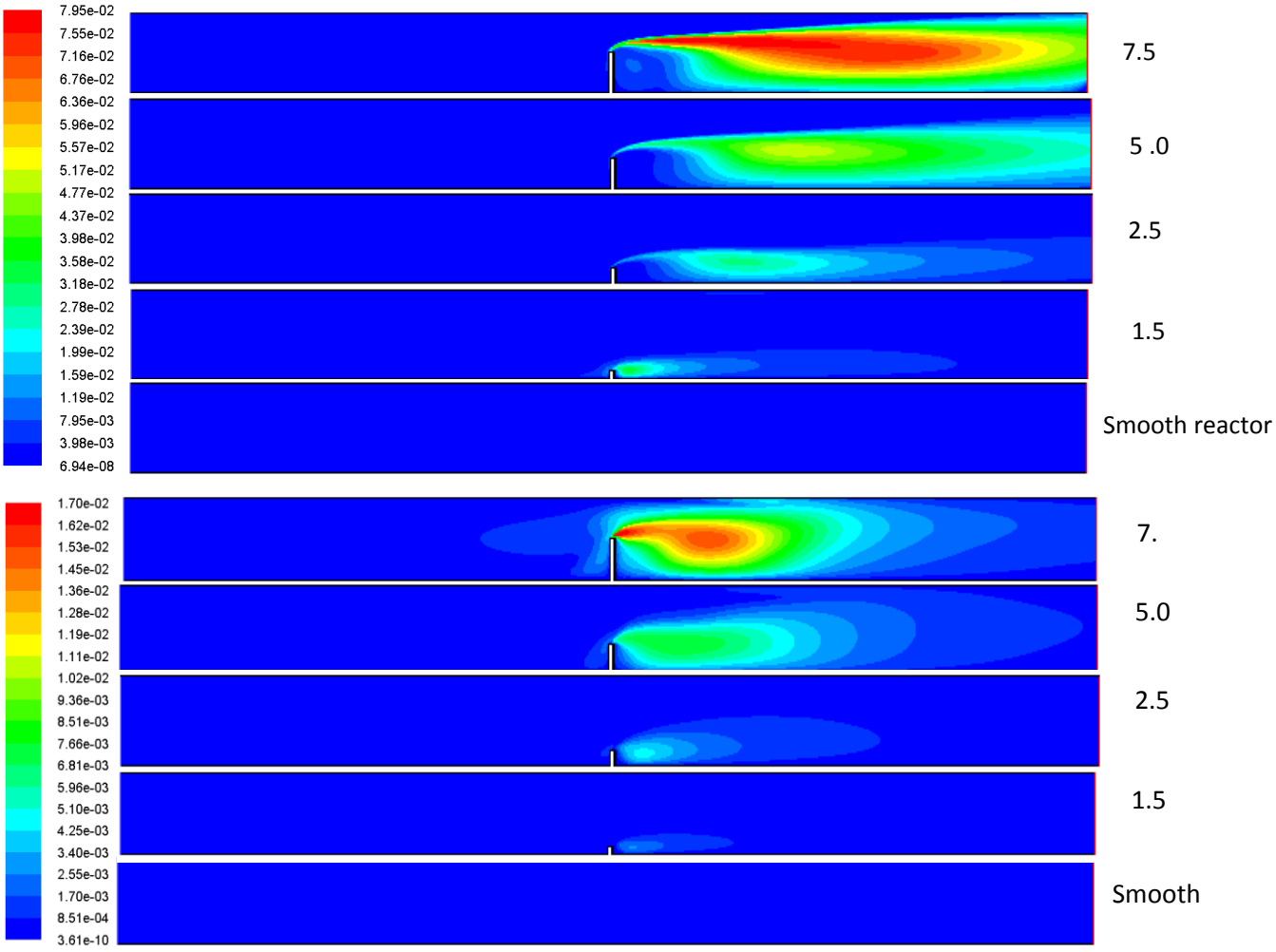

Figure 6.15 Effect of bottom baffle aspect ratios on turbulent kinetic energy (m^2/s^2) distribution for Reynolds number 7500 (top figure) and 2150 (bottom figure) respectively.

The contour plots of turbulent kinetic energy are displayed in Figure 6.15 for different aspect ratios of baffle. The baffles with an aspect ratio of 1.5, 2.5, 5, and 7.5 were fixed at the middle of the reactive module. The peak turbulent intensity values predicted by the RNG k-ε turbulence model are seen on the front region of baffles top. A large turbulent kinetic energy zone is found which is extended over a region close to the main flow and it yields a strong influence through turbulence intensity. However, the turbulent intensity is observed to be very low at adjacent and upstream of the baffle location in the reactive module. By contrast a turbulent kinetic energy zone with lower magnitude is predicted in the reactive module in the absence of baffles which is indicated as a plain reactor in the Figure 6.15. As expected the presence of baffles in the reactor module could enhance the fluid mixing phenomenon which in effect will improve the mass transfer of pollutants from the bulk of the reactive solution to the catalyst surface. The plain reactor exhibits a lower turbulent kinetic energy due to the fact that it does not generate turbulence and thus does not have the scouring effects as compared to the reactor with baffles.

Table 6.2

A Summary of hydrodynamic parameters for various bottom baffles located at 100mm from inlet.

Parameters		**Inlet velocity=0.15m/s (Re=2150)**				**Inlet velocity=0.5m/s (Re=7500)**			
		1.5mm	**2.5mm**	**5mm**	**7.5mm**	**1.5mm**	**2.5mm**	**5mm**	**7.5mm**
Pressure drop (KPa)		0	0	0.1	0.2	0.05	0.1	0.5	0.7
Turbulent kinetic energy (m^2/S^2)	*Max.*	4.25×10^{-3}	5.25×10^{-3}	5.96×10^{-3}	1.7×10^{-2}	1.99×10^{-2}	3.18×10^{-2}	4.51×10^{-2}	7.55×10^{-2}
	Min.	3.61×10^{-10}	8.5×10^{-4}	3.61×10^{-10}	8.51×10^{-4}	4.35×10^{-10}	6.94×10^{-8}	2.5×10^{-3}	6.94×10^{-8}
Wall shear, τ_w (Pa)	*Max.*	0.25	0.5	0.8	1.0	0.5	0.7	0.8	1.5
	Min.	0	0	0	0	0.1	0.1	0.15	0.25
	Avg.	0.15	0.25	0.4	0.55	0.3	0.4	0.6	0.75
Turbulent dissipation rate (m^2/S^3)	*Max.*	3.47×10^{-2}	9.1×10^{-2}	12×10^{-2}	1.1	1×10^{-2}	2×10^{-2}	3.0×10^{-2}	4×10^{-2}
	Min.	1.96×10^{-5}	6.51×10^{-3}	1.75×10^{-2}	6.1×10^{-2}	0	0	0	1×10^{-2}
% Contact loss		10	10	12.5	25	15	25	40	50

In contrast, the highest magnitude of turbulent kinetic energy was observed to be four times lower than that obtained with smaller fluid flow velocity. A summary of significant hydrodynamic parameters achieved with an inlet velocity of 0.15m/s and 0.5m/s for various bottom baffles is presented in Table 6.2.

6.7.10 Influence of Bottom Baffle Spacing on Flow of the Reactive Module

It was hypothesized that more than one baffle could improve the fluid mixing and mass transfer in the reactive module. As a result, additional simulations were carried out in the presence of multiple baffles for a variety of spacing (d). To ensure minimal recirculation size in the region adjacent to the baffle, the tested baffle heights were specified to be 10 and 17% of the reactor height respectively. Using the above mentioned baffles, the effect of baffle spacing on the flow field has been tested for the baffle intervals of 0.1L, 0.125L, 0.15L and 0.25L respectively. The results for multiple baffles simulation are presented in Figure 6.16. The distance between two successive baffles of 0.1H was selected so that they represent the positions in the wake of the first baffle. Interestingly, for the given shape, the second baffle did not increase in the magnitude of velocity very much especially when two successive baffles were located close to each other as indicated in Figure 6.17. It is evident from Figure 6.17 that the velocity contour field is markedly influenced by the baffle spacing under the simulated conditions since it determines the number of baffle required for a given length of the reactive section. It appears in particular that the size of the recirculation zone is related with the baffle intervals which will in turn enhance the fluid mixing and mass transfer through the formation of wall vortices. For a given baffle height, recirculation size was minimal when the baffle interval was fixed at 25mm over the length of the reactive section. In contrast, the range of the recirculation zone was observed to be smaller when the baffle height was set at 50mm. The spanning of recirculation enhances the amount of interfacial distortion with a larger interfacial area between bulk fluid and pollutants in the feed stream which results in substantial enhancement in fluid mixing. For the simulated entire length (L=200mm), when the baffle intervals were 0.1L, 0.125L, 0.15L and 0.25L, the required numbers of baffle were 9, 3, 3 and 2 respectively. It is apparent that the average value of wall shear stress will decrease with the increase of baffle spacing and hence the pressure drop (Ahmed *et al*., 2011c; Liu *et al*., 2009). In order to optimize the design of baffles in a reactive module, the height and spacing of baffles should be taken into account as the two important

parameters, because they can have a significant effect on the distribution of local wall shear stress and pressure drop.

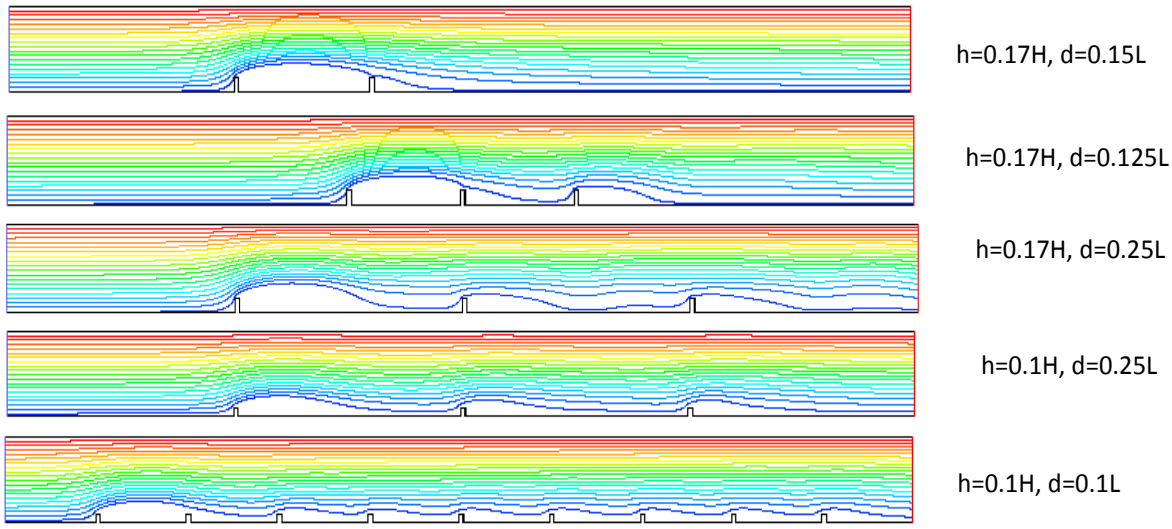

Figure 6.16 Effect of bottom baffle spacing on stream function for baffle height 0.17H (upper three) and 0.1H (lower two) respectively.

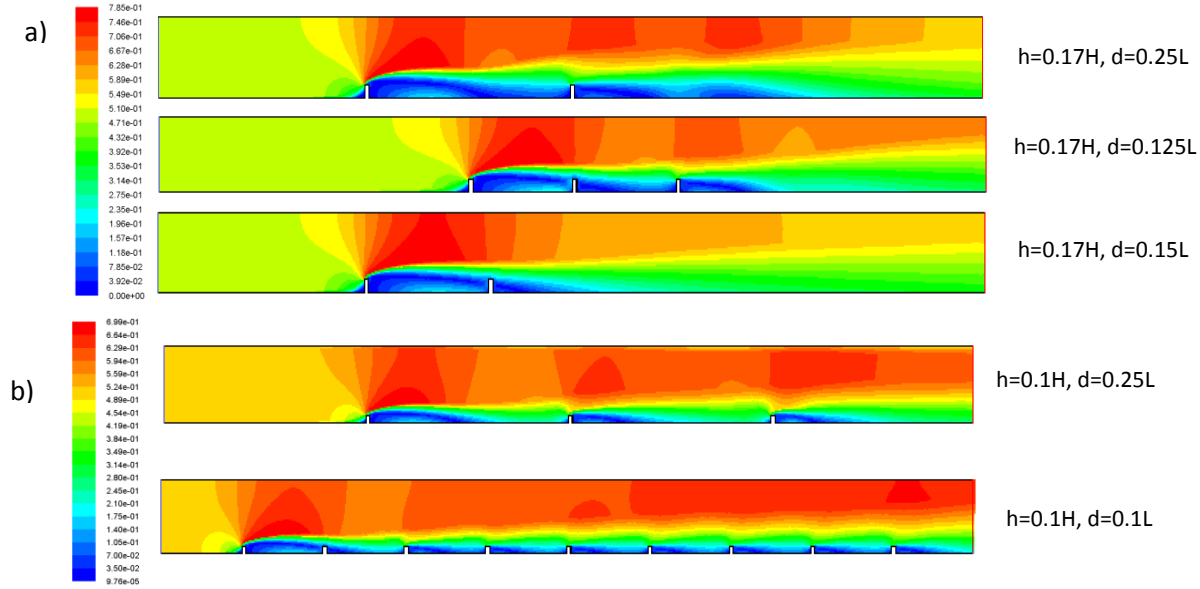

Figure 6.17 Effect of bottom baffle spacing on velocity (ms^{-1}) contours for baffle height a) 0.17H and b) 0.1H respectively.

The influence of baffle spacing on the hydrodynamic parameters was studied by varying the baffle spacing from 12mm to 20mm in the reactive section. The height of the baffle was set at 1.5mm which was fixed at the bottom wall. The simulation results obtained using various spacings is presented in Table 6.3. The calculated average wall velocities at 2.5 mm inside

the bottom wall are found to be 0.2m/s, 0.45m/s, and 0.5m/s for 20mm, 15mm and 12mm spacing respectively. It was found that the increment of turbulent kinetic energy and wall shear stress is linked with the decrease of baffle spacing, which is advantageous to improve the pollutant mass transfer in the reactive module. On the contrary, the increase in pressure drop can also be seen, which is related to the energy consumption. However, the amount of pressure drop was found to vary slightly over the spacing of baffle under the simulation conditions.

Table 6.3

Average values at distance 2.5 mm from bottom walls for different spacing of baffles inserted in the reactive section.

Spacing	Pressure drop (Pa)	Turbulent kinetic energy (m^2/S^2)	Wall shear (Pa)
12mm	300	3×10^{-2}	7
15mm	200	2×10^{-2}	5
20mm	100	7×10^{-3}	1

6.7.11 Influence of Bottom Baffle Height on Mass Transport of Formic Acid

Using an inlet velocity of 0.5m/s (*Re*=7500), the contours of the mass fraction of formic acid in the reactive zone as computed for various baffle heights that range from 1.5mm to 7.5mm are shown in Figure 6.18. The baffle is located at the place with a distance of 0.5L from the inlet. For the baffle heights studied, it can be observed that the concentration of FA along the photocatalyst-coated surface decreases as it approaches and passes the baffle for the given position. Under the conditions simulated, a low FA concentration zone seems to persist adjacent to the baffle in both the upstream and downstream respectively. However, the extent of the low concentration zone gradually disappears as the baffle height decreases from 7.5mm to 1.5mm. This observation can be attributed to the variations in velocity gradient and the formation of recirculation zones near the baffle with different heights. A close examination of the velocity field revealed that a strong recirculation zone with different sizes appears to persist downstream from the baffles which creates a higher velocity gradient in the flow distribution.

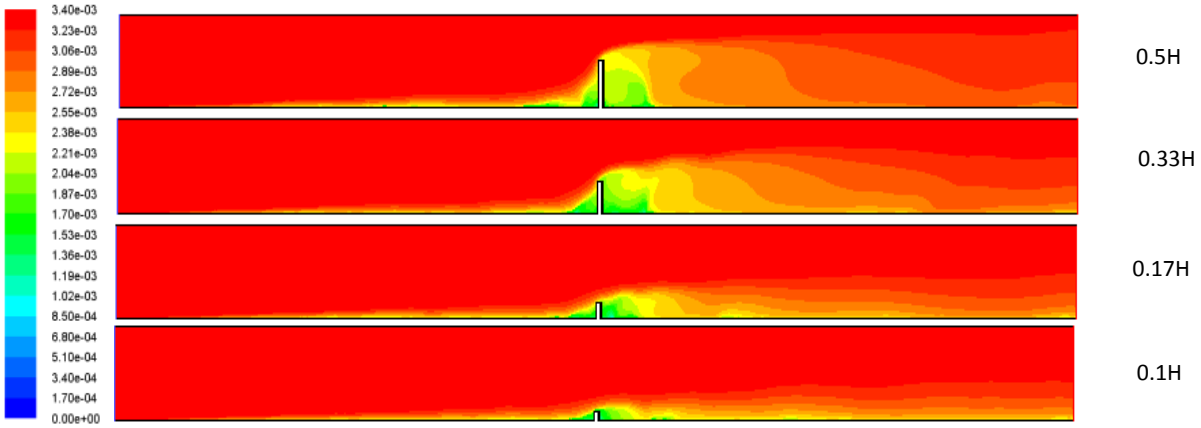

Figure 6.18 Contours of FA for different bottom baffle heights at 0.5L from inlet.

6.7.12 Influence of Bottom Baffle Location on Formic Acid Mass Transport

The reactive section featured with a baffle at different locations is modelled to investigate the effects of baffle location for *Re*=7500. The height of the baffle is assumed to be 0.33H. The baffle was positioned at 0.125L, 0.25L and 0.5L respectively. The contours of the FA concentration are shown in Figure 6.19. For all the cases simulated, the low FA concentration zone spans about 0.25L of the reactive length. The low FA concentration zone seems to present at and adjacent to each of the baffle positions. For all baffle positions studied, this observation was related to a recirculation zone next to the baffle positions which lead to a region with a high velocity gradient in the flow structure.

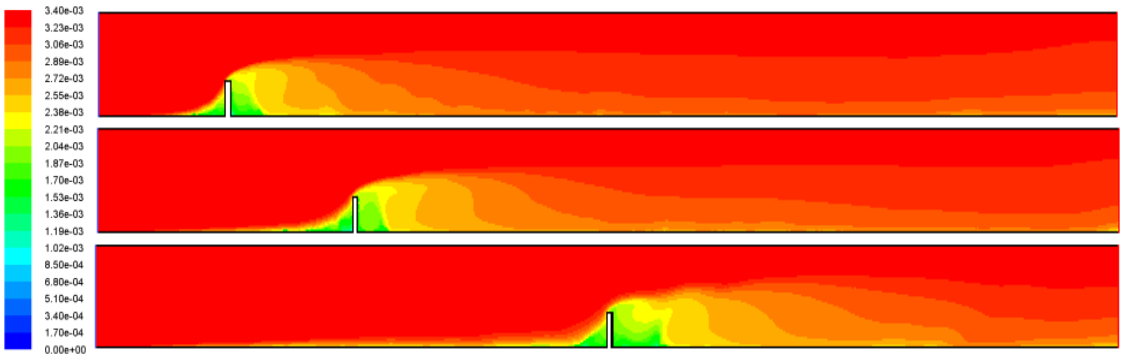

Figure 6.19 Contours of FA concentration for bottom baffle locations at a) 0.125L b) 0.25L c) 0.5L respectively.

6.7.13 Suitability of Baffles for Flat Plate Reactor Design

By examining the hydrodynamic parameters obtained with the top and bottom baffles, it is suggested that the top baffle with 12mm height can be a promising approach as turbulence promoters in the flat plate reactor. Because there is no contact loss of stream lines from the catalyst surface for the 12mm top baffle. Using this baffle, the highest level of turbulence was observed near the catalyst coated surface which is likely to benefit by minimizing the pollutant mass transport resistance and removing the degradation by-products from the catalyst coated surface. In contrast, the use of a bottom baffle in the reactive section causes a significant loss of streamlines contact which may limit the effective exposure of catalyst to the contaminated water stream.

6.8 Conclusion

In this chapter, the effect of baffle position and height on the flow and concentration field of a new flat plate photocatalytic reactor has been investigated using CFD simulation. For the simulation, the reactive section of the reactor was modelled with an array of top and bottom baffles. In order to optimize the fluid mixing and reactor design, the influence of top baffles with differing heights on the flow field of the reactive section has been determined. Under the conditions simulated, the hydrodynamically important flow features, such as the distribution of local stream lines, velocity contours, turbulence characteristics, wall shear stress, pressure drop and boundary layers separation, vortex formation, and the underlying mechanism are examined. At low and high *Re* numbers, the influence of baffle heights on the distribution of species mass fraction of a model pollutant are also investigated. The simulation of qualitative and quantitative properties of fluid dynamics in a baffled reactor provides valuable insight to understand the effect of top baffles on the flow pattern, behaviour, and features and their role on improving mixing in the reactive section of the flat plate reactor.

In case of the bottom baffle, the evaluation of simulation results has led to the following conclusions: (a) the separation and reattachment of boundary layer that occurs downstream of the baffle position in the reactive section, which relies on the height of the baffle and causes a recirculation region that spans approximately 50% of the catalyst coated area which could be unexposed to the contaminated water stream. (b) The presence of recirculation downstream of the baffle base may cause poor photocatalyst utilization and can result in high mass fluxes

of pollutant streams on the active catalyst surface caused by short contact times. This may limit the stable and continuous operation of the reactor where feed water pollutants remain unconverted or oxidized to intermediates which can be more toxic than their original forms in the feed stream. (c) To address these issues, further modifications of the reactive module are investigated in chapter seven by replacing the geometrical shape of the tested bottom baffle with other geometrical shapes such as a top baffle and roughness element to enhance mixing and mass transfer in the reactivemodule.

CHAPTER SEVEN

EFFECT OF COMBINED BAFFLE AND ROUGHNESS ELEMENTS

7.1 Introduction

The application of baffles in an immobilized photocatalytic reactor as a method to improve the fluid mixing and pollutant mass transfer on the TiO_2 coated layer has been suggested in numerous investigations. The presence of a baffle can effectively interrupt the hydrodynamic and concentration boundary layers by creating a recirculation zone or vortices in the flow field downstream of the baffle (Sripattanapipat *et al*., 2009). The flow reattachment behind the baffle can scouring of the catalyst surface and may result in an increase in the mass transfer rate. This method of mass transfer enhancement has been reported by several researchers for use in engineering applications such as chemical reactors in particular the immobilized photocatalytic reactor. Thus several investigations on this topic are documented in the current literature. While contaminant mass transfer is demonstrated to be increased using the mass transfer enhancement elements such as repeated ribs or delta wing mixer in an immobilized annular reactor, the pressure drop in the reactor was also increased due to the smaller cross sectional area for flow (Duran *et al*., 2011a). In their study, the benzoic acid degradation rate in the analyzed reactors was limited by the rate of mass transport in the system. Under the conditions tested, the performance of CFD model was largely determined by the external mass transfer prediction capability of the hydrodynamic models used. Their model was shown to predict the photocatalytic reactor performance when the laminar flow model, for laminar flow conditions, and the Abe-Kondoh-Nagano (AKN) or RSM turbulence models, for transitional and turbulent flow conditions, were applied. The integrated model provided detailed description of the local photoreactor performance and identified the areas where improvements can be made. In order to optimise the reactor design, the spacing and height of baffle are considered as the most important parameters used in the improvement of reactor design that contains baffles. In general, higher mass transfer rate can be achieved using smaller spacing or larger height which may result in non-uniform stream distribution and larger pressure drop. In contrast, larger baffle spacing or smaller baffle height can minimise the pressure drop by creating more longitudinal flow that may reduce the

contaminant mass transfer. As a result, the benefit of baffle application in the photocatalytic reactor is still not clearly understood for a given configuration. Alternatively, the role of combined baffle and roughness elements on the pollutant mass transfer and pressure drop in the photocatalytic system has received limited attention in the earlier studies. In addition, no detailed standard to determine the optimum baffle design is available in the current literature. From the analogy of heat transfer enhancement, the application of baffle height and spacing of 0.5 and 2 times the channel height respectively is studied in most of the previous works (Sripattanapipat *et al*., 2009). Several authors suggested that the use of internals such as baffles would promote the mass transfer resistance in an immobilised photocatalytic reactor (Kabir and Ray, 2003; Duran *et al*., 2009, 2010a). There have been no investigations documented in the open literature that have considered the mass transfer resistance under the influence of turbulence promoting solid baffles. As reported in the previous chapter the pressures drop significantly depends on the height of baffles in the reactor module. In general, the increase of turbulence using promoter/ baffle is associated with the resulting loss due to increased skin friction which can result in higher pressure drop. Since the increase in pressure drop is related to the high energy consumption, the minimization of pressure drop is of importance from the design and the operational points of view. In order to minimize the pressure drop across the reactive module, a number of hypotheses have been tested using the combined top baffle and roughness elements on the upper and lower wall respectively to investigate their role on the flow and mass transfer pattern while ensuring sufficient mixing to improve mass transfer. This arrangement is termed as combined reactor, which is designed to stretch and tilt the flow in order to intensively increase both the residence time and mixing efficiency of the reactive species in the reactor. In the present chapter, the numerical simulation obtained using low and high Reynolds number flows for an array of top baffles fitted on the upper walls and roughness elements on the bottom wall of the reactive section are performed to gain an insight on the observed flow pattern and mass transfer performance.

7.2 Geometry and Meshing

For simulation, the computational domain is considered to be a reactive section with a set of top baffles and roughness elements placed in a staggered arrangement on the upper and lower walls respectively as shown in Figure 7.1. The flow in the combined reactive module is expected to attain a helical flow condition where the velocity field repeats itself from one cell

to another. The fluid enters the reactive section with an inlet concentration, and flows over a staggered array of baffle-roughness elements. The reactive section was considered 15mm in height and 200mm in length where a set of top baffles with 10mm height and roughness with 1.5mm height were specified for simulation. The top baffles represented by a line diagram were placed at 0.2L, 0.4L, 0.6L and 0.8L positions along the reactive channel and the roughness elements were located at 0.1L, 0.3L, 0.5L, 0.7L and 0.9L on the bottom wall respectively. Gambits 2.2.30, a meshing tool was used to create the grid. Quadrilateral cells were used to discretize the entire domain of the reactive module filled with top baffle and roughness elements. For the catalyst coated bottom wall region, where the surface reaction can take place, a boundary-layer mesh was set up.

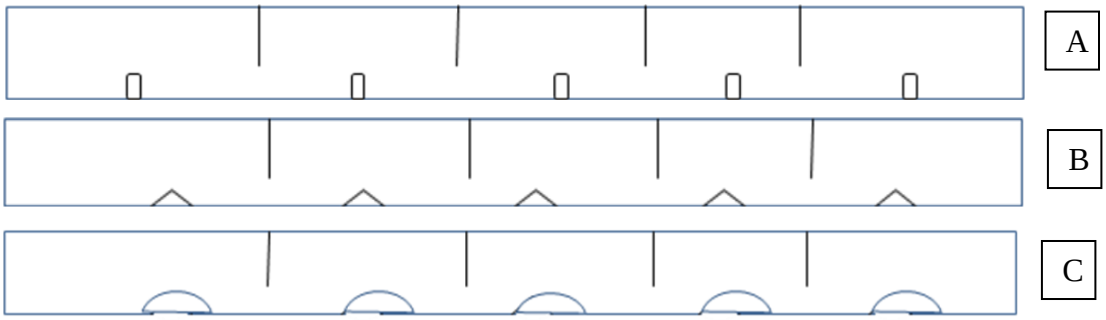

Figure 7.1 Schematic diagram of the reactive section equipped with baffle and roughness elements A) square B) triangle, and C) semi-circle.

7.3 Governing Equations

The following assumptions were made for the development of CFD model for fluid flow and FA mass transport in the reactive channel:

- Steady two-dimensional fluid flow and non-reactive
- The fluid is incompressible
- Constant fluid properties

Additionally, the fluid flow was assumed to be governed by the continuity, the Navier–Stokes equations. The time averaged governing flow equations were used to solve turbulent flow in the reactive domain containing baffle and roughness elements with the consideration of the species (FA) concentration variation. A convection-diffusion equation was included to account for the concentration field of FA under prevailing hydro-dynamics. The RNG k-ε model was applied to conduct CFD simulations with enhanced wall treatment (EWT) available in FLUENT software. EWT is a near-wall modelling method that combined a two-

layer model applicable in regions with fine near-wall meshes, with enhanced wall functions used in regions with coarse meshes (Fluent-Inc. 2006). In order to use enhanced wall treatment, it is thus essential to construct a proper fine mesh where the viscosity-affected near-wall region is required to be fully resolved (Fluent-Inc. 2006). Details on this method are described elsewhere in Fluent-Inc. 2006. It is also necessary to apply a mesh fine enough that allows solving the governing equations all the way to the wall, when modelling turbulent flow using either enhanced wall treatment or low Reynolds number turbulence model approaches. With respect to a previous study (Duran *et al*., 2010b), a y^+ smaller than 0.5 at the wall-adjacent cell, and at least 10 cells within the viscosity-affected near-wall region (Re_y =200) were defined in all the simulations conducted in this study.

7.4 Numerical Solution Method and Strategy

In order to visualize the flow conditions and species mass fraction, no-slip conditions on walls and baffles are used to perform the CFD simulation. For the solution of the governing equations, the segregated steady-state solver based on control volume technique was used. Second order upwind discretization scheme was employed with the exception of pressure for which PRESTO was chosen. The pressure-velocity coupling was resolved with SIMPLE algorithm. High convergence of the numerical simulation was ensured by monitoring the scaled residuals to a level of at least 10^{-4} for the continuity and momentum variables, and10^{-6} for concentration. In addition, the variation of velocity magnitude at one point of the computational domain located in an area of high velocity gradients was used as the indicator of convergence (Duran *et al.,* 2009; 2010a). Because of low FA concentration (mass fraction=0.0034), the presence of FA was assumed not to influence the flow field within the reactor, the solution of CFD model was thus broken down in two steps. The equations of continuity and conservation of momentum were solved first for obtaining the flow field across the computational domain. Then, the velocity field was kept constant and the equation of conservation of species was solved using the converged flows solution. The computation time was reduced by adopting this strategy which brings stability to the solution.

7.5 Results and Discussion

This section highlights the CFD simulation results obtained with an inlet velocity of 0.15m/s and 0.5m/s for the combined top baffle and roughness elements in the reactive section under

laminar and turbulent flow regimes. The fluid flow in an empty reactor without baffles and roughness elements was also simulated for comparison purpose.

7.5.1 Grid Independence

Since the accuracy of the numerical solutions largely depends on the number and size of the cells (Versteeg and Malalasekera, 1995), the grid dependency test was performed by varying the cell size inside the channel and by refining the grid size on the wall. In order to minimise the effect of mesh quality and size on the results, initial simulations were conducted with the gradual increase of resolution that gives constant results in velocity. The optimum simulation mesh size for different combinations of baffle and roughness elements was determined from the initial simulations. For the highest flow rate in the combined top baffle and square roughness element reactive section, the velocity profiles were simulated for three different mesh sizes to examine the mesh dependency: a coarse mesh consisting of 84,346 elements, a medium mesh consisting of 1,44,014 elements and a fine mesh consisting of 3,29,239 elements. With three mesh sizes, the velocity profiles at 2mm inside the bottom wall are shown in Figure 7.2. Nonetheless, they represent a close match for the tested three mesh sizes. Hence, the number quadrilateral elements for the combined channel was chosen to be 3,29,239 to obtain grid-independent results.

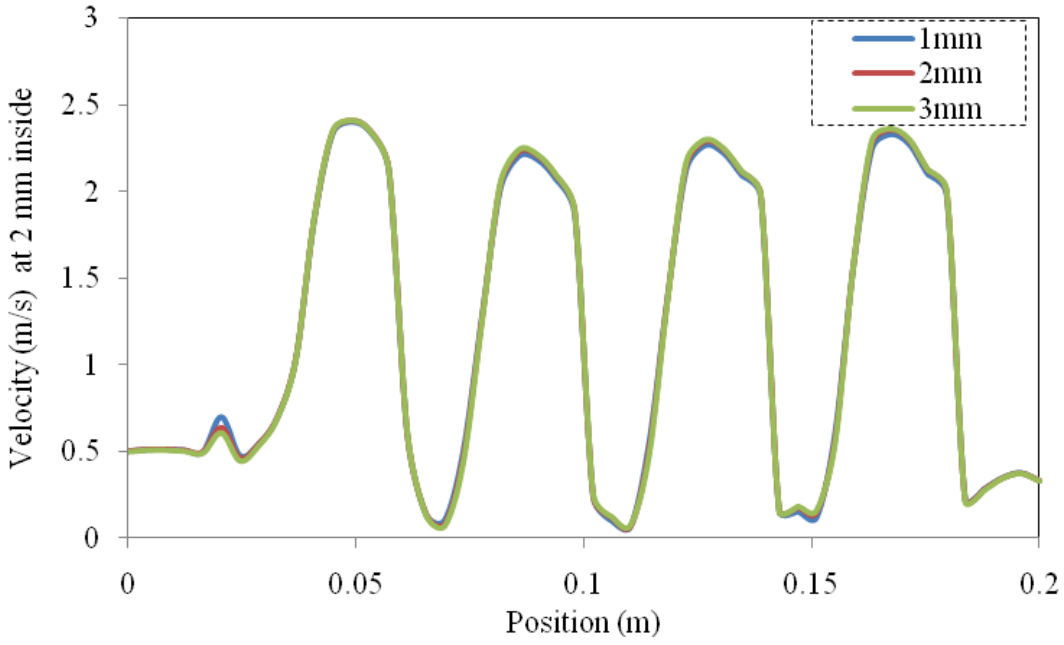

Figure 7.2 Influence of mesh size on the velocity at 2mm inside from the reactor bottom.

7.5.2 Local Stream Lines Contour

With an aim to ensure long-term stability in the reactor operation on sustainable basis, a number of hydrodynamic approaches using top baffle and various roughness elements for creating unsteady flows in the reactor have been tested for three different configurations in this section. In order to investigate the effect of bottom wall roughness on the flow field, three roughness elements, namely a square, a triangular and a semi-circular shape were chosen for simulation. Top baffles were positioned at 0.2L, 0.4L, 0.6L and 0.8L positions along the reactor top wall and the roughness elements were located at 0.1L, 0.3L, 0.5L, 0.7L and 0.9L respectively on the lower catalyst coated wall. The liquid opening at the baffle tip was 0.33H and the spacing was 0.2L. Figure 7.3 represents the influence of top baffles together with the square, triangular and semi-circular roughness elements on the local stream lines and velocity fields computed at *Re* = 2150 and 7500 respectively. The predicted flow pattern for different configurations appears to be similar except for flow areas near the roughness elements. As shown in Figure 7.3, the application of roughness elements on the catalyst coated layer clearly interrupts the local flow near the walls which results in a detachment tendency due to inertia.

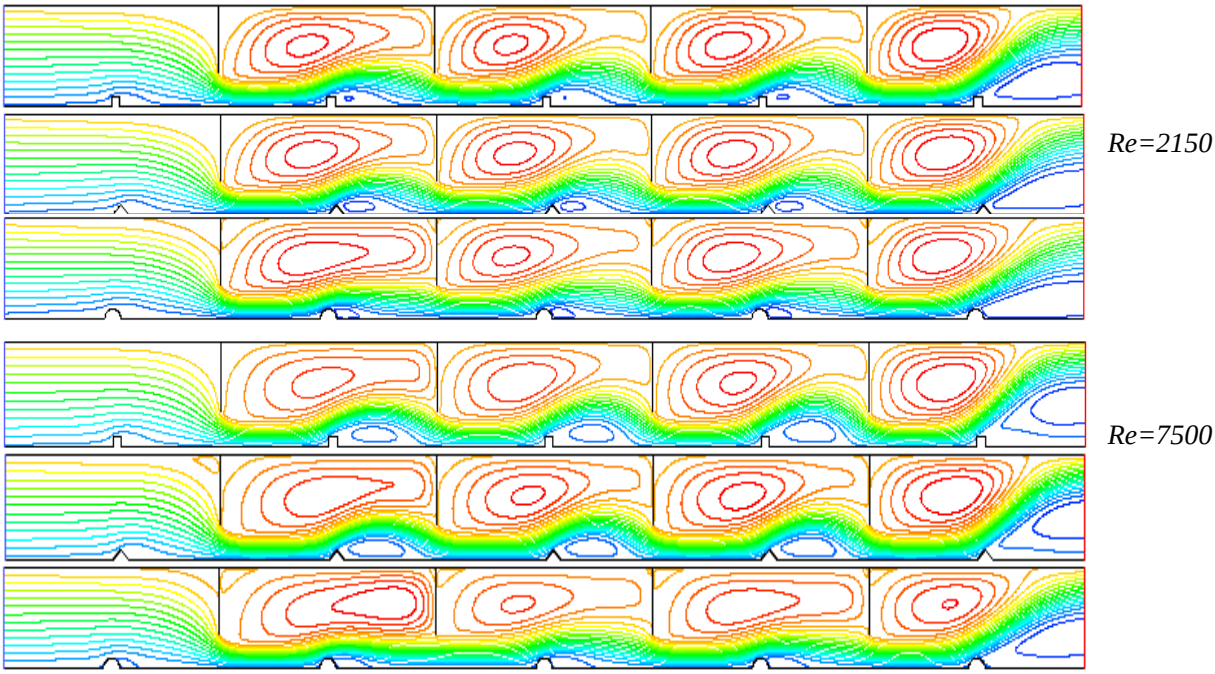

Figure 7.3 Contours of local stream lines obtained with combined top baffle and square, triangular, and semi-circular elements for *Re*=2150 (top) and 7500 (bottom) respectively.

When the fluid passes over the square, triangular and semicircular roughness elements, the flow over rough surfaces tends to induce recirculation at the shadow of the roughness elements. By examining the degree of stream lines distortion induced by the roughness elements, it is evident that the distortion zone caused by the semicircle roughness element is smaller than that of the triangular and square roughness elements at high Reynolds number. The regeneration of the boundary layer usually depends on the flow separation and recirculation due to the roughness elements (Zhang *et al*., 2010). The regeneration of the boundary layer is one of the dominant reasons for the enhancement of convective mass transfer, and the flow separation and recirculation can be associated with the increase in pressure drop. A large recirculation or a central vortex is seen to be formed at the top of the roughness elements for both low and high flow rates. The central recirculation zone tends to extend between the inter-baffle region regardless of the roughness elements. At low *R*e, the vortices formed behind the triangular and semi-circular roughness elements appear to be larger compared with that of the square element. However, the size of the vortex behind the semi-circular element is somewhat smaller than that formed with the square and triangular elements at high Reynolds number. The central recirculation zone thus formed between the top baffle results in the fluid to rotate with a strong motion which may cause the fluid near the wall and baffle to flow in the core region. It is observed that the largest vortex is just about located at mid positions between the successive top baffles. The size of the central recirculation zone is found to be larger compared with the ones that formed in square and triangular roughness elements at the corner. It is generalised that the presence of the baffle leads to a longer flow path with a strong central vortex due to the change in its orientation.

7.5.3 Influence of Combined Top Baffle and Roughness Elements on the Velocity Field

With the same boundary condition (inlet flow rate and no-slip wall) and the same mesh size as empty and top baffle cases, the flows in the combined reactive module experience a series of different physical processes. Figure7.4 shows the contours of velocity magnitude along the reactive section at Reynolds numbers 2150 and 7500 respectively. The local velocity distribution near the bottom wall can provide some insight about the role of roughness elements on the fluid flow. At *Re*=2150, the low velocity region appears to occupy the most part of the reactive section. On the contrary, for *Re*=7500 a strip of low velocity region with a

magnitude of 0.15m/s to 0.27 m/s prevails downstream of the square and triangular elements whereas the extent of the low velocity region is smaller for the semi-circular element. At *Re* =7500, it can be seen that the distortion of streamlines over the square and triangular elements are higher compared with the semi-circular element. The effect of triangular roughness elements on pressure drop along the reactor bottom was observed to be similar to the square roughness elements, and their impact level is higher than the semicircular roughness element. The flow produced by this combined arrangement appears to be helical in pattern which flows along the channel and generates secondary flow to combat the formation of deposited layer immediately above the catalyst TiO_2 coated surface. This flow results in helical flow vortices which create fluid instabilities in the reactive medium and thus automatically scarps the surface of the photocatalyst. The vortices formed by the settings are expected to perform better by improving the mixing between the boundary layer and the bulk fluid to a larger extent than that occurs by simply using the reactor with and without roughness elements.

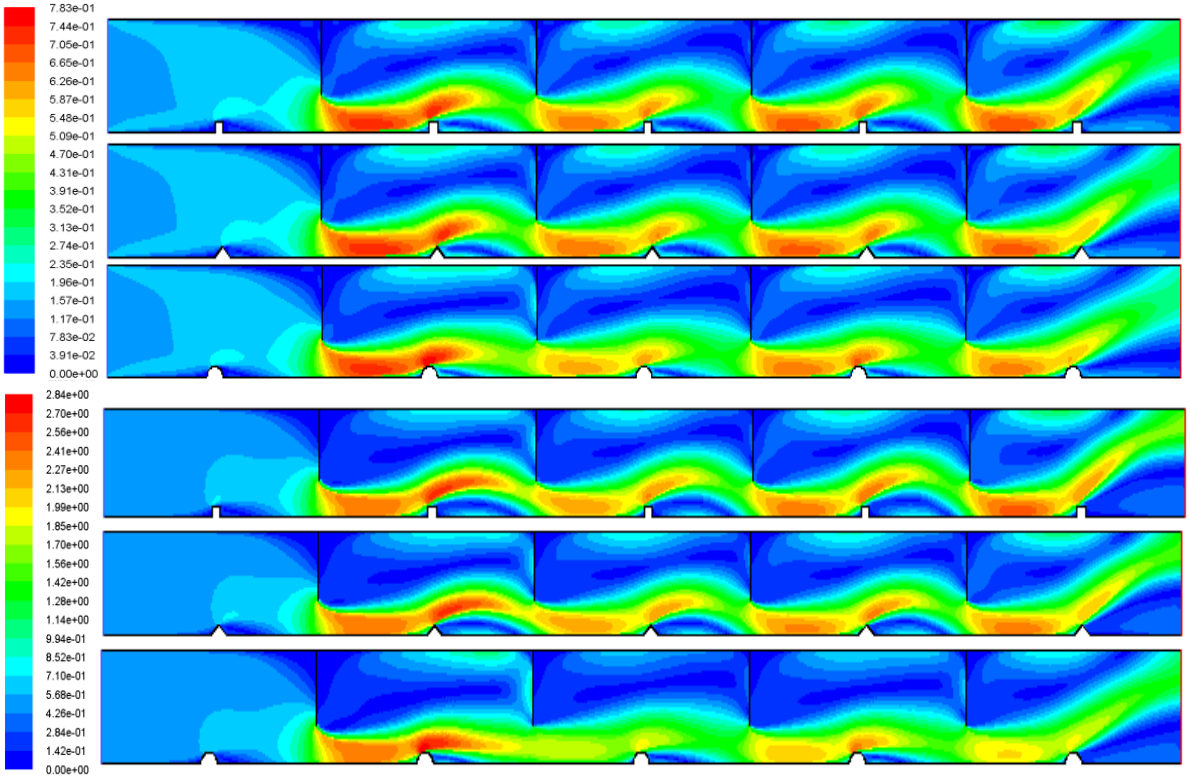

Figure 7.4 Contours of velocity field for *Re*=2150 (top) and 7500 (bottom) respectively.

The combined reactor will generate dispersion and spreading of mixed fluids that lead to more turbulent collisions, and lower pressure drops than that of the smooth and top baffle reactors. It can be seen that the flow varies throughout the reactive section for all the cases at

both *Re*= 2150 and 7500 respectively. Under the conditions examined, the magnitudes of highest velocity appear to persist at the channel bottom for all configurations. In contrast velocities with lower magnitudes prevail in the inter-baffle regions in the upper portion of the reactive section. The laminar flow was observed to become entirely unstable at the higher Reynolds number (Jarandehei and Visscher, 2009) and the threshold of instability would be the flow condition in which *Re* is around 2150. In general as the flow passes the sharp turns, a secondary flow which is transverse to the primary flow is created (Jarandehei and Visscher, 2009). As a result the presence of the top baffles and roughness elements in the reactive section can lead to the formation of vortices. This makes the mean flow velocity comparatively low, and thus, contributes to enlarging the residence time of the flow, in the reactive channels. This periodical back flow results in a pressure gradient opposite to the flow, which might be related to the lower pressure drop across the combined reactor compared with the top baffle and plain reactor.

7.5.4 Influence of Combined Top Baffle and Roughness Elements on Turbulence Kinetic Energy Distribution

The existence of an array of baffles and roughness elements in the flow channel causes the frequent change in flow direction and the rapid velocity fluctuation, which causes high local flow turbulence. The distributions of turbulence kinetic energy (TKE) along the reactive length are shown in Figure 7.5. It can be observed that the magnitude of TKE is lower at the upstream of the first top baffle position than in the remaining area for both low and high Reynolds numbers. A strip of low TKE zone is seen to exist downstream of each top baffle position regardless of the fluid flow rate across the combined reactive module. At low Reynolds number flow rate, the higher values of TKE occur at the right side of the roughness element top for all the cases investigated. In contrast to the smooth reactive section, the use of combined baffle and roughness elements in the reactive section creates higher turbulence kinetic energy, which indicates that the fluid flow in the combined baffled reactive channel is completely turbulent. The fluid motion remains highly turbulent in the entire channel, which can disrupt the concentration boundary layer to a large extent and minimize the deposition of pollutant and its degradation products on the catalyst coated surface. Nonetheless, the simultaneous local energy dissipation rate will be higher as well, which may enlarge the pressure drop in the reactive module due to the turbulent energy dissipation. Duran *et al*., 2011a indicated that the increase in turbulence intensity has significant effect on increasing

the contaminant degradation rate in an immobilized photocatalytic reactor. In order to elucidate the influence of turbulence intensity on the contaminant mass transfer rate, the CFD predicted turbulence intensity in the plain reactor and that of the reactor equipped with the square, triangular and semicircular roughness elements are analysed. Further, the variation of turbulence intensity computed at *Re*=7500 throughout the reactive section was compared with an empty reactive section (data not shown). The predicted turbulence intensity fields were found to be somewhat different for the reactor equipped with the baffle and roughness element compared with the empty reactive module. The simulation results indicate a significant difference between the turbulence intensities close to the wall and the middle of the reactive module.

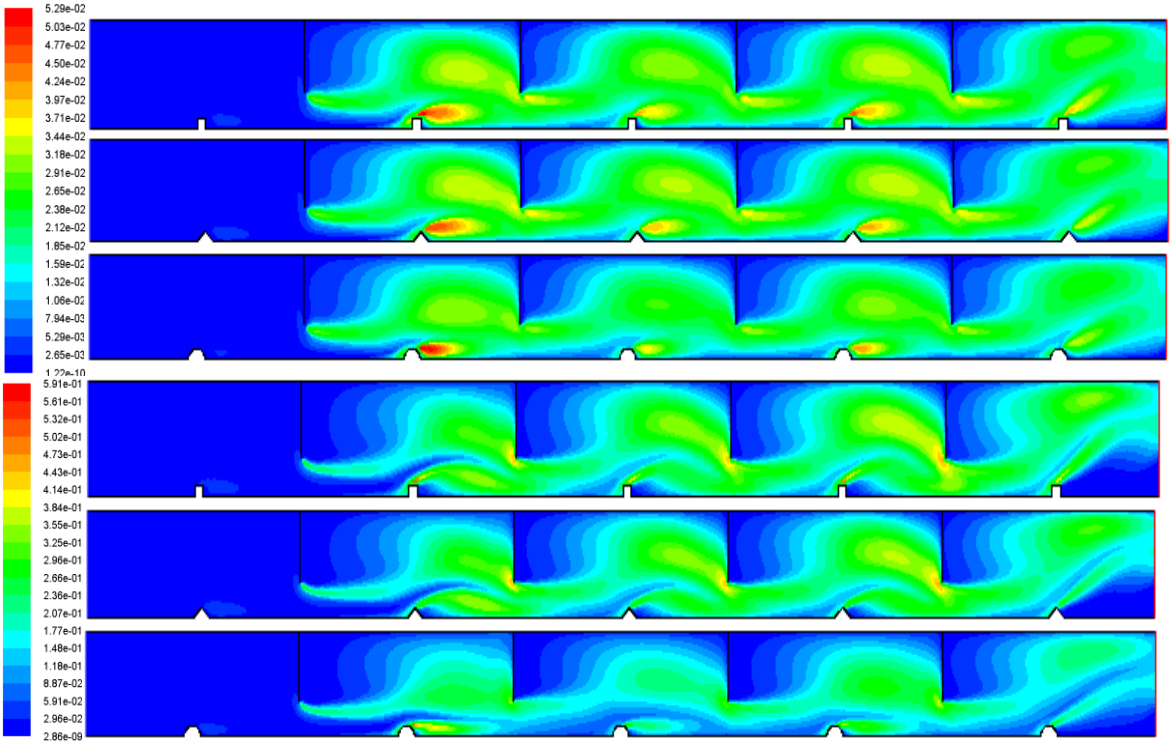

Figure 7.5 Effect of combined baffle and roughness elements on turbulent kinetic energy (m^2/s^2) distribution along the reactive section for *Re*=2150 (top) and 7500 (bottom) respectively.

Nonetheless, the use of top baffle and roughness elements inside the reactor made it possible to predict the changing pattern of turbulence intensity. By examining the predicted turbulence intensity field in the combined reactive module, it was observed that the area near the bottom wall has higher intensities due to the sharp edges of the top baffle. While the swirling flow pattern produced by the semi-circular element was slightly lower than that obtained with the

square and triangular elements. The improved fluid mixing and turbulence intensity as well as the fluid vorticity behind the square and triangular edges surpassed the unfavourable impacts of weakened swirls on mass transfer augmentation. This is important from contaminant mass transfer point of view and it might indicate why more species mass fraction is transferred by the combined baffle and roughness system than that was observed for the roughness element only. The higher turbulence intensity close to the reactor wall has been appeared as one of the reasons that the highest TKE obtained by the square element insert.

7.5.5 Pressure Drop

In general, the enhancement of turbulence is coupled with the loss in terms of increased skin friction which results in higher pressure drop. Pressure drop is an inevitable phenomenon in a baffle-filled reactive channel. The amount of pressure drop in a reactive channel containing baffles is governed by the baffle configurations and the feed water flow rates. Different types of roughness element combined with a top baffle can result in different degrees of pressure drop in the reactive channel under the simulation conditions. Figure 7.6 shows the variation of static pressure in the reactive module for both *Re*= 2150 and 7500 respectively. The square elements which produce the highest velocity magnitude at the lower region of the reactive section resulted in the largest pressure drop followed by triangular and circular elements.

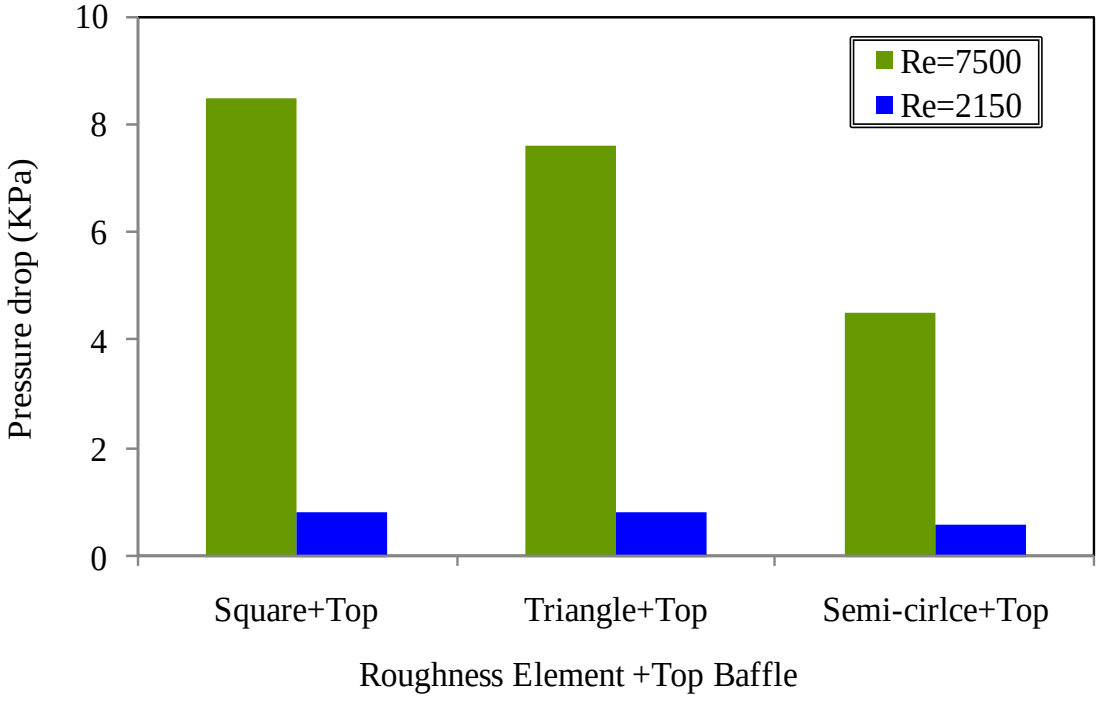

Figure 7.6 Effect of combined top baffle and roughness elements on pressure drop.

It was noticed that the static pressure decreased rapidly for a distance from 0.8L to the reactor exit for the square and triangular elements. The fluid is forced to pass through the constricted area and expands after the top-baffle position to fill up the channel. This periodic contraction and expansion in the flow area results in an increase in the fluid velocity which consequently influences the formation of eddies. This phenomenon appears to directly increase the pressure drop in this confined channel. Due to the development of higher unsteady hydrodynamics at higher feed Reynolds, the square element tends to produce a higher pressure drop when compared with triangular and semicircular elements (Ahmad *et al*., 2005). With increasing feed Reynolds number, the difference in pressure drop caused by various combined reactor configurations becomes more evident. Nonetheless, square and triangular elements generate relatively higher pressure drop followed by the semi-circular roughness element at feed *Re*= 2150. Moreover, current modelling approaches produces different evolution trends as when compared to the reactor system equipped with only a top baffle (triangular elements generate the highest pressure drop followed by the square and semi-circular elements) at higher Reynolds number.

7.5.6 Influence of Combined Top Baffle and Roughness Elements on Wall Shear Stress Distribution

The computed wall shear stress is compared for low and high Reynolds number in Figure 7.7. A consistent and periodic variation of wall shear stress corresponding to the geometries of top baffle and roughness elements was observed for the inlet velocities studied. Under the simulated conditions, the wall shear stress was observed to be higher at the 0.2m, 0.3m, 0.6m and 0.8m positions of the reactive length for square and triangular roughness elements when fluid approaches the reactor exit. For the semi-circular element, the higher values of wall shear stress were found to be at the positions of 0.05m, 0.08m, 0.12m and 0.16m respectively from the inlet of the reactive section. The simulation results presented here indicate that the distribution of wall shear stress gives a maximum value which is located in the middle of the successive roughness elements and a minimal value at the position of the roughness element for any rate of turbulent flow. At low Reynolds number, the higher magnitude of shear stress achieved with square and triangular elements was 5.0 Pa which spans the maximum length of the reactive section. By contrast the value of higher wall shear stress for the semi-circular element ranges from 2.8 to 4.5 Pa. At high Reynolds number, the calculated value of

maximum shear stress obtained using the square and triangular elements was 25 to 35 Pa which spreads for the larger part of the reactive section.

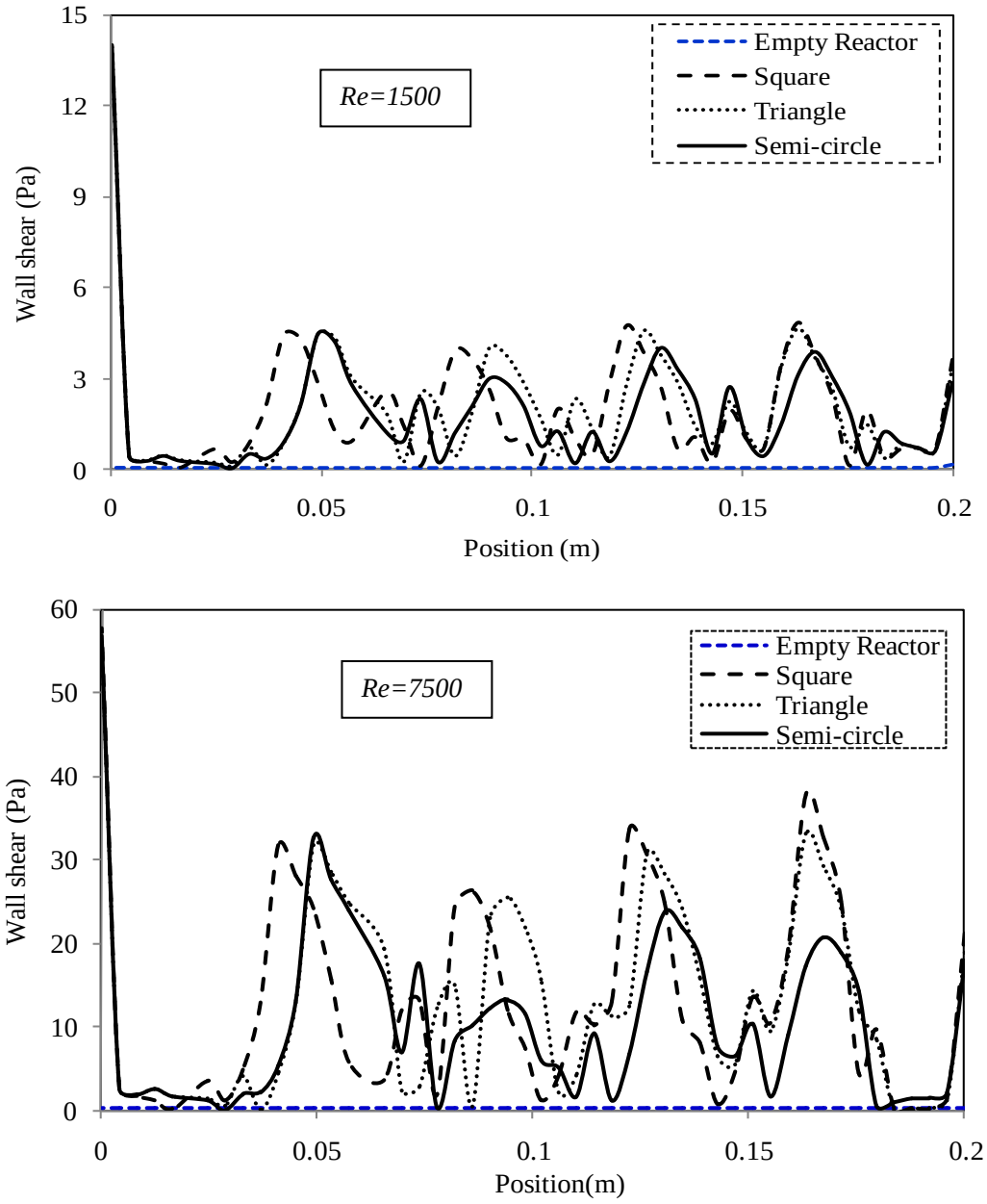

Figure 7.7 Effect of combined baffle and roughness elements on wall shear stress distribution on the catalyst coated layer.

On the contrary, the value of higher wall shear stress varies from 10 to 32 Pa for the semi-circular element under the conditions simulated. In comparison with the empty reactor, the application of combined baffles and roughness elements would also lead to considerable increase in the friction factor. Two minimum friction coefficients appear to be present due to

the separation of the flow through the baffle; one is around the baffle and the other is at the reattachment point behind the baffle.

7.5.7 Influence of Combined Baffle and Roughness Elements on Mass Transport of Formic Acid

To ensure a rapid and efficient mixing is an important step in the design of a photocatalytic reactor. In the laminar flow regime, the mixing of fluids in a reactor is primarily driven by the diffusion process. Under the laminar flow condition, the mixing of fluid requires a long enough path and wide space to ensure complete mixing or a complex geometry to raise, stretch, and tilt the fluid interfaces to ensure complete mixing based on chaotic advection. But in regions with high-turbulence levels, the eddy lifetime, k/ε, is short, mixing is fast, and, consequently, the reaction rate may not be limited by the small-scale mixing. In this limit, the kinetic rate generally has the smallest value (Marshal and Bakker, 2004). In contrast, in regions with low turbulence levels, small-scale mixing may be slow and limit the reaction rate. In this range, the mixing rates are more important. When the mixing in the reactive section is effective, diffusion processes are significantly accelerated; organic pollutant that is near the wall goes into the bulk and vice versa, thereby eliminating a slowdown due to diminishing concentration gradients. Figure 7.8 shows a comparison between the contours of formic acid concentration along the reactive zone as computed at Reynolds number 2150 (top) and 7500 (bottom) under the influence of roughness elements such as square, triangle and semi-circle respectively. For *Re*=2150, it can be observed from the contours that the concentration of FA across the reactive section varies considerably as the flow passes the channels and approaches the exit in both cases for all the roughness elements investigated. Under the conditions simulated, the FA concentration at the shadow of square and triangular elements on the photocatalyst surface decreases considerably compared with the semi-circular element. The distribution of FA concentration with lower magnitudes seems to dominate over the 50% span of the reactive section. This condition was verified through analysis of the velocity field in the system which showed a recirculation zone at the upstream and downstream of the square and triangular elements in the inter-baffle region that creates high velocity gradient regions in the flow distribution. By contrast, at *Re*=7500, a low concentration of FA mass fraction appears to present at the shadow of square, triangular and semi-circular elements compared to that attributed to the case with *Re*=2150.

These higher concentration regions are the consequence of higher fluid velocity gradients in this region (Duran *et al*., 2011b). Comparatively the range of the low concentration zone is considerably smaller in turbulent flow conditions than that in laminar flow conditions. The reactor top and bottom wall featured with top baffles and roughness elements respectively creates dispersion and spreading of mixed fluids that leads to more turbulent collisions than plain straight channels. The main difference between plain and the combined reactor can be explained by the fact that staggered obstacle feature walls in the combined channel force the fluid particles near the walls to co-mingle with the fluid particles in the centre of the channel which is also the reason for the better mixing efficiency.

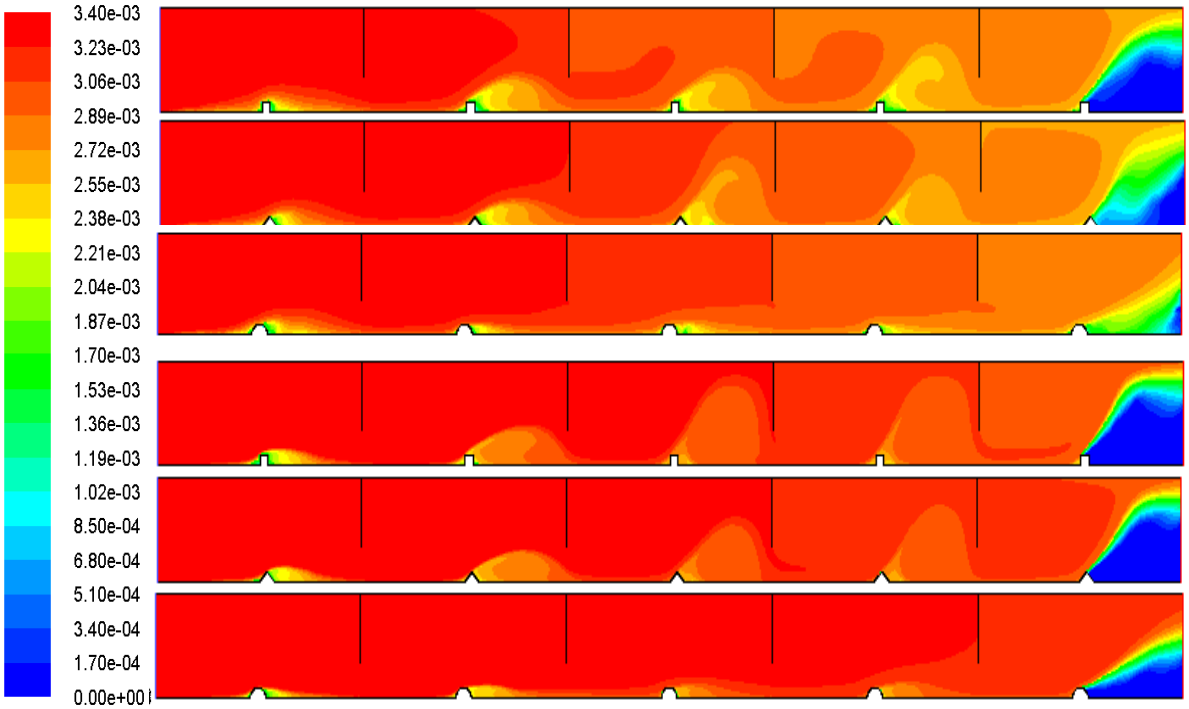

Figure 7.8 Contours mass fraction of formic acid as computed at *Re*=2150 (top figure) and 7500 (bottom figure) respectively.

7.5.8 Influence of Roughness Elements on Flow Field

In order to investigate the effect of bottom wall roughness on the flow field, a number of roughness elements, namely square, triangular and semi-circular shapes with 2.5mm height were used. A reactive section with 12mm in height and 200mm in length was chosen for CFD simulation. Figures 7.9 and 7.10 display the influence of roughness elements on the local stream lines and velocity fields computed at *Re*= 1500 and 7500 respectively. As shown in

Figure 7.9, the presence of roughness elements noticeably perturbs the local flow near the walls coated with catalyst, and the form of the detachment tendency due to inertia is observed. When the fluid passes the triangular and square roughness elements, the flow over rough surfaces tend to induce recirculation at the shadow of the roughness elements (Zhang *et al.*, 2010) . By comparing the extent of the stream lines distortion induced by these three types of roughness elements, it is clear that the distortion zone caused by the semi-circular roughness element is relatively smaller than that of the triangular and square roughness elements. The boundary layer regeneration is commonly associated with the flow separation and recirculation induced by the roughness elements. As indicated in Figure 7.10, the local velocity contours near the bottom wall can give an in-depth understanding of the effects of roughness elements on fluid flow. At *Re*=1500, the low velocity regions tend to appear in the most part of the reactive section. Nonetheless, at *Re*=7500 , a strip of low velocity region with a magnitude of 0.13m/s prevails in the downstream of the all roughness elements whereas the extent of the low velocity region is smaller for the semi-circular element. The distortion of streamlines over the square and triangular elements at *Re*=7500 are found to be higher compared with the semi-circular element. The effect of triangular roughness elements on pressure drop along the reactor bottom was observed to be similar to the square roughness elements, and their impact is higher than the semicircular roughness elements.

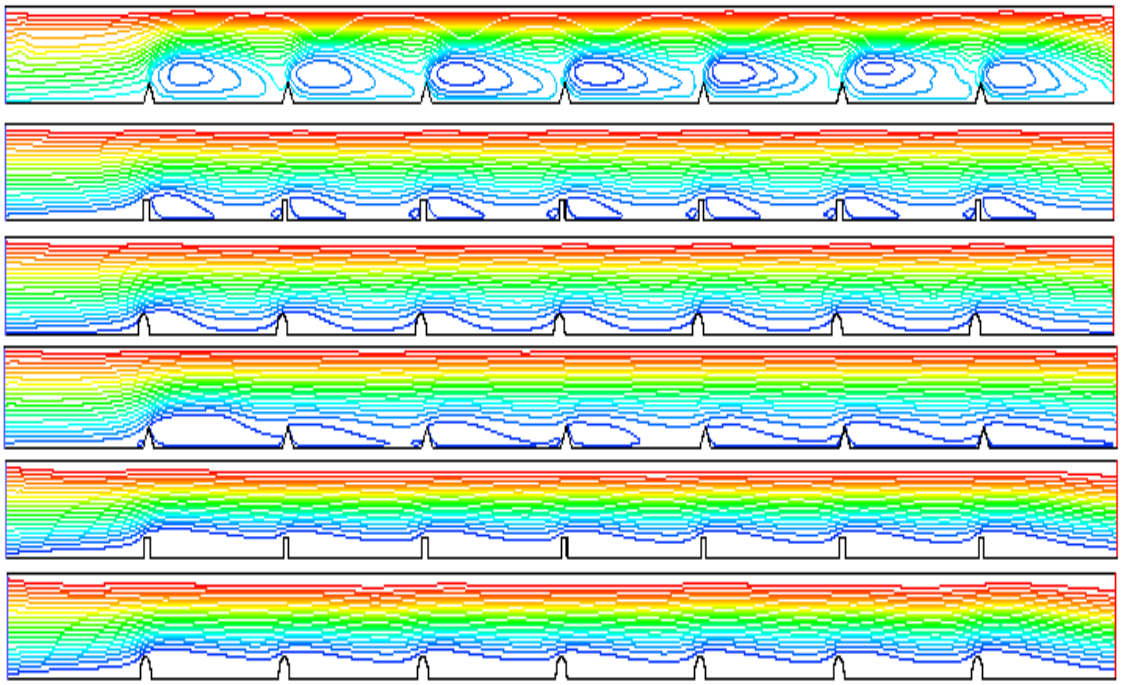

Figure 7.9 Influence of roughness elements on local stream line contours at *Re*= 1500 (top figure) and *R*e=7500 (bottom figure) respectively.

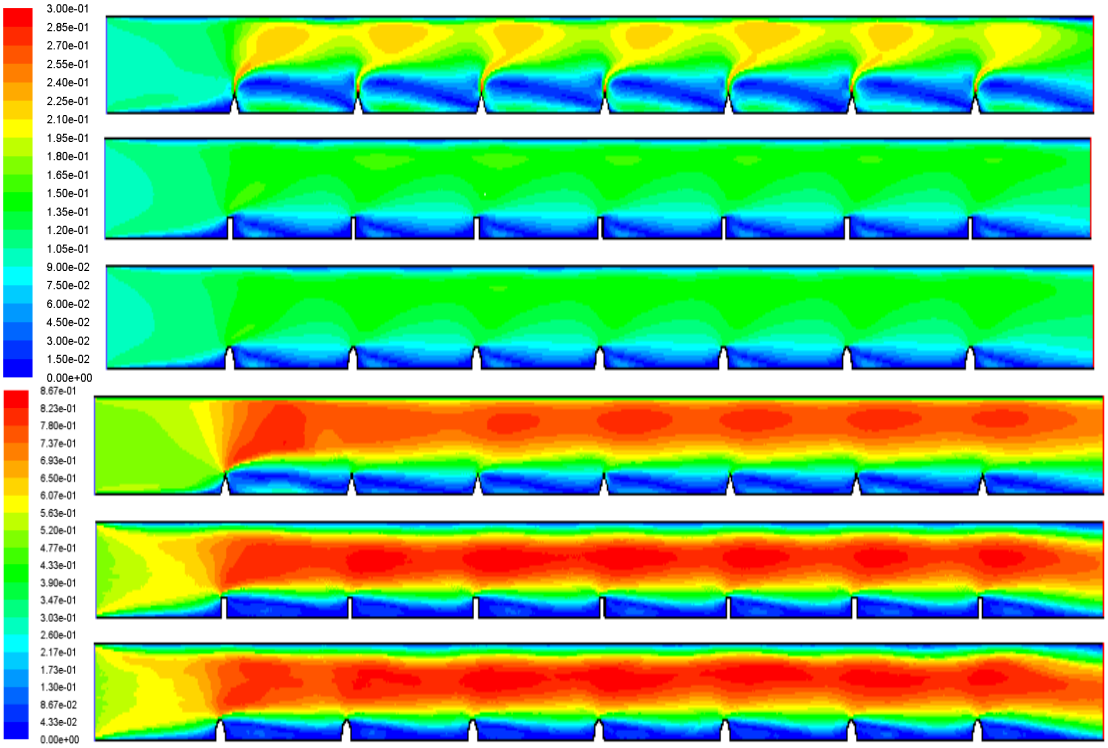

Figure 7.10 Influence of roughness elements on local velocity contours computed at *Re*=1500 (top figure) and 7500 (bottom figure) respectively.

7.5.9 Influence of Roughness Elements on Formic Acid Mass Transport

Figure 7.11 shows the influence of roughness elements (square, triangle and semi-circle) on the the mass transport of formic acid along the reactive section as computed using RNG *k*-*ε* hydrodynamic model at Reynolds number 2150 and 7500 respectively. For *Re*=2150, it can be observed that the concentration of FA across the reactive segment decreases as it approaches the exit for all the elements studied. Under the conditions simulated, the FA concentration at the photocatalyst surface decreases significantly for the square element compared with the triangular and semi-circular element. The distribution of FA with lower magnitude seems to dominate over the latter 50% span of the reactive section. This observation seems to be related with the condition of the velocity field in the system which showed a recirculation zone at some locations that induces high velocity gradient regions across the flow distribution. In contrast, at *Re*=7500, a low concentration of FA mass fraction appears to present at the shadow of the square and semi-circular elements compared to that attributed to the triangular element. These higher concentration regions are linked to the higher velocity gradients in these zones (Duran *et al.*, 2011b). Comparatively the range of the

low concentration zone is considerably smaller at turbulent flow conditions than in laminar flow conditions.

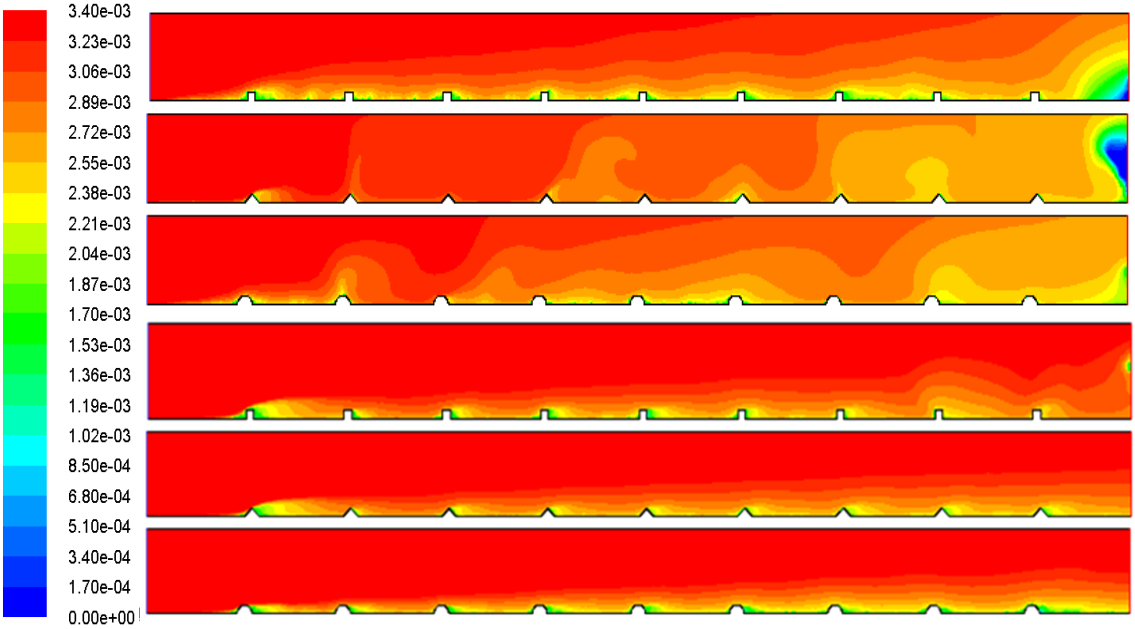

Figure 7.11 Influence of roughness elements on contours of FA mass fraction computed at *Re*=2150 (top figure) and *Re*= 7500 (bottom figure) respectively.

7.5.10 Comparative Evaluation of significant Hydrodynamic Parameters

In order to evaluate the role of combined top baffle and roughness elements on the hydrodynamic performance of the reactive module, a number of parameters that are hydro-dynamically significant were compared for both low and high Reynolds number flows. Tables 7.1 and 7.2 present the maximum, minimum and average values of hydrodynamic parameters predicted with an inlet velocity of 0.1 m/s and 0.5m/s for the square, triangular and semi-circular roughness elements respectively. Table 7.3 and 7.4 present the maximum, minimum and average values of hydrodynamic parameters predicted with an inlet velocity of 0.15 m/s and 0.5m/s for the combined top baffle and roughness elements. The computed pressure drop, turbulent kinetic energy, wall shear stress and turbulent energy dissipation rate for the square, triangle and semi-circular elements are summarised in Tables 7.1-7.4 for both low and high Reynolds number respectively. In terms of pressure drop, the top baffle and semi-circular system appears to be more realistic compared to the square and triangle elements for both cases. In addition, the semi-circular element also seems to be more efficient with respect to the amount of % contact loss. By evaluating the computed hydrodynamic

parameters, it can be generalised that the top baffle coupled with a semi-circular element would provide optimum hydrodynamic performance with minimal pressure drop and energy consumption for both low and high Reynolds number flows.

Table 7.1

Influence of roughness elements on hydrodynamic parameters.

Parameter		**Inlet velocity=0.1m/s (*Re*=1062)**		
		Square	**Triangle**	**Semi-circle**
Pressure drop (KPa)		0	0	0
Turbulent kinetic energy (m^2/S^2)	*Max.*	2.44×10^{-3}	0.39	1.92×10^{-3}
	Min.	4.53×10^{-11}	8.17×10^{-11}	3.48×10^{-11}
Wall shear,τ_w (Pa)	*Max.*	2	3.5	2.0
	Min.	0	0	0
	Avg.	1	1.15	0.85
Turbulent dissipation rate (m^2/S^3)	*Max.*	1×10^{-3}	4×10^{3}	2.5×10^{-2}
	Min.	1×10^{-2}	1×10^{-4}	1×10^{-3}
% Contact loss		87.5	87.5	43.75

Table 7.2

Influence of roughness elements on hydrodynamic parameters.

Parameter		**Inlet velocity=0.5m/s (*Re*=5310)**		
		Square	**Triangle**	**Semi-circle**
Pressure drop (KPa)		0	0	0
Turbulent kinetic energy (m^2/S^2)	*Max.*	2.7×10^{-2}	0.426	2.08×10^{-2}
	Min.	1.18×10^{-8}	1.1×10^{-8}	1.21×10^{-10}
Wall shear,τ_w (Pa)	*Max.*	8	10	7
	Min.	0	0	0
	Avg.	5	7	5
Turbulent dissipation rate (m^2/S^3)	*Max.*	0.6	2×10^{3}	0.4
	Min.	1×10^{-2}	1×10^{-4}	1×10^{-3}
% Contact loss		81.25	85.0	81.25

Table 7.3

Influence of combined top baffle and roughness elements on hydrodynamic parameters.

Parameter		Inlet velocity=0.15m/s (*Re*=2150)		
		Square	**Triangle**	**Semi-circle**
Pressure drop (KPa)		0.8	0.75	0.65
Turbulent kinetic energy (m^2/S^2)	*Max.*	4×10^{-5}	2.5×10^{-5}	0.5×10^{-6}
	Min.	1×10^{-5}	1×10^{-6}	5×10^{-6}
Wall shear,τ_w (Pa)	*Max.*	5.0	5.0	5.0
	Min.	0	0	0
	Avg.	2.5	1.75	2
Turbulent dissipation rate (m^2/S^3)	*Max.*	6	3	0.5
	Min.	0.25	0.25	1.0
% Contact loss		35	34	20

Table 7.4

Influence of combined top baffle and roughness elements on hydrodynamic parameters.

Parameter		Inlet velocity=0.5m/s (*Re*=7500)		
		Square	**Triangle**	**Semi-circle**
Pressure drop (KPa)		8	7.5	5.2
Turbulent kinetic energy (m^2/S^2)	*Max.*	0.394	0.4	0.414
	Min.	3.32×10^{-9}	3.08×10^{-9}	2.86×10^{-9}
Wall shear, (Pa)	*Max.*	40.0	40.0	39.0
	Min.	0	0	0
	Avg.	20	18	17.5
Turbulent dissipation rate (m^2/S^3)	*Max.*	100	50	48
	Min.	0	0	0
% Contact loss		40	40	30

7.5.11 Comparison of Reactive Sections with and without Top Baffles

In contrast to the boundary layers that formed in the reactive section with only square, triangular, and semi-circular roughness elements (Figure 7.9), there is a gradual increase of the separation of the boundary layers in the combined reactive module (Figure 7.3) which increases the formation of vortices in the flow, thereby enhancing the extent of mixing. The produced vortices tend to split up the streams into multiple layers and each layer curls in a different manner. The combination of splitting and curling actions and the co-mingling of the centre streamlines and the edge stream lines will result in enhanced mixing and will tend to improve the performance of the reactor. In contrast, the smooth channel or the channel with only roughness elements does not have this advantage. In the combined top baffle and roughness element section, the fluid passing through the reactive channel is rotated as intended. Some differences are seen that could result from the variation in low and high Reynolds number flows. At high Reynolds number, fluid molecules were widely mixed and the interface of fluid molecules became more distorted. As the fluid passes through the combined reactive section with a helically rotational shape, the fluid molecules are stretched and folded due to the inertial force. This convection can enlarge the interfacial area, which initiates rapid mixing of fluid particles at a higher Reynolds number. The Reynolds number plays an important role in analysing the flow field. The degree of mixing arising solely from diffusion under pure laminar flow conditions decreased rapidly with increasing velocity, as the residence time is reduced within the channel. As the Reynolds number becomes larger, recirculation occurs in the flow of the combined reactive section, the streamline becomes unsymmetrical, and the pressure in the channel undergoes a series of changes as well.

7.6 Conclusion

In order to develop an understanding regarding the role of turbulence and mixing promoters, a new reactive module incorporating a top baffle on the upper wall and a set of roughness elements on the bottom wall has been simulated using CFD code FLUENT. Simulations have been performed for two different flow rates to investigate the role of fluid dynamics in the photocatalytic reactor at Reynolds numbers 2150 and 7500 respectively. Based on the above work, and by comparing the several hydrodynamic features of the reactive module, the combined reactor appears to be a more promising approach in terms of turbulence and pressure drop at low flow regimes which needs further investigation to determine its optimum

residence time, turbulence phenomena, and better mixing than that of the others. As a result, a combined channel reactor design is proposed which exhibits a more favourable velocity profile by guiding fluid streams over alternating, turbulence-generating obstacles. This preliminary work showed that the CFD simulation could be used for the design improvement of the flat plate reactor for storm or wastewater reuse. Indeed, the results presented in this chapter provide a basis for further work in this area. The combination of patterning the reactor bed for splitting and recombining the flow streams can be an effective strategy to develop controlled turbulence in the reactive section. In the optimization of the combined module only a small number of hydrodynamic parameters was investigated. Further optimization of the reactor design with respect to mixing efficiency on an area larger than the tested one should be performed in the future.

The desired criterion for designing the optimal turbulence promoters depends on the ability of the baffle to ensure optimum fluid mixing at specific power consumption. A high pressure drop is not desirable for any practical consideration. To achieve minimum energy consumption while improving mixing and turbulence, optimum design of baffle and geometric arrangements must be carefully evaluated. The choice of optimum combinations might depend on other operating parameters i.e. feed velocity, feed water viscosity, reactor dimensions, etc. The combination of top baffle and roughness element can generate shear-induced secondary flow, promotes local mixing and hence can enhance pollutant mass transfer for all types of elements examined. The observed turbulence enhancement can be linked to the transient wall shear (Cui and Taha, 2003). However, the extent of this enhancement depends on the relative strength of the generated secondary flow and the bulk flow, and the arrangement of the baffle in the reactive section.

CHAPTER EIGHT

CONCLUSIONS, CONTRIBUTION AND RECOMMENDATIONS FOR FUTURE WORK

8.1 Introduction

Photocatalysis is a promising alternative green technology for wastewater detoxification and removing pollutants from storm and wastewater. The lack of a suitable modelling approach and efficient design has limited the applicability of this technology on a commercial scale. The design of heterogeneous photocatalytic reactors requires the selection of suitable reactor geometry, arrangement of the lamp-reactor system, type of photocatalyst, the size, distribution and concentration of catalyst, reactor hydrodynamic behaviour and the mode of operation. Understanding the hydrodynamic properties in the reactor is crucial for a prototype design and efficient operation of the photocatalytic reactor. In terms of solar UV and visible light utilisation, flat plate reactors are generally thought of as commercially efficient. In light of the above considerations, a flat plate photocatalytic reactor developed at Queensland University of Technology (QUT) has been investigated further using CFD code FLUENT to improve its design for water treatment applications. The potential of the CFD modelling lies in its ability to provide detailed local information at a low cost and in shorter time compared to alternative experimental approaches.

Several aspects of the reactor modelling were focused on in this study. One of them is the reactor hydrodynamics using mixing and turbulence promoters, lack of which limits the efficiency of the photocatalytic reactor in terms of pollutant mass transfer and degradation, particularly when the catalyst is immobilised on the supporting material. Earlier studies have suggested that the use of turbulence promoters in the immobilised photocatalytic reactor would improve the mixing and pollutant mass transfer (Periyathamby and Ray, 1999; Sengupta *et al.,* 2001; Kabir and Ray, 2003; Duran *et al*., 2010a). Nonetheless, there have been no systematic studies documented in the current literature that have tested this hypothesis. This work aimed to contribute to the gap in the current literature. In order to ensure improved turbulence and mixing in the photocatalytic reactor, various turbulence

promoters such as top and bottom baffles as well as combined top baffle and roughness elements in the reactive section have been exploited in this research for a systematic investigation.

8.2 Conclusions and Contribution

The work reported in the preceding chapters has led to several conclusions, some of which are specific to the particular studies, and thus are presented in detail in the conclusion sections of each individual chapter. The overall contributions made by this study can be summarised into two categories, the first being based on the hydrodynamic investigation of the flat plate reactor and its photocatalytic performance for model pollutant degradation. And the second encompassing the role of mixing and turbulence promoters on the hydrodynamic performance of the reactive section of the flat plate reactor. The specific conclusions and contributions are provided below:

- The flow structure of the flat plate photocatalytic reactor has been simulated using the CFD technique for various inlet velocities to cover both the laminar and turbulent regime (chapter 5). The reported results suggest that the model developed could predict the hydrodynamic behaviour of the reactor with reasonable accuracy and an uniform flow field was observed in the reactive section of the flat plate reactor. Different hydrodynamic models were investigated and demonstrated their capability to provide an in-depth understanding of the flow field in the flat plate reactor which aids in the optimization of reactor design.

  The predictive analysis based on computational fluid dynamics (CFD) corresponds well with the experimental observation of the flat plate reactor at different flow conditions**.** Depending on the CFD simulation, it was found that the smaller inlet velocity of fluid would provide higher photocatalytic degradation efficiency and a higher fluid inlet velocity results in the decrease of pollutant degradation. The model provides a detailed description of the local information on the performance of the flat plate reactor for pollutant degradation which is useful to better understand the reactor behaviour and design optimisation. Although constant irradiation intensity on the catalyst surface has been assumed for predicting pollutant degradation, additional studies should be pursued for the development of an integrated model of the flat plate

reactor considering the dependency of degradation rate on irradiation intensity. This study demonstrates that it is feasible to predict the performance of a photocatalytic reactor using a three-dimensional CFD approach.

The results presented in chapter five suggest the significance of improved turbulence and fluid mixing in the flat plate photocatalytic reactor as the continuous contact of fluid and catalyst is necessary for efficient pollutant degradation. In addition, the catalyst fouling by degradation by-products and adsorbed non-degraded pollutants can deteriorate the photocatalytic activity. In chapter six, two novel approaches using top and bottom baffles have been examined to promote turbulence and mixing in the reactive section of the flat plate reactor for improved stability in its operation. Furthermore, the use of turbulence and mixing promoters can minimise the catalyst fouling and the deposition of degradation by-products on the catalyst coated surface.

- A set of baffles was exploited at the top of the reactive module termed as "top baffle" for a given set of positions to examine their impact on the flow pattern, behaviour and features for a range of heights 5 mm to 12 mm (chapter 6). The investigation focused on the effect of baffle height on the distribution of local parameters such as stream line contours, velocity, static pressure, wall shear stress, turbulent kinetic energy and turbulent dissipation energy in the reactive module through CFD simulation. The distribution of local hydrodynamic parameters was found to be dependent on the flow conditions and the height of the baffle. The magnitude of pressure drop was observed to increase with increasing baffle height irrespective of the flow regime. Also, the mass transport of formic acid was related to the height of the baffle and Reynolds number. Evaluation of the hydro-dynamically significant parameters provides significant insight which will aid in the design a suitable baffle in the photocatalytic reactor for its viable application.

  Baffles were used at the catalyst coated surface termed as "bottom baffle" and its effect on the hydrodynamics of the reactive section has been studied. The effect of baffle position, height and spacing on the distribution of flow and turbulence kinetic energy has been simulated. Under the conditions simulated it was observed that the use of a bottom baffle can improve the level of turbulence for a variety of baffle heights in the reactive section; however, it may lead to some degree of contact loss

when the height of the baffle increases above a certain level regardless of the position of the baffles used.

A higher degree of mixing of fluid particles and movement of pollutants toward the catalyst coated surface in the reactor is likely to make it an effective reactor suitable for practical application. The use of baffles without any need for stirring will enable the reactor configuration to be more promising and cost effective. CFD simulation results suggested that loss of contact of stream lines might exist as the height of the bottom baffle increases after the location of the baffle in the reactor. The introduction of a baffle in the reactive section might improve mixing performance in the reactor. Simulation results showed that installing a top baffle at the suitable locations might be a better choice than positioning a baffle in the bottom of the reactive section.

- In order to understand further the effectiveness of mixing and turbulence promoters, a new approach for the reactive section that involves a number of top baffles on the upper wall and an array of roughness elements on the bottom wall were used to form a combined module which has been simulated utilising CFD code FLUENT (chapter 7). Simulations have been performed for different hydrodynamic conditions to gain an in-depth understanding on the performance of a combined module in terms of local stream lines contours, flow field, turbulent kinetic energy, pressure drop and wall shear stress. In addition, the distributions of velocity, wall shear stress and turbulent characteristic, the eddy formation, pressure loss along the reactive channel on the catalyst surface were evaluated, respectively. In comparison to the square and triangular roughness elements, the combined module containing the semi-circular roughness element appears to be promising with minimal pressure drop for mixing improvement.

The photocatalytic reaction takes place only in the shear layer of the plate where the catalyst is present, and vortices were shown to be very efficient at enhancing the reaction by transporting the pollutant from the bulk liquid to the catalyst surface (Kabir and Ray, 2003). Hence, the vortices induced by flow instability due to the presence of baffles in the reactive module can expedite the pollutant degradation. The

simulation results under various baffle arrangements suggest the significance of baffle specifications for optimization of the photocatalytic reactor fitted with baffles.

This study demonstrated the potential of CFD as an efficient tool for improved understanding of reactor mixing performance and provided useful information for design optimisation which is required for sustainable operation of the flat plate reactor. Since the baffled reactor was not available at the time of modelling, the validation of the modelling results could not be performed for a baffled reactor, this research was envisaged to provide indications of expected behaviour, rather than quantitative predictions. The results of this study would be supportive to fine tune the reactor design by achieving better fluid catalyst contacting as well as minimizing mass transfer limitations.

8.3 Future Work

The availability of water resources are becoming scarce and deteriorated by toxic organic contaminants. The need to remove this general class of trace contaminants effectively and reliably becomes increasingly important to broaden the water recycling paradigm. Heterogeneous photocatalytic oxidation is one of few promising methods of treating water to degrade these substances but the necessary level of understanding for the pertinent application of this technique has not been reached as yet.

In spite of extensive investigations, the commercial exploitation of photocatalysis has been hindered by the lack of understanding of the photoreactor design and a suitable model, inefficient and low-cost visible light harvesting catalysts as well as inadequate scale-up strategies. Consequently a large amount of scientific and engineering work is still required in order to fully understand and thus be able to make its effective use for commercial application. Using the work reported in this thesis as a starting point, several specific tasks can be outlined that could help in achieving the overall goal of understanding the behaviour of the flat plate reactor for scale-up. There is plenty of room for further research in this area prior to implementing this technology on a commercial basis. The future work recommended in this study is elaborated below.

1. An experimental evaluation of the flow field using modern techniques such as PIV is necessary to capture the outstanding features of the flow in the photocatalytic reactor. Such a study can be useful to find out the suitability of the turbulence model to determine the actual flow field more accurately especially downstream of the baffle.
2. Operating conditions together with the design specifications for scale-up should be ascertained to address its compatibility for the treatment of large volumes of contaminated water.
3. Prototype reactor at pilot-scale operation can reveal both the success and deficiencies in reactor performance as well as address possible deterioration over time.
4. The combination of the photocatalytic process with other physical and chemical processes is worth investigating for wastewater treatment.
5. In the heterogeneous photocatalytic water purification process, the generation of photons driven by solar UV and visible light for catalyst activation is the significant part of the total cost for the operation of the system. The evaluation of the treatment costs is, at this time, one of the aspects that needs more attention.
6. One important area of work, although not close to the line of research work presented here, is the development of novel nano-materials. The current state-of-the-art material used as catalysts can only be activated by UV light which represents approximately 5% of the entire solar spectrum. The development of a more reliable and low-cost photocatalyst that can be activated by visible and solar light or both should be explored for potential application in wastewater treatment.
7. Although the advances in laboratory studies contributed significantly to photocatalytic water treatment for relatively simple and clean solutions, the sustainability of their photocatalytic activity in real wastewater is unclear which essentially requires further investigation. The application of this technique for real world wastewater calls for further exploration to achieve stable pollutant removal through the optimization of process parameters. This would make a significant impact on the potential commercial application of this technique for industrial systems.

REFERENCES

Aal, A.A., Mahmoud, S.A., Aboul-Gheit, A.K., 2009. Nanocrystalline ZnO thin film for photocatalytic purification of water. *Materials Science and Engineering* C 29, 831-835

Abdullah M., Low G., Mathews, R.W., 1990. Effects of common inorganic ions on rates of photocatalytic oxidation of organic carbon over illuminated titanium dioxide. *Journal of Physical Chemistry* 94, 6820

Abramovic, B. Sojic, D.V. Anderluh, V., 2007. Visible-light-induced photocatalytic degradation of herbicide mecoprop in aqueous suspension of TiO_2. *Acta Chimica Slovenia* 54, 558–564

Abramovic, B. Sojic, D.V., Anderlu, V. Abazobic, N. Comor, M.I., 2009. Nitrogen-doped TiO_2 suspensions in photocatalytic degradation of mecoprop and (4-chloro-2-methylphenoxy) acetic acid herbicides using various light sources. *Desalination* 244, 293-302

Adan, C. Bahamonde, A., Fernandez-Garica, M., Martinez-Arias, A., 2007. Structure and activity of nanosized iron-doped anatase TiO_2 catalysts for phenol photocatalytic degradation. *Applied catalysis B: Environmental* 72, 11-17

Adesina, A. A ., 2004. Industrial exploitation of photocatalysis; progress, perspectives and prospects. *Catalysis surveys from Asia* 8(4), 265-273

Advanced photochemical oxidation processes, *EPA Hand Book, 1998*. Cincinnati: USA

Ahmad, A.L., Lau, K.K., Abu Bakar, M.Z.,2005. Impact of different spacer filament geometries on concentration polarization control in narrow membrane channel. *Journal of Membrane Science* 262, 138–152

Ahmed, S., Rasul, M.G., Martens, W.N., Brown, R., Hashib, M.A. 2011a. Heterogeneous photocatalytic degradation of phenols in wastewater: A review on current status and developments. *Desalination* 261 (1-2), 3-18

Ahmed, S., Rasul, M.G., Brown, J.B., Hashib, M.A., 2011b. Influence of Parameters on the Hetererogeneous photocatalytic degradation of pesticides and phenolic contaminants in wastewater: A short review. *Journal of Environmental Management* 92(3), 311-330

Ahmed, S., Rasul, M. G., Brown, J. B., Duran. E., 2011c. Numerical simulation of flow in a photocatalytic reactor containing baffles (AJK 2011-3062). Proceedings of *ASME-JSME-KSME Joint Fluids Engineering Conference* 2011 AJK2011-FED, July 24-29, 2011, Hamamatsu, Shizuoka, JAPAN

Akin, J.E., 1994, Finite elements for analysis and design, San Diego: Academic Press.

Alpert, S.M., Knappe, D.R.U., Ducoste, J.J., 2010. Modeling the UV/ hydrogen peroxide advanced oxidation process using computational fluid dynamics. *Water Research* 44, 1797- 1 808

Al-Ekabi, H., Butters, B., Delany, D., Ireland, J., Lewis, N., Powell, T., Story, J. 1993. TiO_2 advanced photo-oxidation technology: effect of electron acceptors,in Photocatalytic purification and treatment of water and air, edited by D.F.Ollis and H.Al-Ekabi, Elsevier: Amsterdam, 321-334

Al-Qaradawi, S., Salman, S., 2002. Photocatalytic degradation of methyl orange as a model compound. *Journal of Photochemistry and photobiology A; Chemistry* 148, 161-169

Al-Sayyed, G., Oliverra, J.C.D., Pichat, P. 1991. Semiconductor-sensitized photodegradation of 4-chlorophenol in water. *Journal of Photochemistry and Photobiology A: Chemistry* 58, 99-114

Alexiadis, A., Mazzarino, I., 2005. Design guidelines for fixed-bed photocatalytic reactors. *Chemical Engineering and Processing* 44, 453-459

Alfano, O.M., Bahneman, D,. Cassano, A.E., Dillert, R., Goslich, R., 2000. Photocatalysis in water environments using artificial and solar light. *Catalysis Today* 58, 199-

Al-Sayyed, G., D'Oliveira, J.C., Pichat, P., 1991. Semiconductor-sensitized photodegradation of 4-chlorophenol in water. *Journal of Photochemistry and Photobiology A: Chemistry* 58(1), 99-114

Amadelli, R., Samiolo, L., Maldotti, A., Molinari, A., Valigi, M., and Gazzoli, D.,2008. Preparation, characterisation, and photocatalytic behaviour of Co-TiO_2 with visible light response. *International Journal of Photoenergy*, Volume 2008, Article ID 853753

Anandan, S., Kathiravan,K.,Murugesan,V.,Ikuma,Y.,2009. Anionic (IO_3^-) non-metal doped TiO_2 nanoparticles for the photocatalytic degradation of hazardous pollutant in water. *Catalysis Communications* 10, 1024-1019

Ananpattarachai,J., Kajitvichyanukul,P., Seraphin,S.,2009. Visible light absorption ability and photocatalytic oxidation activity of various interstitial N-doped TiO_2 prepared from different nitrogen dopants. *Journal of Hazardous Materials* 168, 253–261

An, T., Liu, J., Li, G., Zhang, S., Zhao, H., Zheng, X., Sheng, G., Fu, J., 2008. Structural and photocatalytic degradation characteriscis of hydrothermally treated mesoporous TiO_2. *Applied Catalysis A: General* 350, 237-243

Aravinth, S., 2000.Prediction of heat and mass transfer for fully developed turbulent .uid .ow through tubes. *International Journal of Heat Mass Transfer* 43, 1399–1408

Arques, A., Amat, A.M., Garciýa-Ripoll, Vicente, R., 2007. Detoxification and/or increase of the biodegradability of aqueous solutions of dimethoate by means of solar photocatalysis. *Journal of Hazardous Materials* 146, 447–452

Anandan, S., Vinu, A., Lovely, K.L.P. S., Gokulakrishnan, N., Srinivasu, P., Mori, T., Murugesan, V., Sivamurugan, V., Ariga, K., 2007. Photocatalytic activity of La-doped ZnO for the degradation of monocrotophos in aqueous suspension. *Journal of Molecular Catalysis A: Chemical* 266, 148-157

Bahnemann, D., 2004. Photocatalytic water treatment: Solar energy applications. *Solar Energy* 77, 445-459

Bandala E., Estrada C., 2007. Comparison of solar collector geometries for application to photodegradation of organic contaminants. *Journal of Solar Energy Engineering* 129, 22-26

Barber, T., 2003. *Validation and Verification*. Lecture notes: The University of New South Wales, p. 8.

Bahnemann, W., Muneer, M., Haque, M.M., 2007. Titanium dioxide-mediated photocatalysed degradation of few selected organic pollutants in aqueous suspensions. *Catalysis Today* 124, 133-148

Bahena, C.L., Martý´nezb,S.S., Guzma´n ,D.M., Herna´ndez, M.T.,2008. Sonophotocatalytic degradation of alazine and gesaprimcommercial herbicides in TiO_2 slurry. *Chemosphere* 71, 982-989

Bangun, J. and Adesina, A.A., 1998. The photodegradation kinetics of aqueous sodium oxalate solution using TiO_2 catalyst. *Applied Catalysis A: General* 175(1-2): 221-235

Barakat, M.A.,Schaeffer, H., Hayes, G., Ismat-Shah,S.,2005. Photocatalytic degradation of 2-Chlorophenol by Co-doped TiO_2 nanopartilces. *Applied Catalysis B; Environmental* 57, 23-30

Baran, W., Adamek, E., Makowski, A., 2008. The infuence of selected parameters on the photocatalytic degradation of azo-dyes in the presence of TiO_2 aqueous suspension. *Chemical Engineering Journal* 145, 242–248

Baldyga, J. Bourne, J.R., 1999. Turbulent mixing and chemical reactions, Wiley, Chichester, 1999

Bessekhouad, Y., Robert, D., Weber, J-V., Chaoui,N.,2004. Effect of alkaline-doped TiO_2 on photocatalytic efficiency. *Journal of Photochemistry and Photobiology A: Chemistry* 167, 49-57

Bhatkhande, D.S.; Pangarkar, V.G.; Beenackers, A.A.C.M. 2002. Photocatalytic degradation for environmental applications. A Review. *Journal Chemical Technology and Biotechnology* 77,102

Blake, D.M., J.Webb, C. Yurchi, and Magrini, K.1991. Kinetic and Mechanistic overview of TiO_2 photocatalyzed oxidation reactions in aqueous solution. *Solar Energy Materials* 24, (1-4), 584-593

Blanco, J., Fernandez, P., Malato, S., 2007. Solar photocatalytic detoxification and disinfection of water: Recent Overview. *Journal of Solar Energy Engineering*, 129, 4-15

Bolton, J.R., Bircher, K.G., Tumas, W., Tolman, C.A., 2001. Figures-of-Merit for the Technical Development and Application of Advanced Oxidation Technologies for Both Electric- and Solar-driven Systems. *Pure and Applied Chemistry* 73(4), 627-637

Bouzaza, A., Vallet, C., Laplanche, A. 2006. Photocatalytic degradation of some VOCs of masstransfer and chemical reaction steps in the photodegradation process. *J. of Photochemistry and Photobiology A-Chemistry* 177: 212-217

Bouras, P., Stathatos, E., and Lianos, P., 2007. Pure versus metal-ion-doped nanocrystalline titania for photocatalysis. *Applied Catalysis B: Environmental* 73(1-2), 51-59

Bolton, J.R, Bircger, K.G., W. Tumas, C.A. Tolman., 2001. Figures- of- merit for the technical development and application of advanced oxidation technologies for both Electric- and Solar-Driven Systems. *Pure Applied Chemistry* 73, 627-637

Brezová, V., Blažková, A., Brezňan, M., Kottáš, P., and Čeppan, M. 1995. Phenol Degradation on Glass Fibres with Immobilized Titanium Dioxide Particles. *Collection of Czechoslovak Chemical Communications 60*, 788-794

Brenner, S. C. and Scott, L. R., 1994, The mathematical theory of finite element methods, New York: Springer-Verlag.

Capel, P., 2008. Design of a photocatalytic water purification reactor for the testing of fixed films semiconductors. Undergraduate thesis submitted to QUT.

Castrillon SRV, Ibrahim H,de Lasa H., 2006. Flow field investigation in a photocatalytic reactor for air treatment (Photo-CREC-air). *Chemical Engineering Science* 61, 3343-3361

Cassano, A.E., Martin, C.A., Brandi, R.J., Alfano, O.M., 1995. Photoreactor analysis and design: Fundamentals and applications. *Industry Engineering and Chemistry Research* 34, 2155-2201

Cassano,A.E., and Alfano, O.M., 2000. Reaction engineering of suspended solid heterogeneous photocatalytic reactors. *Catalysis Today*, 58, 167

Cao, Y., Tan, H.,Shi, T., Tang, T. and Li,J., 2008. Preparation of Ag-doped TiO_2 nano particles of photocatalytic degradation of acetamiprid in water. *Journal of Chemical Technology and Biotechnology* 83, 546-552

Cao, Z., Wiley, D.E., Fane, A.G., 2001. CFD simulation of net- type turbulence promoters in narrow channel, *Journal of Membrane Science* 185,157

Cao, Y., Chen, J., Huang, L.,Wang, Y., Hou, Y., Lu,Y.,2005. Photocatalytic degradation of chlorfenapyr in aqueous suspension of TiO_2. *Journal of Molecular Catalysis A: Chemical* 233, 61-66

Carrier, M., Perol, N., Herrmann, J.M., Bordes, C., Horikoshi, S., Paisse,J.O., Baudot, R., Guillard, C., 2006. Kinetics and reactional pathway of imazapyr photocatalytic degradation Influence of pH and metallic ions. *Applied Catalysis B: Enviornmental* 165, 11-20

Cengel and Cimbala, 2006. Fluid Mechanics: Fundamentals and Applications, Mc Graw Hill

Changrani, R.G., Raupp, G.B., 2000. Two dimensional heterogeneous model for a reticulated -foam photocatalytic reactor. *AIChE J*ournal 52, 2271-2280

Chan, A.H.C., Porter, J.F., Barford, J.P., Chan, C.K. 2001.Photocatalytic thin film cascade reactor for treatment of organic compounds in wastewater. *Water Science and Technology* 44(5), 187-195

Chen, D.W.; Ray, A.K. 1998. Photodegradation kinetics of 4-Nitrophenol in TiO_2 aqueous suspensions. *Water Research* 32, 3223

Chen, D.W.; Ray, A.K. 1999. Photodegradation kinetics of Phenol and Its derivatives over UV-irradiated TiO_2. *Applied Catalysis B: Environmental* 23, 143

Chen, D.W., Li, F. and Ray, A.K., 2000. Effect of mass transfer and catalyst layer thickness on photocatalytic reaction. *AIChE Journal*, Vol. 46, No.5, 1034-1045

Chen, D.W and Ray, A. K., 2001. Removal of toxic metal ions from wastewater by semiconductor photocatalysis. *Chemical Engineering Science* 56, No. 4, 1561-1570

Chen, D., Li, F., Ray, A.K., 2001. External and Internal mass transfer effect on photocatalytic degradation. *Catalysis Today* 66, 475-485

Chen, J-Q., Hu, Z-J., Wang, D., Gao, C-J., Ji,R., 2010. Photocatalytic mineralization of dimethoate in aqueous solutions using TiO_2: Parameters and by-products analysis. *Desalination*, doi:10.1016/j.desal.2010.03.053

Chen, H-W., Ku, Y., Kuo, Y-L., 2007. Effect of Pt/TiO_2 characteristics on temporal behavior of o-cresol decomposition by visible light-induced photocatalysis. *Water Research* 41, 2069- 2078

Chen, J., Wang, D., Zhu, M., Gao, C., 2007. Photocatalytic degradation of dimethoate using nanosized TiO_2 powder. *Desalination* 207, 87–94

Chen, H. C., Patel, V.C., 1988. Near wall turbulence models for complex flows including separation. *AIAA* Journal 26, 641-648

Chiou, C-H., Wu, C-Y., Juang, R-S., 2008. Influence of operating parameters on photocatalytic degradation of phenol in UV/TiO_2 process. *Chemical Engineering Journal* 139, 322-329

Cheng, Y., Sun, H., Jin, W., Xu, N., 2007. Photocatalytic degradation of 4-chlorophenol with combustion synthesized TiO_2 under visible light irradiation. *Chemical Engineering Journal* 128, 127–133

Clark, M. M., 1996. Transport Modeling for Environmental Engineers and Scientists. New York: John Wiley & Sons.

Cooper, S., Coronella, C.J., 2005. CFD simulations of particle mixing in a binary fluidized bed. *Power Technology* 151, 27-36

Cox, S., 2007.Design and analysis of a photocatalytic bubble column reactor. PhD thesis, The University of New South Wales

Cong, Y., Zhang, J., Chen, F., Anpo, M., 2007. Synthesis and characterization of nitrogen-doped TiO_2 nanophotocatalyst with high visible light activity. *Journal of Physical Chemistry* C 111, 6976-6982

Cui, Z., Taha, T., 2003.Enhancement of ultrafiltration using gas sparging: a comparison of different membrane modules. *Journal of Chemical Technology and Biotechnology* 78, 249-253, doi: 10.1002/jctb.763

Daneshvar, N., Salari, D., Niaei, A., Khataee, A. R., 2006. Photocatalytic degradation of the herbicide erioglaucine in the presence of nanosized titanium dioxide: Comparison and modeling of reaction kinetics. *Journal of Environmental Science and Health* Part B, 41:1273–1290

Daneshvar, N., Aber, S., Dorraji. M. S. S., Khataee, A. R., Rasoulifard, M. H., 2007. Photocatalytic degradation of the insecticide diazinon in the presence of prepared nanocrystalline ZnO powders under irradiation of UV-C light. *Separation and Purification Technology* 58, 91-98

DEH (Department of Environment and Heritage) 2002. Introduction to urban stormwater management in Australia. Prepared under the stormwater initiative of the *living cities* PROGRAM

DEC (Department of Environment Conservation) 2006. Managing urban stormwater: harvesting and reuses, NSW, DEC2006/137

Devi, L. G., Murthy, B. N., 2008. Characterization of M_o doped TiO_2 and its ehnaced photocatalytic activity under visible light. *Catalysis Letters* 215, 320-330

Devi, L.G., Murthy, B.N., Kumar, S.G., 2009a. Photocatalytic activity of $V^{5+,}$ Mo^{6+} and Th^{4+} doped polycrystalline TiO_2 for the degradation of chlorpyrifos under UV/solar light. *Journal of Molecular Catalysis A: Chemical* 308, 174-181

Devi, L.G., Murthy, B. N., Kumar, S.G., 2009b. Photocatalytic degradation of imidachloprid under solar light using metal ion doped TiO_2 nano particles; Influence of oxide state and electronic configuration of dopants. *Catalysis Letters* 130, 496-503

Devi, L.G., Murthy, B.N., 2009. Structural characterization of Th-doped TiO_2 photocatalyst and its extension of response to solar light for photocatalytic oxidation of Oryzalin pesticide: a comparative study. *Central European Journal of Chemistry* 7(1),118-129

Devi, L. G., Krishnamurthy, G., 2009. TiO_2 /$BaTiO_3$ assisted photocatalytic mineralization of diclofp- methyl on UV light irradiation in the presence of oxidizing agents. *Journal of Hazardous Materials* 162, 899-905

Denny, F., Scott, J., Pareek, V., Peng, G,D., Amal, R., 2009. CFD modelling for a TiO_2-coated glass-bead photoreactor irradiated by optical fibres: Photocatalytic degradation of oxalic acid. *Chemical Engineering Science* 64, 1695-1706

Denny, F., Scott, J., Pareek, V., Peng, G-D., Amal, R., 2010. Computational fluid dynamics modelling and optimal configuring of a channelled optical fibre photoreactor. *Chemical Engineering Science* 65 , 5029–5040

Demeestere, K.D., Visscher, A., Dewulf, J., Van Leeuwen, m., Van Langenhove, H., 2004. A new kinetic model for titanium dioxide mediated heterogeneaous photocatalytic degradation of trichloroethylene in gas-phase. *Applied Catalysis, B-Environmental*. 54, 261-274

Dijkstra. M.F.J., Buwalda, H., DeJong, A.W.F., Michorius A., Winkelman, J.G.M., Beenackers, A.A.C.M., 2001. Experimental comparison of three reactor designs for photocatalytic water purification. *Chemical Engineering Science* 56, 547

Dijkstra, M.F.J., Pannoman, H.J., J.G.M Winkelman, J.J., Kelly,A.A., V.M. Beenackers, 2002. Modeling the photocatalytic degradation of formic acid in areactor with immobilized catalyst. *Chemical Engineering Science* 57, 4895-4907

Dillon, P., 2002. Current Issues: Water reclamation, 2002, CSIRO Land and Water

Dutta, K.P., Ray, A.K., 2004. Experimental investigation of Taylor vortex photocatalytic reactor for water purification. *Chemical Engineering Science* 59, 5249-5259

Duran, J.E, Mohseni, M., and Taghipour, F.2010a. Computational Fluid Dynamics Modelling of Immobilized Photocatalytic Reactors for Water Treatment. *AIChE Journal*. Doi. 10.1002/aic.12399

Duran, J.E, Mohseni, M., and Taghipour, F.2010b. Modelling of annular reactors with surface reaction using computational fluid dynamics (CFD). *Chemical Engineering Science* 65, 1201–1211

Duran, J. E., Taghipour, F., Mohseni, M. 2009. CFD modelling of mass transfer in annular reactors. *International Journal of Heat and Mass Transfer* 52, 5390–5401

Duran, J.E., Mohseni, M., and Taghipour, F., 2011a. Design Improvement of Immobilized Photocatalytic Reactors Using a CFD-Taguchi Combined Method. *Industry Engineering and Chemistry Research* 50, 824–831

Duran, J. E., Mohseni,M., and Taghipour,F., 2011b. Evaluation of model parameters for simulating TiO_2 coated UV reactors. *Water Science and Technology* 63 (7), 1366-72

Djebbar, K., Zertal,A., Sehili,T.,2006. Photocatalytic degradation of 2,4-dichlorophenoxy acetic acid and 4- chloro-2-methylphenoxy acetic acid in water by using TiO_2. *Environmental Technology* 27, 1191-1197

Dutta, K. P., Ray, A. K., 2004. Experimental Investigation of Taylor Vortex Photocatalytic Reactor for Water Purification. *Chemical Engineering Science* 59, 5249-5259

Dvoranova, D., Brezova, V., Mazur, M., Malati, M.A.,2002. Investigations of metal-doped titanium dioxide titanium dioxide photocatalysts. *Applied Catalysis B: Enviornmental* 37, 91-105

Eiamsa-ard, S., Promvonge, P., 2008. Numerical study on heat transfer of turbulent channel flow over periodic grooves. *International Communications in Heat and Mass Transfer* 35, 844-852

Elyasi S., Taghipour, F., 2006. Simulation of UV photoreactor for disinfection in Eulerian frame work. *Chemical Engineering Science* 61, 4741-4749

Eriksson, E., Baun, A., Mikkelsen, P.S.; Ledin, A., 2007. Risk assessment of xenobiotics in stormwater discharged to Harrestup ^{Ao}, Denmark. *Desalination* 215, 187-197

Erquez, R., Pichat, P., 2006. Different net effect of TiO_2 sintering temperature on the photocatalytic removal rates of 4-chlorophenol, 4-chlorobenzoic acid and dichloroacetic acid in water. *Journal of Environmental Science and Health* Part A, 41:955–966

Evgenidou, E., Bizani, E., Christophoridis, C., Fytianos,K.,2007. Heterogeneous photocatalytic degradation of prometryn in aqueous solutions under UV–Vis irradiation. *Chemosphere* 68, 1877–1882

Fan, J-W., Liu, J-Y., Hong, J., and Zhang, J., 2009. The synthesis of nanostructure TiO_2 co-doped with N and Fe and their application for micro-polluted source water treatment. *Environmental Technology* 30(13), 1447-1452

Fabiyi, M. E. and Skelton, R. L.2000. On the effect of pulsing conditions on reaction rates in a pulsed baffled tube photoreactor (PBTPR*). Trans IChem E*, 78, Part B, 399-404

Ferziger,J.H., Peric,M.,1999. Computational methods for fluid dynamics. Springer-Verlag, Berlin, 1999

Fernandez, A., G., Lassaletta, V.M. Jimenez, A., Jasto, A.R., Gonzalez-Elipe, J.M., Herrmann, Tahiri, H., Ait-Ichou, Y., 1995. Preparation and characterization of TiO_2 photocatalysis supported on various rigid supports (Glass,Quartz, and stainless steel) Comparative studies of photocatalytic activity in water purification. *Applied Catalysis B: Environmental* 7, 49-63

Fluent-Inc., 2006. FLUENT 6.3 User's *Guide.* Modelling Turbulence. Fluent-Inc. Lebanon, NH, Chap.12

Fresno, F., Guillard. C., Coronado, J., Chovelon, Tudela, D., Soria, J., Herrmann, J., 2005. Photocatalytic degradation of a sulfonylurea herbicide over pure and tin-doped TiO_2 photocatalysis. *Journal of Photochemistry and Photobiology A: Chemistry* 173, 13-20

Galindo, F., Gomez, R., Aguilar, M., 2008. Photodegradation of the herbicide 2,4-dichlorophenoxyacetic acid on nanocrystalline TiO_2-CeO_2 sol-gel catalyst. *Journal of Molecular Catalysis A: Chemical* 281, 119-125

Garcia, A., Arques, A., Vicente, R.., Domenech, A., Amat, A.M., 2008. Treatment of Aqueous solutions containing four commercial pesticides by means of TiO_2 solar photocatalysis. *Journal of Solar Energy Engineering* 130, 041011-5

Garcia, A., Amat, A.M; Arques, A., Sanchis, R., Gernjak, W., Maldonado, M.I., Oller, I., Malato, S., 2006. Detoxification of aqueous solution of herbicide"Sevnol" by solar photocatalysis. *Environmental Chemistry Letters* 3, 169-172

Garcia, J.C., Takashima, K., 2003. Photocatalytic degradation of imazaquin in an aqueous suspension of titanium dioxide. *Journal of Photochemistry and Photobiology A: Chemistry* 155, 215–222

Giri, R.R., Ozaki, H., Ota, S., Taniguchi, S., Takanami, R.,2010. Influence of inorganic solids on photocatalytic oxidation of 2,4-dichlorophenoxy acetic acid with UV and TiO_2 fiber in aqueous solution. *Desalination* 255, 9-14

Glaze, W.H., Kenneke, J.F., Ferry,J.L., 1993. Chlorinated by products from the TiO_2-mediated photodegradation of trichloroethylene and tetrachloroethylene in Water. *Environmental Science and Technology* 27(1), 177-184

Goslich, R., Dillert, R., Bahnemann, D.,1997. Solar water treatment principles and reactors. *Water Science and Technology* 35(4), 137-148

Górska, P., Zaleska, A., Suska, A., Hupka, J.,2009. Photocatalytic activity and surface Properties of carbon- doped titanium Dioxide. *Physicochemical Problems of Mineral Processing* 43, 21–30

Goonetilleke, A., Thomas, E., Ginn, S., Gilbert, D., 2005. Understanding the role of land use in urban stormwater quality management. *Journal of Environmental Management* 74, 31-42

Gorska, P., Zaleska, A., Kowalska, E., Klimczuk, T., Sobczak, J.W., Skwarek, E., Janusz, W., Hupka, J.,2009. TiO_2 photoactivity in vis and UV light: The influence of calcination temperature and surface properties. *Applied catalysis B: Environmental* 84, 440-447

Goswami, D.Y., 1997. A review of engineering developments of aqueous phase solar photocatalytic detoxification and disinfection processes. *Journal of Solar Energy Eng*. 119,101-107

Grace J.R., Taghipour F., 2004. Verification and validation of CFD models and dynamic similarity for fluidized beds. *Power Technology* 139, 99-110

Greens, D. J., Hass, N. C., Faruok B., 2006. Computational fluid dynamics analysis of the effects of reactor configurations on disinfection efficiency. *Water Environment Research* 78, 909-919

Gutailler. G., Valette, J.C., Guillard, C., Paisse, O., Faure, R., 2001. Photocatalysed degradation of cyromazine in aqueous titanium dioxide suspension: Comparison with photolysis. *Journal of Photochemistry and Photobiology A: Chemistry* 141, 79-84

Ha, H.Y., Anderson, M., 1996. Photocatalytic degradation of formic acid via metal-supported titania. *Journal of Environmental Engineering* 122, 217-221

Haque M.M., Muneer, M., Bahnemann, D.W.,2006. Semiconductor-mediated photocatalyzed degradation of a herbicide derivative, chlortoluron, in aqueous suspensions. *Environmental Science and Technology* 40, 4765-4770

Haque, M.M., Muneer, M., 2003. Heterogeneous photocatalysed degradation of a herbicide derivative, isoproturon in aqueous suspension of titanium dioxide. *Journal of Environmental Management* 69, 169–176

Hatt, B., and Deletic, A., Fletcher, T., 2004. Integrated stormwater treatment and re-use Inventory of Austalian practices. *A review of Australian storm water recycling practices.*

HDR (Human Development Report, 2006). Beyond scarcity: power, poverty and the global water crisis. United Nations Development Program (UNDP)

Herrmann, J. 1999. Heterogeneous Photocatalysis: Fundamentals and Applications to the removal of various types of aqueous pollutants. *Catalysis Today* 53, 115-129

Herrmann, J., 2005. Heterogeneous photocatalysis: state of the art and present applications. *Top Catalysis* 34, 49–65

Hjertager, L. K. ann Hjertager, B. H. and Solberg, T. 2005. Experiments and CFD modelling of fast chemical reaction in turbulent liquid flow. *International Journal of Chemical Reaction Engineering*, 3:A55

Hoffman, M.R., Martin S.T., Choi, W; Bahnemann, D.W. 1995. Environmental application of semiconductor photocatalysis. *Chemistry Reviews* 95, 69-96

Hossain, M.M., Raupp, G.B., Hay, S.O., Obee, T.N., 1999. Three-dimensional developing flow model for photocatalytic monolith reactors. *AIChE Journal* 45, 1309-1321

Hong, X., Wang, Z., Cai, W., Lu, F., Zhang, J., Yang, Y., Ma, N., Liu, Y., 2005. Visible-light activated nanoparticle photocatalyst of Iodine-doped titanium dioxide. *Chemistry Materials* 17, 1548-1552

Hurun, D. C., Agrios, A. G., Gray, K. A., Rajh, T and Thurnaur, M. C., 2003. Explaining the enhanced photocatalytic activity of Degussa P 25 mixed-phase TiO_2 using EPR. *Journal of Physical Chemistry* B,107, 4545-4549

Huang, D-G., Liao, S-J., Liu , J-M., Dang, Z., Petrik, L., 2006. Preparation of visible-light responsive N–F- codoped TiO_2 photocatalyst by a sol–gel-solvothermal method. *Journal of Photochemistry and Photobiology A: Chemistry* 184,282–288

Huan, Y., Xuxu, Z., Zhongyi, Y., Feng, T., Beibei, F., Keshan, H., 2007. Preparation of nitrogen- doped TiO_2 nanoparticle catalyst and its catalytic activity under visible light. *Chinese Journal of Chemical Engineering* 15, 802-807

Iliev,V., Tomova,D., Bilyarska, L.,Tyuliev,G.,2007. Influence of the size of gold nanoparticles deposited on TiO_2 upon the photocatalytic destruction of oxalic acid. *Journal of Molecular Catalysis A: Chemical* 263, 32–38

IIiev,V., Tomova,D., Rakovsky,S.,2010. Nanosized N-doped TiO_2 and gold modified semiconductors- photocatalysts for combined UV-visible light destruction of oxalic acid in aqueous solution. *Desalination* doi:10.1016/j.desal.2010.04.058

Imberdorf, G.E., Irazoqui, H,A., Alfano, O.M., Cassano, A.E., 2006. Scaling up from first principles of a phorocatalytic reactor for air pollution remediation. *Chemical Engineering Science* 62, 793-804

Iwasaki, M., Hara, M., Kawada, H., Tada, H., Ito, S., 2000. Cobalt ion-doped TiO_2 photocatalyst response to visible light. *Journal of colloidal and Interface Sci*ence 224(1), 202-204

Jarandehei, A., Visscher, A. D., 2009. Three-Dimensional CFD Model for a Flat Plate Photocatalytic Reactor: Degradation of TCE in a Serpentine Flow Field. *AIChE Journal* 55(2), 312-320

Janex, M. L., Sanoye, P., Do-Quang, Z., Blatchley, E. R., laine, J. M., 1998. Impact of water quality and reactor hydrodynamics on wastewater disinfection by UV: Use of CFD modelling for performance optimization. *Water Science and Technology* 30, 71-78

Jiang Y, Khadilkar MR, Al-Dahhan MH, Dudukovic A.P., 2002. Computational fluid dynamics of multiphase flow in packed-bed reactors: I. K-fluid modelling issues. *AIChE Journal* 48,701-715

Jin,S., Shiraishi.,2004. Photocatalytic activities enhanced for decompositions of organic compounds over metal-photodepositing titanium dioxide. *Chemical Engineering Journal* 97,203-211

Ji, P., Zhang, J., Chen, F., Anpo, M., 2008. Ordered mesoporous CeO_2 synthsized by nanocasting from cubic la 3d mesoporous MC-48 silica: Formation, Characterization and Photocatalytic activity. *Journal of Physical Chemistry* C 112(46), 17809-17813

Ji, P., Zhang, J., Chen, F., Anpo, M., 2009. Study of adsorption and degradation of acid Orange 7 on the surface of CeO_2 under visible light irradiation. *Applied Catalysis B: Enviornmental* 85, 148-154

Kamble, S. P.; Deosarkar, S. P.; Wawant, S.B., Moulin, J.A. Pangarkar, V.G., 2004. Photocatalytic deggradtion of 2, 4-dichlorophenoxyacetic acid using concentrated solar radiation: batch and continuous operation. *Industrial Engineering and Chemistry Research 43*, 8178

Kamble, S.P., Sawant, S.B., Pangarkar, V.G. 2003. Batch and continuous photocatalytic degradation of benzenesulfonic acid using concentrated solar radiation. *Industry Engineering and Chemistry Research* 42, 6705

Kabir, M. F., Ray, A. K., 2003. Performance enhancement of a chemical reactor utilizing flow instability. *Journal of Chemical Technology and Biotechnology* 78, 314–320, DOI: 10.1002/jctb.778

Kader, B. A., 1981. Temperature and concentration profiles in fully turbulent boundary layers. *International Journal of Heat and Mass Transfer* 24, 1541-1544

Kamimura, M., Furukawa, S., Hiratsuji, J., 2002. Development of a simulator for Ozone/UV reactor based on CFD analysis. *Water Science and Technology* 46, 13-19

Kaci, H. M., Lemenand, T., Valle, D. D., Peerhossaini, H. 2009. Effects of embedded streamwise vorticity on turbulent mixing. *Chemical Engineering and Processing* 48, 1457–1474

Kaneco, S., Itoh, K., Katsumata, H., Suzuki, T., Ohta,K.,2009.Titanium dioxide mediated solar photocatalytic degradation of thiram in aqueous solution: kinetics and mineralization, *Chemical Engineering Journal* 148, 50-56

Kaneco, S., Rahman, M.A., Suzuki, T., Katsumata, H., Ohta, K.,2004. Optimization of solar photocatalytic degradation conditions of bisphenol A in water using titanium dioxide. *Journal of Photochemistry and Photobiology A: Chemistry* 163, 419-424

Kato, S., Hirano, Y., Iwata, M., Sano, T., Takeuchi, K., Matsuzawz,S.,2005. Photocatalytic degradation of gaseous sulphur compounds by silver-deposited titanium dioxide. *Applied Catalysis B: Environmental* 57,109-115

Katsumata, H., Sada, M.; Nakaoka, Y., Kaneco, S., Suzuki, T., Ohta,K.,2009. Photocatalytic degradation of diuron in aqueous solution by platinized TiO_2. *Journal of Hazardous Materials* 171(1-3) 1081–1087

Kerdouss F, Bannari A, Proulx P., 2006. CFD modelling of gas dispersion and bubble size in a double turbine stirred tank. *Chemical Engineering Science* 61, 3313-3322

Khun. H. J., Braslavsky S.E., Schmidt. R., 2004. Chemical actinometry (IUPAC technical report). *Pure and Applied Chemistry* 76(12), 2105-2146

Kim, T., Kim, J., Choi, J., Stenstrom, M.K., Zoh, K., 2006. Degradation mechanism and the toxicity assessment in TiO_2 photocatalysis and photolysis of parathion. *Chemosphere* 62, 926–933

Kim, II-K., Ha, H-J., Lee, S-K., Lee, J-K.,2005. Degradation of chlorophenol by photocatalysts with various transition metals. *Korean Journal of Chemical Engineering*., 22(3), 382-386

Kim, D.H., Choi, D-K., Kim, S-J., Lee, K.S., 2008. The effect of phase type on photocatalytic activity in transition metal doped TiO_2 nanoparticles. *Catalysis Communications* 9, 654-657

Konstantinou, I.K., Albanis,T.A,2003. Photocatalytic transformation of pesticides in aqueous titanium dioxide suspensions using artificial and solar light: intermediates and degradation pathways. *Applied Catalysis B: Environmental* 42, 319-335

Koeltzsch, K.,2000. The height dependence of the turbulent Schmidt number within the boundary layer. Atmospheric Environment. 34,1147–1151

Ku Y, Tseng, K.Y, Wang, W.Y., 2005. Decomposition of gaseous acetone in an annular photoreactor coated with TiO_2 thin film. *Water Air Soil Pollution* 168, 313-323

Kusvuran, E., Samil, A., Atanur, O. M., Erbatur, O., 2005. Photocatalytic degradation of di- and tri- substituted phenolic compounds in aqueous solution by TiO_2/UV. *Applied Catalysis B: Environmental* 58, 211-216

Kundu, S., Pal, A., Dikshit, A.K., 2005. UV induced degradation of herbicide 2,4-D: Kinetics,mechanism and effect of various conditions on the degradation. *Separation and Purification Technology* 44, 121-129

Kun, R., Tarjan, S., Oszko, A., Seemann, T., Zollmer, V., Busse, M., Dekany, I.2009. Preparation and characterization of mesoporous N-doped and sulfuric acid treated anatase TiO_2 catalysts and their photocatalytic activity under UV and Vis illumination. *Journal of Solid State Chemistry* 182, 3076-3084

Kuo, C-Y., Wu, C-H., Lin, H-Y., 2010. Photocatalytic degradation of bisphenol A in a visible light/TiO_2 system. *Desalination* 256, 37–42

Ku Y, Tseng, K.Y., Wang, W.Y., 2005. Decomposition of gaseous acetone in an annular photoreactor coated with TiO2 thin film. *Water Air Soil Pollution* 168, 313- 323

Lamping SR, Zhang H, Allen B, Shamlou PA., 2003. Design of a prototype miniature bioreactor for high throughput automated bio processing. *Chemical Engineering Science* 58, 747-758.

Launder, B.E., Spalding. D.B., 1974. The numerical computational of turbulent flow. *Computer Methods in Applied Mechanics and Engineering* 3,269-289

Lapertot, M., Pichat, P., Sandra Parra, S., Guillard, C., Pulgarin, C.,2006.Photocatalytic Degradation of *p*-Halophenols in TiO_2 Aqueous Suspensions: Halogen Effect on Removal Rate, Aromatic Intermediates and Toxicity Variations. *Journal of Environmental Science and Health* Part A, 41:1009–1025

Lachheb, H., Houas, A., Herrmann, J-M., 2008. Photocatalytic degradation of polynitrophenols on various commercial suspended or deposited titania catalyst using artificial and solar light. *International Journal of Photoenergy*. Article ID 497895. Doi: 1155/2008/497895

Lathasree, S., Rao, A.N., Siva Samlor, B., Sadasivam, V., Rengaraj, K., 2004. Heterogeneous photocatalytic mineralization of phenols in aqueous solutions. *Journal of Molecular Catalysis A: Chemical* 223, 101-105

Lea,J. Adesina, A.A 1998. The photooxidative degradation of sodium dodecyle sulphate in aerated aquous TiO_2 suspension. *Journal of Photochemistry and Photobiology A: Chemistry* 118, 111-122

Lee, W., Do, Y.R., Dwight, K., Wold,A.,1993. Enhancement of photocatalytic activity of Titanium (IV) oxide with Molybdenum(VI)oxide. *Materials Research Bulletin* 28(11), 1127-1134

Lee, C.C.H. 1995. Photocatalytic degradation of aqueous-phase organic contaminants in a fluidized bed reactor. M.Sc thesis, Chemical Engineering, University of Waterloo

Lee, S., Yun,C.Y., Hahn,M.S., Lee,J., Yi,J.,2008. Synthesis and characterization of carbon-doped titania as a visible-light-sensitive photocatalyst. *Korean Journal of Chemical Engineering* 25(4), 892-896

Legrini, O., Oliveros, E., Braun, A.M., 1993. Photochemical process for water treatment. *Chemistry Reviews* 93, 671–698

Lettmann. C., Hildenbrabd, K., Kisch, H., Macyk, W., Maier, W.F., 2001. Visible light photodegradation of 4-chlorophenol with a coke-containing titanium dioxide photocatalyst. *Applied Catalysis B; Environmental* 32, 215-227

Lhomme, L, Brosillon. S., Wolbert,D., 2008. Photocatalytic degradation of pesticides in pure water and a commercial agricultural solution on TiO_2 coated media. *Chemosphere* 70, 381–386

Lifen, G., Jing, Z., Jinbin, Z., Wenfeng, C., Xi, C., Xiaoru, W., 2009. Photocatalytic degradation of dicofol and pyrethrum with boric and cerous co-doped TiO_2 under light irradiation. *Chinese Journal of Chemistry* 27, 88-92

Linder, M., Theurich, J., Bahnemann, D.W., 1997. Photocatalytic detoxification of organic compounds: Accelerating the Process Efficiency. *Journal of ASME-Solar Eng*. 95,399-408

Lin, H.F., Valasaraj, K.T., 2006. An optical fiber monolith reactor for photocatalytic wastewater treatment. *AIChE, Journal* 52, 2271-2280

Lin, Y-J., Tseng, S-L., Huang, W-J., and Wu, W-J.,2006. Enhanced Photocatalysis of pentachlorophenol by metal-modified titanium(IV) oxide. *Journal of Environmental Science and Health* Part B 41, 1143-1158

Lin, C-F., Wu,C-H., Onn,Z-N.,2008. Degradation of 4-chlorophenol in TiO_2, WO_3, SnO_2, TiO_2/WO_3 and TiO_2/SnO_2 systems. *Journal of Hazardous Materials* 154, 1033–1039

Lin, C., Lin, K.,2007. Photocatalytic oxidation of toxic organohalides with TiO_2/UV: The effects of humic substances and organic mixtures. *Chemosphere* 66, 1872–1877

Li,X., Liu,S.,2008. Characterization of visible light response N-F codoped TiO_2 photocatalyst prepared by acid catalyzed hydrolysis. *Acta Physico-Chimica Sinica* 24(11), 2019-2024

Liqiang, J., Xiaojun, S., Baifu, X., Baiqi, W., Weimin, C., Hongganga, F.,2004. The preparation and characterization of La doped TiO_2 nanoparticles and their photocatalytic activity. *Journal of Solid State Chemistry* 177, 3375–3382

Liqiang, J., Dejun ,W., Baiqi, W., Shudan, L., Baifu, X., Honggang, F., Jiazhong,S.,2006. Effects of noble metal modification on surface oxygen composition, charge separation and photocatalytic activity of ZnO nanoparticles. *Journal of Molecular Catalysis A: Chemical* 244, 193–200

Litter, M. I., 1999. Heterogeneous photocatalysis: Transition metal ions in photocatalytic systems. *Applied Catalysis B: Environmental* 23 (2-3): 89-114

Liu, D., Ducoste,J., Wu,C.,& Linden,K.G.2007. Numerical Simulation of UV Disinfection Reactors: Evaluation of Alternative turbulence Models. *Applied Mathematical Modelling* 31, 1753-1769

Liu, Y., & Ducoste, J. 2006. Numerical Simulation of Chloramines Formation in Turbulent Flow Using a Multi-Fluid Micromixing Model. *Environmental Modelling & Software, 21*, 1198-1213

Liu,S.X., Peng, M., Vane,L.M. 2005. CFD simulation of effect of baffle on mass transfer in a slit-type pervaporation module. *Journal of Membrane Science* 265, 124–136

Liu, Y., Feng, H., Olsen, M. G., Fox, R. O., Hill,J.C.2006. Turbulent mixing in a confined rectangular wake. *Chemical Engineering Science* 61, 6946-6962

Liu,Y., He,G., Liu,X., Xiao,G., Li,B., 2009. CFD simulations of turbulent flow in baffle-filled membrane tubes. Separation and Purification Technology 67, 14–20

Liu,W., Chen,Shifu, Zhao,W., Zhang,S.,2009. Study on the photocatalytic degradation of trichlorfon in suspension of titanium dioxide. *Desalination*, doi:10.1016/j.desal.2008.12.058

Li,X., Liu,S.,2008. Characterization of visible light response N-F codoped TiO_2 photocatalyst prepared by acid catalyzed hydrolysis. *Acta Physico-Chimica Sinica* 24(11), 2019-2024

Lukac,J., Klementora, M., Bezdicka, P., Bakardjieva,S., Subrt, J., Szatmay,L., Bastl,Z., Jirkovsky,J.,2007. Influence of Zr and TiO_2 doping ion on photocatalytic degradation of 4-chlorophenol. *Applied Catalysis B: Environmental* 74, 83-91

Low, G., Mathews, R.W. 1990. Flow- injection determination of organic contaminants in water using an ultraviolet mediated titanium dioxide film reactor. *Analytica Chimica Acta* 231(1), 13-20

Ma, C.M., Ku, Y., 2006. Photocatalytic oxidation trichloroethylene by UV/TiO_2 process. *Reaction Kinetics and Catalysis Letters* 89, 293-301

Malato, S., Blanco, J. Vidal A., Alarcon D., Maldonado, M.I., Caceres, J., Gernjak,W.,2003. Applied studies in solar photocatalytic detoxification; An Overview. *Solar Energy* 75, 329-336

Malato, S., Blanco, J., Maldonado, M.I., Fernandez, P., Alarcon,D., Collares, M., Farinha, J., Correia, J., 2004. Engineering of solar photocatalytic collectors. *Solar Energy* 77,513-524

Malato, S., Blanco, J., Alarcon, D., Maldonado, M., Fernandez, P., Gernjak, W., 2007. Photocatalytic decontamination and disinfection of water with solar collectors. *Catalysis Today* 122, 137-149

Malato, S., Blanco, J., Vidal, A., Richter, C., 2002. Photocatalysis with solar energy at a pilot- plant scale: an overview. *Applied Catalysis B: Environment* 37, 1-15

Mathews, R.W., 1986. Photo-oxidation of organic material in aqueous suspension of titanium dioxide. *Water Research* 20(5), 569-78

Mathews, R.W., 1987. Photo-oxidation of organic impurities in water using thin film of TiO_2. *Journal of Physical Chemistry* 91, 3328-33

Mathews, R.W., 1988. Kinetics of photocatalytic oxidation of organic solutes over TiO_2. *Journal of Catalysis* 111, 264-272

Mathews, R.W., 1991. Photooxidative degradation of colored organics in water using supported catalysts,TiO_2 on sand. *Water Research* 25, No.10, 1169-1176

Mathews, R.W., 1990. Purification of water with near-UV illuminated suspensions of titanium dioxide. *Water Research* 24(5), 653-660

Madani, M.E., Guillard C, Perol N, Chovelon, J.M.; El Azzouzi,M. Zrineh A, Herrmann J.M., 2006. Photocatalytic degradation of diuron in aqueous solution in presence of two industrial titania catalysts, either as suspended powders or a deposit on flexible industrial photoresistant papers. *Applied Catalysis B: Environment* 65, 70-76

Mahmoodi, N.M., Armani, M., Lymaee, N. Y. Gharanjig, K.,2007.Photocatalytic degradation of agricultural N-heterucyclic organic pollutants using immobilized nanoparticles of titania. *Journal of Hazardous Materials* 145(1-2), 65-71

Mahalakshmi, M., Arabindoo, B., Palanichamy, M., Murugesan,V., 2007. Photocatalytic degradation of carbofuran using semiconductor oxides. *Journal of Hazardous Materials* 143, 240–245

Marinas, A., Guillard, C., Marinas, J. M., Fernandez-Alba., Aguera, A., Herrmann, J-M., 2001. Photocataltic degradation of pesticide-acaricide formetanate in aqueous suspension of TiO_2. *Applied Catalysis B: Environmental* 34,241-252

Marshall, E. M., Bakker, A., 2004. Computational Fluid Mixing, in Handbook of Industrial Mixing: Science and Practice (eds E. L. Paul, V. A. Atiemo-Obeng and S. M. Kresta), John Wiley & Sons, Inc., Hoboken, NJ, USA. doi: 10.1002/0471451452.ch5

McMurray, T.A., Byrne, J.A., Dunlop, P.S.M., Winkelman, J.G.M., Eggins, B.R., McAdams, E.T., 2004. Intrinsic kinetics of photocatalytic oxidation of formic and oxalic acid on immobilised TiO_2 films. *Applied Catalysis A: General* 262, 105–110

McMurray, T.A., Dunlop, P.S.M., Byrne, J.A., 2006. The photocatalytic degradation of atrazine on nanoparticulate TiO_2 films. *Journal of Photochemistry and Photobiology A: Chemistry* 182, 43–51

Mehrotra, K., Ray, A.K., 2003.Performance enhancement of photocatalytic reactor utilizing flow instability. *International Journal of Chemical Reactor Engineering* 1, Article A_{12}

Meng, Y., Chen, J., Wang, Y., Ding, H. Shan,Y.,2009. (N,F)-codped TiO_2 nanocrystals as visible light - activated photocatalyst. *Journal of Material Science Technology* 25(1), 73-76

Methos, M.S., Turchi, C.S., 1993. Field testing solar photocatalytic detoxification on TCE contaminated ground water. *Environmental progress* 12, No.3, 194-199

Mohseni M, Taghipour F., 2004. Experimental and CFD analysis of photocatalytic gas phase vinyl chloride(VC) oxidation. *Chemical Engineering Science* 59, 1601-1609

Moctezuma, E., Leyva, E., Palestino,G., Lasa, H.D.,2007. Photocatalytic degradation of methyl parathion: Reaction pathways and intermediate reaction products. *Journal of Photochemistry and Photobiology A: Chemistry* 186, 71–84

MOU, 2009, http://www.minerals.org.au, (accessed on 6th July, 2009)

Mitchell, V.G., Mein, R.G., Mcmahon, T. A., 2002. Utilising storm water and wastewater resources in urban areas. *Australian Journal of Water Resources* 6, 31-43

Mukherjee, P.S., Ray, A. K., 1999. Major challenges in the design of a large-scale photocatalytic reactor for water treatment. *Chemical Engineering Technology* 22, pp 253-260

Mijin, D., Savic, M., Snezana, P., Smiljanic, A., Glavaski, O., Jovanovic, M., Petrovic, S., 2009. A study of the photocatalytic degradation of metamitron in ZnO water suspensions. *Desalination* 249, 286-292

Mukherjee, P.S., Ray, A. K., 1999. Major challenges in the design of a large scale photocatalytic reactor for water treatment. *Chemical Engineering Technology* 22, 253-260

Mills, A., Morris,S .,1993.Photo-mineralization of 4-chlororphenol sensitized by titanium dioxide: a study of the initial kinetics of carbon dioxide photo-generation. *Journal of Photochemistry and Photobiology A: Chemistry* 71, 75-83

Muneer, M., Qamar,M.; Saquib,M., Bahnemann,D.,2005. Heterogeneous photocatalysed reaction of three selected pesticide derivatives, propham, propachlor and tebuthiuron in aqueous suspensions of titanium dioxide. *Chemosphere* 61, 457–468

Munner, M.,Bahnemann,D.,2002. Semiconductor-mediated photocatalysed degradation of two selected pesticide derivatives, terbacil and 2,4,5-tribromoimidazole, in aqueous suspension. *Applied Catalysis B: Environmental* 36, 95-111

Naeem, K., Feng, O.,2008. Parameters effect on hetereogeneous photocatalysed degradation of phenol in aqueous dispersion of TiO_2. *Journal of Environmental Science* 21, 527-533

Naeem, K., and Ouyang,F.,2009. Preparation of Fe^{3+}-doped TiO_2 nanoparticles and its photocatalytic activity. *Physica B: Condensed Matter* 405(1), 221-226

Nahar, M. S., Hasegawa,K., Kagaya,S.,2006.Photocatalytic degradation of phenol by visible light-responsive iron-doped TiO_2 and spontaneous sedimentation of the TiO_2 particles. *Chemosphere* 65,1976-1983

Nelissen, G., Van den Bossche, B., Deconinck, J., Theemsche, A. V., Dan,C.,2003. Laminar and turbulent mass transfer simulations in a parallel plate reactor, *Journal Applied Electrochemical* 33, 863–873

Nghiem, L. D., Schäfer,A.I.,2006.Critical risk points of nanofiltration and reverse osmosis processes in water recycling applications. *Desalination* 187, 303–312

Okamoto, K., Yamamoto, Y., Tanaka, H., Tanaka,M., Itaya, A., 1985a. Hetereogeneous photocatalytic decomposition of phenol over TiO_2 powder. *Bulletin of Chemical Society in Japan* 58, 2015-202

Okamoto, K., Yamamoto, Y., Tanaka, H., Tanaka, M., Itaya, A., 1985b. Kinetics of heterogeneous photocatalytic decomposition of phenol over anatase TiO_2 powder. *Bulletin of Chemical Society in Japan* 58, 2023-2038

Ohko, Y., Hashimoto, K., Fujishima, A.1997. Kinetics of photocatalytic reactions under extremely low-intensity UV illumination on titanium dioxide thin films. *Journal of Physical Chemistry* 101, 8057-8062

Ollis D.F., Pelizzetti E, Serpone N., 1991. Destruction of water conatminants. *Environmental Science and Technology* 25(9), 1523-9

Ollis, D.F., C. Turchi,C., 1990. Hereogeneous photocatalysis for water purification: Contaminant mineralization kinetics and elementary reactor analysis. *Environmental Progress* 9(4), 229-234

Ollis, D.F., 1991. Solar-assisted photocatalysis for water purification: issues, data, questions, in: E. Pelizzeti, M. Schiavello (Eds.). *Photochemical Conversion and Storage of Solar Energy*. Kluwer Academic Publishers. The Netherlands, 593-622

Parent, Y., Blake, D. Magrini, B. K., Lyons, C., Turchi, A., Watt, E, Wolfrum, M. Praire, 1996. Solar photocatalytic process for the purification of water: State of development and barriers to commercialization. *Solar Energy* 56, 429-437

Pareek, V.K., Adesina, A.A.2003. Analysis of photocatalytically reactive systems: kinetic modelling and reactor design via computational fluid dynamics. *Handbook of Photochemistry Photobiology* 1, 345-412

Pareek, V.K., Cox, S.J., Brungs, M.P., Young, B., Adesina, A.A., 2003. Computational fluid dynamic(CFD) simulation of a pilot scale annular bubble column photocatalytic reactor. *Chemical Engineering Science* 58, 859-865

Pareek, V.K., Adesina, A.A., 2004. Light intensity distribution in a photocatalytic reactor using finite volume. *AIChE Journal* 50(6), 1273-1288

Pareek, V., 2005. Light Intensity distribution in a dual-lamp photocatalytic reactor. *International Journal of Chemical Reactor Engineering* 3, Article 56

Pareek, V., Chong, S., Tade, M., Adesina, A., 2008. Light intensity distribution in heterogeneous photocatalytic reactors. *Asia-Pacific Journal of Chemical Engineering* 3,171-201

Pardeshi, S. K., Patil, A.B., 2009. Effect of morphology and crystallite size on solar photocatalytic activity of zinc oxide synthesized by solution free mechanochemical method. *Journal of Molecular Catalysis A: Chemical* 308, 32–40

Pardeshi, S. K., Patil, A.B., 2008. A simple route for photocatalytic degradation of phenol in aqueous zinc oxide suspension using solar energy. *Solar Energy* 82, 700-705

Parida, K.M., Parija,S., 2006. Photocatalytic degradation of phenol under solar radiation using microwave irradiation zinc oxide. *Solar Energy* 80, 1048-1054

Parida, K. M., Dash, S. S., Das, D.P., 2006. Physico-chemical characterization and photocatalytic activity of zinc oxide presented by various methods. *Journal of Colloid and Interface Science* 298,787- 793

Parida, K. M., Sahu, N., Biswal, N. R., Naik, B., Pradhan, A.C., 2008. Preparation, characterization, and photocatalytic activity of sulfate-modified titania for degradation of methyl orange under visible light. *Journal of Colloid and Interface Science* 318, 231–237

Park, J-H., 2009. Photochemical degradation and toxicity reduction of methyl1-[butylamino] carbonyl]-1H- benzimidazol-2-ylcarbamate in agricultural wastewater: Comparative study of photocatalysis and sonophotocatalysis. *Desalination* 249, 480-485

Park, Y., Kim, W., Park, H., Tachikawa, T. Majima, T., Choi,W.,2009. Carbon-doped TiO_2 photocatalyst synthesized without using an external carbon precursor and the visible light activity. *Applied Catalysis B: Environmental* 91, 355–361

Pacheco, J., Watt, A. S., Turchi, C.S. 1993. Solar detoxification of water: Outdoor testing of prototype photoreactors. *ASME-Solar Engineering* 93, 43-49

Parra, S., Elena Stanca,S., Guasaquillo,I., Thampi,K.R., 2004.Photocatalytic degradation of atrazine using suspended and supported TiO_2. *Applied Catalysis B: Environmental* 51,107-116

Peiro, A.M., Ayllon,J.A., Peral,J., Domenech,X.,2001. TiO_2-photocatalysed degradation of phenol and ortho-substituted phenolic compounds. *Applied Catalysis B; Environmental* 30,359-373

Periyathamby, U and Ray, A. K., 1999. Computer simulation of a novel photocatalytic reactor using distributive computing. *Chemical Engineering Technology* 22,253-260

Perry, R. H., Green, D. W. *Perry's Chemical Engineers' Handbook*, 7th ed.; McGraw-Hill: New York, 1997

Pizarro P., Guillard, C., Perol,N., Herrmann,J.M.,2005. Photocatalytic degradation of imazapyr in water: Comparison of activities of different supported and unsupported TiO_2-based catalysts. *Catalysis Today* 101,211–218

Poulios, I., Kositzi, M., 2006. Photocatalytic oxidation of methomyl in the presence of semi conducting oxides. *International Journal of Environment and Pollution* 28(1/2), 33-44

Pourata, R., Khataee, A. R., Aber,S., Daneshvar,N.,2009. Removal of the herbicide Bentazon from contaminated water in the presence of synthesized nanocrystalline TiO_2 powders under irradiation of UV-C light. *Desalination* 249,301–307

Priya, M. H., Madras, G., 2006. Photocatalyticdegradton of nitrobenzenes with combustion syntheiszed nano-TiO_2. *Journal of Photochemistry and Photobiology A: Chemistry* 178,1-7

Puma, G. L., Yue, P.l., 2002. Effect of the radiation wavelength on the rate of photocatalytic oxidation of organic pollutants. *Industrial Engineering and Chemistry Research* 41, 5594-5600

Pugh, K. C., Kiserow, D. J., Sullivan, J. M., Grinstead Jr., J.H., 1995. Photocatalytic destruction of atrazine using TiO_2 mesh. *Emerging Technologies in Hazardous Waste Management* V, 174-194

Qamar,M., Muneer,M., Bahnemann,D.,2006. Heterogeneous photocatalysed degradation of two selected pesticide derivatives, triclopyr and daminozid in aqueous suspensions of titanium dioxide. *Journal of Environmental Management* 80, 99–106

Qamar, M., Muneer, M.,2005. Comparative photocatalytic study of two selected pesticide derivatives, indole-3-acetic acid and indole-3-butyric acid in aqueous suspensions of titanium dioxide. *Journal of Hazardous Materials* B120,219–227

Qamar, M., Muneer, M., 2009. A comparative photocatalytic activity of titanium dioxide and zinc oxide by investigating the degradation of vanillin. *Desalination* 249, 535-540

Ranade,V.V., 2002. Computational flow modelling for chemical reactor engineering. Academic Press, London, (Chap.3)

Radcliffe, J.C., 2004. Water recycling in Australia. Australian Academy of Technological Sciences and Engineering, Melbourne, 2004, *http:www.atse.orge.au/index.php?sectioned:597*

Radcliffe, J.C., 2006. Future directions for water recycling in Australia. *Desalination* 187,77-87

Rao, K. V. S., Subrahmanyam, M., Boule, P., 2004. Immobilized TiO_2 photocatalyst during long- term use: decrease of its activity. *Applied Catalysis B: Environmental* 49, 239-249

Raupp, G., Aleaxiadis, A., Hossain,M., Changrani,R., 2001. First-principles modelling, scaling laws and design of structured photocatalytic oxidation reactors for air purification. *Catalysis Today* 69, 41-49

Rahimi, M., Shabanian, S.R., Alsairafi, A.A.,2009. Experimental and CFD studies on heat transfer and friction factor characteristics of a tube equipped with modified twisted tape inserts. *Chemical Engineering and Processing* 48, 762-770

Ray, A.K., Beenackers, A.A.C.M., 1997. Novel swirl-flow reactor for kinetic studies of semiconductor photocatalysis. *AIChE Journal* 43(10), 2571-2578

Ray, A.K., Beenackers.A.A.C.M.,1998. A Novel photocatalytic reactor for water purification. *AIChE Journal* 44(2), 477-483

Ray, A.K., 1998. A new photocatalytic reactor for destruction of toxic water pollutants by advanced oxidation process. *Catalysis Today* 44, 357

Ray, A.K., 1999. Design, modelling and experimentation of a new photocatalytic reactor for water treatment. *Chemical Engineering Science* 54(16), 3113-3125

Rahman, M., Muneer, M., Bahnemann, D.,2003. Photocatalysed degradation of a herbicide derivative, a diphenamid in aqueous suspension of titanium dioxide. *Journal of Advanced Oxidation Technology* 6(1), 100-107

Rahman, M.A., Muneer, M.,2005a. Heterogeneous photocatalytic degradation of picloram, dicamba, and floumeturon in aqueous suspensions of titanium dioxide. *Journal of Environmental Science and Health* 40, 247-267

Rahman, M.A., Muneer, M.,2005b. Photocatalysed degradation of two selected pesticide derivatives, dichlorvos and phosphamidon, in aqueous suspensions of titanium dioxide, *Desalination* 181,161-172

Rahman, M. A., Qamar, M.,Muneer, M., Bahnemenn,D.,2006. Semicondcutor mediated photocatalysed degradation of a pesticide derivative, acephate in aqueous suspensions of titanium dioxide. *Journal of Advanced Oxidation Technology* 9(1), 103-109

Rabindranathan, S., Devipriya, S., Yesodharan, S.,2003. Photocatalytic degradation of phosphamidon on semiconductor oxides. *Journal of Hazardous Materials* B102, 217–229

Reddy, J. N., Gartling, D. K., 1994, The finite element method in heat transfer and fluid dynamics, Boca Raton, FL: CRC Press.

Reeves, P., Ohlhausen, R., Sloan, D., Pamplin, K., Scoggins, T., Clark, C., Hutchinson, B., Green, D., 1992. Photocatalytic destruction of organic dyes in aqueous suspensions using concentrated simulated and natural solar energy. *Solar Energy* 48 (6), 413-420

Rengaraj, S., Li, X.Z., 2006. Photocatalytic degradation of bisphenol A as an endocrine disruptor in aqueous suspension using Ag-TiO_2 catalysts. *International Journal of Environment and Pollution* 27(1/2/3), 20-37

Rengaraj, S., Li, X. Z., Tanner, P. A., Pan, Z. F., Pang, G.K. H., 2005. Photocatalytic degradation of methylparathion-An endocrine disruptor by Bi^{3+}-doped TiO_2. *Journal of Molecular Catalysis A: Chemical* 247, 36-43

Rengifo-Herrera,J.A., Pulgarin,C.,2009. Photocatalytic activity of N, S co-doped and N-doped commercial anatse TiO_2 powders towards phenol oxidation and E. *coli* inactivation under simulated solar light irradiation. *Solar Energy*, Doi: 10.1016/j. solener. 2009.09.08

Rockafellow, E.R., Stewart, L.K., Jenks,W.S.,2009. Is sulphur-doped TiO_2 an effective visible light photocatalyst for remediation. *Applied Catalysis B: Environmental* 91, 554-562

Rosen, C., Traegaardh,C.,1995. Prediction of turbulence high Schmidt number mass transfer using a low Reynolds number k–e turbulence model. *Chemical Engineering Journal* 59, 153-159

Romero, R. L., Alfano, O.M., Cassano, A.E., 1997. Cylindrical photocatalytic reactors, radiation absorption and scattering effects produces by suspended fine particles in an annular space. *Industry Engineering and Chemistry Research* 36, 3094-3109

Sabate, J., Anderson, M. A., Kikkawa, H., Edwards, M, M ., Hill Jr., C.G(1991). A kinetic study of the photocatalytic degradation of 3- Chlorosalicyclic Acid over TiO_2 membranes supported on glass. *Journal of Catalysis*, 127,167-77

Salah, N.H., Bouhelassa, M., Bekkouche, S., Boultif, A., 2004.Study of photocatalytic degradation of phenol. *Desalination* 166, 347-354

Salvado-Estivill, I, Hargreaves, D.M., Puma, G.L, 2007. Evaluation of the intrinsic photocatalytic oxidation kinetics of indoor air pollutants. *Environmental Science and Technology* 41, 2028-2035

Sanchez, E., Lopez, T., 1995. Effect of the preparation method on the bandgap of titania and platinum-titania sol-gel materials. *Materials Letters* 25(5-6), 271-275

Saien, J., Khezrianjoo, S. 2008. Degradation of the fungicide carbendazim in aqueous solutions with UV/TiO_2 process: Optimization, kinetics and toxicity studies. *Journal of Hazardous Materials* 157, 269–276

Sakthivel, S., Neppolian,B., Shankar,M.V., Arabindo,B.,Palanichamy,M.,Murugesan,V.,2003. Solar photocatalytic degradation of azo dye: comparison of photocatalytic efficiency of ZnO and TiO_2. *Solar Energy Materials Solar Cell* 77, 65-82

Sayeh, A., Coulomb, B., Boudenne, J.L., Belkadis, F., 2007.Elimination of pollutants phenyl urea herbicides by advanced oxidation process in aqueous solution. *Journal of Engineering and Applied Sciences* 2(4), 664-670

Senthilnathan, J., Philip, L., 2010. Photocatalytic degradation of lindane under UV and visible light using N-doped TiO_2. *Chemical Engineering Journal*, doi: 10.1016 /j.cej. 2010.04.034

Sengupta, T., Kabir, M.F., Ray, A.K., 2001. A Taylor vortex photocatalytic reactor for water purification. *Industry Engineering and Chemistry Research* .40, 5268-5281

Serrano, B., de Lasa, H.,1997. Photocatalytic degradation of water organic pollutants: Kinetic modelling and energy efficiency. *Industry Engineering and Chemistry Research*, 36, 4705-4711

Selvam, K., Muruganandham, M., Muthuvel,I., Swaminathan,M.,2007. The influence of inorganic oxidants and metal ions on semiconductor sensitized photodegradtion of 4-flurophenol. *Chemical Engineering Journal* 128, 51-57

Senthilnathan, J., Philip,L., 2009. Removal of mixed pesticides from drinking water system by photodegradation using suspended and immobilized TiO_2. *Journal of Environmental Science and Health* Part B 44,262-270

Shaw, C.T., 1992. Using computational fluid dynamics. Prentice Hall International (UK) Ltd.

Sherwood, T.K., Pigford, R.L., Wilke, C. R. *Mass Transfer*. 1975, New York: McGraw-Hill.

Shafaei, A., Nikaza, M., Arami, M., 2010. Photocatalytic degradation of terephthalic acid using titania and zinc oxide photocatalysts: Comparative study. *Desalination* 252, 8–16

Sakthivel, S., Janczarek, M. Kisch, H., 2004. Visible light activity and photoelectrochemical properties of Nitrogen-doped TiO_2. *The Journal of Physical Chemistry* B, 108(50), 19384-19387

Shankar, M.V., Anandan, S., Venkatachalam, N., Arabindoo, B., Murugesanm, V., 2006. Fine route for an efficient removal of 2,4-dichlorophenoxyacetic acid(2,4-D) by zeolite-supported TiO_2. *Chemosphere* 63, 1041-1021

Sharma, M.V.P., Kumari,D., Subrahmanyam,M., 2008a. TiO_2 supported over SBA-15: An efficient photocatalyst for the pesticide degradation using solar light. *Chemosphere* 73, 1562–1569

Sharma,.M.V.P., Kumari,D., Subrahmanyam M.,2008b. Photocatalytic degradation of isoproturon herbicide over TiO_2/Al-MCM-41 composite systems using solar light. *Chemosphere* 72, 644–651

Sharma, M.V.P., Sadanandam, G., Ratnamala, A., Kumari,V., Subrahmanyam, M., 2009. An efficient and novel porous nanosilica supported TiO_2 photocatalyst for pesticide degradation using solar light. *Journal of Hazardous Materials* 171, 626–633

Shifu, C., Yunzhang, L.,2007. Study on the photocatalytic degradation of glyphosate by TiO_2 photocatalyst. *Chemosphere* 67, 1010–1017

Shifu, C., Gengyu, C., 2005. Photocatalytic degradation of pesticides using floating photocatalyst TiO_2.SiO_2 beads by sunlight. *Solar Energy* 79,1-9

Shih, T.H., Liou, W.W., Shabbir, A., Yang, Z., Zhu, J., 1995. A new k-ε eddy viscosity model for high Reynolds number turbulent flows model development and validation. *Computers Fluids* 24, 227–238

Silva, A. M.T., Silva,C. G., Draz¡ic,G., Faria,J.L.,2009. Ce-doped TiO_2 for photocatalytic degradation of chlorophenol. *Catalysis Today* 144, 13–18

Silveyra, R., Torre Sa´enz, L. D., Flores, W.A., Martý´nez,V.C., Elgue´zabal,A.A., 2005. Doping of TiO_2 with nitrogen to modify the interval of photocatalytic activation towards visible radiation. *Catalysis Today* 107–108, 602–605

Singh,H.K.., Muneer,M., Bahnemann, D.,2003. Photocatalysed degradation of a herbicide derivative, bromacil, in aqueous suspensions of titanium dioxide. *Photochemistry Photobiology Science* 2, 151-156

Singh, H. K., Muneer, M., 2004. Photodegradation of a herbicide derivative, 2, 4-dichlorophenoxy acetic acid in aqueous suspensions of titanium dioxide. *Research on Chemical Intermediates* 30(3), 317-329

Singh, H.K., Saquib, M. Haque, M., Muneera, M., Bahnemann, D., 2007a. Titanium dioxide mediated photocatalysed degradation of phenoxyacetic acid and 2,4,5-trichlorophenoxyacetic acid, in aqueous suspensions. *Journal of Molecular Catalysis A: Chemical* 264, 66–72

Singh, H.K., Saquib, M., Haque, M. Muneer.M., 2007b.Heterogeneous photocatalysed degradation of 4- chlorophenoxyacetic acid in aqueous suspensions. *Journal of Hazardous Materials* 142, 374-380

Singh, H.K., Saquib, M., Haque, M., Muneer,M.,2007c. Heterogeneous photocatalyzed degradation of uracil and 5-bromouracil in aqueous suspensions of titanium dioxide. *Journal of Hazardous Materials* 142, 425–430

Sirisaksoontorn, W., Thachepan, S., Songsasen,A.,2009. Photodegradation of phenanthrene by N-doped TiO_2 photocatalyst. *Journal of Environmental Science and Health* Part A 44, 841–846

Sleiman, M., Conchon, P., Ferronato, C., Chovelon, J.M., 2007. Iodosulfuron degradation by TiO_2 photocatalysis: Kinetic and reactional pathway investigations. *Applied Catalysis* B: *Environmental* 71, 279–290

Song. X-M., Wu,J-M., Yan,M.,2009. Photocatalytic degradation of selected dyes by titania thin films with various nanostructures. *Thin Solid Films* 517, 4341-4347

Sonawane, R.S., Dongare, M.K.,2006. Sol-gel synthesis of Au/TiO_2 thin films for photocatalytic degradation of phenol in sunlight. *Journal of Molecular catalysis A: Chemical* 243, 2006, 68-79

Sozzi, D.A., Taghipour, F.2006a. Computational and experimental study of annular photoreactor hydrodynamics. *International Journal of Heat and Mass Flow* 27, 1043-1053

Sozzi, D.A., Taghipour, F. 2006b. UV reactor performance modelling by Eulerian and Lagrangian methods. *Environmental Science and Technology* 40, 1609-1615

Sozzi, D. A .,Taghipour,F. 2007. The importance of hydrodynamics in UV advanced oxidation reactors. *Water Science and Technology* 55(12), 53-58

Šojić, D. V., Despotović, V.N., Abazović, N.D., Mirjana I. Čomor,M.I., Abramović, B.F.,2010. Photocatalytic degradation of selected herbicides in aqueous suspensions of doped titania under visible light irradiation. *Journal of Hazardous Materials* 179, 49–56

Spalding, D.B., 1971. Concentration .uctuations in a round turbulent free jet. *Chemical Engineering Science* 26, 95–107

Spalding, B., 1998. Turbulent Mixing and chemical reaction; the Multi-Fluid Approach (A lecture), from *http://www.simuserve.com/phonics/d_polis/d_lecs?mfm.mfm0*.htm

Stephen, C., Stefan, M.I., Bolton J.R, Safarzadeh, A., 2000. UV/H_2O_2 treatment of methyl tert-butyl ether in contaminated waters. *Environmental Science Technology* 34, 659-662

Stafford, U., Gray, K.A., Kamat,P.V.,1997a. Photocatalytic degradation of 4-Chlorophenol: The Effects of varying TiO_2 Concentration and Light wavelength. *Journal of Catalysis* 167, 25-32

Sripattanapipat, S., Promvonge, P.2009. Numerical analysis of laminar heat transfer in a channel with diamond-shaped baffles. *International Communications in Heat and Mass Transfer* 36, 32–38

Swarnalatha, B., Anjaneyulu,Y.,2004. Studies on the heterogeneous photocatalytic oxidation of 2,6- dinitrophenol in aqueous TiO_2 suspension. *J. Molecular Catalysis A: Chemical* 223, 161–165

Sun, Z. M., Liu, B.T., Yuan, X.G., Liu, C.J., Yu, K. T., 2005. New turbulent model for computational mass transfer and its application to a commercial-scale distillation column. *Industry Engineering and Chemistry Research* 44, 4427–4434

Sun, H., Bai,Y., Liu,H., Jin,W., Xu,N.,2009. Photocatalytic decomposition of 4-chlorophenol over an efficient N-doped TiO_2 under sunlight irradiation. *Journal of Photochemistry and Photobiology A:Chemistry* 201, 15-22

Taghipour, F., Mohseni, M., 2005.CFD simulation of UV photocatalytic reactors for air treatment. *AIChE Journal* 51, 3039-3047

Taghipour, F., Sozzi,A., 2005. Modelling and design of ultraviolet reactors for disinfection by-product precursor removal. *Desalination* 176, 71-80

Taha, T., Cui, Z.F., 2006. CFD modelling of slug flow in vertical tubes. *Chemical Engineering*
Science 61, 676-687

Tada, H., Tanaka, M.1997. Dependence of TiO_2 photocatalytic activity upon its film thickness. *Langmuir* 13, 360-364

Tanaka, K., Hisanaga, T. 1994. Photodegradation of chloroflurocarbon alternatives on metal oxide. *Solar Energy* 52(5), 447-450

Terzian, R., Serpone,N., 1991. Hetergeneous photocatalysed oxidation of creosote components; mineralization of xylenols by illuminated TiO_2 in oxygenated aqueous media. *Journal of Photochemistry and Photobiology A: Chemistry* 89, 163-175

Thiruvenkatachari, R., Vigneswaran, S., Moon, S., 2008. A review on UV/TiO_2 photocatalytic oxidation process. *Korean Journal of Chemical Engineering* 25(1), 64-72

Tian, G., Fu, H., Jing, L., Tian, C., 2009. Synthesis and photocatalytic activity of stable nanocrystalline TiO_2 with high crystallinity and large surface area. *Journal of Hazardous Materials* 161, 1122-1130

Tofteberg, T., Skolimowski, M., Andreassen, E., Geschke, O., 2010. A novel passive micromixer: lamination in a planar channel system. *Microfluid Nanofluid* 8, 209–215 DOI 10.1007/s10404-009-0456-z

Trujillo F.J., Lee, I., Hsu, C., Safinski, T., Adesina. A .A 2008. Hydrodynamically-Enhanced light intensity distroibution in an externally-irradiated novel aerated photoreactor: CFD simulation and Experimental studies. *International Journal of Chemical Reactor Engineering 6, Article 58*

Trujillo F.J., C., Safinski, T., Adesina. A .A 2007. CFD Analysis of the radiation distribution in a new immobilized catalyst bubble column externally-illuminated photoreactor. *Journal of Solar Energy Engineering* 129, 27-36

Trujillo, F.J., Safinski,T., Adesina,A. A. 2009. Solid–liquid mass transfer analysis in a multi-phase tank reactor containing submerged coated inclined-plates: A computational fluid dynamics approach. *Chemical Engineering Science* 42, 1143 – 1153

Turchi, C.S., Ollis, D. F., 1989. Mixed reactant photocatalysis: intermediates and Mutual rate inhibition. *Journal of Catalysis 119*, 483-96

Turchi, C.S., Lasa, H. D., 1997. Photocatalytic degradation of water organic pollutants, kinetic modelling and energy efficiency. *Industry Engineering and Chemistry Research* 36, 4705-4711

Turchi, C.S., Ollis, D.F., 1988. Photocatalytic reactor design: An example of mass transfer limitations with an immobilized catalyst. *Journal of Physical chemistry* 92, 6852-6853

Turchi C.S., Ollis D.F., 1990. Photocatalytic degradation of organic water contaminant mechanisms involving hydroxyl radical attack. *Journal of Catalysis* 122, 178-92

Tryba, B., 2008. Increase of the photocatalytic activity of TiO_2 by carbon and iron modification. *International Journal of Photoenergy*, Article ID 721824, DOI: 10.1155/2008/ 721824

Turchi C.S., Ollis D.F., 1990. Photocatalytic degradation of organic water contaminant mechanisms involving hydroxyl radical attack. *Journal of Catalysis* 122, 178-92

United Nations Development Program (UNDP) 2006. *Human development report 2006*. Beyond scarcity: power, poverty and the global water crisis.

UNESCO; The 2nd UN World Water Development Report: Water, a shared responsibility; *http://www.UNESCO.org/water/wwdr2/table-contents.shtml*

Vanderhoef, M.A., Annaland, M.V., Kuipers, J., 2004. Computational fluid dynamics for dense gas-solid fluidized beds: a multi-scale modelling strategy. *Chemical Engineering Science* 59, 5157-5165

Valenzuela, M. A., Bosch, P., Jiménez-Becerrill, J., Quiroz,O., Páez,A.I.,2002. Preparation, characterization and photocatalytic activity of ZnO, Fe_2O_3 and $ZnFe_2O_4$. *Journal of Photochemistry and Photobiology A: Chemistry* 148, 177–182

Venkatachalam, N., Palanichamy, M., Murugesan, V.,2007a. Sol–gel preparation and characterization of alkaline earth metal doped nano TiO_2: Efficient photocatalytic degradation of 4-chlorophenol. *Journal of Molecular Catalysis A: Chemical* 273, 177–185

Venkatachalam, N., Palanichamy, M., Arabindo, B., Murugesan, V., 2007b. Enhanced photocatalytic degradation of 4-chlorophenol by Zr^{4+} doped nano TiO_2. *Journal of Molecular Catalysis A: Chemical* 266,158-165

Venkatachalam, N., Palanichamy, M., Arabindoo, B., Murugesan, V., 2007c. Alkaline earth metal doped nanoporous TiO_2 for enhanced photocatalytic mineralisation of bisphenol-A. *Catalysis Communications* 8, 1088–1093

Vora, J.J. Chauhan, S. K., Parmar, K. C., Vasava, S. B., Sharma, S., Bhutadiya, L.S.,2009. Kinetic study of application of ZnO as a photocatalyst in heterogeneous medium. *E-Journal of Chemistry* 6(2), 531-536

Versteeg, H. K., Malalasekera, W., 1995. An introduction to computational fluid dynamics: The finite volume method, Reading, MA: Addison-Wesley.

Vezzoli, M., Martens, W. N., Bell, J. M., 2011. Investigation of phenol degradation: true reaction kinetics on fixed film titanium dioxide photocatalyst. Submitted to *Applied Catalysis B: Environmental*

Vulliet, E., Chovelon, J. M., Guillard,C., Herrmann,J.M.,2003.Factors influencing the photocatalytic degradation of sulfonylurea herbicides by TiO_2 aqueous suspension. *Journal of Photochemistry and Photobiology A: Chemistry* 159,71–79

Wang, W., Chiang, L.W, Ku, Y., 2003. Decomposition of benzene in air streams by UV/TiO_2 process. *Journal of Hazardous Materials* 101, 133-146

Wang, W., Ku, Y., Ma, C.M. Jeng, F. T., 2005. Modelling of the photocatalytic decomposition of gaseous benzene in a TiO_2 coated optical fibre photoreactor. *J. Appl. Electrochem*. 35, 709-714

Wang, Z., Cai, W., Hong, X., Zhao, X., Xu, F., Cai, C., 2005. Photocatalytic degradation of phenol in aqueous nitrogen-doped TiO_2 suspensions with various light sources. *Applied Catalysis B: Environmental* 57, 223-231

Wang, J., Li, R., Zhang, Z., Sun, W., Xie, Y., Xu, R., Xing, Z., Zhang, X., 2008. Solar photocatalytic degradation of dye wastewater in the presence of heat-treated anatase TiO_2 powder. *AIChE, Environmental Progress*, 27: 242–249

Wang. N. Chen, Z., Zhu, L., Jiang, X., Lv, B., Tang, H., 2007. Synergistic effects of cupric and fluoride ions on photocatalytic degradation of phenol. *Journal of Photochemistry and Photobiology A: Chemistry* 191, 193-200

Wawrzyniak, B., Morawski, A. W., Tryba, B., 2006. Preparation of TiO_2-Nitrogen-doped photocatalyst active under visible light. *International Journal of Photoenergy*, Article ID 68248, Pages 1–8 DOI 10.1155/IJP/2006/68248

Watts. R. J., Kong, S., Orr, M. P., Miller, G.C., 1994. Titanium dioxide-mediated photocatalysis of a biorefractory Chloroether in secondary wastewater effluents. *Environmental Technology* 15(5), 469-475

Wei, L., Shifu. C., Wei, Z., Sujuan, Z., 2009. Titanium dioxide mediated photocatalytic degradation of methamidophos in aqueous phase. *Journal of Hazardous Materials* 164, 154–160

Wilcox, D.C., 2004. Turbulence Modelling for CFD (Second ed.).La Canada, California: DCW Industries, Inc.

Wilcox, D. C., 2006. Turbulence Modelling for CFD. DCW Industries, La Cañada, Calif, (Chap. 4)

Wong, C. C., Chu, W., 2003. The direct photolysis and photocatalytic degradation of alachlor at different TiO_2 and UV sources. *Chemosphere* 50, 981-987

Wolfeshtein, M.,1969. The velocity and temperature distribution in one-dimensional flow with turbulence augmentation and pressure gradient. *International Journal of Heat and Mass Transfer* 12, 301-318

Wu, R-J., Chen, C-C., Lu, C-S, Hsu, P-Y., Chen, M-H., 2009a. Phorate degradation by TiO_2 photocatalysis: parameter and reaction pathway investigations. *Desalination*, doi:10.1016/j.desal.2009.03.026

Wu, R., Chena, C., Chen, M., Lu, C., 2009b.Titanium dioxide-mediated heterogeneous photocatalytic degradation of terbufos: Parameter study and reaction pathways. *Journal of Hazardous Materials* 162, 945–953

Xiao, Q., Zhang, J., Xiao, C., Si, Z., Tan, X., 2008. Solar photocatalytic degradation of methylene blue in carbon-doped TiO_2 nanoparticles suspension. *Solar Energy* 82,706-713

Xing, M., Zhang, J., Chen, F., 2009. New approaches to prepare nitrogen-doped TiO_2 photocatalysts and study on their photocatalytic activities in visible light. *Applied Catalysis B: Environmental* 89, 563–569

Yang, Y-T., Hwang, C-Z., 2003. Calculation of turbulent flow and heat transfer in a porous-baffled channel. *International Journal of Heat and Mass Transfer* 46, 771-780

Yan, J., Huang, K., Wang, Y., Liu, S., 2005. Study on anti-pollution nano-preparation of dimethomorph and its performance. *Chinese Science Bulletin* 50(2), 1008-112

Yao., B-H., Wang, C., Wang, Y-X., Zhao, G-Y.,2007. Preparation of performances of RuO_2/TiO_2 films photocatalyst supported on float pearls. *Chinese Journal of Chemical Physics* 20(6), 789-795

Yakhot, V., Orszag, S. A., 1986. Renormalization-Group Analysis of Turbulence. *Physical Review Letters 57*(14), 1722-1724

Yimer, I. Campbel, I., Jiang, L-Y., 2002. Estimation of the turbulent Schmidt number from experimental pro.les of axial velocity and concentration for high- Reynolds-number jet flows. *Canadian Aeronautics Space Journal* 48 (3) 195–200

Yufen, R., Xiaoke, W., Zhiyun, Ouyang, Hua, Z., Xiaonan, D., Hong, M., 2008. Stormwater runoff quality from different surfaces in an urban catchment in Beijing, China. *Water Environment Research* 80(8), 719

Yu, J., Wang, J., Zhang, J., He, Z., Liu, Z., Ai, X., 2007. Characterization and photoactivity of TiO_2 sols prepared with triethylamine. *Materials Letters* 61, 4984–4988

Zalazar, C.S., Labas, M. D., Martin, C. A., Brandi, R.J., Cassano, A.E., 2004. Reactor Scale-Up in AOPs: from laboratory to Commercial Scale. *Water Science and Technology*, 49(4), 13-18

Zaleska, A., Sobczak, J. W., Grabowska, E., Hupka, J., 2008. Preparation and photocatlytic activity of boron- modified TiO_2 under UV and visible light. *Applied Catalysis B: Environmental* 78, 92-100

Zhao, D., Wang, J., Zhang, Z., Zhang, J., 2009a. Photocatalytic degradation of omethoate using NaY Zeolite- supported TiO_2. *Frontiers Chemical Engineering in China* 3(2), 206-210, DOI 10.1007/11705-009-0053-4

Zhao, D., Wang, J., Zhang, Z., Zhao, X., Zhang, J., 2009b. TiO_2/NaY composite as photocatalyst for degradation of omethoate. *Chemistry Research in Chinese Universities* 25(4), 543-549

Zhang, L., Yan, F., Su., M., Han, G., and Kang, P., 2009. A study on the degradation of methamidophos in the presence of nano-TiO_2 catalyst doped with Re. *Russian Journal of Inorganic Chemistry* 54(8), 1210-1216

Zhang, C., Chen, Y., Shi, M., 2010. Effects of roughness elements on laminar flow and heat transfer in microchannels. *Chemical Engineering and Processing* 49, 1188-1192

Zhang,Y., Crittenden, J.C., Hand, D.W., Perram, D.L., 1994. Fixed bed photocatalysts for solar decontamination of water. *Enviornmental Scienc and Technology* 28, 435-442

Zhou, Z., and Ray,A.K., 2003. Kinetic studies for photocatalytic degradation of Eosin B on a thin film of titanium dioxide. *Industry Engineering and Chemistry Research* 42, 6020-6033

Zhu, J., Chen, F., Zhang, J., Chen, H., Anpo, M., 2006. Fe^{3+}-TiO_2 photocatalysts prepared by combining sol-gel method with hydrothermal treatment and their characterization. *Journal of Photochemistry and Photobiology A: Chemistry* 180,196-204

Zhu, X., Yuan, C., Bao, Y., Yang, J.Wu, Y., 2005. Photocatalytic degradation of pesticide pyridaben on TiO_2 particles. *Journal of Molecular Catalysis: Chemical* 229, 95-105

Zimont, V. L., 2000. Gas premixed combustion at high turbulence. turbulent flame closure comustion model. *Experimental Thermal and Fluid Science*, 21:179–186

Zydney, A. L., Colton, C. K., 1986. A concentration polarization model for the filtrate flux in cross-flow microfiltration of particulate suspensions. *Chemical Engineering Communication* 47, 1–21